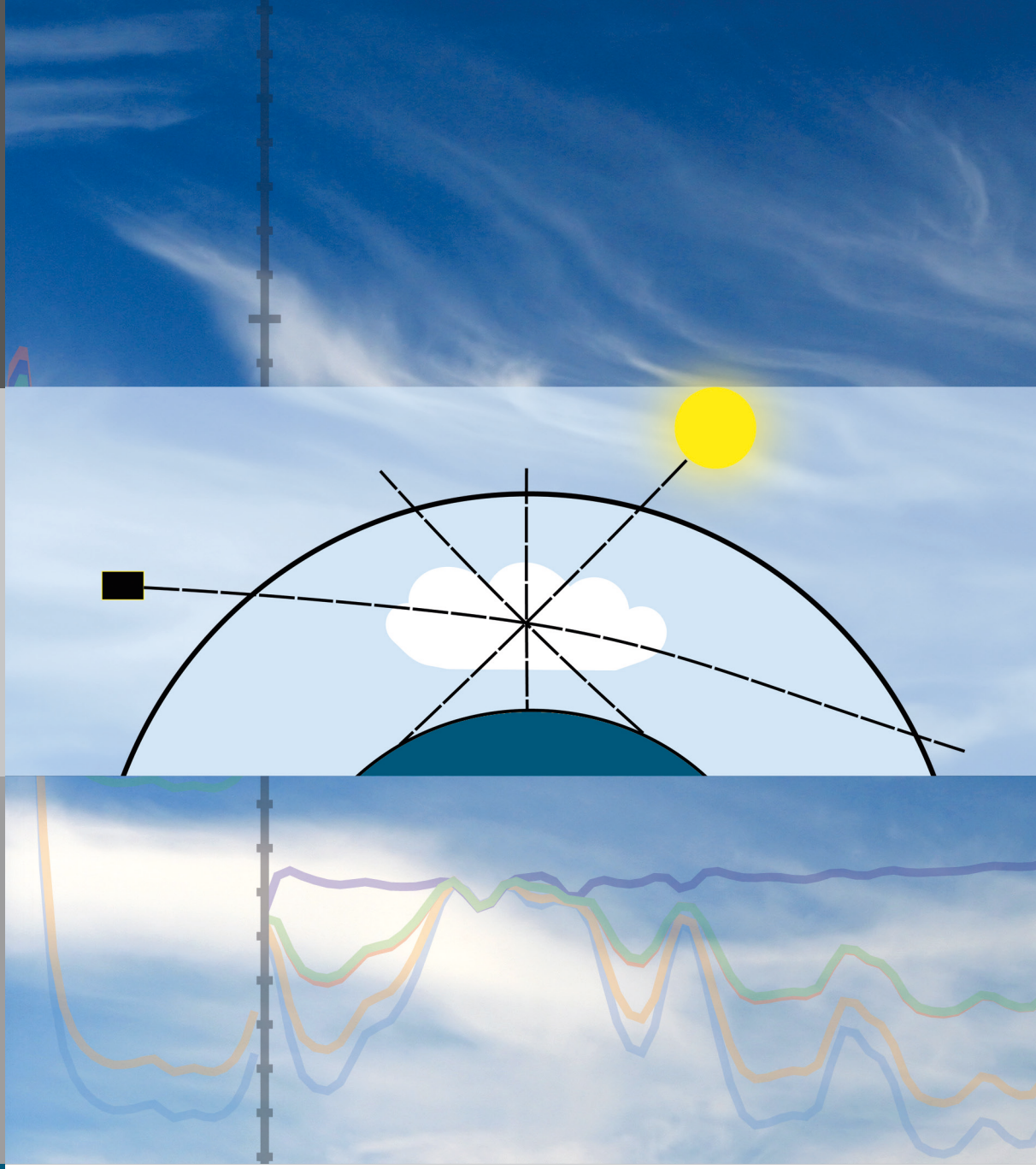

# Clouds and aerosol in infrared radiative transfer calculations for the analysis of satellite observations

Sabine Grießbach

Member of the Helmholtz Association

JÜLICH
FORSCHUNGSZENTRUM

Schriften des Forschungszentrums Jülich
Reihe Energie & Umwelt / Energy & Environment Band / Volume 139

Forschungszentrum Jülich GmbH
Institute of Energy and Climate Research (IEK)
Stratosphere (IEK-7)

# Clouds and aerosol in infrared radiative transfer calculations for the analysis of satellite observations

Sabine Grießbach

Schriften des Forschungszentrums Jülich
Reihe Energie & Umwelt / Energy & Environment Band / Volume 139

ISSN 1866-1793 ISBN 978-3-89336-785-6

Bibliographic information published by the Deutsche Nationalbibliothek.
The Deutsche Nationalbibliothek lists this publication in the Deutsche Nationalbibliografie; detailed bibliographic data are available in the Internet at http://dnb.d-nb.de.

| | |
|---|---|
| Publisher and Distributor: | Forschungszentrum Jülich GmbH<br>Zentralbibliothek<br>52425 Jülich<br>Phone +49 (0) 24 61 61-53 68 · Fax +49 (0) 24 61 61-61 03<br>e-mail: zb-publikation@fz-juelich.de<br>Internet: http://www.fz-juelich.de/zb |
| Cover Design: | Grafische Medien, Forschungszentrum Jülich GmbH |
| Source Cover Image: | © Thierry Maffeis (cirrus clouds) / Fotolia.com |
| Printer: | Grafische Medien, Forschungszentrum Jülich GmbH |
| Copyright: | Forschungszentrum Jülich 2012 |

Schriften des Forschungszentrums Jülich
Reihe Energie & Umwelt / Energy & Environment Band / Volume 139

D 468 (Diss., Wuppertal, Univ., 2011)

ISSN 1866-1793
ISBN 978-3-89336-785-6

The complete volume is freely available on the Internet on the Jülicher Open Access Server (JUWEL) at http://www.fz-juelich.de/zb/juwel

# Abstract

High-altitude clouds play an important role in the Earth's atmosphere. Polar stratospheric clouds are involved in processes leading to polar ozone destruction. The radiative impact of cirrus clouds is one of the least understood processes affecting the climate. Aside from this, clouds and aerosols affect the measured spectra of remote sensing instruments such as the Michelson Interferometer for Passive Atmospheric Sounding Envisat (MIPAS). In this thesis, the JUelich RApid Spectral SImulation Code (JURASSIC), which is a spectrally averaging forward model, was substantially extended by implementing a scattering module to account for scattering on aerosols and clouds. The new code was carefully cross-checked at a high spectral resolution with the well-established line-by-line models Reference Forward Model (RFM) and the Karlsruhe Optimized and Precise Radiative transfer Algorithm (KOPRA). The comparison shows that JURASSIC agrees with RFM within the MIPAS noise equivalent radiance. At several line centres, larger differences were found up to a factor of 7 of the noise equivalent radiance at the $792\,\mathrm{cm}^{-1}$ $CO_2$ line centre. The difference between RFM and KOPRA was as much as a factor of 55 of the noise equivalent radiance at this line centre. This may have implications for temperature retrievals in the troposphere. The microphysical properties of stratospheric and tropospheric aerosol and cloud particles required for the scattering calculations are collected. The single scattering properties and their effect on simulated spectra are studied. Because of the large variability of the tropospheric aerosol it is found that tropospheric aerosol extinction coefficients in the infrared generally should not be scaled from one wavelength to another. Instead it is suggested that the extinction coefficient for every wavelength should be calculated. Due to the lack of information on the vertical profile of aerosol log-normal parameters, which are of great value not only for remote sensing applications, but also for climate modelling and cloud simulations, a new climatology is compiled from published log-normal distributions. A first study on the detectability and discrimination of measured volcanic ash particles of the Eyjafjallajökull eruption with MIPAS demonstrates that MIPAS is able to detect and discriminate volcanic ash. The MIPAS measurements are used to assess the quality of the predictions of the location of the ash cloud by the EURopean Air pollution Dispersion model (EURAD). It was found that the model predicts ash cloud filaments where no particles are detected in MIPAS. Further, for several profiles the model overestimates the altitude of the ash layer by up to 3 km. The spectra of profiles in which clouds are detected, however, resemble ice cloud spectra. No unambiguous ash cloud spectrum could be identified in MIPAS observations.

# Zusammenfassung

Hochreichende Wolken spielen eine wichtige Rolle in der Erdatmosphäre. Polare Stratosphärenwolken sind nachweislich verknüpft mit den Ozonabbauprozessen, die zum Ozonloch führen. Der Einfluss von Cirruswolken auf den Strahlungshaushalt ist einer der am wenigsten verstandenen Klimafaktoren. Außerdem beeinflussen Wolken die von Fernerkundungsinstrumenten wie Michelson Interferometer for Passive Atmospheric Sounding Envisat (MIPAS) gemessenen Spektren. Um bei der Auswertung der Spektren die Streuung von Strahlung an Aerosol- und Wolkenteilchen berücksichtigen zu können, wurde in dieser Arbeit das spektral integrierende Vorwärtsmodell JUelich RApid Spectral SImulation Code (JURASSIC) wesentlich erweitert, indem ein Streumodul entwickelt wurde. Der neue Code wurde sorgfältig mit den anerkannten monochromatisch rechnenden Modellen Reference Forward Model (RFM) und Karlsruhe Optimized and Precise Radiative transfer Algorithm (KOPRA) verglichen. Der Vergleich zeigt, dass JURASSIC sehr gut mit RFM übereinstimmt. Die Abweichungen waren meist kleiner als die rauschäquivalente Strahlungsdichte. An einigen Linienzentren gab es größere Abweichungen, die die rauschäquivalente Strahlungsdichte bis um das Siebenfache überschritten, wie im Fall des $CO_2$ Linienzentrums bei $792\,\mathrm{cm}^{-1}$. Allerdings überschreiten die Unterschiede zwischen RFM und KOPRA an diesem Linienzentrum die rauschäquivalente Strahlungsdichte um das 55fache. Diese großen Unterschiede dürften Auswirkungen auf Temperaturretrieval in der Troposphäre haben. Die mikrophysikalischen Eigenschaften von stratosphärischem und troposphärischem Aerosol und Wolken, die für die Berechnung der Streuparameter benötigt werden, wurden zusammengetragen. Die Streuparameter sowie ihre Auswirkungen in simulierten Spektren wurden systematisch untersucht. Wegen der großen Variabilität des tropsphärischen Aerosols können Extinktionskoeffizienten nicht mit hoher Genauigkeit von einer Wellenlänge auf eine andere skaliert werden. Vielmehr sollte die Berechnung explizit für die gewünschte Wellenlänge durchgeführt werden. In Ermangelung von vertikal aufgelösten Klimatologien von troposphärischen Aerosolgrößenverteilungsparametern wurde eine Datenbank von publizierten Lognormal-Verteilungen erstellt. Diese Datenbank ist nicht nur für Fernerkundungsanwendungen von großem Wert, sondern auch für Klimamodellierungen und Wolkensimulationen. Eine erste Studie zur Detektierbarkeit und Identifizierbarkeit von vulkanischem Aerosol des Ausbruchs des isländischen Vulkans Eyjafjallajökull mit MIPAS wurde durchgeführt. Es zeigte sich, dass MIPAS in der Lage ist, die vulkanischen Aerosolpartikel zu detektieren und von Wolken zu unterscheiden. Bei der Analyse der vermeintlich aschehaltigen gemessenen Spektren zeigte sich, dass keine eindeutigen Aschesignaturen vorhanden waren. Vielmehr wurden Cirruswolken beobachtet. Im Rahmen dieser Studie wurde die Qualität der Ascheausbreitungssimulationen des EURopäischen Ausbreitungs- und Depositionsmodells (EURAD) überprüft. Es konnte gezeigt werden, dass EURAD die Asche zum Teil an den falschen geographischen Koordinaten und in zu großen Höhen simuliert.

# Contents

# Chapter 1

# Introduction

Clouds in the upper troposphere and stratosphere play an important role in the Earth's radiation budget by absorbing and transmitting the radiance emerging from the Sun and the Earth's surface. According to IPCC (2001) the level of scientific understanding of the contribution of cirrus clouds to the radiative forcing is very poor. Besides, clouds also play an important role in the life cycle of the Earth's most important green house gas water vapour. They do not only contribute to the Earth's energy exchange through the transport of water in the troposphere, they also are involved in processes hydrating and dehydrating the stratosphere through tropical cirrus clouds (e.g., Davis et al., 2010). High-altitude clouds also provide the surfaces for heterogeneous chlorine reactions, which lead to ozone destruction in the polar stratosphere and the tropopause region (Solomon et al., 1986; Solomon et al., 1997).

For estimations of the influence of cirrus clouds on the radiative forcing climatological data about the cloud occurrence frequency as well as information about micro-physical properties are needed. A global data set on clouds, which provides climatologies and monitors changes, is provided by the International Satellite Cloud Climate Project (ISCCP), which collects data from satellite measurements since July 1983 (Rossow and Schiffer, 1999). In Figure 1.1 the annual mean cloud coverage for July 1983 – June 2008 is shown. Generally the highest cloud occurrence frequencies are found in the maritime mid-latitudes with more than 80%. For the high-altitude clouds however, the maximum is found in the tropics, with more than 45% occurrence frequency. The radiance data for the ISCCP cloud climatologies is solely obtained from passive nadir viewing weather satellites.

In a recent study in the tropics, Davis et al. (2010) showed that even an active lidar instrument with nadir viewing geometry specialised on cloud and aerosol detection such as the Cloud–Aerosol Lidar and Infrared Pathfinder Satellite Observation (CALIPSO)

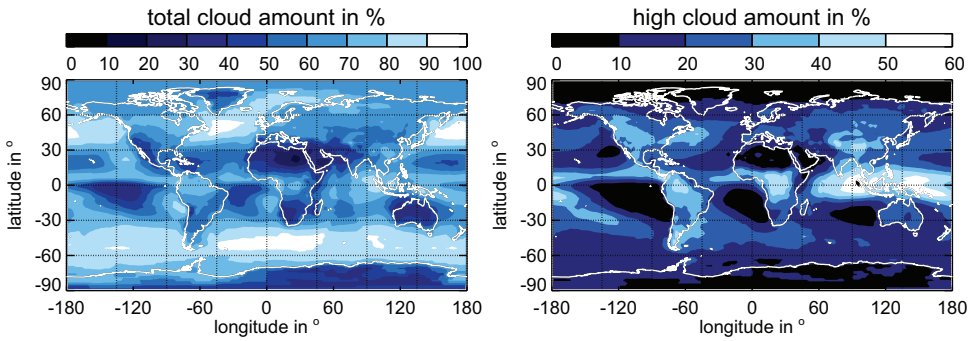


***Figure 1.1:*** *Climatology for 07/1983 – 06/2008 of the total cloud amount (left panel) and high-altitude cloud amount (right panel). The ISCCP D2 data were obtained from the International Satellite Cloud Climatology Project web site ISCCP (2011).*

is likely to miss up two thirds of sub-visible cirrus clouds (SVC) measured with in situ instruments. SVCs are optically and vertically very thin cirrus clouds near the tropopause with an optical depth smaller than 0.03 (Sassen et al., 1989). As aircraft cloud measurements near the tropical tropopause are rare, little is known about the spatial and temporal distribution and variability of micro-physical properties of the SVCs. Hence their radiative impact on the energy budget is not properly accounted for in climate models.

Calculations of the radiative forcing of cirrus clouds net effect are controlled by the cirrus crystal size distribution and their shape (Zhang et al., 1999). The radiative forcing net effect of cirrus clouds is the sum of the radiative forcing due to the solar radiance and the infrared radiance, which both depend on particle shape and size. Therefore it is difficult to get an accurate estimation. In Figure 1.2 the cloud radiative forcing as a function of the mean crystal size and the shape is shown. Clearly, the net effect strongly depends on both, crystal size and shape. High-altitude cirrus clouds cause positive net radiative forcing (Lee et al., 2009). However for the SVCs, whose size distributions have effective radii between 8 – 11 $\mu$m (Lawson et al., 2008), the net radiative forcing is negative.

Limb measurement experiments are highly sensitive to clouds due to long paths through the atmosphere. A first climatology of total cloud occurrence frequency including SVCs measured by the Stratospheric Aerosol and Gas Experiment II (SAGE II) at visible and near-infrared wavelengths was presented by Wang et al. (1996). The maximum SVC occurrence frequency of about 45% was found near the equator at 15 km altitude. In mid- and high latitudes the occurrence frequency reaches up to 20%. The SVCs were found to reach up to 3 km above the mean tropopause altitude. In the mid-infrared Mergen-

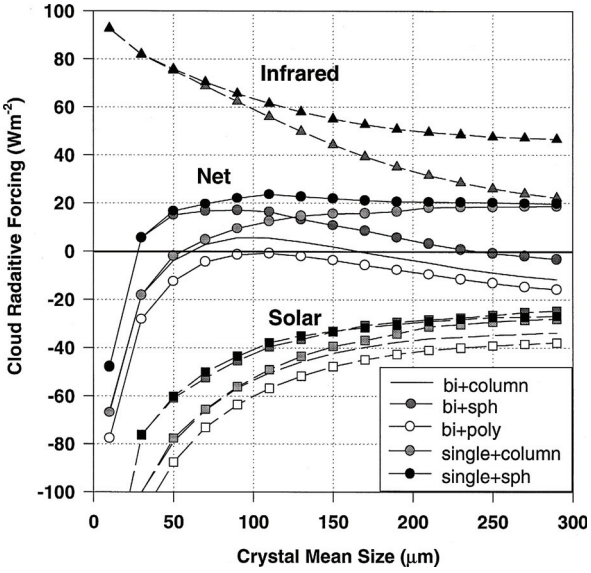


***Figure 1.2:*** *Radiative forcing as a function from particle size and shape. Figure from Zhang et al. (1999)*

thaler et al. (1999) confirmed the results deduced from SAGE II measurements with data from the Cryogenic Limb Array Etalon Spectrometer (CLAES). Also Cryogenic Infrared Spectrometers and Telescopes for the Atmosphere (CRISTA) observations are in good agreement with SAGE (Spang et al., 2002). For the currently operating Michelson Interferometer for Passive Atmospheric Sounding (MIPAS) (Fischer et al., 2008), Spang et al. (2004) and Greenhough et al. (2005) presented studies addressing cloud detection and cloud occurrence frequencies.

However, as mentioned before, the particle size and shape also must be known for radiative forcing calculations. Knowledge only about occurrence frequency and cloud top height is not sufficient. Going one step further in the recently finished European Space Agency (ESA) project MIPclouds (Spang et al., 2011), a method to distinguish liquid and frozen cloud particles as well as a retrieval of the effective radius of high-altitude clouds is developed. Furthermore the differentiation between the types of polar stratospheric clouds (PSC) is addressed. Spang et al. (2004) and Höpfner et al. (2009) showed that different types of PSCs can be distinguished the MIPAS spectra.

The main application of infrared limb sounding instruments is to derive trace gas concentrations from the measured radiances. The tangent heights of the MIPAS instrument reach down to 6 km, an altitude well within the troposphere. The cloud oc-

currence frequency in the upper tropical troposphere is about 45% (Wang et al., 1996; Mergenthaler et al., 1999). Currently, no reasonable trace gas retrieval for infrared limb measurements can be performed from cloud-contaminated spectra. However, just considering the remaining 55% cloud free spectra will definitively lead to biased trace gas climatologies, in particular for water vapour.

Another uncertainty factor that distorts the trace gas retrievals are the omnipresent aerosol particles. Generally in the stratosphere the aerosol particle composition and size distribution is quite homogeneous. However, in case of volcanic eruptions such as Mount Pinatubo in June 1991, the amount of aerosol particles significantly increases and causes errors in trace gas retrievals. Under these circumstances information on stratospheric aerosol needs to be retrieved to obtain reliable trace gas retrievals (Hervig et al., 1995). For aerosol in the upper troposphere no climatology is available (Gras, 2003). Numerous measurements however indicate that it is not as homogeneous as the commonly used term background aerosol implies (Clarke and Kapustin, 2002). Rather there are regions in the upper troposphere in which nucleation occurs and the particle number concentration increases (Yu et al., 2010).

The scattering of radiance in the infrared on atmospheric particles must be considered to get an appropriate aerosol correction, to allow for trace gas retrievals in thin clouds and to be able to retrieve micro-physical cloud parameters. In this work aerosol and cloud particles that are relevant in the upper troposphere and the stratosphere and their micro-physical properties are compiled and introduced in Chapter 2. Assuming the particles to be spherical their single scattering properties are calculated, applying Mie theory, and presented in Chapter 3. As ice crystals usually are not spherical, bulk scattering properties for non-spherical cirrus crystals are also shown. So far scattering is mostly implemented in line-by-line radiative transfer models (e.g., Höpfner and Emde, 2005). However, line-by-line forward calculations as well as scattering calculations are computationally expensive. To overcome this obstacle, fast band models are often employed for the near-real-time operational processing (Francis et al., 2006). For that reason the Mie scattering as well as an interface for the use of databases containing scattering parameters for non-spherical ice crystals are implemented in the spectrally averaging JUelich RApid Spectral SImulation Code (JURASSIC) (Hoffmann, 2006), which is described in Chapter 4. In Chapter 5 JURASSIC is shown to be capable of reproducing the results of the established line-by-line model Karlsruhe Optimized and Precise Radiative transfer Algorithm (KOPRA). An extensive and systematic model comparison quantifies the differences in three micro-windows relevant to cloud parameter retrieval and one micro-window relevant to temperature and trace gas retrievals without and with clouds. The application of scattering in a forward calculation of spectra suspected to contain volcanic ash from the recent Eyjafjallajökull eruption in 2010 is presented in Chapter 6 and compared with MIPAS spectra.

# Chapter 2

# Aerosol and Clouds

Atmospheric aerosol is a mixture of liquid or solid particles and air. This definition also includes clouds which are visible aerosol particles. However, traditionally in atmospheric sciences cloud particles, which are hydro-meteors, are distinguished from other aerosol particles. Like the gaseous components of the atmosphere also aerosol and clouds contribute to the radiative emission of the atmosphere. In the infrared spectral region typically only emission and absorption need to be taken into account for the gaseous components, but for aerosol particles and clouds, the scattering of radiance also needs to be considered. For trace gas retrievals usually cloud free measurements are chosen and scattering of radiance can be neglected. However, aerosol is always present, so a precise treatment is desirable (Hervig et al., 1995). To understand and model the radiative effects some basic knowledge about macro- and micro-physical properties of aerosol and clouds is necessary and summarised in this chapter.

## 2.1 Stratospheric Aerosol and Clouds

The stratospheric aerosol layer, also known as the Junge layer, was first reported by Junge et al. (1961). It covers the whole Earth and is quite uniform in time and latitude. The layer extends from about 15 – 30 km with maximum particle concentrations around 20 km. The particles mainly consist of a 75% $H_2SO_4$/25% $H_2O$ solution of sulfuric acid and water. One source for the sulfuric acid droplets are natural carbonyl sulfide (OCS) emissions at the Earth's surface with the OCS being photo-oxidised to sulfate in the stratosphere. However the main contribution comes from high reaching volcanic eruptions that inject $SO_2$ into the stratosphere, which converts to sulfuric acid droplets. The residence time of these particles is about two years.

In the polar winter stratosphere at temperatures below 195 K the background aerosol droplets can grow by $H_2O$ and $HNO_3$ uptake and form polar stratospheric clouds (PSCs). These clouds typically occur at altitudes between 15 – 25 km. Depending on temperature different types of cloud particles or mixtures develop, and are commonly categorised into two types. Type I PSCs already form above the ice frost point and are divided again into Type Ia and Type Ib for solid and liquid particles respectively.

Type Ia PSCs consist of nitric acid trihydrate particles $HNO_3{\cdot}3H_2O$ (NAT). Measured particle radii range from 0.5 – 4 $\mu$m. A well established theory by Peter (1997) suggests that the NAT particles are formed from liquid Type Ib (see below) particles which serve as condensation nuclei for the ice phase and then get coated by NAT. For this process the temperatures must fall below the ice frost point, which is around 188 K for polar stratospheric conditions. The NAT equilibrium temperature is around 196 K (Hanson and Mauersberger, 1988; Peter, 1997). However measurements of Larsen et al. (2004) show NAT particles that have formed under conditions not reaching the ice frost point. The formation processes as well as microphysical properties such as the shape of NAT particles is not fully understood and hence subject to current research.

Type Ib are supercooled ternary solutions (STS) consisting of sulfuric acid, nitric acid and water ($H_2SO_4/HNO_3/H_2O$) with temperature dependent mixing ratios (Carslaw et al., 1994). They form at temperatures below 193 K (Peter, 1997) and have typical radii around 0.3 $\mu$m. Often the PSCs are not of one type but mixed clouds as recent measurements by Larsen et al. (2004), Höpfner et al. (2009) and Pitts et al. (2009) report.

The Type II PSCs consist of ice and require temperatures below the ice frost point of about 188 K to form. Their typical radii are larger than 5 $\mu$m. In the Antarctic these temperatures are reached every winter and PSC conditions persist up to several months, whereas in the Arctic these conditions last only several days up to weeks. Regularly cold temperatures are induced by mountain waves. These PSCs have a typical lifetime of several hours (Eckermann et al., 2009).

Observations of cirrus cloud particles in the lower tropical stratosphere have been reported by de Reus et al. (2009). The ice crystals were found above an overshooting large convective system up to 1.4 km above the local tropopause. At mid-latitudes Keckhut et al. (2005) reported cirrus clouds detected by lidar measurements, which reached up to 3 km above the local (dynamical 1.6 PVU) tropopause. A trajectory analysis indicated that moist subtropical upper tropospheric air was transported quasi-isentropically into the mid-latitudinal lowermost stratosphere.

## 2.2 Tropospheric Aerosol and Clouds

Tropospheric aerosol is highly variable in space, time and composition while measurements are sparse and irregular in location and time. Hence there is no global climatology of tropospheric aerosol available (Clarke and Kapustin, 2002; Gras, 2003). In the boundary layer there are countless measurements of aerosol properties while there are less numerous measurements in the free troposphere. However, these measurements already provide valuable basic knowledge about size distributions, chemical compositions and seasonal, regional and altitudinal variability.

One distinguishes primary and secondary aerosol. Primary aerosol particles are directly emitted into the atmosphere whereas secondary aerosol forms chemically by gas-to-particle conversion from the atmospheric gaseous constituents or by chemical conversion of primary aerosol. Aerosols serve as condensation nuclei for cloud particles. As cloud particles often evaporate several times before forming rain drops, cloud processing also changes the properties of the aerosol before being washed out.

For satellite infrared limb measurements the tropospheric aerosol above about $4-5\,\mathrm{km}$ altitude is often important. About 15 years ago it was generally accepted that the number concentration of the so-called background aerosol decreases exponentially from the ground to the free troposphere and remains at a constant low level up to the tropopause (Jaenicke, 1993). However, over time many new measurements became available and a more differentiated view has evolved. Several in situ measurements at high-altitude mountain stations (Nyeki et al., 1998; Venzac et al., 2009; Kivekäs et al., 2009; Schmeissner et al., 2011) and from airborne platforms (Kim et al., 1993) show distinct seasonal cycles. In other publications, layers of enhanced concentrations are reported (Han et al., 2003; Petzold et al., 2002). Measurements also show that under certain conditions the upper tropospheric region is a region of aerosol production (Clarke and Kapustin, 2002; Petzold et al., 2002) so that the particle number concentration of the fine particle mode is increased.

Most of the large primary aerosol particles such as sea salt or mineral dust usually do not reach the middle troposphere because they sediment fast within days. Measurements of the composition of free tropospheric aerosol (Schneider et al., 2006; Cozic et al., 2008; Murphy et al., 2006) indicate that, depending on season, organic aerosol constitutes the largest part of the aerosol mass followed by sulfate and ammonium.

The cloud types found in the upper troposphere are, according to the recent WMO classification system (Deutscher Wetterdienst, 1990), cirrus, cirrostratus and cirrocumulus. Cirrus clouds consist of ice crystals whereas cirrocumulus and cirrostratus may also contain supercooled water droplets. Water droplets can exist down to the threshold temperature for homogeneous freezing of about $-40\,^{\circ}\mathrm{C}$ (Lynch et al., 2002). Besides

the defined cirrus clouds in the upper troposphere also contrails and subvisible cirrus clouds can be found.

Cirrus cloud formation can occur all over the globe. It depends on water vapour pressure, temperature and condensation nuclei availability. So, it is closely related to regional meteorological processes. Due to this regionality the properties of cirrus clouds such as ice water content (IWC), particle shape and number density as well as horizontal and vertical extent may differ significantly.

Contrails (condensation trails) are human-induced cirrus clouds. They form in the wake of airplanes when emitted water vapour and condensation nuclei mix with the ambient air. The resulting trail consists of a very small ice crystals in a high number concentration. Under certain conditions such as high humidity the contrails develop into a cirrostratus and become indistinguishable from natural cirrus (Lynch et al., 2002), which is called contrail induced cirrus.

Subvisible cirrus clouds (SVC) (also subvisual cirrus) are thin cirrus clouds with optical depths lower than 0.03 in the visible (Lynch et al., 2002). They consist of rather small particles with radii up to 50 $\mu$m (Lawson et al., 2008) (in one measurement particles larger than 50 $\mu$m were found (Heymsfield, 1986)), and occur in very thin layers with a vertical extent of up to 1 km (Davis et al., 2010). SVCs are mainly detected near the tropical tropopause at altitudes between 15 – 20 km and temperatures below $-70$ °C (Lynch et al., 2002) but have also been observed at mid-latitudes (Sassen and Campbell, 2001; Lawson et al., 2008). Their global and annual occurrence is poorly determined because they are hardly detectable by most instruments (Lynch et al., 2002; Davis et al., 2010). However there are some climatologies from remote sensing instruments (Wang et al., 1996; Spang et al., 2002). Ultrathin tropical tropopause clouds (UTTCs) belong to the class of SVCs (Peter et al., 2003).

## 2.3 Microphysical Properties

To include aerosol and clouds in radiative transfer calculations, their optical properties must be known. The optical properties are determined by three microphysical properties: the number size distribution, the complex refractive indices and the particle shape. The following subsections give a brief introduction into these fundamental quantities.

| Particle Type | Mode | $n_i$ in $cm^{-3}$ | $\mu_i$ in $\mu m$ | $\sigma_i$ | Source |
|---|---|---|---|---|---|
| Stratospheric aerosol | 1 | 23.81 | 0.0217 | 1.77 | Jaenicke (1988) |
| Tropospheric aerosol | 1 | 227.96 | 0.05 | 1.71 | Nyeki et al. (1998) |
| PSC | 1 | 8.23 | 0.26 | 1.39 | Deshler et al. (2000) |
| | 2 | 0.005 | 1.68 | 1.34 | |
| Stratospheric cirrus | 1 | 0.101 | 4.5 | 1.55 | de Reus et al. (2009) |
| | 2 | 2.303 | 12.5 | 1.55 | |
| | 3 | $9.21 \cdot 10^{-4}$ | 32.5 | 1.75 | |
| Sub-visible cirrus | 1 | 0.032 | 3.6 | 1.6 | Iwasaki et al. (2007) |
| Cirrus | 1 | 0.055 | 81 | 1.8 | Tian et al. (2010) |

***Table 2.1:*** *Log-normal number size distribution parameters for Equation 2.1 for the size distributions shown in Figure 2.1.*

### 2.3.1 Size Distribution and Effective Radius

To describe the size distribution for aerosol particles (Jaenicke, 1993; Hinds, 1999) and polar stratospheric clouds (Deshler et al., 2003) usually a multimodal log-normal size distribution is used:

$$\frac{\mathrm{d}N(r)}{\mathrm{d}r} = \sum_{i=1}^{n} \frac{n_i}{\sqrt{2\pi}\ln\sigma_i r} \exp\left[-\frac{(\ln r - \ln\mu_i)^2}{2(\ln\sigma_i)^2}\right] \tag{2.1}$$

where $\frac{\mathrm{d}N}{\mathrm{d}r}$ is the concentration of particles in the radius interval $[r, r + \mathrm{d}r]$. The three parameters $n_i$, $\sigma_i$, $\mu_i$ represent the total number concentration, the distribution width and the median radius of the mode with index $i$. Other common distributions especially for clouds are the gamma and general exponential distribution. However for cirrus clouds a recent study by Tian et al. (2010) showed that the log-normal distribution provides the best fit. For stratospheric aerosol and PSCs a large amount of number size distribution parameters have been measured and published (Deshler, 2011; Hofmann and Deshler, 1991). For SVCs and stratospheric clouds there are only a few log-normal distribution parameters published by Rosenfield et al. (1998), de Reus et al. (2009), and Frey et al. (2011). For cirrus clouds there are many measurements, but log-normal distribution parameters are rare. Some can be found in e.g. Tian et al. (2010).

Figure 2.1 shows typical number size distributions for the different aerosol types and clouds introduced in Sections 2.1 and 2.2. Within the specific size ranges, the number of modes and concentrations of each aerosol and cloud type varies heavily. The log-normal parameters for the number size distributions are listed in Table 2.1.

Figure 2.2 depicts a mean vertical profile of 241 aerosol particle number size distri-

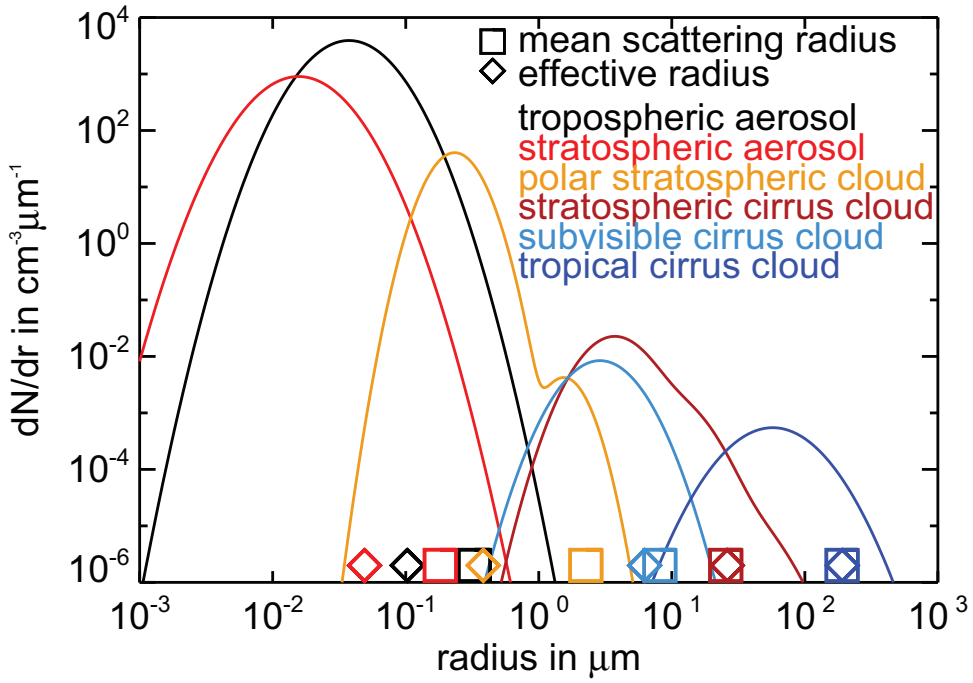


***Figure 2.1:*** *Typical number size distributions for tropospheric and stratospheric aerosol, a PSC, an SVC and a cirrus cloud. For each number size distribution the mean scattering radius and the effective radius for a wavelength of 10 µm is calculated (see Equations 3.7 and 2.2). The data is taken from Nyeki et al. (1998) (tropospheric aerosol annual mean), Jaenicke (1988)(stratospheric aerosol), Deshler et al. (2000) (PSC at 23.89 km), de Reus et al. (2009) (stratospheric cirrus), Iwasaki et al. (2007) (SVC case 1), Tian et al. (2010) (cirrus case 2 at 40 km relative distance.) The mean scattering radius is defined and discussed in detail in Section 3.2.*

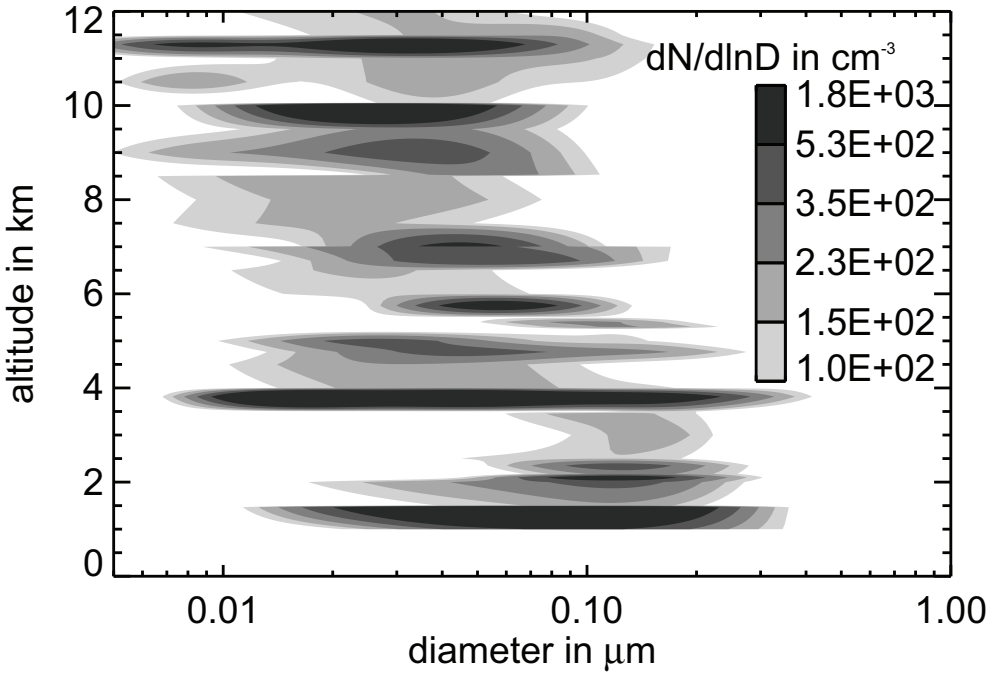


***Figure 2.2:*** *Mean vertical profile of 241 measured aerosol number size distributions collected from the literature (see Appendix A). At altitudes between 10 – 12 km the plot shows high concentrations of small freshly nucleated particles.*

butions collected from the literature (see Appendix A). There is a large number of published measurements of vertical aerosol number size distributions, but most authors do not report fitted size distribution parameters. Here all available log-normally parameterised data are used for the averaged vertical profile in Figure 2.2. For better statistics e.g. the discrimination between tropical and mid-latitudinal profiles it would be desirable to have more parameterised number size distributions available. The layered structure of the profile is due to the fact that it is not composed of complete vertical profiles as in Clarke and Kapustin (2002) but rather a composition of single measurements made at different times, altitudes and locations. The main feature is that the mode maxima move to smaller particles with altitude and high particle concentrations also can be found in the upper troposphere. This is consistent with the observations Clarke and Kapustin (2002) made for six equatorial vertical profiles.

For inversion problems, such as the retrieval of atmospheric parameters from remote sensing measurements, it is desirable to have less free parameters than those required to

describe the full size distribution ($n_i$, $\mu_i$, $\sigma_i$) (Iwasaki et al., 2007). Therefore an effort was made to find representative parameters for the number size distribution (Hansen and Travis, 1974). A commonly used parameter to describe the size distribution is the effective radius $r_{\text{eff}}$, which is defined as the ratio between the volume and the surface of the particles:

$$r_{\text{eff}} = \frac{\int_{r_1}^{r_2} \pi r^3 \frac{\mathrm{d}N}{\mathrm{d}r} \,\mathrm{d}r}{\int_{r_1}^{r_2} \pi r^2 \frac{\mathrm{d}N}{\mathrm{d}r} \,\mathrm{d}r} \tag{2.2}$$

If the number size distribution $N(r)$ can be described by a mono-modal log-normal distribution, the effective radius may be expressed as

$$r_{\text{eff}} = \mu \exp\left[2.5(\ln \sigma)^2\right], \tag{2.3}$$

where $\mu$ is the median parameter of a mono-modal log-normal distribution and $\sigma$ the width. Thus, the effective radius represents the combination of the $\mu$ and $\sigma$ parameters of a size distribution. The relevance of the effective radius to scattering on aerosol and cloud particles in the infrared is discussed in Section 3.2.

### 2.3.2 Complex Refractive Indices

The complex refractive index of a substance is characteristic for its chemical composition. It depends on the wavelength and is important for the radiative properties of aerosol and cloud particles, because the real part characterises the wavelength dependent scattering and the imaginary part the absorption of a particle. For non-absorbing particles the imaginary part is zero.

Spectrally resolved complex refractive indices in the mid-infrared for aerosol and cloud particles can be obtained from several sources. The High Resolution Transmission spectral database (HITRAN) (Rothman et al., 2009) provides the most comprehensive data set. In the following, the refractive indices are discussed for the spectral range of $4-16\,\mu$m ($2500-625\ \text{cm}^{-1}$). For several substances multiple measurements exist in HITRAN. For these cases the most appropriate data sets for the atmospheric conditions, in which the particles are most likely to be found, are chosen.

Stratospheric aerosol particles consist mainly of $H_2SO_4/H_2O$ droplets (Junge et al., 1961). The weight percentages are temperature dependent and vary between 80 – 45 wt% $H_2SO_4$ for $230-195\,$K. In Figure 2.3 the yellow curve shows the refractive indices of a 75 wt% sulfuric acid solution at 215 K. This concentration is thermodynamically most likely and is consistent with measurements (Steele et al., 2003). The data presented are from Hummel et al. (1988), which is summarised in the so-called Shettle data subset of HITRAN.

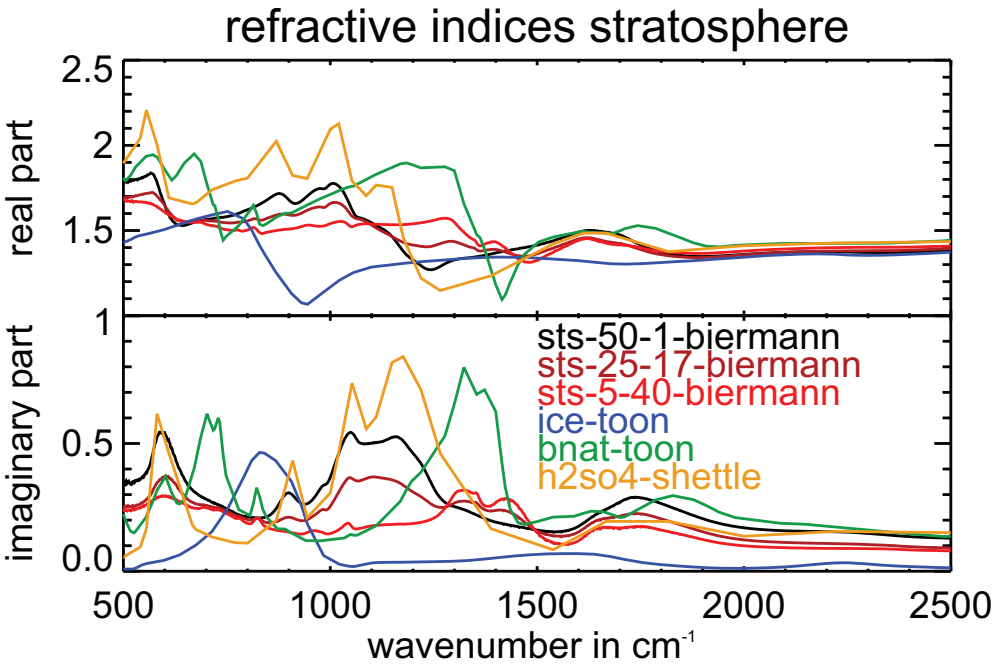


***Figure 2.3:*** *Complex refractive indices for stratospheric clouds and aerosol. For STS three different mixing ratios for the three temperatures of 195, 192 and 190 K are presented. The real part representing the wavelength dependent scattering is shown in the top panel and the imaginary part representing the wavelength dependent absorption is shown in the bottom panel.*

The refractive indices of the three types of polar stratospheric clouds are shown in Figure 2.3. The data for ice PSCs was measured at 163 K and is from Toon et al. (1994). For STS particles the mass concentration of $H_2SO_4/HNO_3/H_2O$ is temperature dependent as reported by Carslaw et al. (1994). The mixing ratios change significantly around 192 K. In Figure 2.3, the refractive indices for three distinct temperatures of 190, 192 and 195 K and their corresponding mixing ratios of (1) 5% $H_2SO_4$/40% $HNO_3$, (2) 25% $H_2SO_4$/17% $HNO_3$, and (3) 50% $H_2SO_4$/1% $HNO_3$ are presented. The data is taken from Biermann et al. (2000). The NAT data is taken from Toon et al. (1994) for $\beta$-NAT, as it is considered as the best measurement when examining the whole spectral range (Höpfner, 2008). For a detailed discussion on PSC refractive indices see Höpfner (2008).

Mass spectrometric measurements of aerosol particle composition in the middle and

upper troposphere (Schneider et al., 2006; Murphy et al., 2006) indicate that the aerosol mainly consists of organics, sulfate and ammonium. Nitrate abounds in the lower troposphere whereas it is absent or at least below the detection limit in the upper troposphere. For the secondary organic aerosol (SOA), which is chemically processed primary organic aerosol, the refractive indices of the terpene carvone measured by Dohm et al. (2004) are shown in Figure 2.4. Although carvone is an essential oil and hence a primary aerosol, it is considered a representative proxy for secondary organic aerosol. Aldehydes and ketones which are products of the gas phase oxidation of volatile organic compounds possess the same carbonyl functional group as carvone (Dohm et al., 2004). For sulfuric acid, ammonium sulfate and the sporadically occurring volcanic dust, data from Hummel et al. (1988) is taken.

For ice clouds refractive indices of Warren and Brandt (2008) are used in Figure 2.4. For super-cooled water droplets there is data from Wagner et al. (2005) ranging from about $1100-4500\ \mathrm{cm}^{-1}$ for four temperatures. This data shows that there is no significant temperature dependency in the infrared. However, it does not cover the required $625-2500\ \mathrm{cm}^{-1}$ range. Instead the refractive indices of water at 283 K from Hummel et al. (1988) are taken as they cover the complete range and do not show any significant difference to the Wagner et al. (2005) data.

### 2.3.3 Particle Shape

The shape of liquid particles such as water cloud droplets, stratospheric aerosol and STS particles as well as some tropospheric aerosol, such as sulfuric acid and ammonium sulfate, can be assumed to be spherical. The SOA is assumed to be liquid and hence also spherical. However, recent analyses provide direct evidence that SOA particles also exist as solids (Virtanen et al., 2010; Vaden et al., 2010). The shape of these particles is almost spherical. Ice and NAT PSC particles are solid. In theoretical calculations for CALIPSO retrievals their shape is presumed to be oblate spheroids with an aspect ratio of 1.2 (Pitts et al., 2009). Larsen et al. (2004) assumed a smaller aspect ratio of 1.05 for NAT particles.

The shapes of tropospheric cirrus cloud particles are manifold. Measurements with the cloud particle imager (CPI), which can resolve particle sizes from 10 $\mu$m to 2 mm (Lawson et al., 2001) show vertical profiles of cirrus crystals (Lawson et al., 2006). The particle size and shape varies with height as it is temperature dependent as noted by Lawson et al. (2006) and also depends on the cloud formation processes. While in synoptically generated cirrus clouds with low updraft velocities the particle size decreases with altitude, in cirrus clouds above convective systems with high updraft velocities, large particles can also be found in upper cloud layers (Baum et al., 2005b). Baumgardner et al. (2005) report about 10% of their measured particles to be approx-

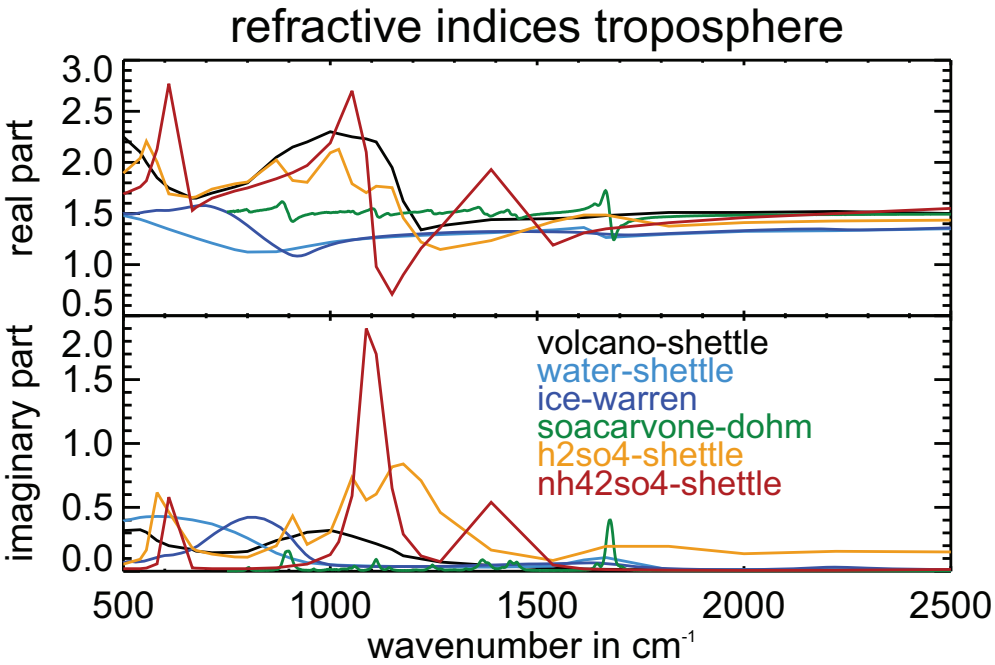


***Figure 2.4:*** *Complex refractive indices for tropospheric cloud and aerosol particles. High tropospheric clouds usually consist of ice crystals and sometimes contain water droplets. The aerosol at higher altitudes most likely contains organics and sulfates. In certain situations also volcanic material can be found.*

imately spherical. For modelling purposes assumptions about the particle shapes must be made. The idealised non-spherical shapes range from spheroids, droxtals, plates, hexagonal solid and hollow columns to bullet rosettes and aggregates (Baran, 2004; Yang et al., 2005) which, however, not consider craggy surfaces. Therefore, the Mie theory presented in Chapter 3 is an approximation for the calculation of scattering parameters for cirrus clouds.

About SVC particles little is known, since only few measurements are available. Davis et al. (2010) and Lawson et al. (2008) report most particles to be quasi-spherical or spheroids. In contrast McFarquhar et al. (2000) evaluated data by Heymsfield (1986) which were collected in 1973 and found columnar and trigonal crystals. The smaller trigonal ice crystals are smaller than 30 $\mu$m but the larger ones measure about 50 $\mu$m. The length of the columnar crystals ranges from about 10 to 40 $\mu$m. Lawson et al. (2008) admit that the CPI images are not as sharp as the images from Heymsfield

(1986) but assure that the shapes of particles larger than 30 $\mu$m can be identified. The different results are regarded as trustworthy and the reason for the difference is still a point of debate.

# Chapter 3

# Scattering on Atmospheric Particles in the Infrared

The properties of a particle, which are needed to describe its scattering behaviour, are particle radius, shape, wavelength of electromagnetic radiation and the wavelength dependent complex refractive index in air.

The atmospheric aerosol and cloud particles introduced in Chapter 2 are all within the radius range of $10^{-3} - 10^{3}\,\mu$m. The complex refractive indices for typical atmospheric particle types and the relevant wavelength range of $4 - 16\,\mu$m are shown in Figures 2.3 and 2.4. In Figure 3.1 the different scattering regimes depending on wavelength and particle radius are shown. To decide, which scattering regime is relevant, a non dimensional size parameter $x$ (Petty, 2006) is defined by:

$$x = \frac{2\pi r}{\lambda}, \tag{3.1}$$

where $r$ is the particle radius and $\lambda$ the wavelength. The size parameter $x$ ranges from $3.9 \times 10^{-4}$ to $1.6 \times 10^{3}$ for the relevant radius and wavelength ranges here. It is mainly due to the large variability of the atmospheric particle's sizes that the size parameter covers six orders of magnitude. The green boxes in Figure 3.1 include the radius and wavelength range. The overlapping region of both boxes indicates that the relevant scattering regimes are Rayleigh and Mie scattering. The Rayleigh theory can be applied when the particles are sufficiently small compared to the wavelength. With this theory the scattering on atmospheric molecules, which causes the blue colour of the sky and red sunsets, can be explained. However, the Mie theory is the more general approach. In the limit of small particles compared to the wavelength the Rayleigh scattering is included in the Mie theory (Mie, 1908). Because atmospheric particles

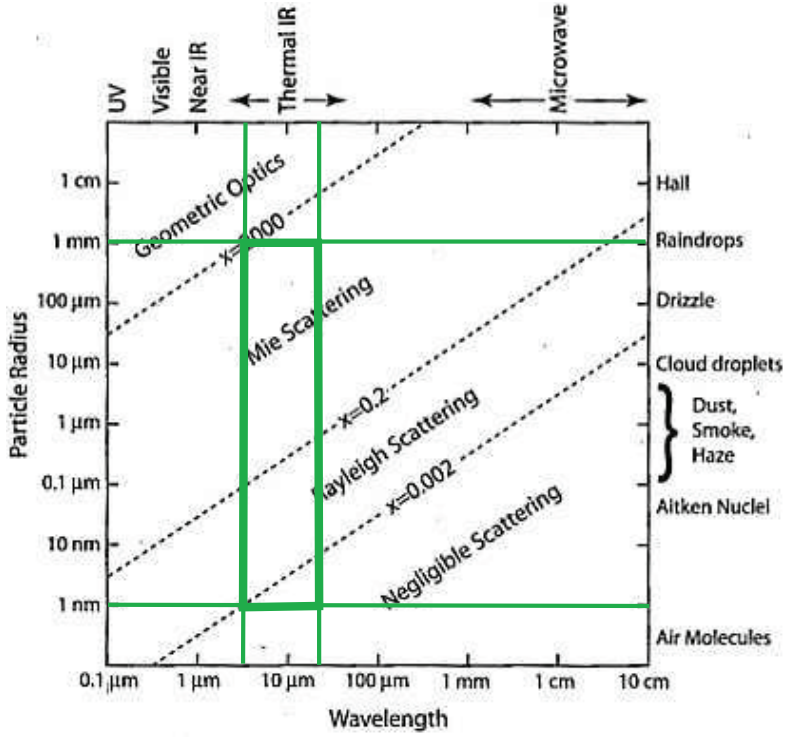


***Figure 3.1:*** *Scattering regimes depending on particle size and wavelength. The size parameters that represent the boundaries between the scattering regimes are rough estimations. The green boxes indicate the radius and wavelength ranges relevant to this work. Figure adapted from Petty (2006).*

are polydisperse and their size distributions span radius ranges reaching into the Mie regime, the Mie theory is introduced and applied in the following.

## 3.1 Mie Theory

About 100 years ago, the development of a theory that describes how much radiation is scattered by a particle in each direction was a research topic of interest to several scientists. A detailed essay on the history of the Mie theory and its alternative names is given in Kerker (1969). In 1908 Gustav Mie presented an exact solution for a plane electromagnetic wave scattered by a colloidal gold solution. He assumed the gold particles to be small and homogeneous spheres. The derivation of formulae for practical calculations starts with the Maxwell equations in polar spherical coordinates, from which the wave equation is derived. In the end there are the Mie scattering coefficients $a_n$ and $b_n$, which only depend on the size parameter $x$ (Equation 3.1) and the complex refractive index $m(\lambda)$, and the scattering amplitude functions $S_1(\Theta)$ and $S_2(\Theta)$, which are functions of $a_n$ and $b_n$ and additionally depend on the scattering angle $\Theta$. The scattering coefficients are obtained by series expansion where each coefficient gets smaller with increasing index $n$. In case of a very small size parameter $x << 1$, all terms except for the first one of the series expansion are negligible. In this limit, the Mie theory yields the same result as the Rayleigh scattering.

From the scattering coefficients $a_n$, $b_n$ the scattering and extinction efficiencies $Q_e$, $Q_s$ are calculated:

$$Q_s = \frac{2}{x^2} \sum_{n=1}^{\infty} (2n+1)(|a_n|^2 + |b_n|^2) \tag{3.2}$$

$$Q_e = \frac{2}{x^2} \sum_{n=1}^{\infty} (2n+1) \Re \{a_n + b_n\} \tag{3.3}$$

In Figure 3.2 the scattering and extinction efficiencies are shown for ice particles with radii ranging from $10^{-3} - 10^{3}\,\mu$m at a wavelength of $10\,\mu$m. A steep gradient in both, scattering and extinction extinction efficiency, can be seen between $1 - 10\,\mu$m. Both efficiencies peak at a radius somewhat larger than $10\,\mu$m and converge towards constant values. For the extinction efficiency this value is two. The extinction efficiency can be described as the radiant power that is scattered and absorbed by a particle over the radiant power that is incident on the particle's geometrical cross section. This means that in the Mie scattering regime larger particles attenuate about twice as much radiance as its geometric cross section would do. Since this is counterintuitive this phenomenon is called the "extinction paradox".

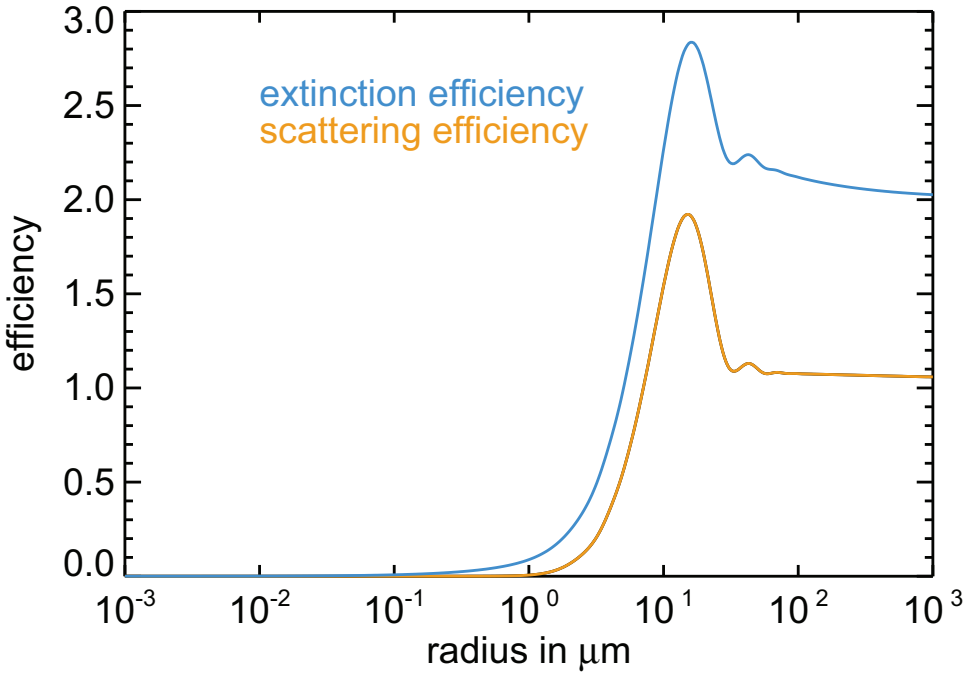


***Figure 3.2:*** *Scattering and extinction efficiencies $Q_s$ and $Q_e$ for ice particles at a wavelength of 10 µm. When the particle size is much larger than the wavelength, the scattering and extinction efficiencies run towards a constant limit.*

The scattering amplitude functions $S_1(\Theta)$ and $S_2(\Theta)$ are used to calculate the elements of the $4 \times 4$ scattering matrix $S_{i,j}(\Theta)$, where $i$ and $j$ are the matrix indices. The scattering matrix describes the relation between incident and scattered radiant field when the radiant field is expressed as a Stokes vector. The Stokes vector is a four-element vector with the scalar intensity as the first element. The other three elements contain information on the degree of horizontal or vertical, linear and circular polarisation. Because natural radiation is unpolarised, here just the first matrix element is relevant

$$S_{11}(\Theta) = \frac{1}{2}(|S_1|^2 + |S_2|^2). \tag{3.4}$$

As Hansen and Travis (1974) show, the $S_{11}(\Theta)$ element is used to calculate the normalised phase function

$$P_{11}(\Theta, r) = \frac{\lambda^2 S_{11}}{\pi^2 r^2 Q_s}. \tag{3.5}$$

This phase function describes how much of the unpolarised incident radiance is scat-

tered towards any angle $\Theta = 0 - 180\,^\circ$. So the integral of the phase function over the whole solid angle has to fulfil the condition:

$$\int_0^{2\pi} \int_0^{\pi} \frac{P_{11}(\Theta)}{4\pi} \sin\Theta \, \mathrm{d}\Theta \, \mathrm{d}\Phi = 1, \tag{3.6}$$

where $\Phi$ is the azimuthal angle. Examples of phase functions are shown in Figure 3.6 for angles $\Theta$ between $0 - 180\,^\circ$. For homogeneous spheres, as assumed here, the phase function is axially symmetric around the line of incoming radiance.

For the calculations reported here, the routine BHMIE for the calculation of Mie scattering by Bohren and Huffman (1983) was adapted both in an IDL and in a C++ code.

## 3.2 Mean Scattering Radius

The scattering behaviour of a particle is highly dependent on its size. As Figure 3.2 shows, scattering is nearly negligible for particles about one magnitude smaller than the wavelength of the radiation. The parameter representing the dependency on the particle size distribution and scattering efficiency is the mean radius for scattering $r_{sca}$, defined in Hansen and Travis (1974) as

$$r_{\mathrm{sca}} = \frac{\int_{r_1}^{r_2} \pi r^3 Q_s(r, \lambda, m_c) \frac{\mathrm{d}N}{\mathrm{d}r} \, \mathrm{d}r}{\int_{r_1}^{r_2} \pi r^2 Q_s(r, \lambda, m_c) \frac{\mathrm{d}N}{\mathrm{d}r} \, \mathrm{d}r}, \tag{3.7}$$

with the particle radius $r$, the complex refractive index $m_c$, the wavelength $\lambda$ and the scattering efficiency $Q_s$ defined in Equation 3.3.

However, in cases where the number size distribution covers a radius range for which the scattering efficiency is constant, the mean scattering radius is approximated by the effective radius, which is defined in Section 2.3.1 (Equation 2.2). For the example of the scattering efficiency at $10\,\mu$m wavelength shown in Figure 3.2, the effective radius is a good approximation to the mean scattering radius for particle radii between $100 - 1000\,\mu$m, because the scattering efficiency is nearly constant here. For particle sizes between $1 - 100\,\mu$m the effective radius is not a good approximation to the mean scattering radius, because of the steep gradients of the scattering efficiency in this particle size region. Generally speaking the effective radius should be used only when the particle size is significantly larger than the wavelength.

In Figure 2.1 typical size distributions for stratospheric and tropospheric aerosol, PSC, sub-visible cirrus and a tropical cirrus cloud are shown. To demonstrate for which

particle sizes the effective radius is a valid approximation, the mean scattering radii for a wavelength of 10 $\mu$m and the effective radii are calculated and represented in Figure 2.1 by squares and diamonds respectively in Figure 2.1. The absolute values and their relative differences are listed in Table 3.1. Clearly, in the mid-infrared the use of the effective radius as an approximation to the mean scattering radius is appropriate for cirrus clouds but not for aerosols and PSCs. For SVCs and stratospheric cirrus clouds it is at least ambiguous. To yield accurate results for the radiation properties of aerosol and cloud particles, the effective radius should rather be used as an alternative parameter for the size distribution than to substitute for $\mu$ and $\sigma$.

| | $r_{\text{sca}}$ in $\mu$m | $r_{\text{eff}}$ in $\mu$m | relative difference in % |
|---|---|---|---|
| tropospheric aerosol | 0.33 | 0.1 | 69 |
| stratospheric aerosol | 0.18 | 0.05 | 73 |
| polar stratospheric cloud | 2.26 | 0.38 | 83 |
| stratospheric cirrus cloud | 25.44 | 26.13 | −3 |
| sub-visible cirrus cloud | 8.14 | 6.25 | 23 |
| tropical cirrus cloud | 190.51 | 191.16 | −0.3 |

***Table 3.1:*** *Mean scattering and effective radii and the corresponding relative differences with respect to the scattering radius for the number size distributions shown in Figure 2.1.*

Because the effective radius is a good approximation for the mean radius of scattering at shorter wavelengths and for larger cirrus particles and it only depends on the size distribution, it is widely used to describe a particle size distribution. In cases where the mean radius for scattering is smaller than the wavelength and hence the condition for the effective radius does not hold, the effective radius is also often used together with $\sigma$ and $n$ as another parameter for describing the number size distribution of cloud and aerosol particles.

## 3.3 Scattering and Extinction Coefficients and Phase Function

The scattering and extinction coefficients $\beta_e$ and $\beta_s$ describe how much radiation is attenuated per unit length. These quantities are usually used in radiative transfer calculations. Cloud and aerosol particles are never mono-disperse. Rather they are approximately log-normally distributed around a median radius and the scattering and extinction coefficients and the phase function are calculated by integrating the

scattering and extinction efficiencies $Q_s$ and $Q_e$ and the dimensionless normalised phase function $P(\Theta)$ over the number size distribution $n(r)$ of the particles:

$$\beta_s = \int_{r_1}^{r_2} \pi r^2 Q_s(r) n(r)\,\mathrm{d}r \tag{3.8}$$

$$\beta_e = \int_{r_1}^{r_2} \pi r^2 Q_e(r) n(r)\,\mathrm{d}r \tag{3.9}$$

$$\beta_a = \beta_e - \beta_s \tag{3.10}$$

$$P(\Theta) = \frac{1}{\beta_s} \int_{r_1}^{r_2} \pi r^2 Q_s(r) P_{11}(\Theta, r) n(r)\,\mathrm{d}r \tag{3.11}$$

where $\beta_a$ is the absorption coefficient.

The extinction coefficient is the sum of absorption and scattering coefficient. To quantify the fraction of scattering in the total extinction, the single scattering albedo is defined by:

$$\tilde{\omega} = \frac{\beta_s}{\beta_e}. \tag{3.12}$$

### 3.3.1 Spherical Particles

Because Mie theory is exact only for spherical particles, it is a good approximation for liquid particles and some solid particles found in the atmosphere. Even for non-spherical ice crystals it can be a reasonable approximation as long as their maximum dimension is smaller than about 30 $\mu$m (Baran et al., 2003). In Figures 3.3, 3.4, and 3.5 the extinction coefficients, normalised extinction coefficients and single scattering albedos are plotted for the six typical particle size distributions introduced in Chapter 2.3.1 in Table 2.1 and Figure 2.1. The extinction coefficients for stratospheric and tropospheric aerosol particles are calculated for sulfuric aerosol with the refractive indices of a binary $H_2SO_4$ solution. For the PSCs the refractive indices for 25 % $H_2SO_4$/17 % $HNO_3$ STS at 192 K from Biermann et al. (2000) and for cirrus clouds the ice refractive indices from Warren and Brandt (2008) were taken.

In Figure 3.3 the extinction coefficients for the number size distributions in Figure 2.1 are shown as a function of wavelength. The extinction coefficients range over eight orders of magnitude for the different particle types. The larger the particle's mean scattering radius, the larger their extinction coefficient. However, the spectral shape of the three ice clouds looks flat without any significant structure except for a little dip around 10 $\mu$m. Whereas for the PSC some structure can be seen between 4 – 10 $\mu$m and for the aerosol particles structure is evident over the whole spectrum.

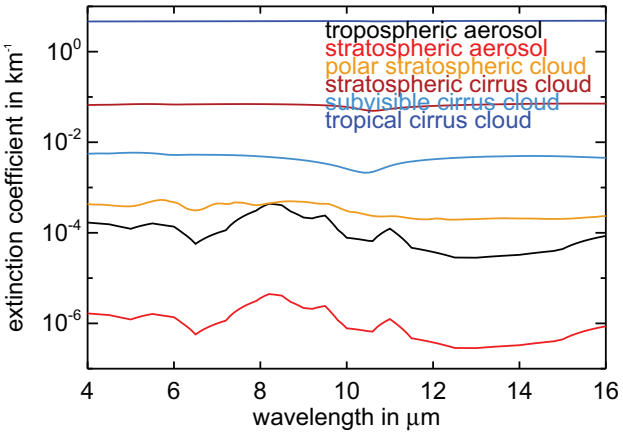


***Figure 3.3:*** *Extinction coefficients for typical tropospheric and stratospheric aerosol and cloud types. The corresponding number size distributions are given in Table 2.1.*

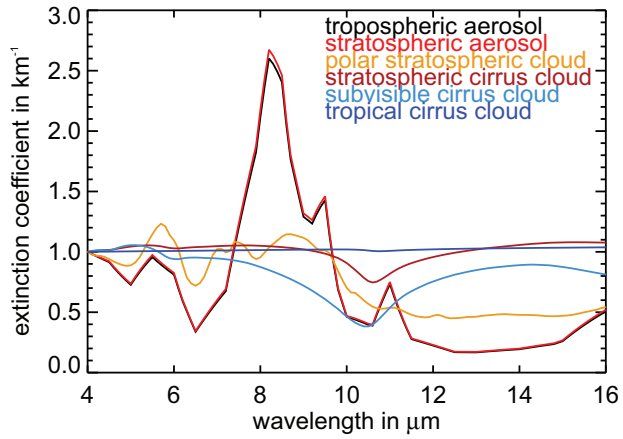


***Figure 3.4:*** *Extinction coefficients for typical tropospheric and stratospheric aerosol and cloud types. The corresponding number size distributions are given in Table 2.1. The extinction coefficients are normalised to 1 at 4 µm to allow for a better comparison of the spectral signature.*

To show these structures more clearly the extinction coefficient spectra are normalised to 1 at 4 $\mu$m in Figure 3.4. Now the relative spectral slope can be examined. Despite of different number size distributions, the tropospheric and stratospheric aerosol particles have a nearly identical spectral signature with a distinct maximum between 8 – 10 $\mu$m. However, later it is shown that the spectral signature of the extinction coefficient of tropospheric aerosol varies strongly with the number size distribution. For the PSC there is a maximum at about 6 $\mu$m followed by a relative minimum. Between 10 – 12 $\mu$m there is a decrease of the extinction coefficient and for wavelengths above 12 $\mu$m the extinction coefficient remains constant. For the stratospheric and subvisible cirrus clouds, both optically thin cloud types, the dip between 10 – 11 $\mu$m becomes more pronounced for the scaled spectra. The tropical cirrus cloud shows no structure at all. The spectral signatures of the different cloud and aerosol particle types can be summarised into three groups: aerosol particles, PSCs and ice clouds. The groups differ from each other because of their different chemical composition, which affects the calculated extinction coefficients via the different refractive indices. In general the spectral slope of the extinction coefficient is characteristic for each particle type and thus allows for identification of the particle type. Within the group of the ice clouds there are distinct and visible differences, which are caused by the different number size distributions. So, in case of optically thin clouds the number size distribution also has a measurable effect to the extinction coefficient spectra.

The single scattering albedo $\tilde{\omega}$ for the particle distributions in Figure 2.1 is shown in Figure 3.5. For both, the stratospheric and tropospheric aerosol, scattering does not contribute significantly to extinction compared to clouds. Just at the shorter wavelengths near 4 $\mu$m the scattering on tropospheric aerosol particles makes up to 1.5 % of the extinction. This is caused by the larger particles of the coarse mode. Episodic events, such as volcanic eruptions or Saharan dust outbreaks, can inject coarse particles into the atmosphere up to the stratosphere. Hence somewhat more scattering than for the aged aerosol shown here can be expected. For the Pinatubo aerosol Echle et al. (1998) estimated a single scattering albeo $\tilde{\omega}$ of up to 0.3 in the infrared.

The integrated phase functions $P(\Theta)$ for the number size distributions in Figure 2.1 are depicted in Figure 3.6 as a function of the scattering angle $\Theta$. The phase functions are shown for angles between 0 °, which is forward scattering, to 180 °, which is backward scattering. For 3D geometry, the phase functions are axially symmetric around the axis of the incoming ray. To facilitate the comparison of the shape of the phase functions, the function for tropospheric aerosol is displaced upwards in Figure 3.6. Compared to the phase functions for different distinct particle radii shown in many textbooks (Bohren and Huffman, 1983; Liou, 2002; Petty, 2006), the integrated phase functions in Figure 3.6 do not exhibit the characteristic wiggled structure. The wiggled structure is smoothed out by the integration over a radius range. The tropospheric and stratospheric aerosol show a nearly isotropic scattering except for angles around 90 °, where

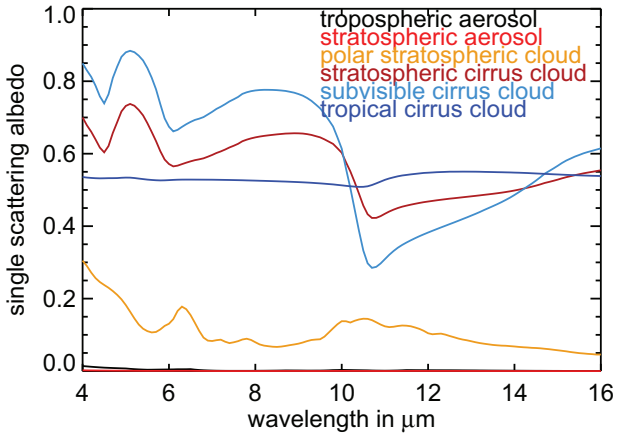


***Figure 3.5:*** *Single scattering albedo $\tilde{\omega}$ for typical tropospheric and stratospheric aerosol and cloud types. The corresponding number size distributions are given in Table 2.1.*

a minimum is observed. For the PSC, more radiance is directed into forward than into backward directions. The forward scattering increases with the mean scattering radius of the particles. The three cirrus cloud types show this effect clearly. They are characterised by very little backward and side-ward scattering, but strong forward scattering.

### Aerosol Particles

The effect of the size distribution on the spectral signature of the extinction coefficients of aerosol particles is analysed in more detail below. As aerosol particles are ubiquitous in the atmosphere, vertical extinction coefficient profiles are essential for radiative transfer calculations and retrievals. These profiles can be obtained either by calculation from measured aerosol number size distributions or by direct extinction coefficient measurements. For stratospheric aerosol the HALogen Occultation Experiment (HALOE) provides a large data-set of aerosol extinction measurements at 5.26 $\mu$m. Averaged extinction profiles for mid-latitudes and the equator can be found in Thomason and Peter (2006)[1]. On average, the extinction increases nearly exponentially from higher to lower altitudes.

For tropospheric aerosol the vertical extinction profile is as variable as the aerosol itself. To allow for calculations and variability analyses of the vertical profile of the extinction

[1] p. 242

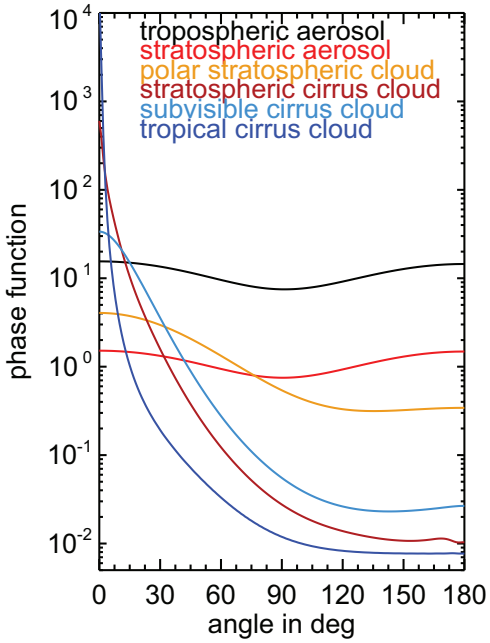


***Figure 3.6:*** *Phase functions for typical tropospheric and stratospheric aerosol and cloud types. The corresponding number size distributions are given in Table 2.1. For better visibility the phase function of the tropospheric aerosol is shifted upwards by a factor 10.*

coefficients for different aerosol types, information about the vertical profile of the number size distribution is needed. Efforts to provide optical properties of aerosols and clouds (OPAC) and tropospheric aerosol number size distributions have been made by D'Almeida et al. (1991) and Hess et al. (1998). However, the optical properties such as extinction coefficients are provided on a rather coarse spectral resolution in the desired infrared wavelength range of 4 to 16 $\mu$m, which is not sufficient to discriminate aerosol effects from trace gas signatures. Detailed information on aerosol types and number size distributions is mainly derived from boundary layer measurements. For the vertical profile an exponential decrease in number concentration is assumed. Yet in Chapter 2.3.1 it is shown that the number concentration does not always decrease with altitude, but can also increase in the upper troposphere. For the calculation of the extinction coefficient it is crucial to note that also the median and hence the mean scattering radius decreases with altitude, which is not taken into account in the OPAC database. As shown in Figure 3.4 for ice particles the shape and median radius of the

number size distribution also affects the spectral signature of the extinction coefficient of aerosol particles.

For that reason more detailed information on the variability of the vertical profile of aerosol number size distribution is needed. The parameters for multimodal log-normal distributions of aerosol particles measured in the free troposphere were compiled in an aerosol database (see Appendix A). The aerosol particles are assumed to consist of $H_2SO_4$, $(NH_4)_2SO_4$ or SOA and the extinction coefficients for all number size distributions in the aerosol database are calculated. In Figure 3.7 the extinction coefficients at 830 $cm^{-1}$ ($\sim$12.05 $\mu$m) for all background number size distributions are depicted. It is clearly visible that the calculated extinction coefficients span a range of four orders of magnitude at all altitudes. For any given size distribution the calculated extinction coefficient is largest for $H_2SO_4$ aerosol particles. The lowest extinction coefficients are obtained for SOA and $(NH_4)_2SO_4$ aerosol lies in between. The solid line in Figure 3.7 shows the median extinction vertical profile and the dotted lines are the minimum and maximum profiles for this data set calculated on a 1 km vertical grid[2]. For all three chemical compositions of the aerosol considered, the extinction coefficient decreases exponentially from the lower troposphere up to about 5 km. The large spike to lower extinction coefficients at 3 km is caused by one mountain station providing many data and just a few measurements from other sites at that altitude (see Appendix A). In the middle and upper troposphere the minimum, median and maximum extinction profiles are reasonably constant. Above about 10 km, they show a tendency towards larger extinction coefficients. However for a comprehensive climatology, which allows for statistics to create seasonally and zonally averaged climatologies, much more data is needed.

Another robust information that can be derived from the aerosol database is the spectral signature of the extinction coefficients for the collected number size distributions and these three aerosol types. In Figure 3.4 it is shown that the spectral signature depends on both, the chemical composition and on the number size distribution. For both, tropospheric and stratospheric aerosol, the extinction coefficients look nearly identical, because both are composed of $H_2SO_4$ and the number size distributions are similar. However, from the database it can be deduced that there are manifold number size distributions leading to various spectral signatures of particular extinction coefficients. In Figures 3.8 – 3.10 the extinction coefficients normalised to one at 4 $\mu$m are shown as a function of wavelength. The extinction coefficients are calculated for all number size distributions in the aerosol database at 5 km altitude for aerosol particles consisting of $H_2SO_4$ in Figure 3.8, $(NH_4)_2SO_4$ in Figure 3.9 and SOA in 3.10. It can be seen that the general spectral slope differs significantly between the three aerosol particle types.

[2]For forward calculations within this thesis the atmospheric properties are given on a 1 km grid. For that reason all number size distributions given for e.g $6.5 < z \leq 7.5$ km are assigned to $z = 7$ km.

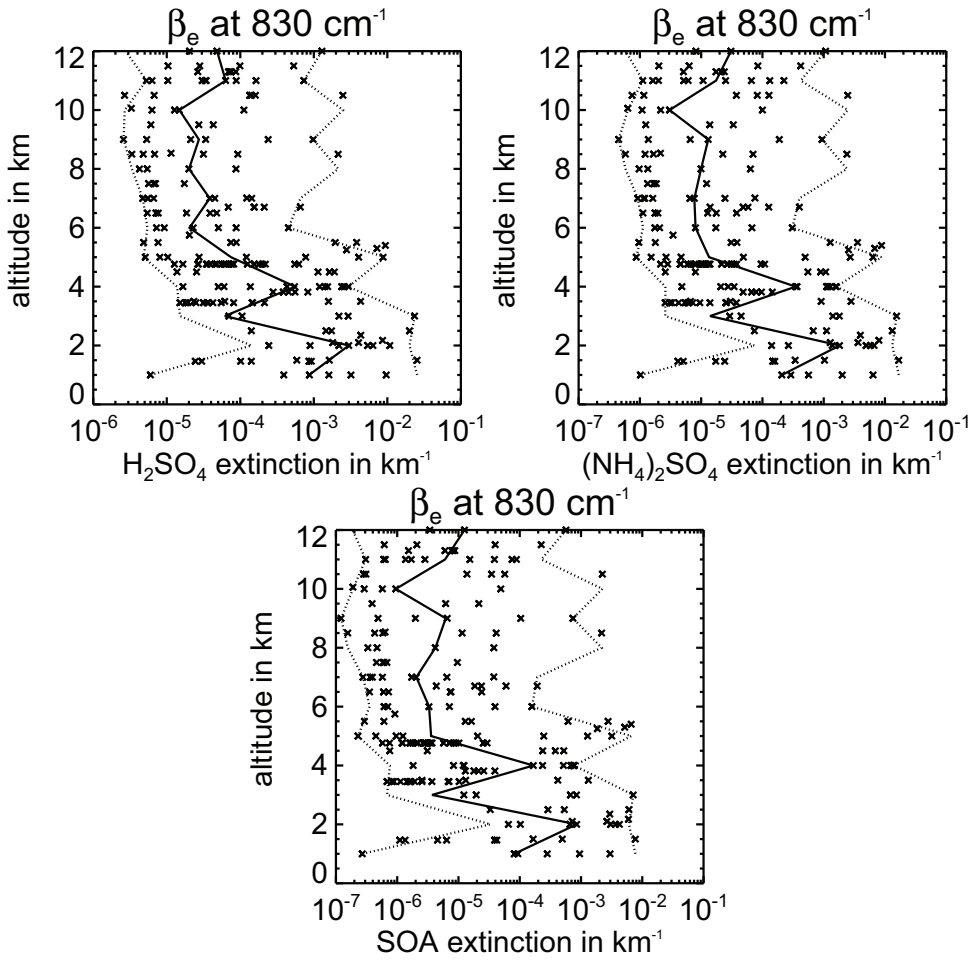


***Figure 3.7:*** *Extinction coefficient vertical profile for tropospheric aerosol. The large variability of free tropospheric aerosol translates into the extinction coefficient, which spans a range of four orders of magnitude at all altitudes. The underlying number size distributions are from the aerosol database (see Appendix A). The extinction coefficients are calculated for $H_2SO_4$ (top left panel), $(NH_4)_2SO_4$ (bottom panel) and SOA (top right panel).*

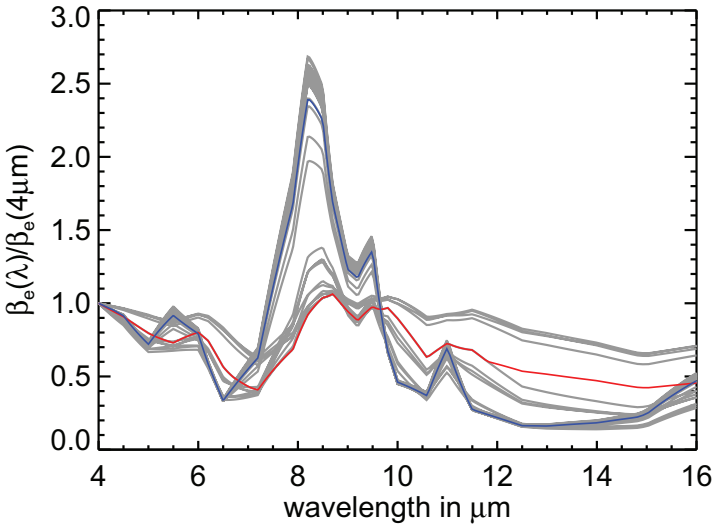


***Figure 3.8:*** *Spectrally resolved extinction coefficients for $H_2SO_4$ aerosol. The extinction spectra are calculated for all the number size distributions at 5 km altitude in the aerosol database. They are normalised to 1 at 4 µm. The blue line indicates the spectrum of the aerosol number size distribution, for which the smallest extinction coefficient in the whole unscaled spectra is obtained. The red spectrum belongs to the size distribution yielding the largest extinction coefficient.*

However, within each Figure there is also a variation caused by the different number size distributions. For larger extinctions coefficients the spectral signature becomes less pronounced, as is seen when comparing the maximum and minimum extinction coefficients in Figures 3.8 – 3.10. From this finding it is deduced that scaling of the tropospheric aerosol extinction coefficient from one wavelength to another is not as accurate as for stratospheric aerosol. Because of the variability of tropospheric aerosol in chemical composition and number size distribution it is preferable to calculate the extinction coefficient for any desired wavelength.

### PSC Particles

The effect of the size distribution on the spectral signature of the extinction coefficients of cloud particles is analysed in more detail below. In Figures 3.11 and 3.12 the extinction coefficients and corresponding single scattering albedos for STS and NAT PSCs are presented. The extinction coefficients are calculated for size distributions with a width of 1.6 and median radii covering the typical range of the PSC types

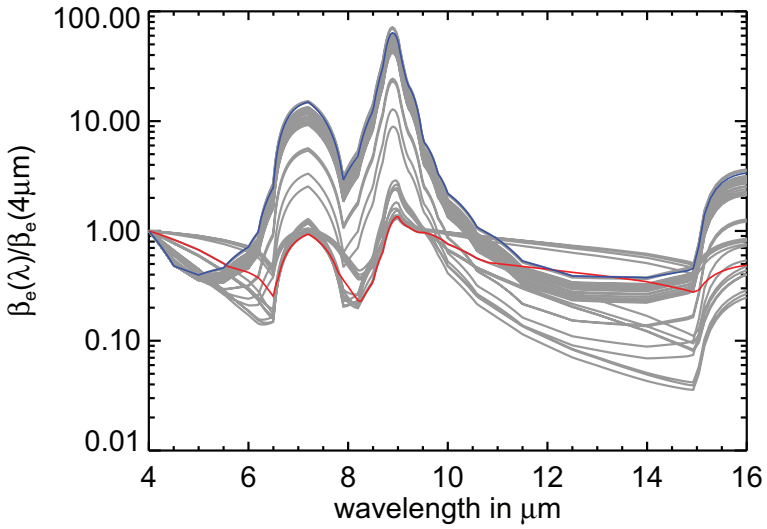


***Figure 3.9:*** *Spectrally resolved extinction coefficients for $(NH_4)_2SO_4$ aerosol. The extinction spectra are calculated for all the number size distributions at 5 km altitude in the aerosol database. They are normalised to 1 at 4 µm. The blue line indicates the spectrum of the aerosol number size distribution, for which the smallest extinction coefficient in the whole unscaled spectra is obtained. The red spectrum belongs to the size distribution yielding the largest extinction coefficient.*

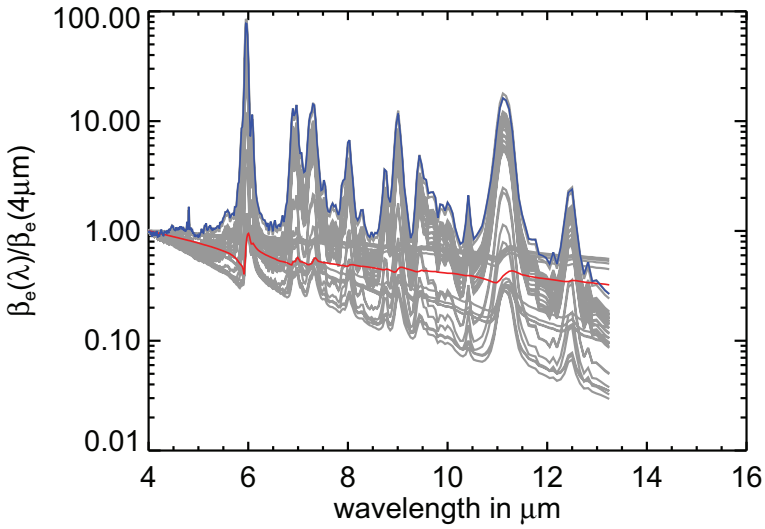


***Figure 3.10:*** *Spectrally resolved extinction coefficients for SOA. The extinction spectra are calculated for all the number size distributions at 5 km altitude in the aerosol database. They are normalised to 1 at 4 µm. The blue line indicates the spectrum of the aerosol number size distribution, for which the smallest extinction coefficient in the whole unscaled spectra is obtained. The red spectrum belongs to the size distribution yielding the largest extinction coefficient.*

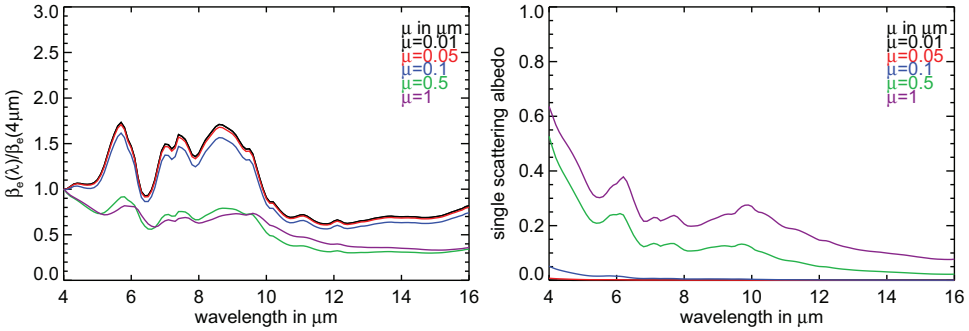


***Figure 3.11:*** *Extinction coefficients (left panel) for STS PSC particles and corresponding single scattering albedos (right panel). The extinction coefficients are normalised to 1 at 4 μm. The extinction coefficients and single scattering albedos are calculated for five number size distributions with a width $\sigma = 1.6$ and median radii $\mu$ covering the typical range of STS particles.*

introduced in Chapter 2.

The extinction coefficients for STS, shown in the left panel of Figure 3.11, are calculated for median radii ranging from 0.01 to 1 $\mu$m and are normalised to 1 at 4 $\mu$m. For small median radii they show a more distinct structure than for larger median radii. The transition is between 0.1 and 0.5 $\mu$m. This transition also occurs in the single scattering albedo $\tilde{\omega}$ shown in the right panel. For median radii up to 0.1 $\mu$m there is no significant scattering contribution to the extinction coefficient. For larger particles the contribution is highest at short wavelengths and decreases with increasing wavelength.

For NAT the extinction coefficients are calculated for median radii ranging from 0.1 – 10 $\mu$m and also are normalised to 1 at 4 $\mu$m. In the left panel of Figure 3.12 the extinction coefficients for particles larger than 5 $\mu$m show nearly no structure. For the median radii of 0.1, 0.5 and 1 $\mu$m there are distinct maxima between 7 and 8 $\mu$m and around 14 $\mu$m. The single scattering albedo $\tilde{\omega}$ in the left panel shows that scattering makes nearly no contribution to the extinction coefficient for the median radius of 0.1 $\mu$m. For median radii of 0.5 and 1 $\mu$m $\tilde{\omega}$ decreases from about 0.47 – 0.57 at 4 $\mu$m to about 0.03 – 0.13 at 16 $\mu$m. At a wavelength of 7 $\mu$m there is a distinct minimum in $\tilde{\omega}$. For the larger particles the spectral shape of $\tilde{\omega}$ is less structured and scattering makes up about 50% of the extinction.

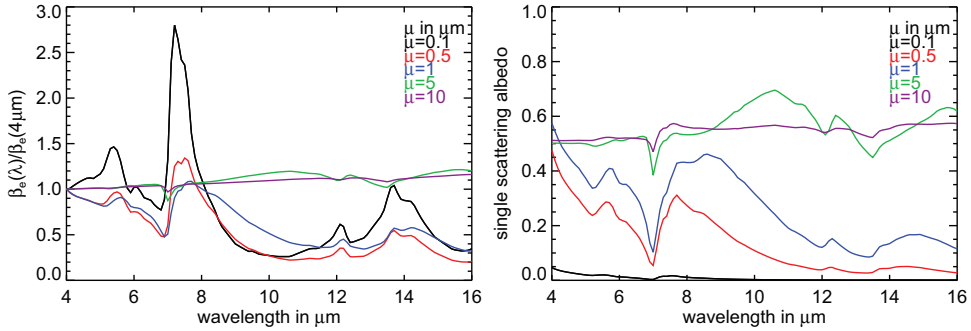


***Figure 3.12:*** *Extinction coefficients (left panel) for NAT PSC particles and corresponding single scattering albedos (right panel). The extinction coefficients are normalised to 1 at 4 μm. The extinction coefficients and single scattering albedos are calculated for five number size distributions with a width $\sigma = 1.6$ and median radii $\mu$ covering the typical range of NAT particles.*

### Ice Particles

In Figure 3.13 the normalised extinction coefficients and the single scattering albedos $\tilde{\omega}$ are shown for ice particles. The extinction coefficients for spherical ice crystals show a pronounced minimum between $10-11\,\mu$m for small effective radii. This minimum diminishes with growing particle size until almost no spectral signature can be found for the large particles. Nearly the same effect is observed for the single scattering albedo. There is a maximum in $\tilde{\omega}$ at around $5\,\mu$m, where the contribution of scattering to the extinction coefficient is as much as 80% for particles smaller than $13\,\mu$m. For the mid-size particles between 13 and $35.8\,\mu$m there is a second maximum between $9-10\,\mu$m wavelength. For the larger particles $\tilde{\omega}$ is between 0.5 - 0.6, which means that scattering accounts for a bit more than 50% of the extinction coefficient, and shows hardly any spectral signature.

As ice particles are known to be non-spherical, more complex parameterisations than Mie theory have been developed, and can be applied to account for the effects of the non-sphericity of ice particles (Baum et al., 2005b). To allow for comparison with non-spherical ice crystals the extinction coefficients shown in Figure 3.13 are calculated for number size distributions having the same effective radii as in the database for non-spherical particles in Section 3.3.2.

The phase functions at $10\,\mu$m wavelength for the ice particle size distributions are shown in the left panel of Figure 3.14. For all phase functions it can be seen that forward scattering dominates over side-ward and backward scattering. The phase function

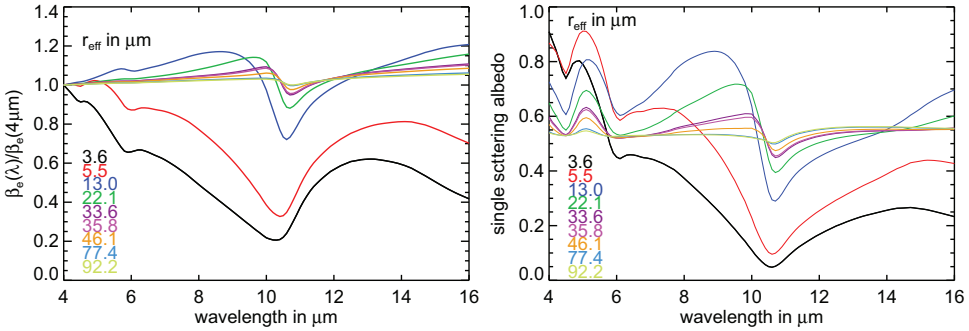


***Figure 3.13:*** *Extinction coefficients (left panel) for spherical ice particles and corresponding single scattering albedos (right panel). The extinction coefficients are normalised to 1 at 4 µm. The extinction coefficients and single scattering albedos are calculated for nine number size distributions with effective radii given in the plot in µm, which cover the typical range of ice particles.*

maxima are at 0 ° and the phase function decreases until about 120 °–150 °. For the backward directions there is a very smooth increase again. Yet for the small particles with $r_{\text{eff}} = 3.6\,\mu$m the backward scattering is only one magnitude smaller than the forward scattering. As the particle size increases the difference between forward and backward scattering increases. Finally for the largest particles with $r_{\text{eff}} = 92.2\,\mu$m the backward scattering is about 5 magnitudes smaller than the forward scattering.

In the right panel of Figure 3.14 the phase functions for 0 °, 30 ° and 180 ° are shown as a function of wavelength. The phase functions for 0 ° are the largest with no distinct spectral features, but with increasing wavelength, the phase function decreases. For the 30 ° side-ward direction the phase function is nearly constant for the size distributions with small effective radii of $r_{\text{eff}} = 3.6\,\mu$m and $r_{\text{eff}} = 5.5\,\mu$m. For the size distributions with larger effective radii there is a small maximum around 5 $\mu$m and an increase with increasing wavelength. For the backward scattering direction of 180 ° there is an increase of the phase function with wavelength and a local maximum around 5 $\mu$m and a local minimum around 10.5 $\mu$m for the size distribution with an effective radius larger than 5.5 $\mu$m.

### 3.3.2 Non-spherical Particles

Cirrus clouds mostly do not consist of spherical particles. To describe the bulk scattering of cirrus clouds, it is best to assume a mixture of different particle shapes (Francis et al., 1999). For idealised particle shapes such as spheroids, plates, columns droxtals,

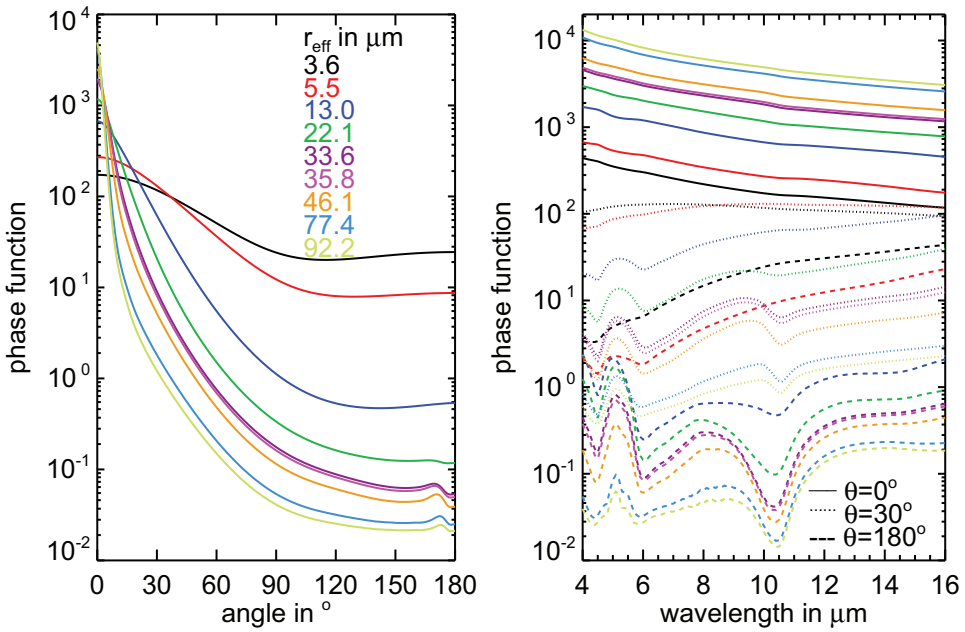


***Figure 3.14:*** *Phase functions of spherical ice particles for nine effective radii covering the typical range of cirrus particles. On the left the phase functions are shown for the nine effective radii at a wavelength of 10 µm. On the right the wavelength dependency of the phase functions is shown for three scattering angles of 0°, 30° and 180° (solid, dotted and dashed lines respectively).*

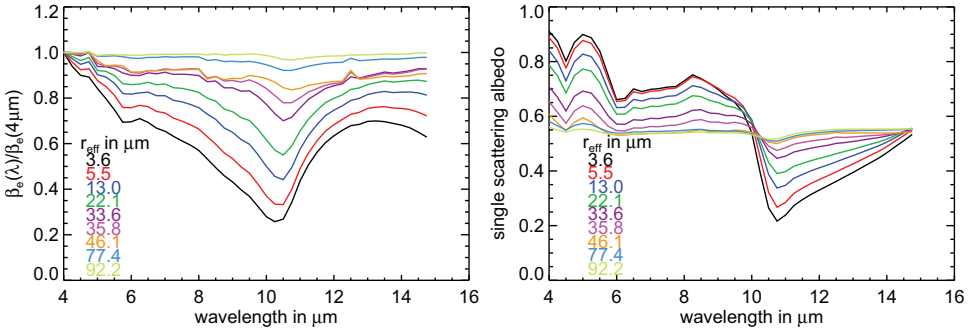


***Figure 3.15:*** *Cirrus bulk property extinction coefficients (left panel) and single scattering albedos (right panel) for nine effective radii covering the typical range of ice particles. These parameters consider the non-sphericity of ice crystals.*

bullet rosettes and aggregates, extensive calculations to obtain the single-scattering properties were performed and summarised by Yang et al. (2005). As cirrus cloud composition is not homogeneous, Baum et al. (2005a, 2007) compiled 1117 particle size distributions from several measurements and derived a set of 18 different effective diameters ranging from $10-180\,\mu$m. For each effective diameter the single scattering properties are provided.

The data by Baum et al. (2007) are similar to the data shown in Figure 3.15 and 3.16, which represent the bulk scattering properties used for the MIPClouds study (Spang et al., 2008; Kerridge, 2004). In contrast to the extinction coefficients for spherical particles, the extinction coefficients for the bulk properties are more regularly spaced so that the curves do not overlap for the larger effective radii. Similar to the spherical particles shown in Figure 3.13, for the bulk properties there is also a distinct minimum at $10\,\mu$m wavelength, which diminishes as the effective radii get larger. The same behaviour is found for the single scattering albedo in the right panel. The overall structure for the effective radii larger than $13\,\mu$m is similar to the spherical particles but the sequence for the different sizes is more regular. For particles smaller than $13\,\mu$m the single scattering albedo differs in the wavelength range between $6-10\,\mu$m from the spherical particles.

The phase function of the cirrus cloud bulk properties shown in the left panel of Figure 3.16 is rather smooth with strong forward scattering. For smaller particles the forward scattering is weaker than for the large particles and the scattering to all other directions is larger. However compared to the phase function of spherical ice particles the phase functions for the number size distributions with an effective radius up to $13\,\mu$m the forward scattering is much stronger for the non-spherical particles. For

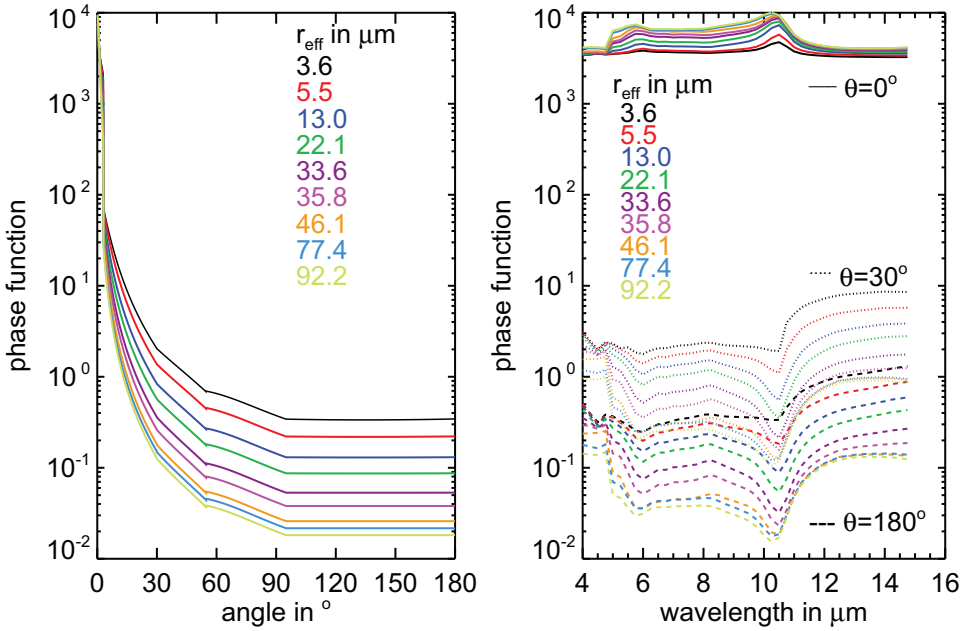


***Figure 3.16:*** *Phase functions for non-spherical ice crystals. The cirrus phase functions are shown for nine effective radii covering the typical range of ice particles. In the left panel the phase functions are shown at a wavelength of 10 µm. In the right panel the wavelength dependence of the phase functions is shown for three scattering angles: 0, 30 and 180°.*

the size distributions with an effective radius larger than 13 $\mu$m the forward scattering of the non-spherical ice particles is still larger than for the spherical ice particles. The larger the particles are, the more similar the phase functions for spherical and non-spherical particles get in shape and magnitude.

The wavelength dependence of the phase functions, is shown in the right panel of Figure 3.16. In contrast to the non-spherical particles, which show a decrease of the phase function in forward direction at 0 ° with increasing wavelength, the phase function is rather constant for the size distributions with smaller effective radii and develops a broad maximum between 5 – 10.5 $\mu$m as the effective radius gets larger. For the sideward 30 ° and backward 180 ° directions the phase function increases with wavenumber for all effective radii. Instead of a discrete maximum found at about 5 $\mu$m for the spherical ice particles, the non-spherical ice particles show a rather broad minimum extending from 5 – 10.5 $\mu$m.

Another database suitable for small particles such as spheroids has been compiled by Rother et al. (2006) and Rother (2009). Lawson et al. (2008) reported spheroids to be the main crystal shape in SVCs. To account for the effect of rough surfaces of ice crystals or aerosol particles, Rother et al. (2006) also provides scattering properties of Chebyshev particles. This database provides the scattering parameters for single particles and the integration over an appropriate size distribution must be performed by the user.

# Chapter 4

# Scattering in Radiative Transfer Calculations

To deduce information on the state of the atmosphere from remote sensing measurements the calculation of the radiative transfer is necessary. For this purpose the Juelich Rapid Spectral Simulation Code (JURASSIC) is applied and developed further within this thesis to account for scattering on aerosol and cloud particles.

## 4.1 Atmospheric Radiative Transfer

The radiative transfer calculation is the main task of the forward model of JURASSIC, which is described in Section 4.1.2. The forward model simulates the radiances that can be measured by a remote sensing instrument. Therefore the path through the atmosphere as well as the atmospheric state must be known. Detailed reviews on atmospheric radiation are given e.g. in Goody and Yung (1989); Liou (2002) and Petty (2006). In the following a short summary of the theory is given.

### 4.1.1 Equation of Radiative Transfer

In a non-scattering atmosphere the radiative transfer in the infrared along an arbitrary path can be described by the Schwarzschild equation

$$\mathrm{d}I\left(\nu,s\right)=\beta_a\left(\nu,s\right)\left[B\left(\nu,s\right)-I\left(\nu,s\right)\right]\,\mathrm{d}s, \tag{4.1}$$

where $I$ is the radiance in $\mathrm{W}/(\mathrm{m}^2\,\mathrm{sr}\,\mathrm{cm}^{-1})$ (power per unit area and unit solid angle and spectral unit (wavenumber $\nu$)), $s$ the coordinate in direction of radiance propagation,

$\beta_a$ the absorption coefficient as defined in Equation 3.10 and $B(\nu, s)$ is Planck's function

$$B\left(\nu, T\left(s\right)\right) = \frac{2h\nu^3c^2}{\exp\left(\frac{h\nu c}{kT}\right) - 1} \tag{4.2}$$

where $k$ is Boltzmann's constant, $\nu$ the wavenumber, $c$ the speed of light, $h$ Planck's constant and $T$ the temperature in K. In case of thermodynamic equilibrium, which typically applies in the troposphere and stratosphere, $B(\nu, T\left(s\right))$ is the blackbody emission in W/(m$^2$ sr cm$^{-1}$) at a temperature $T$. The atmosphere is not a blackbody and hence does not emit like one. Following Kirchhoff's law, the spectrally dependent emission is a function of the spectrally dependent absorption coefficient.

If aerosol or cloud particles are present along a path, the radiance is not only attenuated by absorption but also by scattering on the particles. Just like radiation along the path is scattered into other directions, radiation from other directions is scattered into the path. In addition to emission, scattering also acts as source $S(\nu, s)$ of radiation, so that Equation 4.1 is expanded to

$$\mathrm{d}I\left(\nu, s\right) = -\beta_e\left(\nu, s\right) I\left(\nu, s\right) + \beta_a\left(\nu, s\right) B\left(\nu, s\right) + \beta_s\left(\nu, s\right) S\left(\nu, s\right)\, \mathrm{d}s. \tag{4.3}$$

The first term describes the attenuation of radiance by extinction, which is the sum of absorption and scattering. The second term is the emission by the gaseous components of the atmosphere. Analogous the third term is the scattering source. The scattering source term

$$S\left(\nu, s\right) = \frac{1}{4\pi}\int_0^{4\pi} P\left(\Omega', \Omega\right) I\left(\nu, \Omega'\right)\, \mathrm{d}\Omega' \tag{4.4}$$

is the incident radiance from all directions $\Omega'$ scattered into direction $\Omega$ of the line of sight and weighted with the phase function $P\left(\Omega', \Omega\right) = P\left(\Theta\right)$ in Equation 3.11, which describes the likelihood for a single photon for being scattered from $\Omega'$ into direction $\Omega$. The particles considered here are isotropic, so that the phase function only depends on the angle $\Theta$ between the directions $\Omega'$ and $\Omega$.

Solving Equation 4.3 for a path with starting point $s_0 = 0$ and end point $s_1$ yields

$$\begin{aligned} I(\nu, s_1) &= I(\nu, 0)\exp\left[-t\left(s_1, 0\right)\right] + \\ &\quad \int_0^{s_1} \exp\left[-t\left(s_1, s\right)\right] \cdot \left[\beta_a\left(\nu, s\right) B(\nu, s) + \beta_s\left(\nu, s\right) S\left(\nu, s\right)\right]\, \mathrm{d}s \end{aligned} \tag{4.5}$$

where the optical thickness or optical depth (also optical path)

$$t\left(s_0, s_1\right) = \int_{s_0}^{s_1} \beta_e\, \mathrm{d}s \tag{4.6}$$

is the integral of the extinction coefficient along a path from$s_1$ to $s_2$. The transmittance $\tau$ is defined by

$$\tau = \exp(-t) \tag{4.7}$$

and the emissivity $\epsilon$ is defined by

$$\epsilon = 1 - \tau, \tag{4.8}$$

following Kirchhoff's law.

### 4.1.2 Modelling of Radiative Transfer

To analyse large data sets of infra-red limb measurements the *Ju*elich *Ra*pid *S*pectral *Si*mulation *C*ode (JURASSIC) was originally developed by Hoffmann (2006). JURASSIC is a coupled forward and retrieval model, which allows the application to different instruments. Successful analyses with JURASSIC have been performed on MIPAS (Hoffmann, 2006; Hoffmann et al., 2008), CRISTA-NF (Hoffmann et al., 2009; Weigel, 2009) and AIRS (Hoffmann and Alexander, 2010; Grimsdell et al., 2010) data. It has also been applied in studies of large-scale inverse problems by Geppert (2010); Wang (2010), and Ungermann (2011). Within this thesis significant efforts were made to develop the model further to be able to handle scattering of infrared radiation.

In the following, the forward model and the new developments are described in more detail. At the beginning of every radiative transfer calculation the path of a single ray through the atmosphere, which is referred to as pencil beam, has to be calculated. In the case of limb geometry the pencil beam is not just a straight line tangentially through the atmosphere but a curve refracted towards the Earth's surface. The degree of curvature depends on the change of the refractive index of the atmosphere with altitude. The refractive index depends on wavelength and on atmospheric conditions such as temperature, pressure, and water vapour partial pressure. In JURASSIC, the iterative scheme by Hase and Höpfner (1999) is applied to calculate the pencil beam. The step length chosen for the raytracing has to fulfil two constraints: on the one hand fewer steps are advantageous when considering the computation time and on the other hand the step length must be short enough so that the atmosphere along one step can be assumed as homogeneous. An adequate step length for limb measurements is approximately 10 km (Hase and Höpfner, 1999; Hoffmann, 2006).

After raytracing the evaluation of the radiative transfer is done by calculating spectrally averaged radiances, emissivities and Planck's functions applying pre-calculated emissivity tables according to the instrument's characteristics (Riese et al., 1997, 1999). This approach of JURASSIC follows the so-called broad band approximation and continuum approximation (Gordley and Russell, 1981). The calculation of spectrally integrated radiances on the instruments spectral resolution is advantageous because the

use of line-by-line models is computationally expensive. Computation time is typically saved by first choosing the bands according to the instrument's spectral resolution and second by avoiding extensive line-by-line radiative transfer calculations by linear interpolation of pre-calculated emissivity look-up tables. These look-up tables can be calculated with any line-by-line model that is capable of calculating the transmittance of homogeneous gas cells depending on temperature $T$, pressure $p$ and column density $u$,

$$u = \frac{qp}{\mathrm{k}T}\,\mathrm{d}s, \tag{4.9}$$

where $q$ is the volume mixing ratio of the trace gas and k Boltzmann's constant. The emissivities must be calculated for all combinations of $T$, $p$ and $u$ spanning the complete range of atmospheric conditions, and with an appropriate resolution of $T$, $p$ and $u$ to achieve the required accuracy (Gordley and Russell, 1981; Riese, 1994; Marshall et al., 1994; Rodgers, 2000; Hoffmann, 2006). For this work the emissivity tables are calculated with the MIPAS Reference Forward Model (RFM) by Dudhia (2004). In the Advanced MIPAS Level 2 Data Analysis (AMIL2DA) (von Clarmann et al., 2003) the RFM was successfully compared with five other radiative transfer models. The line data and cross section data for the atmospheric gases needed for the calculations are obtained from the HITRAN database (Rothman et al., 2009), which was also applied in AMIL2DA.

JURASSIC is further characterised by the combined use of the Curtis-Godson approximation (CGA) (Curtis, 1952; Godson, 1953) and the emissivity growth approximation (EGA) (Weinreb and Neuendorffer, 1973; Gordley and Russell, 1981) to reduce errors due to the band and continuum approximation. For the CGA the inhomogeneous path through the atmosphere is approximated by an equivalent homogeneous path that is defined by the integral column density $u_{CG}$, a mean temperature $T_{CG}$ and a mean pressure $p_{CG}$, for which the mean emissivity $\epsilon$ is interpolated from the look-up tables. For the EGA the direct interpolation of the emissivity $\epsilon$ from the tables is substituted by the segmental estimation of the pseudo column density $u*$ and calculation of the segmental growth of the emissivity. After interpolating the emissivities for every single gas, following EGA and CGA, the total emissivity is calculated by the product of all transmittances

$$\bar{\epsilon} = 1 - \prod_i \left(1 - \bar{\epsilon}_i\right) + \Delta\epsilon. \tag{4.10}$$

Here, the error term $\Delta\epsilon$ arises due to neglecting spectral correlations among the different emitters and spectral correlation of the transmittance and Planck function along the path. This error is not present in exact line-by-line calculations, where the radiative transfer is calculated monochromatically and spectral averaging is done afterwards to account for the spectral instrument function. However, under certain conditions, such as one gas having a nearly constant spectral signature or when the spectral band is

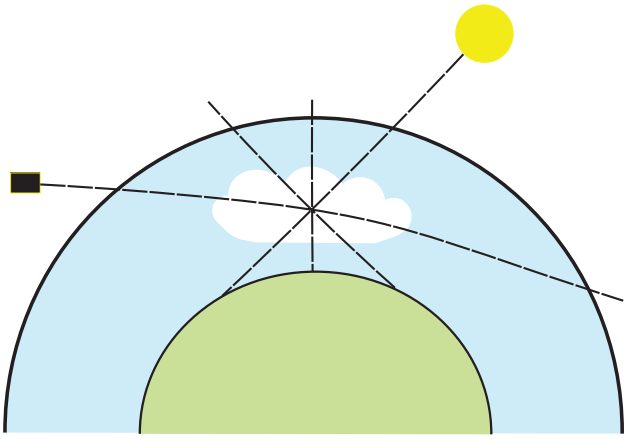

***Figure 4.1:*** *Geometry of a limb path through a cloudy atmosphere. The path is split into segments for which the atmosphere is assumed to be homogeneous. Due to refraction in the Earth's atmosphere the path is refracted towards the Earth's surface. The incoming radiance from all directions is scattered towards the detector by cloud particles.*

large and many lines are considered, the correlations are negligible (Goody and Yung, 1989). A typical error of the EGA is about 1 % in the stratosphere.

## 4.2 Implementation of Scattering

To simulate the scattering of infrared radiance on aerosol and cloud particles along a path through the atmosphere the JURASSIC forward model was extended. In Figure 4.1 the pencil beam through a cloudy atmosphere to a detector is depicted schematically for the limb geometry. Every pencil beam is segmented, indicated by the dashed line, and each segment is considered as a homogeneous gas cell, from the entry to exit point of the defined atmosphere. To account for scattering on particles the segments located in the cloud are determined first. For each segment in the cloud the extinction and scattering coefficients as well as the phase function are calculated and new ray paths ending at that segment are set up to determine the incoming radiance from all directions. The incoming ray paths also pass through the cloud and undergo scattering processes. Based on this approach single or multiple scattering can be computed.

The implementation of scattering in JURASSIC carried out during this work is not limited to the extension of the radiative transfer calculation by scattering terms. Attention

is also paid on the description of different cloud and aerosol types in the atmosphere and their respective scattering parameters, to the optimisation of raytracing, and to the inclusion of the radiation emitted from the sun and the Earth's surface. These new developments will be discussed in more detail below.

The properties of a cloud are additional parameters in the atmospheric input data, which is a defined set of atmospheric parameters, such as temperature, pressure and trace gas volume mixing ratios, given for 1D, 2D, or 3D atmospheres. For cloud or aerosol particles, the log-normal parameters (see Section 2.3.1) for up to three modes can be specified for each grid point. The refractive indices, which account for the chemical composition of the particles, however, are part of the global setup information and not included in the atmospheric input data. The log-normal-parameters and the refractive indices are then used in the Mie module to calculate the scattering parameters. The atmospheric input data used for the following calculations are the version 3.1 climatological data derived for the analysis of Envisat MIPAS measurements by Remedios (1999).

For the forward calculations made in this thesis, the MIPAS climatological data are always used and called model atmospheres. The calculations are also always performed for the spectral resolution of the MIPAS instrument in the chemical mode, which is $0.025\,\mathrm{cm}^{-1}$ (Fischer et al., 2008). Unless stated otherwise the observer is located outside the atmosphere at an altitude of 700 km. For accuracy checks of the model calculations the noise equivalent spectral radiance of MIPAS channels A ($685-970\,\mathrm{cm}^{-1}$) and B ($1215-1500\,\mathrm{cm}^{-1}$), which is about $3{\cdot}10^{-4}\,\mathrm{W/(m^2\ sr\ cm^{-1})}$ and smaller than $2{\cdot}10^{-4}\,\mathrm{W/(m^2\ sr\ cm^{-1})}$ respectively (Kleinert et al., 2007; Hoffmann, 2006), is used.

The step length $\mathrm{d}s$ used for the raytracing that provides the best trade-off in terms of accuracy and computation time is 10 km for limb geometries (Hoffmann, 2006) and 0.5 km for nadir geometries (Hoffmann et al., 2009). However, a single step length variable as initially implemented in JURASSIC does not meet the requirement to calculate limb and nadir ray paths at once. As an example in Figure 4.2, nadir spectra for the wavenumber band of $1224-1228\,\mathrm{cm}^{-1}$ for a tropical, mid-latitude and polar atmosphere calculated with step lengths $\mathrm{d}s$ of 10, 1 and 0.1 km are shown. From the spectra it is obvious that 10 km is not an adequate length because it leads to large errors due to the strong gradients of atmospheric temperature and pressure with altitude. When comparing the 1 and 0.1 km step length, there are just small differences. In the lower panel the relative differences between the 1 and 0.1 km case are shown. They are below 0.8 % for the polar, 1.2 % for the mid-latitude and 2.2 % for the tropical atmosphere. The errors are getting larger when moving from the pole to the equator. This is caused by the steeper temperature gradients in the tropical atmosphere than in the colder polar atmosphere. When comparing the absolute differences between the 1 and 0.1 km case the error is always below the noise equivalent spectral radiance of

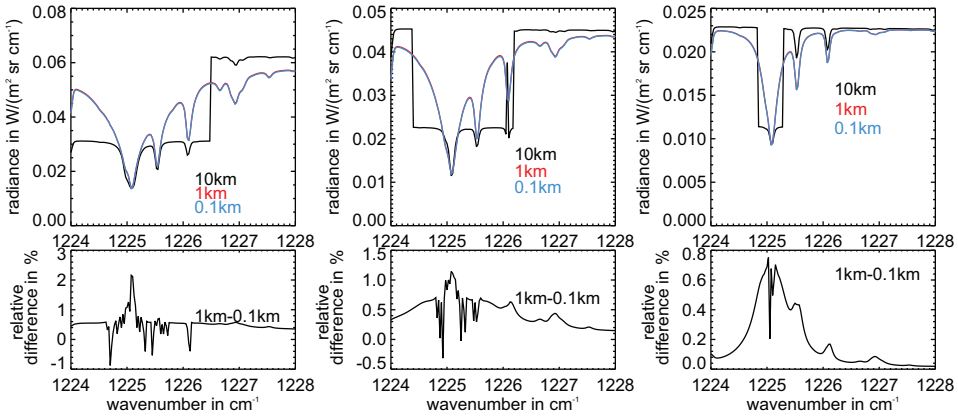


***Figure 4.2:*** *Calculated nadir spectra for tropical (left), mid-latitude (middle) and polar (right) atmospheres with different step length of 10 (black), 1 (red) and 0.1 (blue) km step lengths. The relative errors in the bottom panels show very small errors between 1 and 0.1 km.*

$2{\cdot}10^{-4}\,\mathrm{W/(m^2\ sr\ cm^{-1})}$ for MIPAS (Michelson Interferometer for Passive Atmospheric Sounding), with one exception in the tropical atmosphere.

Clearly, the step length of 10 km is not adequate for nadir geometry. Rather 1 km or 100 m are suitable. However using a step length of 100 m also for the limb calculations, the computational time growth unnecessarily. In order to be able to simulate nadir and limb geometries at the same time, the raytracing algorithm in JURASSIC is modified. Now the step length $\mathrm{d}s$ is estimated from two new parameters $\mathrm{d}s_\mathrm{h}$ and $\mathrm{d}s_\mathrm{v}$. As illustrated in Figure 4.3, $\mathrm{d}s_\mathrm{h}$ is the maximum horizontal step length, as well as the maximum total step length $\mathrm{d}s$, and $\mathrm{d}s_\mathrm{v}$ the maximum vertical step length component. For every given combination of $\mathrm{d}s_\mathrm{h}$ and $\mathrm{d}s_\mathrm{v}$ it is ensured that the resulting step length $\mathrm{d}s$ neither exceeds $\mathrm{d}s_\mathrm{h}$ in total nor $\mathrm{d}s_\mathrm{v}$ in the vertical component.

Appropriate values for horizontal and vertical step lengths are 10 km and 1 km, respectively, representing limb and nadir geometry. The calculation of the resulting step length for the raytracing follows

$$\text{for } \cos\alpha \leq \frac{\mathrm{d}s_\mathrm{v}}{\mathrm{d}s_\mathrm{h}}\text{:} \quad \mathrm{d}s = \mathrm{d}s_\mathrm{h} \tag{4.11}$$

$$\text{for } \cos\alpha > \frac{\mathrm{d}s_\mathrm{v}}{\mathrm{d}s_\mathrm{h}}\text{:} \quad \mathrm{d}s = \frac{\mathrm{d}s_\mathrm{v}}{\cos\alpha}, \tag{4.12}$$

where $\alpha$ is the angle between the line of sight and the nadir direction.

The effect of the ground and the sun on the radiance compared to limb lines of sight are

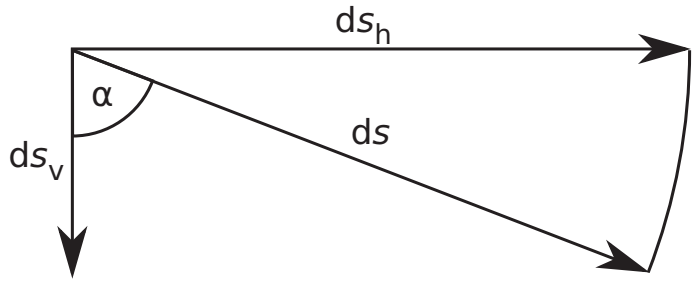


***Figure 4.3:*** *The estimation of the appropriate step length for different geometries is confined by the maximum step length* $\mathrm{d}s_\mathrm{h}$ *and vertical step length component* $\mathrm{d}s_\mathrm{v}$.

shown in Figure 4.4. The radiances are calculated for an observer at 11 km altitude at mid-latitudes for the angular range of 0 – 180°, where 0° is the nadir and 180° the zenith direction. The black curve shows the calculation for a wavenumber of 1225.1 $\mathrm{cm}^{-1}$ where the centre of an emission line of water can be found and the blue curve is for 1226.5 $\mathrm{cm}^{-1}$ where only weak line emissions are present.

For ground looking directions (0°), the radiances are much higher than for the lines of sight directing into space (180 °). The difference between the black and the blue curve is due to the fact that the water vapour at 1225.1 $\mathrm{cm}^{-1}$ absorbs a large amount of upwelling radiation and emits at higher altitudes, where the temperature is smaller, so that the radiance is smaller than for 1226.5 $\mathrm{cm}^{-1}$ for angles between 0 – 90 °. However between 90 – 180° the radiance of the black curve is higher because of the larger water vapour emissions. The crosses at 106 ° denote the position of the sun in this particular simulation and the additional contribution to the radiance made by the sun. To calculate the scattering source term, the radiance from all directions between 0 – 180 ° and the sun direction is needed. Because the slope of these curves is smooth, even under optically thin conditions, it is sufficient for 1D atmospheres, which are horizontally homogeneous, to calculate the incoming radiances for 28 angles dexterously spaced over the angle range.

For the ground hitting lines of sight the exact intersection point with the ground is calculated. The length of the last ray path segment is adapted in order to get the correct ray path length. The ground itself is implemented as a blackbody source emitting with the temperature given at 0 km in the model atmosphere. When calculating the incoming radiance, which is scattered by the particles towards the detector, the radiance emitted by the sun must not be neglected, especially at shorter wavelengths (Höpfner, 2004). For that reason the position of the sun is determined. If the sun can be seen from the position of the scattering particle, the radiance $I_\odot$ reaching the

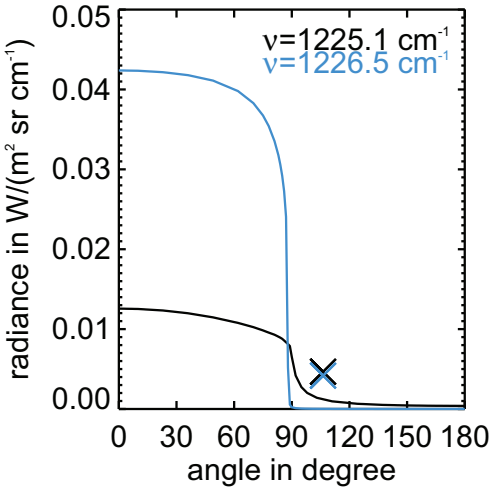


***Figure 4.4:*** *Radiances calculated for an observer at 11 km altitude for nadir to zenith viewing directions and a line of sight to the sun (crosses) at two wavenumbers.*

particle from the sun is calculated by

$$I_\odot = B\left(\nu, T_\odot\right) \tau \Omega_\odot, \tag{4.13}$$

where $B\left(\nu, T_\odot = 5780\,\mathrm{K}\right)$ is Planck's function at the sun's surface temperature, $\tau$ the transmittance through the atmosphere and $\Omega_\odot = 6.764 \cdot 10^{-5}\,\mathrm{sr}$ the solid angle of the sun.

The computation of the integrated scattering parameters $\beta_s$, $\beta_e$ and $P\left(\Theta\right)$ in Equations 3.8 – 3.11 is carried out in a new module of JURASSIC. Depending on the input given, the parameters are either calculated or extracted from the database for non-spherical particles described in Chapter 3.3.2. To use the database, the effective radius $r_{\mathrm{eff}}$ and the ice water content[1] must be given. In contrast, the Mie calculations require refractive indices and number size distributions. Following Höpfner (2008), the numerical integration of the Mie scattering parameters over the number size distribution is accomplished by the Gauss-Hermite quadrature routine from Press et al. (2007). To apply this efficient method, the square root of the argument in the exponent of the number size distribution in Equation 2.1 is substituted by $z$

$$z\left(r\right) = \frac{\ln r - \ln \mu_i}{\sqrt{2} \ln \sigma_i}, \tag{4.14}$$

[1]The ice water content (IWC) is the volume of all particles of a number size distribution multiplied with the density of ice $\rho_{ice}$. $\mathrm{IWC} = \rho_{ice} V = \frac{4\pi}{3} \rho_{ice} \int_{r_1}^{r_2} \frac{n_i r^3}{\sqrt{2\pi} \ln \sigma_i r} \exp\left[-\frac{(\ln r - \ln \mu_i)^2}{2(\ln \sigma_i)^2}\right] \mathrm{d}r$

so that Equation 3.9 can be transformed to

$$\beta_e = \sqrt{\pi} n_i \int_{z(r_1)}^{z(r_2)} Q_e\left(r\left[z\right]\right) r\left(z\right)^2 \exp\left[-z^2\right] \, \mathrm{d}z. \tag{4.15}$$

Equations 3.8 and 3.11 are transformed and solved analogously.

The implementation of scattering into JURASSIC is schematically shown in Figure 4.5. In the input block, the pre-calculated emissivity tables, the atmospheric data containing pressure, temperature, volume mixing ratios of atmospheric gases, the number size distribution parameters, and the control file, which e.g. contains the name of the refractive index file and the step lengths, are given.

In the forward model, the raytracing of the line of sight is calculated first. For this line of sight the segments inside a cloud are identified. Before calculating the radiative transport, the additional source terms due to scattering are estimated for every cloudy segment. For this purpose, the Mie parameters are calculated, then the incident radiation from all directions and the direct radiance from the sun are calculated and weighted with the phase function, to determine which amount is scattered towards the observer. Finally, the extinction and scattering coefficients and the additional source terms for every cloud segment are taken into account in the radiative transfer calculations, which leads to the desired spectrum at the point of observation. Because the incident lines of sight in every cloudy segment may also be scattered the scattering module is capable of calculating multiple scattering by recursively calling the radiative transfer model until the desired order of scattering is reached. For single scattering the extinction of radiance due to scattering and absorption of the incoming radiance is included.

## 4.3 Modelled Spectra

The implementation of scattering presented above incorporates multiple scattering as well as 3D atmospheres. However in the following, (unless stated otherwise), calculations are restricted to homogeneous cloud layers scattering in 1D atmospheres, because of the rapidly increasing computation time when considering multiple scattering or 3D atmospheres and high spectral resolution.

To show the effect of single scattering of different aerosol types and cloud types on infrared limb emission spectra, in the following, scattering spectra are calculated with JURASSIC. For an observer located outside the atmosphere, at an altitude of 700 km, four different scenarios are examined. In the first scenario spectra at mid-latitudes for a tangent height of 6.5 km for clear air and three types of tropospheric aerosol are

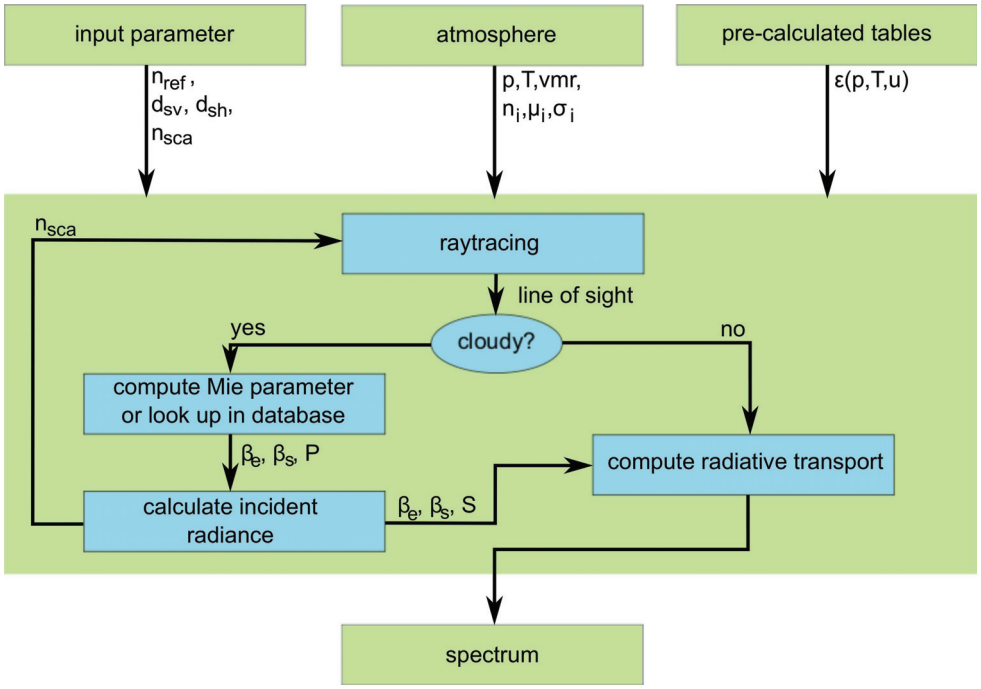


***Figure 4.5:*** *Schematic representation of a forward calculation including scattering. The input parameters $n_{ref}$, $ds_{\mathrm{v}}$, $ds_{\mathrm{h}}$ and $n_{sca}$ are the complex refractive index, the vertical and horizontal step length and the scattering order, respectively. The atmospheric data are pressure $p$, temperature $T$, volume mixing ratio $vmr$ of the gases, number concentration of particles $n_i$, median radius of particle size distribution $\mu_i$ and standard deviation $\sigma_i$ for mode $i$. The emissivities $\epsilon\,(p, T, u)$ in the pre-calculated look-up tables are a function of pressure, temperature and column density $u$.*

| Particle Type | Volume Density in $\mu m^3 cm^{-3}$ |
|---|---|
| Tropospheric aerosol | $4.36 \cdot 10^{-1}$ |
| PSC | 1.13 |
| Sub-visible cirrus | 16.9 |
| Cirrus | $5.76 \cdot 10^5$ |

***Table 4.1:*** *Volume density of the tropospheric aerosol and the cloud types used for the simulated spectra in Figures 4.6 to 4.9. Their particle size distributions are given in Section 2.3.1.*

calculated. The tropospheric aerosol extends from the ground to 12 km altitude. In the second scenario an STS PSC is located between 18 to 20 km altitude in a polar atmosphere. The spectra are calculated for 18 km tangent height. In the third scenario the SVC is located between 15 to 16 km in the tropical model atmosphere and the tangent height is 15.5 km. In the fourth scenario a thick tropical cloud is located between 6 to 12 km and the spectra are calculated for a tangent height of 11 km. The size distributions of the cloud particles chosen for this calculation, are the same as in Table 2.1, as they are typical for these cloud types. For the aerosol the median profile from the aerosol database is chosen. In Table 4.1 their corresponding volume density is listed.

The spectra are calculated for three spectral regions that are sensitive to scattering on particles. The three micro-windows are chosen following Mendrok (2006). They are in channel A and B of the MIPAS instrument and are located in the atmospheric window region between $8-12\,\mu m$ at $825-830\,cm^{-1}$ (w1), $946-951\,cm^{-1}$ (w2) and $1224-1228\,cm^{-1}$ (w3). The micro-windows are characterised by few and weak gas lines and hence they are very sensitive to aerosol and cloud particles. The lines corresponding to the dominating gaseous constituents are marked in Figure 4.7. For the first window between $825-830\,cm^{-1}$ $CO_2$, $H_2O$, $HNO_3$, $NO_2$, OCS, $O_3$, $ClONO_2$, CFC11, HCFC22, and $N_2O_5$ are included in the calculation. The region from $820-834\,cm^{-1}$ has been used by Spang and Remedios (2003) for PSC detection and type classification. The second window between $946-951\,cm^{-1}$ is a commonly employed window for cloud detection (Höpfner, 2004; Ewen et al., 2005). Here $CO_2$, $H_2O$, $HNO_3$, $NO_2$, $N_2O$, $O_3$, $N_2O_5$, and $SF_6$ are included. For the third window between $1224-1228\,cm^{-1}$ $CO_2$, $H_2O$, $CH_4$, $HNO_3$, $NO_2$, $N_2O$, $O_3$, and $N_2O_5$ are the dominating gases.

In Figures 4.6 to 4.9 the black curves show clear air spectra at 6.5, 18, 15.5, and 11 km tangent height for the four scenarios, respectively. The cloud free emission spectra in the stratosphere and upper troposphere are characterised by distinct emission lines of the gaseous atmospheric constituents. Because of lower temperatures, pressure and trace gas volume mixing ratios the emission lines at higher altitudes are weaker and narrower than at lower altitudes. In the troposphere, concentrations of some trace

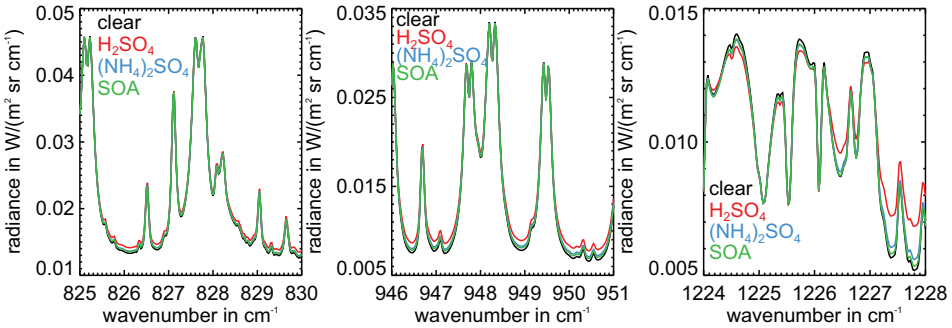


***Figure 4.6:*** *Clear air and aerosol spectra for a tangent height of 6.5 km in three micro-windows. The spectra are calculated for the three previously (Chapter 2 and 3) described tropospheric aerosol types, $H_2SO_4$, $(NH_4)_2SO_4$, and SOA.*

gases, such as water vapour for example, increase rapidly, so that emission lines get saturated and change to absorption lines. This can be seen when comparing the clear air spectrum at 6.5 km in Figure 4.6 with the clear air spectrum at 15.5 km tangent height in Figure 4.8, where the water vapour emission line at 1225.1 $cm^{-1}$ flips to an absorption line.

In the nadir case, which is not shown here, only absorption spectra are observed. This is because the highest temperatures are reached at the ground and the radiance emitted from the ground is much stronger than that emitted by the atmosphere above and gets absorbed by the atmospheric gases along the line of sight. In Figure 4.4 this effect was already shown for weak emission at 1226.5 $cm^{-1}$ and for the water vapour line centre at 1225.1 $cm^{-1}$. When the up-welling radiance is scattered into a limb path, the radiance reaching the observer is typically enhanced by this additional strong radiances from lower altitudes. The spectral slope also changes from pure emission spectra to spectra including absorption features. Hence, the scattered spectra typically look like a combination of limb emission and nadir absorption spectra. In Figure 4.8 this effect is distinctly visible for the scattered radiation for the water line at 1225.1 $cm^{-1}$.

The spectra influenced by absorption and scattering on aerosol particles are shown in Figure 4.6. Comparing the spectra calculated with scattering to those calculated only with extinction (not shown here) the difference is about $1{\cdot}10^{-5}$ W/($m^2$ $cm^{-1}$ sr) (less than 0.1 %), which is negligible compared to the MIPAS noise equivalent radiance. However, for other aerosol cases such as volcanic eruptions or Saharan dust outbreaks, where the aerosol particle sizes are larger than in this case, scattering is not negligible (a case study on volcanic aerosol is presented later). The scattering spectra for three different aerosol types differ from the clear air spectra especially when there is little

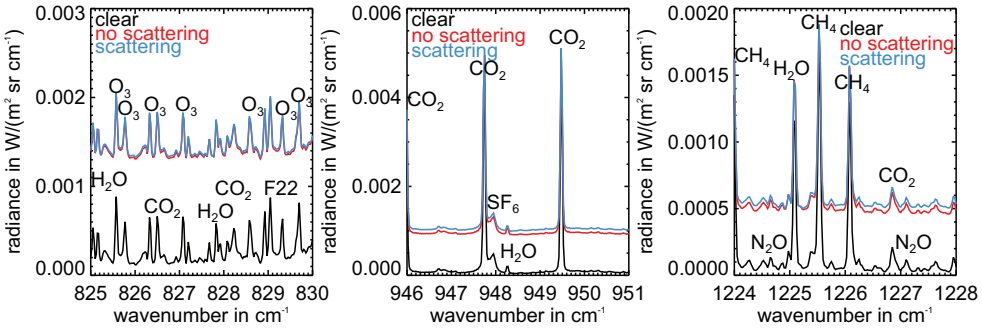


***Figure 4.7:*** *Clear air and PSC extinction and scattering spectra at 18 km tangent height in a polar winter model atmosphere.*

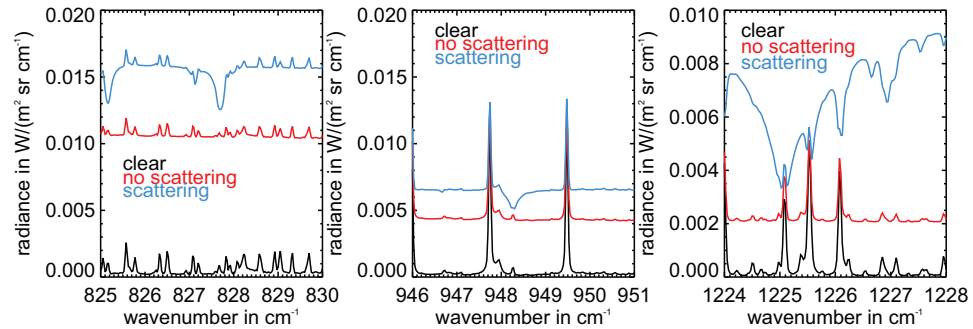


***Figure 4.8:*** *Clear air and SVC extinction and scattering spectra at 15.5 km tangent height in a tropical model atmosphere.*

emission or absorption by trace gases. The largest differences are $8.7{\cdot}10^{-4}$ W/(m$^2$ cm$^{-1}$ sr) at 829.95 cm$^{-1}$, $1.2{\cdot}10^{-3}$ W/(m$^2$ cm$^{-1}$ sr) at 950.45 cm$^{-1}$ and $1.7{\cdot}10^{-4}$ W/(m$^2$ cm$^{-1}$ sr) at 1227.8 cm$^{-1}$ for $H_2SO_4$. For $(NH_4)_2SO_4$ and SOA the maximum differences are slightly above the MIPAS instrument's noise. For that reason the high resolution calculations in these windows are less suitable for discrimination of aerosol types with rather small particle sizes with MIPAS.

In Figure 4.7 the spectra for a (thin) STS PSC between 18 –20 km altitude, a tangent height of 18 km and the number size distribution from Table 2.1 are shown. The spectra, calculated for simple extinction and scattering, are significantly enhanced compared to the clear air spectra. The difference between extinction and scattering calculation is about 2 –9· $10^{-5}$ W/(m$^2$ cm$^{-1}$ sr), which is below the MIPAS instrument noise. The enhancement of the radiation is attributed to the continuum-like emission by the cloud

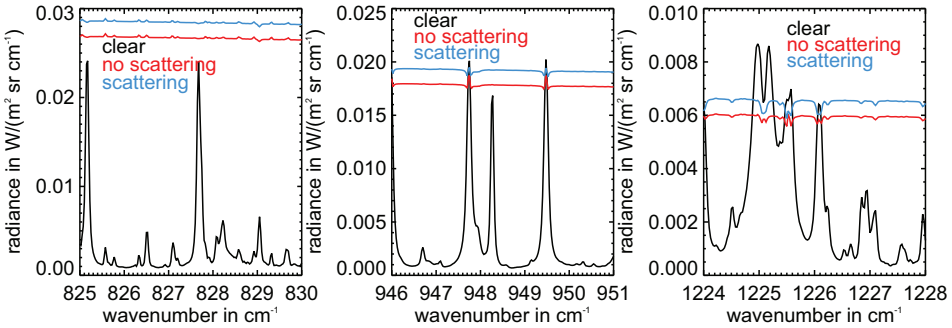


***Figure 4.9:*** *Clear air and cirrus extinction and scattering spectra at 11 km tangent height in a tropical model atmosphere.*

particles and not to scattering.

Spectra for an SVC as in Table 2.1 located in a tropical atmosphere between 15 and 16 km altitude are shown in Figure 4.8. The tangent height is 15.5 km. Extinction and scattering spectra are clearly enhanced compared with the clear air spectra. Here, however, they differ significantly from each other. The scattering spectra are more enhanced and they exhibit absorption features at the wavenumbers where the water lines are located (825.2, 827.8, 948.3 and 1225.1 $cm^{-1}$). This is due to the radiation from lower altitudes being scattered into the line of sight as described above.

For the case of a thick tropical cirrus cloud with the size distribution given in Table 2.1, which is located between 6 and 12 km, the spectra at a tangent height of 11 km are shown in Figure 4.9. Both, extinction and scattering spectra are enhanced, but the scattering spectra are more enhanced than the extinction spectra. The emission features completely vanish except for small dips at the $CO_2$ lines. In the case of thick clouds the extinction and scattering spectra again lie closer to each other, because less up-welling radiance from the ground can pass through the cloud and is scattered into the line of sight. However, the difference is still larger than the MIPAS instrument's noise.

# Chapter 5

# Model Comparison

Models never agree perfectly, because usually there is more than one way to represent the physical and chemical processes to be described, and because in different models rarely completely the same processes are included. This holds for numerical models in general and for the radiative transfer models investigated here in particular. A comparison between the radiative transfer models, all build for the same purpose of simulating the radiative transfer in the infrared through a specific atmosphere, is required to detect and quantify differences and to find out for what reason they arise. The key question to be answered is: Do the differences observed in the model comparison pose any problem to the scientific objectives that are to be achieved with the models? In this chapter the model comparison between the spectrally averaging model JURASSIC and the line-by-line models RFM and KOPRA is performed. The comparison with RFM focuses on the differences that arise from the spectrally averaging approach, and the comparison with KOPRA focuses on calculating scattering of the radiance on aerosol and cloud particles under realistic conditions with model atmospheres containing multiple trace gases.

## 5.1 Comparison of Clear Air High Resolution Spectra

The first step of the model comparison is to compare the clear air calculations of the spectrally averaging model JURASSIC with the MIPAS Reference Forward Model (RFM) (Dudhia, 2004) line-by-line model, which is used to compute the emissivity look-up tables for JURASSIC. Hence both models rely on the same spectroscopy and line physics. Primarily differences arise from approximations in the calculation of

the radiative transfer in JURASSIC. Because the RFM does not include scattering, the Karlsruhe Optimized and Precise Radiative transfer Algorithm (KOPRA) (Stiller, 2000; Stiller et al., 2002) is chosen as a second model for the comparison. In the AMIL2DA project (von Clarmann et al., 2003), in which five groups compared their radiative transfer models, KOPRA and RFM showed the best overall agreement. Only at the $CO_2$ Q-branches, where line mixing is important, RFM and KOPRA show significant differences. The direct diagonalisation approach, which is implemented in KOPRA, "is considered more accurate" at high pressures than the Rosenkranz approximation implemented in RFM (von Clarmann et al., 2003).

The atmospheric data used in this comparison for the model atmospheres are the V3.1 MIPAS reference atmospheres by Remedios et al. (2007), available from Dudhia (2004). An equatorial day-time, mid-latitude day-time, mid-latitude night-time, polar summer and polar winter atmosphere are chosen, to cover a representative range of different atmospheric conditions. The model atmospheres contain temperature, pressure and volume mixing ratio profiles for 30 trace gases on a 1 km grid from 0 – 120 km altitude. The observer is located at 700 km altitude and the tangent heights 8, 10, 12 and 14 km are chosen for the comparison of limb spectra, as they cover the upper troposphere in the tropics, mid-latitudes and polar region and the lower stratosphere in the mid-latitudes and polar region.

In Table 5.1 the four spectral micro-windows and the trace gases contributing to the radiance are listed. The first window between 785 – 795 $cm^{-1}$ is selected, because the distinct $CO_2$ Q-branch line around 792 $cm^{-1}$ is used for temperature retrievals, and it contains several other lines of important gases. The other three windows are chosen because they contain only a few weak and not so closely spaced lines, making these micro-windows suitable for the investigation of scattering on cloud an aerosol particles. The second micro-window located between 825 – 830 $cm^{-1}$, is characterised by weak $O_3$, $CO_2$ and $H_2O$ lines. In the range of 946 – 951 $cm^{-1}$, the third micro-window is dominated by two $CO_2$ and one $H_2O$ line. The fourth micro-window between 1224 – 1228 $cm^{-1}$ contains no $CO_2$ lines, but $H_2O$ and $CH_4$ lines. These micro-windows are different from the spectral regions in the AMIL2DA comparison. Only for 790 to 794 $cm^{-1}$ there is an overlap.

Model comparisons between line-by-line and band models have been performed by several authors and for different instruments. The accuracy of the band models depends on the methods used for the band approach. In Jurassic the CGA, EGA, a linear combination of both and additionally a linear regression can be used (see Chapter 4.2). The CGA method works well for atmospheric trace gases, whose concentration increases with pressure. The agreement was found to be within 1 % (Curtis, 1952). However, $O_3$, which is present in all four micro-windows, reaches its maximum concentration in the stratosphere and larger errors as much as 23 % are reported by Goody (1964) for

| MW | Spectral Range | Trace Gases |
|---|---|---|
| 1 | $785-795\,\mathrm{cm}^{-1}$ | $CO_2$, $HNO_3$, $H_2O$, $NO_2$, $O_3$, $CCl_4$, $ClONO_2$, HCFC-22, $N_2O_5$ |
| 2 | $825-830\,\mathrm{cm}^{-1}$ | $CO_2$, $HNO_3$, $H_2O$, $NO_2$, $O_3$, $ClONO_2$, CFC-11, HCFC-22, $N_2O_5$ |
| 3 | $946-951\,\mathrm{cm}^{-1}$ | $CO_2$, $HNO_3$, $H_2O$, $NO_2$, $O_3$, $N_2O$, $N_2O_5$, $SF_6$ |
| 4 | $1224-1228\,\mathrm{cm}^{-1}$ | $CO_2$, $HNO_3$, $H_2O$, $NO_2$, $O_3$, $CH_4$, $N_2O$, $N_2O_5$ |

***Table 5.1:*** *Spectral range of the four micro-windows (mw) and gases contributing to the radiance in each window.*

nadir calculations.

For the EGA method Weinreb and Neuendorffer (1973) show that it is exact for monochromatic radiation. In their example they examine two spectral intervals with 5 and $8\,\mathrm{cm}^{-1}$ width for nadir geometry and $H_2O$ as the only gas. The averages of the absolute errors of the transmittances ranging from $1-0.7242$ and $1-0.0009$ are 0.0013 and 0.0014 respectively. Gordley and Russell (1981) examine the radiances for limb geometry with tangent heights between $12-40\,\mathrm{km}$. The intervals for $O_3$, $H_2O$ and $HNO_3$ have a spectral width of 50, 200 and $67\,\mathrm{cm}^{-1}$ respectively. In most cases the error is smaller than 0.5 %. The largest errors are found for $H_2O$.

The linear combination of EGA and CGA has been found to be the best method to obtain high accuracy by Marshall et al. (1994) and Francis et al. (2006), because the errors of both methods are in opposite directions and compensate each other when averaged. The typical error in Marshall et al. (1994) was about $1-2$ % for tangent heights between $15-65\,\mathrm{km}$. This error was estimated statistically for a variety of atmospheric states. In regions of steep vertical temperature gradients they report errors larger than 5 %. Marshall et al. (1994) also report about an unpublished study by Rodgers in which the errors were as much as 10 %. In Francis et al. (2006) it is stated that the error of the band model should not be larger than 0.5 % for the temperature retrieval and 1 % for trace gas retrievals. They also show that the errors of most of their channels, which have a width of more than $30\,\mathrm{cm}^{-1}$, fulfil this requirement at tangent heights between $10-60\,\mathrm{km}$.

The studies mentioned above focus on rather broad channels containing several significant trace gas lines. For the analysis of the scattering effect, regions with few gaseous contributions are preferred. In these regions the radiances are small and the relative error might appear large. For that reason the absolute error is also shown in the following comparison. As a quality measure the MIPAS instrument's noise, which is $3{\cdot}10^{-4}\,\mathrm{W/(m^2\ sr\ cm^{-1})}$ in channel A ($658-970\,\mathrm{cm}^{-1}$), and $2{\cdot}10^{-4}\,\mathrm{W/(m^2\ sr\ cm^{-1})}$ in channel B ($1215-1500\,\mathrm{cm}^{-1}$) (Hoffmann, 2006; Kleinert et al., 2007), is chosen.

| mw | spectral range in $cm^{-1}$ | noise equivalent radiance in $W/(m^2\ sr\ cm^{-1})$ | mean noise equivalent radiance in $W/(m^2\ sr\ cm^{-1})$ |
|---|---|---|---|
| 1 | 785 – 795 | $3{\cdot}10^{-4}$ | $1.5{\cdot}10^{-5}$ |
| 2 | 825 – 830 | $3{\cdot}10^{-4}$ | $2.1{\cdot}10^{-5}$ |
| 3 | 946 – 951 | $3{\cdot}10^{-4}$ | $2.1{\cdot}10^{-5}$ |
| 4 | 1224 – 1228 | $2{\cdot}10^{-4}$ | $1.6{\cdot}10^{-5}$ |

***Table 5.2:*** *Noise equivalent radiances for high resolution spectra and mean noise equivalent radiances for the four averaged micro-windows.*

### 5.1.1 JURASSIC – RFM – Limb and Nadir Spectra

For the clear air spectra with $0.025\,cm^{-1}$ resolution, the EGA, CGA and a combination of both methods were tested. Contrary to the results of Marshall et al. (1994) and Francis et al. (2006), the EGA method alone yields the best overall accuracy. This is expected because high resolution calculations are closer to monochromatic calculations, for which the EGA is exact (Weinreb and Neuendorffer, 1973). In Appendix B.1.1 the spectra for the four micro-windows, the absolute differences, and the relative differences between JURASSIC and RFM are shown in Figures B.1 – B.5. To compare the mean differences between JURASSIC and RFM for each micro-window with the spectrally averaging model differences found in e.g. Francis et al. (2006), the mean difference and the standard deviation of the differences as well as the relative mean difference are calculated and given in Appendix B.1.1 Tables B.1 – B.6.

#### Limb Spectra

While Figures B.1 – B.5 reveal that under certain conditions the difference between JURASSIC and RFM exceeds the MIPAS noise at individual lines, the baseline of the difference is near zero in all atmospheres and at all tangent heights. For 8 km tangent height a positive shift of the baseline of about 0.5 % can be observed.

The mean difference of each micro-window is always one magnitude below the MIPAS noise. Yet the MIPAS noise of 2 and $3{\cdot}10^{-4}\,W/(m^2\ sr\ cm^{-1})$ is valid for a single spectral point. When combining several spectral points the noise error reduces by a factor of $\frac{1}{\sqrt{n}}$, with the number of spectral points $n$. The resulting mean noise equivalent radiances for each micro-window are given in Table 5.2. Compared to this mean noise, in all cases the mean difference has the same magnitude as the mean noise. The standard deviation is below the MIPAS noise except for the first micro-window in the polar summer atmosphere, which is due to the larger differences at the $O_3$ lines and the $CO_2$ line at $792\,cm^{-1}$.

The mean relative error is always within the 1 % range, which is postulated as the acceptable limit by Francis et al. (2006) for trace gas retrievals, for the 785 – 795 and 1224 – 1228 $cm^{-1}$ micro-windows. In the 946 – 951 $cm^{-1}$ micro-window the error is always positive but mostly below 1 %, which means that the radiances calculated by JURASSIC are systematically larger than those calculated by RFM. With a linear regression, reducing the radiances by about 0.5 %, the errors for all tangent heights and atmospheres would fall within the 1 % range. In the 825 – 830 $cm^{-1}$ micro-window the radiances calculated by JURASSIC are systematically below the radiances calculated by RFM. Again, some of the errors could be reduced with a linear regression, but not in the polar summer model atmosphere. The reason for the larger differences in the polar summer atmosphere is explained below.

In Figures 5.1 and 5.2 the high resolution spectra for the polar and the equatorial model atmospheres, which represent the best and worst agreement with the line-by-line calculations, are shown. In the polar winter model atmosphere the errors are well within the MIPAS noise for the micro-windows 2 – 4. Just at the $CO_2$ lines and water lines small errors arise. The relative difference is as much as 3 % at the $O_3$ and $H_2O$ lines. In micro-window 1 the absolute difference is mostly within the MIPAS noise, except for three $CO_2$ lines and the relative difference is as much as 5 %. When looking at the equatorial model atmosphere the absolute differences are larger, especially at lower tangent heights and at the 792 $cm^{-1}$ $CO_2$ line. The absolute differences exceed the MIPAS noise up to a factor 7. In the micro-windows 2 – 4 the $H_2O$ lines and the $CO_2$ lines in micro-window 3 show the largest absolute differences at lower tangent heights. There the MIPAS noise is exceeded up to a factor 3. The relative difference is still mostly in the 5 % range due to higher radiances.

These errors can be attributed to the limitations of the EGA method. On the one hand, the method is direction dependent, which means that it should be applied in the direction of increasing absorption to yield best results (Weinreb and Neuendorffer, 1973). On the other hand errors might arise when modelling highly-temperature dependent lines, such as hot bands (Gordley and Russell, 1981). Another source of error are interfering gas lines.

The $CO_2$ lines in micro-windows 1, 2 and 3 are hot bands (Paso et al., 1980; Johns and Noel, 1992). $O_3$ has its concentration maximum in the stratosphere, so in all model atmospheres there is a negative concentration gradient from the stratosphere to the tangent heights used here. This explains the differences at the ozone lines in general. In the polar summer the differences at the $O_3$ lines between the spectrally averaging model and the line-by-line model are largest. In the polar summer the UV radiation from the sun is present day and night. Through absorption of the UV radiation the $O_3$ heats the stratosphere, so that additionally a strong temperature gradient is generated. The high stratospheric temperatures enhance the error due to $O_3$. Hence the larger

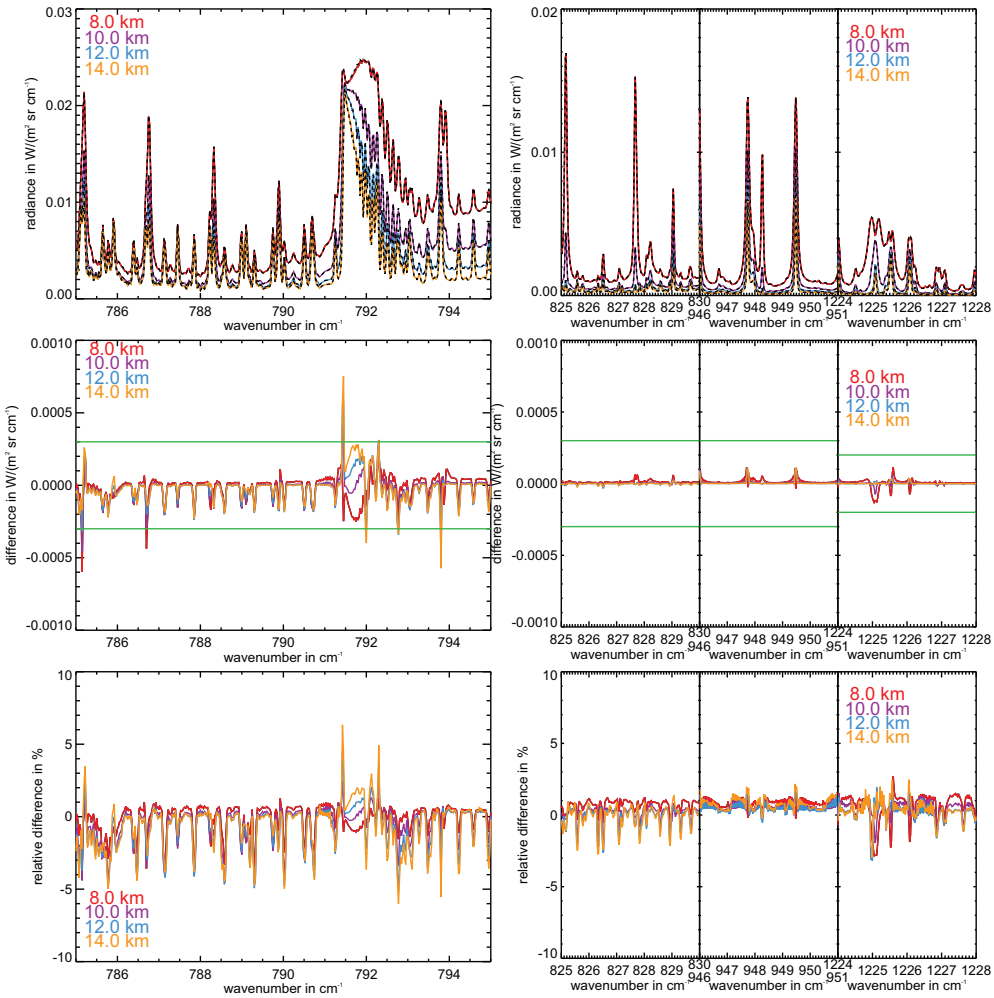


***Figure 5.1:*** *Clear air limb spectra of JURASSIC (coloured solid lines) and RFM (black dashed lines) for the polar winter model atmosphere for four tangent heights (top panel) and the absolute (middle panel) and relative differences (bottom panel) between both models (JURASSIC−RFM). The green lines in the middle panel denote the MIPAS noise equivalent radiance.*

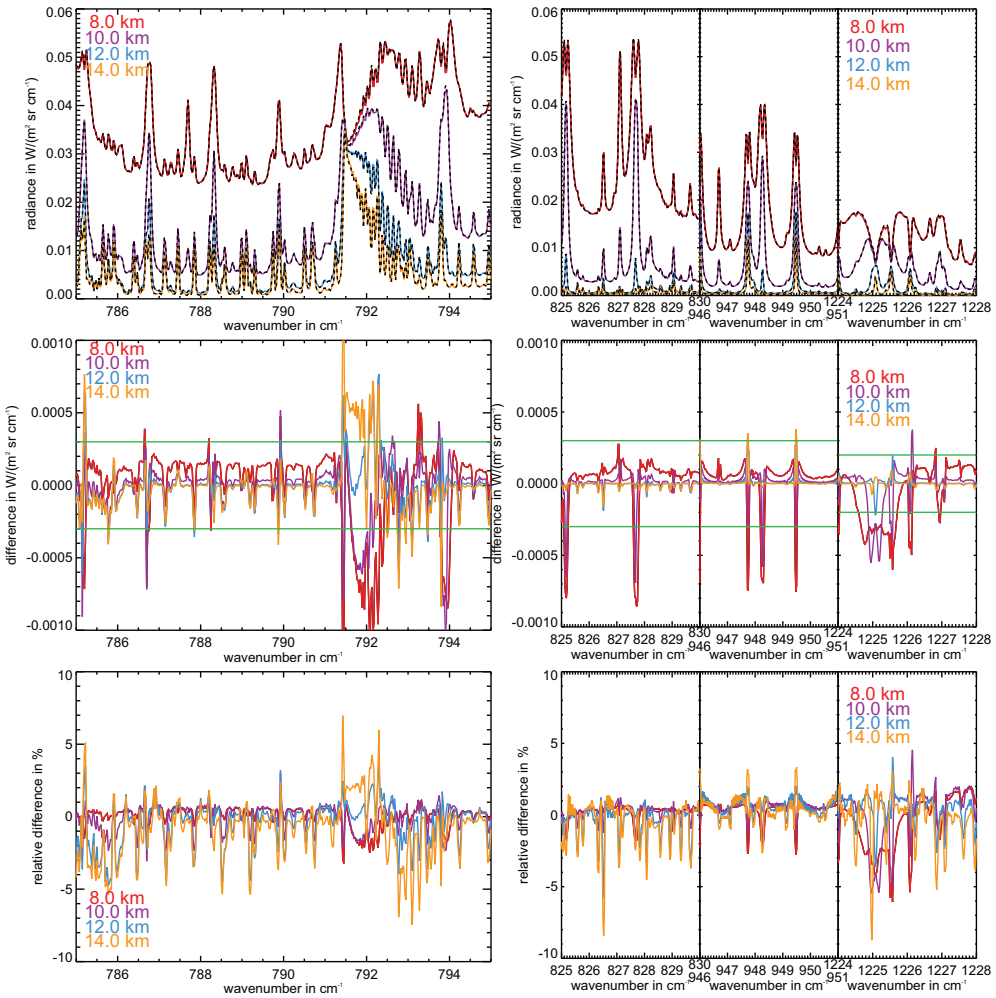


***Figure 5.2:*** *Clear air limb spectra of JURASSIC (coloured solid lines) and RFM (black dashed lines) for the equatorial model winter atmosphere for four tangent heights (top panel) and the absolute (middle panel) and relative differences (bottom panel) between both models (JURASSIC−RFM). The green lines in the middle panel denote the MIPAS noise equivalent radiance.*

relative differences in the polar summer atmosphere in micro-window 2 arise from the many $O_3$ lines, which all cause a negative deviation.

### Nadir Spectra

In Figure 5.3 the nadir radiances for an observer altitude of 14 km, which is representative for the cloud modelling cases, are shown for the five model atmospheres. The spectra for mid-latitude day and night lie on top of each other, as they do not differ in temperature, but only in concentrations of $NO_2$ and $N_2O_5$, which does not lead to any visible differences. The absolute differences exceed the MIPAS noise only in the equatorial and mid-latitudinal atmospheres at the $CH_4$ lines in micro-window 4 and the $CO_2$ and $O_3$ lines in the other windows for the reasons already explained above. The mean absolute difference is always of the same magnitude as the mean MIPAS noise or one magnitude smaller and the mean relative error is always below or equal 0.1 %.

### Discussion

The comparison between the spectrally averaging model JURASSIC and the line-by-line model RFM in the UTLS region determines the accuracy, which can be expected for high resolution JURASSIC calculations for the four analysed micro-windows in the atmospheric window region. For the averaged micro-windows JURASSIC performs very well under all atmospheric conditions, except for micro-window 2 in the polar summer atmosphere due to its $O_3$ lines. The requirement of Francis et al. (2006), that the error of the spectrally averaging model should not exceed 1 %, is fulfilled.

However, the high resolution limb spectra reveal sometimes larger relative errors around $O_3$, $CO_2$ and $H_2O$ line centres. These errors are highly dependent on the model atmosphere type and the micro-window. Yet, several lines, which cause a relative error larger than 1 %, do not cause an absolute error larger than the MIPAS instrument's noise. As the modelling error cannot be distinguished from the instrument's noise, the spectrally averaging model is sufficiently accurate.

For the objective of retrieving cloud properties, the errors around the line centres do not pose any problem, even if they are larger than the instrument noise. The radiance enhancement, caused by scattered radiation, is best observed in gas free windows, for which JURASSIC works extremely well. In scattering calculations the radiation from ground viewing directions plays an important role, because it is much stronger than from the limb directions. For the nadir view from an observer within the atmosphere

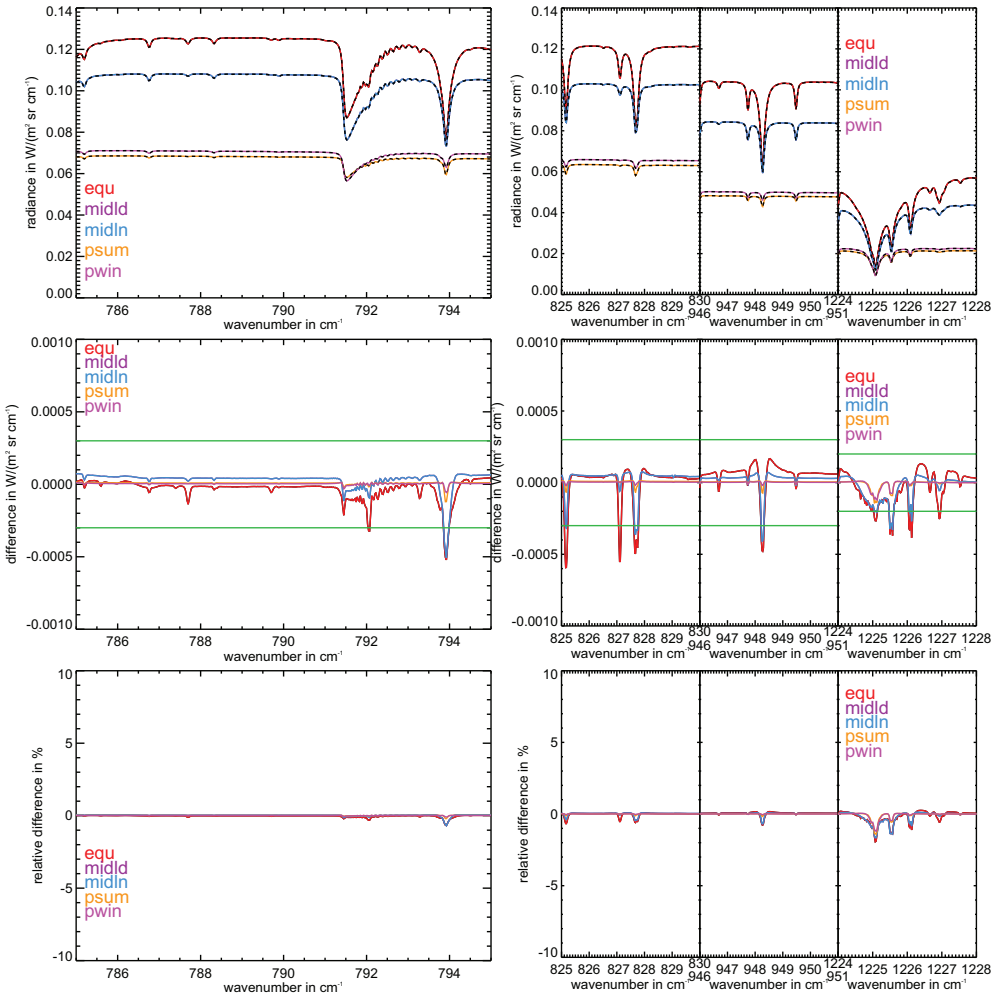


***Figure 5.3:*** *Nadir spectra of JURASSIC (coloured solid lines) and RFM (black dashed lines) for clear air in five different atmospheres (top panel) and the absolute (middle panel) and relative differences (bottom panel) between both models (JURASSIC−RFM). The spectra for the mid-latitude day model atmosphere are congruent with the mid-latitude night spectra. The green lines in the middle panel denote the MIPAS noise equivalent radiance.*

at 14 km, the relative difference of each 0.025 $cm^{-1}$ sampling point is below 1 % except for 1225 – 1226 $cm^{-1}$, which is also extremely good.

### 5.1.2 JURASSIC – KOPRA – Limb and Nadir Spectra

To separate the differences between the two line-by-line models from the differences between JURASSIC and KOPRA, RFM and KOPRA are compared first, before comparing JURASSIC with KOPRA. A thorough comparison of the clear air spectra is prerequisite to understand, which differences are inherently present in the models, and how they might affect the scattering calculations. The clear air comparisons revealed that despite the small differences found in von Clarmann et al. (2003) for the comparison of the water vapour continuum between RFM and KOPRA, it causes larger differences in the four micro-windows examined here, especially at the lowest tangent height of 8 km. For that reason the water vapour continuum is switched off in the following calculations.

#### RFM–KOPRA

In the difference spectra for the comparison between RFM and KOPRA in Appendix B.1.2 in Figures B.6 – B.10 a good overall agreement is observed. The baseline of the difference is close to zero in all atmospheres and at all tangent heights. Generally the $CO_2$, $H_2O$ and $CH_4$ lines, which show the largest differences in the comparison between JURASSIC and RFM, are always within the MIPAS noise, except for the Q-branch $CO_2$ line at 792 $cm^{-1}$ and the HCFC-22 line at 829 $cm^{-1}$. The reasons for these differences are given below. Representative for all model atmospheres, the differences between RFM and KOPRA are described for the mid-latitude night model atmosphere shown in Figure 5.4.

In the first micro-window the large differences around the Q-branch $CO_2$ line at 792 $cm^{-1}$ are a prominent and eye-catching pattern. At the band head the difference is up to 7 % for all tangent heights. In the wings the difference is up to 80 % (0.0078 $W/(m^2\ sr\ cm^{-1}\ )$ at about 791 $cm^{-1}$. This is consistent with the results of von Clarmann et al. (2003), who found a deviation of 0.6 % at the band head and a net effect of 10 % due to the line mixing, which increases up to a factor of 10 when considering the MIPAS instruments line shape, which is also considered here, and the field of view (not considered). Possible explanations for such behaviour are discussed in von Clarmann et al. (2003). However, in this comparison the line mixing certainly has a non-negligible part in the difference, because all tangent heights are below 15 km, which was investigated in von Clarmann et al. (2003) and the differences increase with

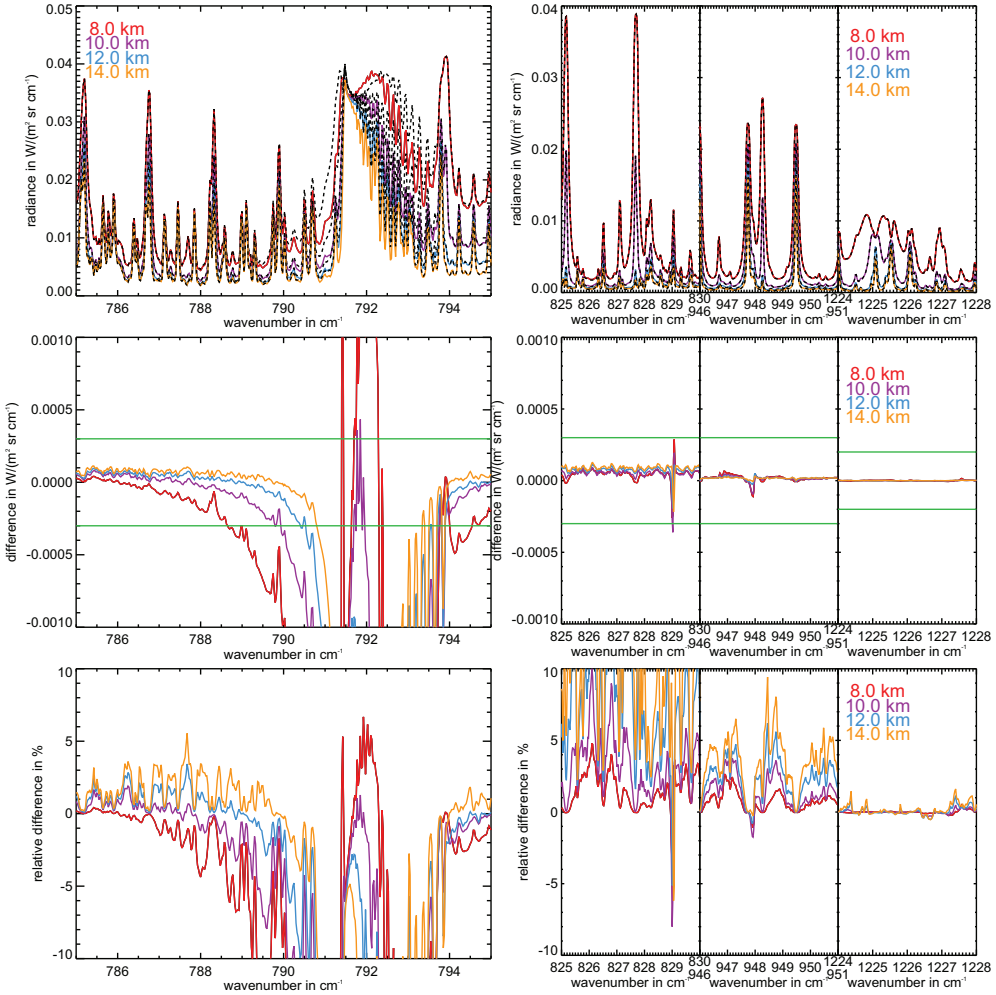


***Figure 5.4:*** *Clear air limb spectra of RFM (coloured solid lines) and KOPRA (black dashed lines) for the mid-latitude night atmosphere for four tangent heights (top panel) and the absolute (middle panel) and relative differences (bottom panel) between both models (RFM−KOPRA). The green lines in the middle panel denote the MIPAS noise equivalent radiance.*

decreasing tangent height. The line wings of the $CO_2$ line affect nearly the complete micro-window at 8 km tangent height. At the other tangent heights the absolute difference is within the MIPAS noise between 785 – 789 $cm^{-1}$ and 794 – 795 $cm^{-1}$.

In the second micro-window the absolute difference is small and very well within the MIPAS noise, except for the 829 $cm^{-1}$ HCFC-22 line. This difference is due to the different handling of the absorption cross section data of HCFC-22 in both models. Generally the radiances calculated by RFM are larger than the radiances calculated by KOPRA. However, even though the relative differences exceed 10 % for the two higher tangent altitudes, the absolute differences are tiny compared to the MIPAS noise. The relative differences become so large only because of the small radiances in this micro-window.

In the third and fourth micro-windows the absolute difference is also very small and always within the MIPAS noise. Only at the 948 $cm^{-1}$ $SF_6$ line a significant difference is found. Because $SF_6$ also is a so called cross section gas, for which no detailed line data is available, again the different handling of the cross section data is the source of the difference. The absolute as well as the relative differences are nearly always positive, which means, that the radiances calculated by RFM are systematically larger than the radiances calculated by KOPRA.

The nadir spectra for the comparison between RFM and KOPRA are shown in Figure 5.5. Generally they show an excellent overall agreement in absolute and relative difference, except for the Q-branch $CO_2$ line around 792 $cm^{-1}$. In contrast to the limb spectra, the difference is now positive, which means the radiances calculated by RFM are much higher than that by KOPRA around this line. A closer look at the absolute difference of each micro-window reveals that the radiances calculated by RFM are generally slightly larger than the radiances calculated by KOPRA.

### JURASSIC–KOPRA

The comparison between JURASSIC and KOPRA shows, that the differences are a combination of the general line-by-line model differences between RFM and KOPRA and the differences that arise due to the spectrally averaging model approach in JURASSIC. In Appendix B.1.3 in Figures B.11 – B.15 all spectra and their corresponding absolute and relative differences are shown. In all atmospheres and at all tangent heights the baseline of the difference is close to zero. The differences due to single trace gas lines are discussed for the mid-latitude night spectra in Figure 5.6.

In micro-window 1 the difference of the Q-branch $CO_2$ line at 792 $cm^{-1}$ is the dominant feature that results from the different line mixing treatment including different line wing cut-off criteria (von Clarmann et al., 2003). The differences at the $O_3$ lines that exceed

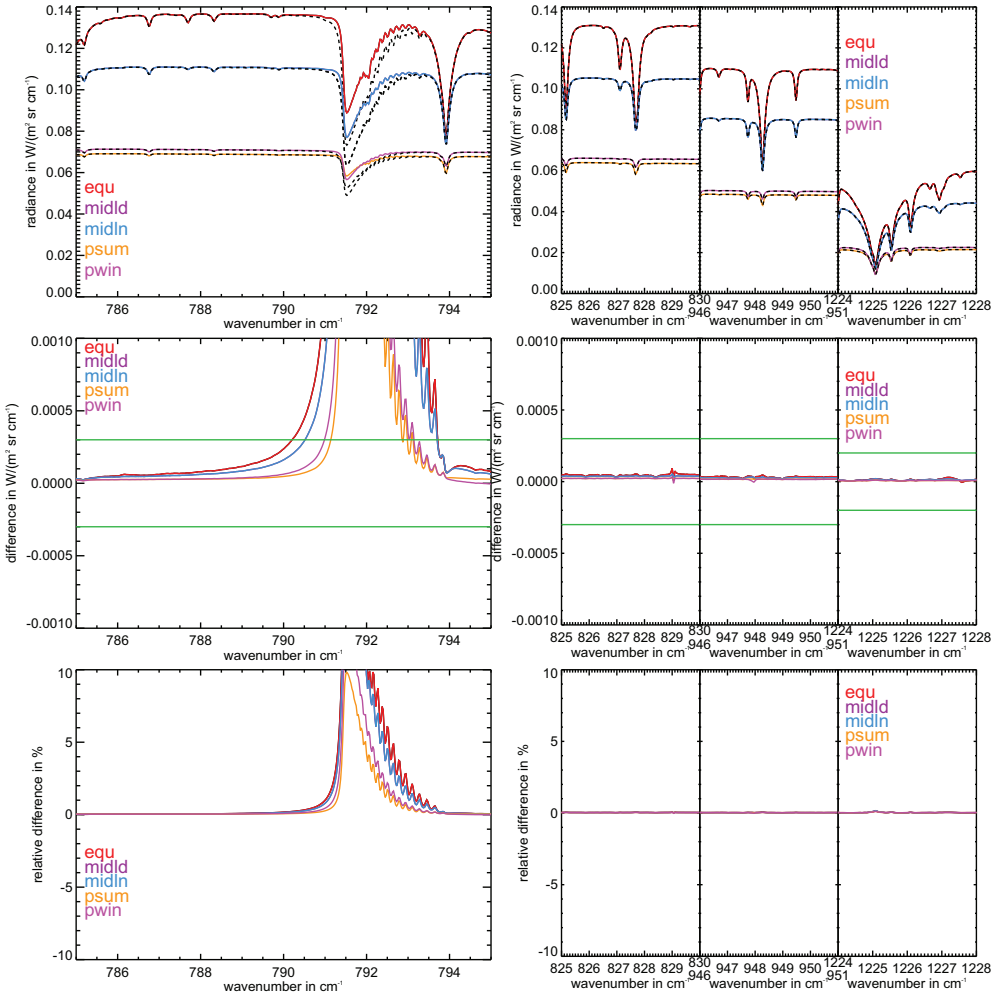


***Figure 5.5:*** *Nadir spectra of RFM (coloured solid lines) and KOPRA (black dashed lines) for clear air in five different atmospheres (top panel) and the absolute (middle panel) and relative differences (bottom panel) between both models (RFM−KOPRA). The green lines in the middle panel denote the MIPAS noise equivalent radiance.*

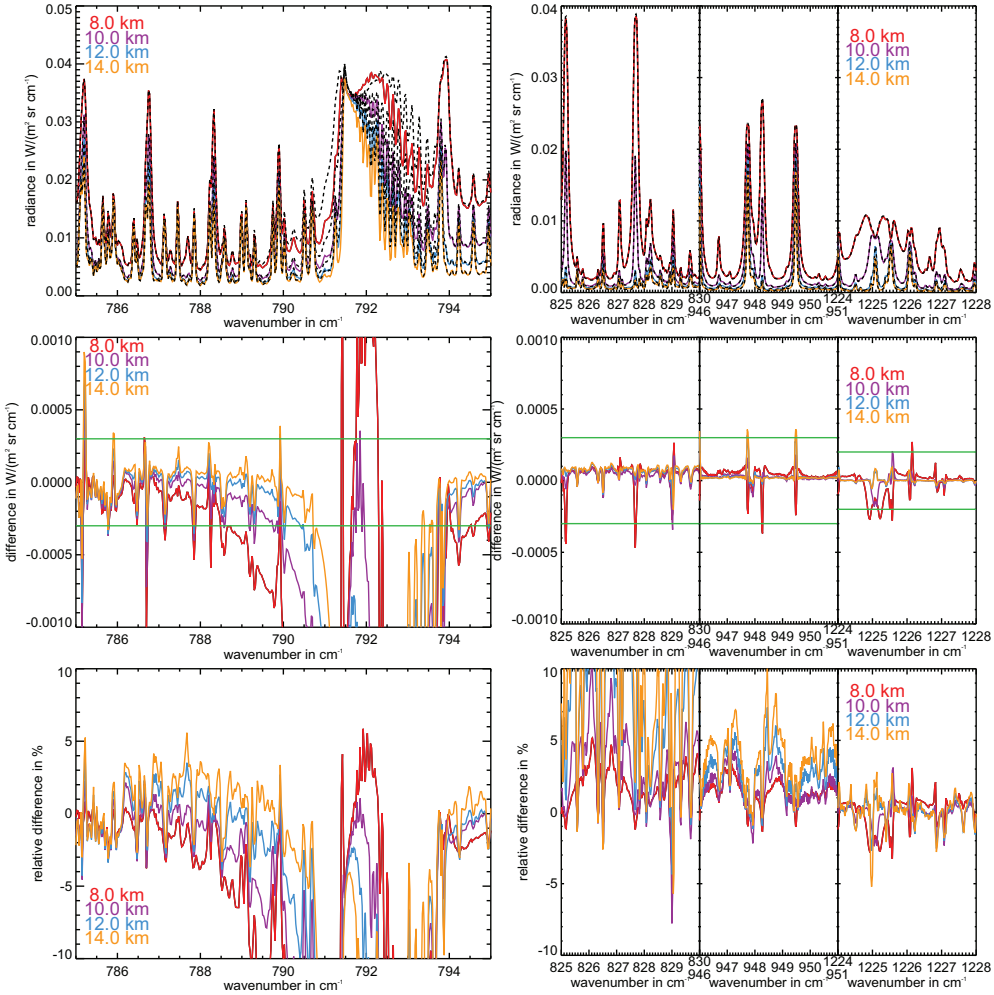


***Figure 5.6:*** *Clear air limb spectra of JURASSIC (coloured solid lines) and KOPRA (black dashed lines) for the mid-latitude night atmosphere for four tangent heights (top panel) and the absolute (middle panel) and relative differences (bottom panel) between both models (JURASSIC−KOPRA). The green lines in the middle panel denote the MIPAS noise equivalent radiance.*

the MIPAS noise arise from the spectrally averaging approach. The only differences exceeding the MIPAS noise in micro-window 2 are two $H_2O$ lines at 8 km tangent height, which are caused by the spectrally averaging approach, and the HCFC-22 line at 829 $cm^{-1}$ that is caused by different cross section gas handling in RFM and KOPRA. The same explanations apply for the $CO_2$ lines and the $SF_6$ line in micro-window 3. In micro-window 4 all differences can be assigned to the spectrally averaging approach of JURASSIC.

As for the comparison between JURASSIC and RFM, the mean differences and standard deviations of the differences as well as the relative mean differences for each micro-window are calculated and given in Appendix B.1.3 in Tables B.7 – B.12. Due to the large differences around 792 $cm^{-1}$, the mean absolute difference of micro-window 1 is negative for all tangent heights and model atmospheres. The mean absolute difference as well as the standard deviation are up to two magnitudes larger than the mean MIPAS noise given in Table 5.2. The mean relative difference is also always negative and varies between 5.6 – 10.5 %.

For micro-windows 2, 3, and 4 the mean absolute difference between JURASSIC and KOPRA and the standard deviation are slightly larger than for the comparison between JURASSIC and RFM. Both are in most cases of the same magnitude as the mean MIPAS noise (see Table 5.2). In micro-window 3, the standard deviation exceeds this magnitude for the polar summer model atmosphere. The relative differences vary between −2.5 and 7.4 % in micro-window 2, 0 and 2.8 % in micro-window 3, and −1 and 0.4 % in micro-window 4.

The clear air nadir spectra and their corresponding absolute and relative differences between JURASSIC and KOPRA are shown in Figure 5.7. The differences between the nadir spectra are also a combination of the differences between the spectrally averaging model JURASSIC and the line-by-line model RFM, and both line-by-line models RFM and KOPRA. The first micro-window is dominated by the $CO_2$ line difference at 792 $cm^{-1}$, which is of opposite sign than in the limb spectra. Beyond the range affected by this line, the absolute difference is within the MIPAS noise, except for some spectral regions in the equatorial model atmosphere. The relative difference, however, is smaller than 1 % except for the $CO_2$ line. In the other three micro-windows the MIPAS noise is exceeded at the $CO_2$, $H_2O$ and $CH_4$ lines, which were already identified in Section 5.1.1, and especially in the equatorial model atmosphere. This is due to the steep temperature gradients. However, the relative differences are small and always within the 1 % range except for 1224.5 – 1225.5 $cm^{-1}$.

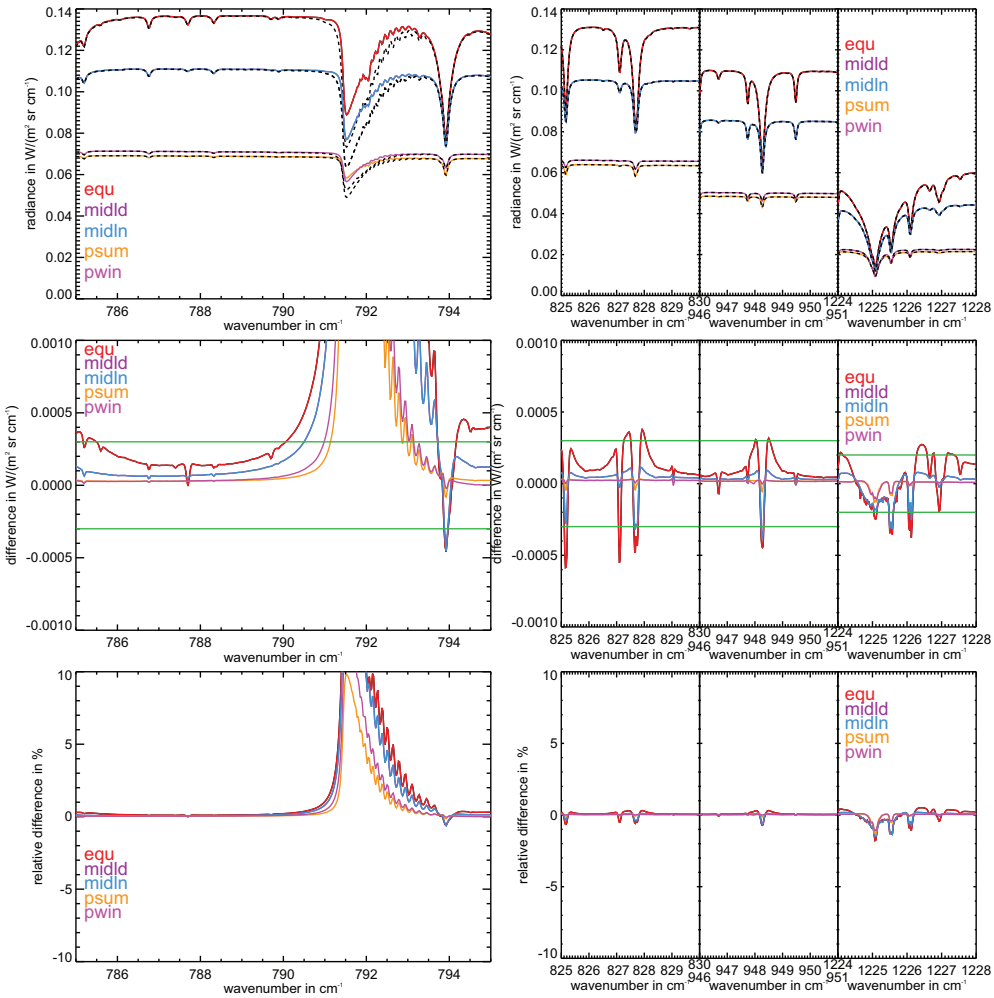


***Figure 5.7:*** *Nadir spectra of JURASSIC (coloured solid lines) and KOPRA (black dashed lines) for clear air in five different atmospheres (top panel) and the absolute (middle panel) and relative differences (bottom panel) between both models (JURASSIC−KOPRA). The green lines in the middle panel denote the MIPAS noise equivalent radiance.*

**Discussion**

When looking at the absolute differences of the spectra, generally the differences between JURASSIC and KOPRA are smaller in the cold polar winter model atmospheres and at high tangent heights. For lower tangent heights and warmer atmospheres, the temperature gradient increases as well as the water vapour concentration gradient. The largest differences between the two models are either found in the equatorial or polar summer model atmospheres. However, the largest differences found, are due to differences between both line-by-line models. Different implementations of, for example, line mixing and the water vapour continuum cause by far larger differences than the spectrally averaging approximation made in JURASSIC.

Because the baselines of the differences between JURASSIC and KOPRA are always within the MIPAS noise and close to zero, the model differences are not expected to cause any problems for the scattering calculations in windows 2, 3, and 4. The large differences of the Q-branch $CO_2$ at $792\,\mathrm{cm}^{-1}$ are likely to cause difficulties to temperature retrievals and need some attention. Weigel et al. (2010) minimised the differences between JURASSIC and RFM for CRISTA-NF retrievals by applying a linear regression method, which is not used in this comparison. For scattering calculations, it is expected that the differences get smaller, because of the opposite directions of the differences for limb and nadir view.

## 5.2 Comparison of Cloudy Air High Resolution Spectra

### 5.2.1 Scattering Module Demonstration

For the comparison between the single scattering implemented in JURASSIC and KOPRA, a simpler setup than for the clear air gas phase comparison in Section 5.1 is used. It is based on the setup of the comparison of single with multiple scattering in Höpfner and Emde (2005). A cloud is placed between $9.5-12.5\,\mathrm{km}$ altitude in a mid-latitude model atmosphere containing only $CO_2$ and $H_2O$ as trace gases. The cloud is defined as an ice cloud with the refractive indices of ice taken from Toon et al. (1994). The number concentration of the ice particles is constant between $10-12\,\mathrm{km}$ and decreases linearly to zero at the cloud edges between $10-9.5$ and $12-12.5\,\mathrm{km}$. To simulate clouds of different optical depth, the number concentration is increased by one order of magnitude four times. This leads to five scenarios, for which the number concentration and the corresponding optical opacities for nadir and limb direction are given in Table 5.3. The median radius of $4\,\mu\mathrm{m}$ and the width of the number size distribution of 1.35 are

| Scenario | $n$ in $\mathrm{cm}^{-3}$ | Nadir Optical Depth | Limb Optical Depth |
|---|---|---|---|
| 1 | 0.01 | translucent | translucent |
| 2 | 0.1 | translucent | translucent |
| 3 | 1 | translucent | opaque |
| 4 | 10 | translucent | opaque |
| 5 | 100 | opaque | opaque |

***Table 5.3:*** *Number densities $n$ of the cloud scenarios used for the comparison of JURASSIC with KOPRA.*

kept constant. The spectral window to be analysed ranges from $947 - 950\,\mathrm{cm}^{-1}$ and the single scattering albedo in the middle of this range is 0.24.

The spectra, calculated for an observer at 700 km altitude looking a tangent height of 11 km and a vertical step length of 1 km, are shown in the top left panel of Figure 5.8. Scenario 1, whose number density is comparable to an STS PSC (Höpfner and Emde, 2005), looks similar to the clear air spectrum but the continuum is enhanced because of the radiance from the ground, which is scattered into the line of sight. In scenario 2, whose number concentration is comparable to an ice PSC (Höpfner and Emde, 2005), even more radiance from the ground is scattered into the line of sight, so that the emission spectrum becomes flat and turns into an absorption spectrum. For scenario 3 the largest radiances are obtained. In scenario 4 the radiance decreases, because the radiance from the ground is absorbed within the cloud to some extent. In scenario 5 the cloud is optically thick even in nadir direction. It is expected that even more radiation from the ground is absorbed in the cloud and hence the radiance for scenario 5 would be below scenario 4. However for both models this is not the case. The radiance for scenario 5 is larger than for scenario 4. An explanation for that is given below.

In the bottom right panel of Figure 5.8 the difference between the clear air spectra is examined in detail. While RFM and KOPRA do not show any difference, there is a small difference between JURASSIC and KOPRA at the $CO_2$ lines, which is due to the spectrally averaging model approach as explained in Section 5.1.1. In the bottom left panel the absolute differences for clear and cloudy air spectra are shown. For scenarios 1 to 3 they lie within the MIPAS instrument's noise. For scenario 3 the difference is almost zero over the entire spectral range analysed. The differences for scenarios 4 and 5 are above the noise. Generally the radiances calculated by JURASSIC slightly overestimate the radiances calculated by KOPRA.

The relative differences for this comparison are shown in the top right panel of Figure 5.8. For the clear air spectrum it can be seen that even though the absolute difference is almost zero, the relative difference ranges from $-4$ to 6 % at single sampling points. The relative difference for scenario 1 ranges from about 1 to 4 % and for

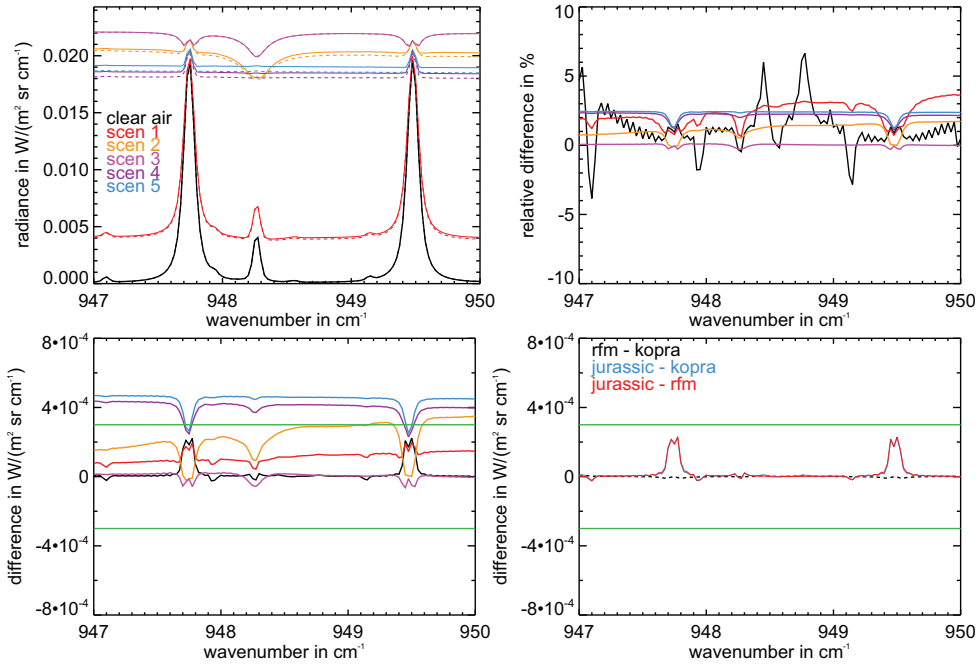


***Figure 5.8:*** *Forward model comparison between JURASSIC and KOPRA for clear air limb spectra at 11 km tangent height and for five cloud scenarios. The solid lines show the JURASSIC calculations whereas the dashed lines show the KOPRA calculations. The colours correspond to the different scenarios given in Table 5.3. The black line shows the radiance for a clear air spectrum. In the top left panel the spectra are shown, the relative differences between JURASSIC and KOPRA are shown in the top right panel and the absolute differences in the bottom left panel. In the bottom right panel the detailed absolute differences for the clear air calculations for JURASSIC, KOPRA and RFM are presented as well.*

scenario 2 from 1 to 2 %. The relative difference of scenario 3 is close to 0 % and the relative differences of scenarios 4 and 5 are slightly above 2 %.

In Table 5.4 the mean differences between JURASSIC and KOPRA and the differences for the comparison between KOPRA and ARTS (Atmospheric Radiative Transfer Simulator), which is the multiple scattering model used for the comparison in Höpfner and Emde (2005), are given. The mean difference between the radiances calculated by JURASSIC and KOPRA is generally positive, except for scenario 3. This means that radiances calculated by JURASSIC are slightly larger than the radiances calculated by

KOPRA. The comparison between the single scattering in KOPRA and the multiple scattering in ARTS shows that the radiances calculated by KOPRA are slightly smaller than the radiances calculated by ARTS. As the relative difference between JURASSIC and KOPRA is of opposite sign than the relative difference between KOPRA and ARTS, it can be assumed that the comparison between JURASSIC and ARTS would result in comparable differences.

| Scenario | JURASSIC - KOPRA | KOPRA - ARTS |
|---|---|---|
| 1 | +2.5 % | −0.5 % |
| 2 | +1.5 % | −0.5 % |
| 3 | 0 % | −2 % |
| 4 | +2.1 % | −2.5 % |
| 5 | +2.3 % | −2 % |

***Table 5.4:*** *Mean relative differences for the five scenarios between JURASSIC and KOPRA, KOPRA and the multiple scattering model ARTS.*

In Höpfner and Emde (2005), for the cases of the single scattering albedo $\tilde{\omega} = 0.24$ and $\tilde{\omega} = 0.84$, it is concluded that the single scattering is a good simplification for thin clouds as in scenarios 1 and 2. The largest differences were found in scenarios 3 and 4, because of the larger contribution due to multiple scattering in ARTS. For the JURASSIC calculations, which are performed for $\tilde{\omega} = 0.24$ only, the smallest relative differences to KOPRA are found for scenarios 2 and 3 and the smallest absolute differences for scenario 1 and 3 (see Figure 5.8). This leads to the conclusion that the single scattering module of JURASSIC is appropriate to calculate the effect of thin clouds.

In Figure 5.9 the same calculation is shown, but for a vertical step length of 100 m instead of 1 km in JURASSIC. For the clear air spectrum and scenarios 1 and 2 no difference to Figure 5.8 can be seen. A close look at scenario 4 and 5 makes it obvious that the radiance in scenario 5 is now slightly smaller than in scenario 4, as one would expect. In a cloud, which is optically thick in nadir direction (scenario 5), the radiance is expected to be that of a blackbody emitting with cloud temperature. When the cloud is permeable for the radiation from the ground (scenario 4), the radiance from the ground is scattered into the line of sight and increases the radiance, so that the radiance (in scenario 4) is larger than the radiance for the optically thick cloud in nadir direction (in scenario 5).

Here the radiance of scenario 4 is not significantly larger than in scenario 5. Not only the radiance from the nadir direction, but all radiance from the ground contributes to the enhancement. However from 11 km altitude the ground can be seen up to an angle of approximately 87° and the larger the angle, the longer the path through the cloud

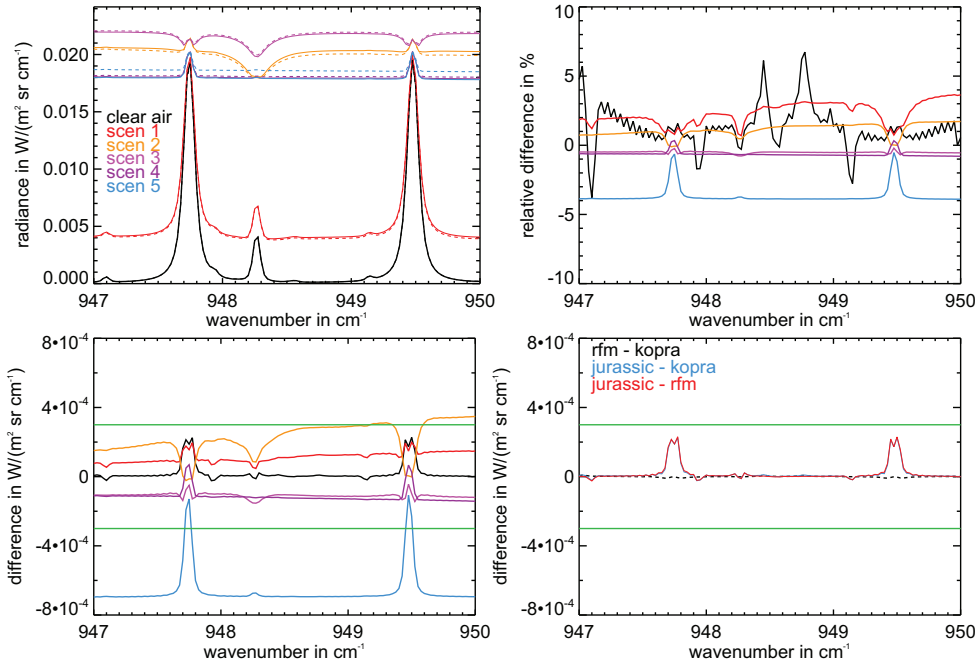


***Figure 5.9:*** *Forward model comparison between JURASSIC and KOPRA for clear air limb spectra at 11 km tangent height and for five cloud scenarios but calculated with a vertical step length of 100 m. The solid lines show the JURASSIC calculations whereas the dashed lines are the KOPRA calculations. The colours correspond to the different scenarios of Table 5.3. The black line shows the radiance for a clear air spectrum. In the top left panel the spectra are shown, the relative differences between JURASSIC and KOPRA are shown in the top right panel and the absolute differences in the bottom left panel. In the bottom right panel the detailed absolute differences for the clear air calculations for JURASSIC, KOPRA and RFM are presented.*

and the more radiance is absorbed by the cloud particles before reaching the scattering particle in the line of sight. When assuming multiple scattering, the radiance from the ground is not only absorbed but also scattered. Generally due to multiple scattering more radiance reaches the scattering particle in the limb line of sight and enhances the radiance as shown in scenarios 3 and 4. However, in a thicker cloud it is likely that the radiance from the ground is scattered more often and less radiance arrives at the scattering particle in the limb line of sight to enhance the radiance. That is why the radiance in scenario 4 is smaller than in scenario 2 and 3. In scenario 5 much less radiance can be scattered into the line of sight by single as well as by multiple

scattering. For that reason single scattering is also a good approximation for thick clouds with a small single scattering albedo.

The choice of the vertical step length is crucial, because, if chosen too large, it leads to an overestimation of the radiances by about $1{\cdot}10^{-3}\,\mathrm{W/(m^2\ sr\ cm^{-1})}$ ($\sim$5 %) for the thick clouds (compare top left panels of Figures 5.9 and 5.8). The thinner the clouds the smaller the error. This is plausible because with a step length of 1 km in the nadir case, the part of the cloud between 9.5 – 10 km is missed completely and hence also cannot absorb parts of the incoming radiation, so that the resulting radiance is always too large. In the following section the issue of the impact of the vertical step length is addressed again and discussed in more detail.

### 5.2.2 Cloud Spectra Comparison

The setup for this comparison between JURASSIC and KOPRA is the same as in Section 5.1.2. Two different clouds are added and radiances calculated by JURASSIC and KOPRA are compared. In the first step the radiance is calculated with both models by accounting just for the extinction due to the clouds but neglecting the scattering source term. Therefore the absorption coefficient $\beta_a$ is set to $\beta_e$ and the scattering source $S(\nu, s)$ is set to zero in Equation 4.3. In the second step, the complete scattering is calculated and the radiances are compared.

#### Cloud Scenario Setup

For the comparison, two different ice cloud layers with respect to their number size distribution, are placed between 14 – 15 km altitude. Within the cloud the number concentration is constant. At the lower and upper boundary there is a 10 m range, in which the number concentration decreases linearly to zero to have sharp cloud edges. The parameters of the number size distributions are given in Table 5.5. The clouds are representative for a very thin cirrus or a sub-visible cirrus cloud. Both have a single scattering albedo of 0.45, which is about twice as large as the single scattering albedo of the clouds in Section 5.2.1. They mainly differ in their nadir optical depth, which is comparable to scenarios 1 and 2 in Section 5.2.1 for cloud 1 and 2 respectively.

The model atmospheres polar winter, polar summer, mid-latitude day and night, equatorial night, and tangent heights of 8, 10, 12 and 14 km, are chosen for this comparison analogous to the clear air comparison. However, because of the very small differences between the mid-latitude night and mid-latitude day model atmospheres, here only results for the mid-latitude night model atmosphere are presented. In the scattering

| Parameter | Cloud 1 | Cloud 2 |
|---|---|---|
| $n$ | $5.9{\cdot}10^{-3}$ cm$^{-3}$ | $2.4{\cdot}10^{-2}$ cm$^{-3}$ |
| $\mu$ | 11.2 $\mu$m | 7.89 $\mu$m |
| $\sigma$ | 1.6 | 1.9 |
| $\tilde{\omega}\,(948.5\text{cm}^{-1})$ | 0.45 | 0.45 |
| $t$ | $7.1{\cdot}10^{-3}$ | $2.05{\cdot}10^{-2}$ |

***Table 5.5:*** *Number size distribution parameters $n$, $\mu$, $\sigma$, single scattering albedos $\tilde{\omega}$ and nadir optical depths $t$ of the two clouds used for the comparison of the single scattering in JURASSIC and KOPRA.*

calculation for the mid-latitude day and equatorial day model atmospheres, where direct radiation from the sun is included, no striking difference is found in the spectra and even the relative differences between both models differ only in the per mill range for the mid-latitude night and day as well as for the equatorial night and day cases. With respect to the tangent heights, only the 14 km tangent point is within the clouds. For the other three tangent heights the line of sight passes trough the cloud layer, dives through the cloud free atmosphere beneath the cloud and passes through the cloud layer again. The lower the tangent height, the steeper the angle at which the cloud is entered and the shorter the path through the cloud.

For this relatively thin cloud in the vertical, the vertical step length of $\mathrm{d}s_\mathrm{v} = 1$ km chosen for the KOPRA calculations, leads to difficulties in the cloud sampling of JURASSIC. As already noted in Section 5.2.1 a vertical step length chosen too large causes sampling errors in JURASSIC. This effect is illustrated in Figure 5.10. In the top panel vertical profiles of the radiances calculated for a vertical step length of 1 km and 100 m in a polar model atmosphere at 1226.6 cm$^{-1}$ for clear air and the cloud 1 case are shown. In the middle and bottom panel the absolute and relative differences are presented respectively. While for the clear air profile the step length does not have any significant impact, there are obvious differences in the cloudy air profile. Tests with even smaller vertical step length up to 10 m showed, that the cloudy radiance profile converges and that 100 m are a good agreement.

In the polar winter model atmosphere at around 10 km tangent height, the difference between the two vertical step lengths exceeds the MIPAS noise significantly. The relative difference is as much as 17 %. Figure 5.10 shows that the difference strongly depends on the tangent height. In the other model atmospheres, however, large differences are found at other tangent heights. The reason for that behaviour is that a cloud of only 1 km vertical extent cannot be sampled properly with a vertical step length of 1 km in JURASSIC. When analysing thin cloud layers, such as cirrus and sub-visible cirrus clouds as well as lee-wave induced PSCs, an appropriate vertical step length for

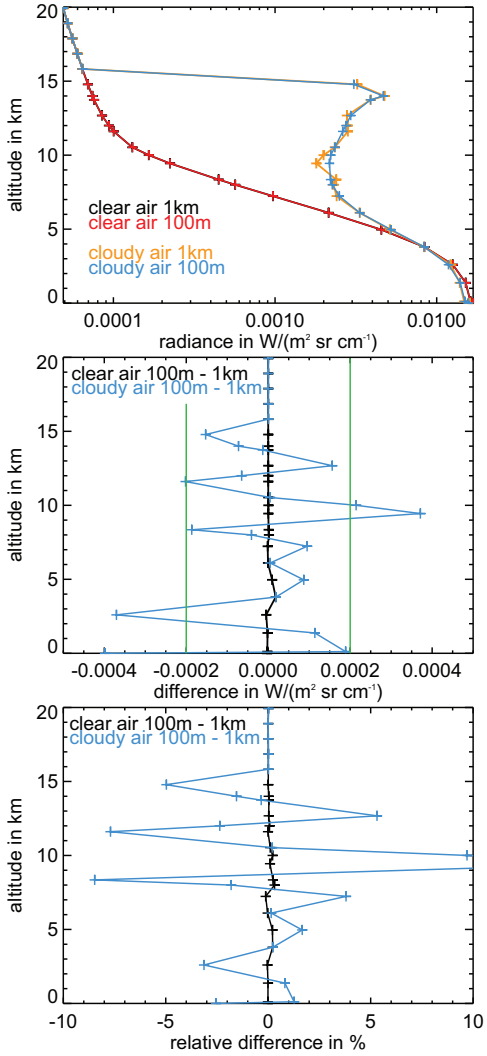


***Figure 5.10:*** *Simulated vertical radiance profile at 1226.6 cm$^{-1}$ in the polar winter model atmosphere. In the top panel the profiles in clear air for 100 m (red) and 1 km (black) vertical step length and cloudy air for 100 m (blue) and 1 km (yellow) vertical step length are shown. In the middle and bottom panel the absolute and relative differences for clear air (black) and cloudy air (blue) can be seen. The green lines in the middle panel represent the MIPAS noise equivalent radiance.*

the vertical extent of the cloud layer must be chosen in JURASSIC. Because a vertical step length of 1 km causes sampling problems that lead to differences in the radiance in the range of −3 % to 17 % for the chosen tangent heights, all cloud spectra for the comparison between JURASSIC and KOPRA are calculated with a vertical step length of 100 m in JURASSIC.

### Extinction Comparison

In this comparison the scattering source $S(\nu, s)$ in Equation 4.3 is set to zero and the absorption coefficient $\beta_a$ is set to the extinction coefficient $\beta_e$. This setup allows for the comparison of the effect of the extinction coefficient, calculated by the Mie module, on the spectra alone. In Appendix B.2.1 the spectra and their corresponding differences are shown in Figures B.16 – B.23.

The extinction spectra for cloud 2 in the mid-latitude night model atmosphere are shown in Figure 5.11. The spectra are nearly congruent, only at lower tangent heights differences become visible. Both, the mean difference and the relative difference at 14 km tangent height are near zero. At lower tangent heights the absolute differences increase and show that the radiances calculated by KOPRA are larger than the radiances by JURASSIC. Yet, the increase does not only depend on the tangent height, but also on the micro-window. The largest differences are found in micro-window 1, even when neglecting the large differences around the 792 $\mathrm{cm}^{-1}$ $CO_2$ line. The baseline of the absolute difference is beyond the MIPAS noise in micro-window 1, in micro-window 2 it is similar to the noise, and in micro-window 3 within the noise. Only in micro-window 4 the baseline is near zero. The relative difference shows, that the baseline varies around −2 % in micro-windows 1 to 3 and around 0 % in micro-window 4.

Generally the radiances calculated by JURASSIC are lower than the radiances by KOPRA. In Table 5.6 the total and the baseline differences for every atmosphere type and both clouds are given. When excluding the differences due to the 792 $\mathrm{cm}^{-1}$ $CO_2$ line, the differences for cloud 1 are always within −9 – +4 % and for cloud 2 within −5.5 – +3 %. For cloud analysis, the shift of the baseline is most relevant. The baseline of cloud 1 differs between −5 – +2 % and the baseline of cloud 2 differs between −3 – +2 % from KOPRA. The differences for cloud 2 are generally smaller than the differences for cloud 1. As in the clear air comparison the largest differences are found in the equatorial model atmosphere due to the steep temperature gradient. In contrast to the clear air comparison, which shows the radiances calculated by JURASSIC to be slightly larger than the radiances by KOPRA in polar winter, mid-latitude and equatorial night model atmospheres, the JURASSIC radiances for the extinction comparison are smaller than the KOPRA radiances.

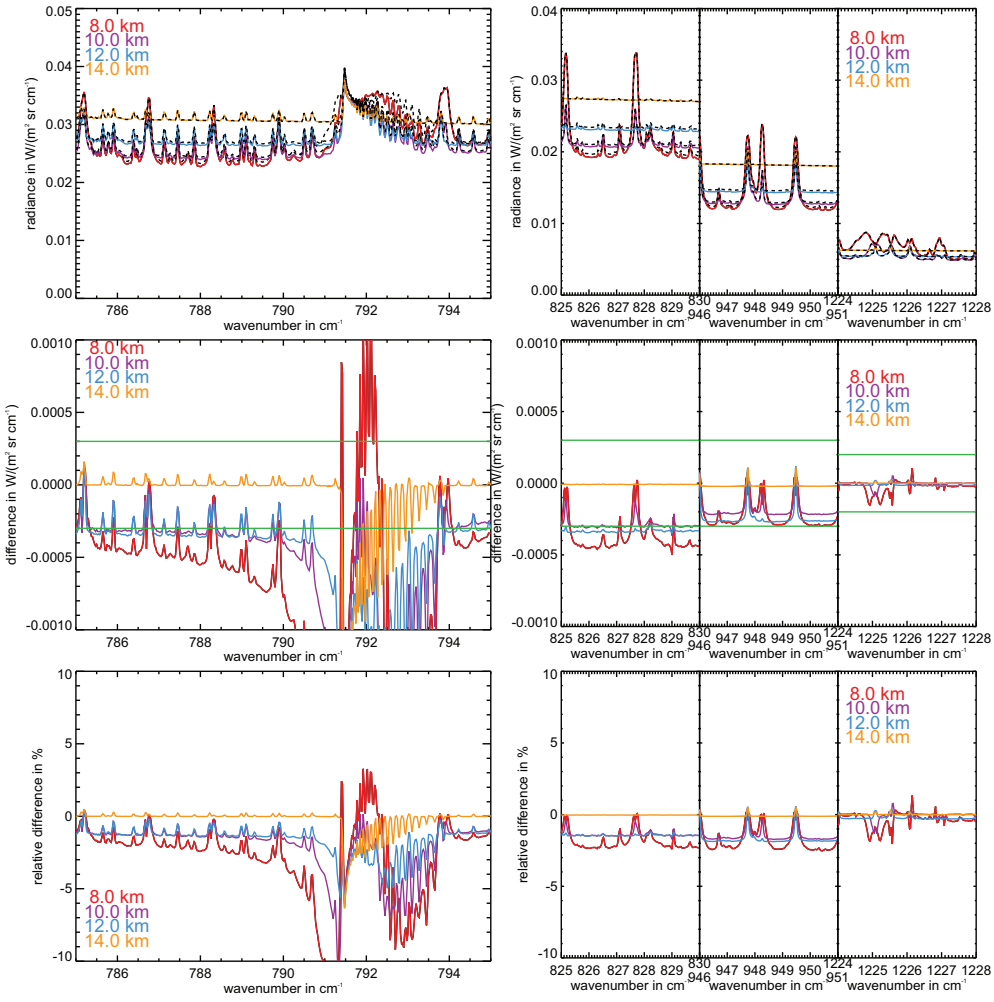


***Figure 5.11:*** *Extinction spectra for cloud 2 in the mid-latitude night model atmosphere for JURASSIC (coloured solid lines) and KOPRA (black dashed lines) (top panel) and the absolute (middle panel) and relative differences (bottom panel) between JURASSIC and KOPRA. The green lines in the middle panel represent the MIPAS noise equivalent radiance.*

| Model Atmosphere | Difference Cloud 1 | | Difference Cloud 2 | |
|---|---|---|---|---|
| | total | baseline | total | baseline |
| polar winter | −5.5 – +3 % | −5 – 0 % | −3 – +2 % | −3 – +2 % |
| polar summer | −5.5 – +2.5 % | −5 – 0 % | −3.5 – +2 % | −3 – +1 % |
| mid-latitude night | −6 – +3 % | −4 – 0 % | −3.5 – +1.5 % | −2.5 – 0 % |
| equatorial night | −9 – +4 % | −4 – +2 % | −5.5 – +3 % | −3 – +2 % |

***Table 5.6:*** *Relative differences between JURASSIC and KOPRA radiances of the extinction calculation for both cloud scenarios. The total difference is given for the four micro-windows, but excluding large differences due to the 792 $cm^{-1}$ $CO_2$ line. For the baseline differences all peaks due to trace gas lines are neglected.*

The absolute differences are within the MIPAS noise in most cases. For some lines they exceed the MIPAS noise as in the clear air comparison. The best results are obtained for micro-window 4, where the baseline is always within the noise. In micro-window 3 the differences for 8 and 10 km tangent height in the polar summer model atmosphere are below the noise. In micro-window 2 again the differences for 8 and 10 km tangent height in the polar summer model atmosphere and the differences for 12 and 8 km tangent height in the mid-latitude night model atmosphere are below the noise. In micro-window 1, however, only the differences for 14 km tangent height are within the noise in all model atmospheres. An explanation for the generally smaller radiances calculated by JURASSIC is discussed below.

### Scattering Comparison

In the scattering comparison, the radiances calculated by JURASSIC and KOPRA, using their complete single scattering modules, are compared. The spectra and their corresponding differences are shown in Appendix B.2.2 in Figures B.24 – B.31.

In Figure 5.12 the scattering spectra of cloud 2 in the mid-latitude night model atmosphere are shown. The baselines of the absolute differences in micro-windows 1, 2 and 3 exceed the MIPAS noise equivalent radiance, except for the baseline at 14 km tangent height in micro-window 3. Only in micro-window 4 all baselines of the differences of are within the noise equivalent radiance. The baseline of the relative difference is shifted about 2 percentage points towards larger negative relative differences compared to the extinction spectra. Larger differences around the 792 $cm^{-1}$ $CO_2$ line still exist. However, compared to the enormous differences in the clear air comparison, the relative differences are much smaller, due to the combination of opposite differences in the emission and absorption spectra of the limb and nadir case.

As the total and relative baseline differences in Table 5.7 show, the radiances calculated

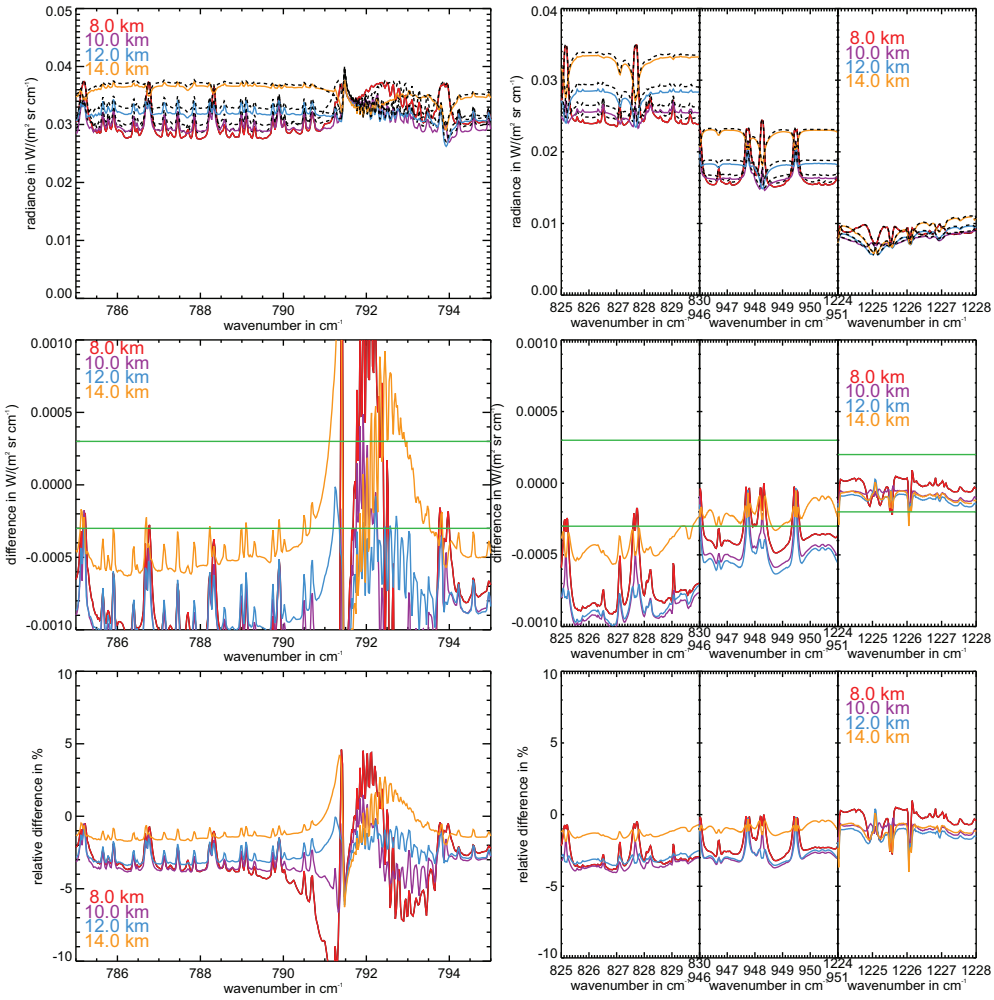


***Figure 5.12:*** *Scattering spectra for cloud 2 in the mid-latitude night model atmosphere for JURASSIC (coloured solid lines) and KOPRA (black dashed lines)(top panel) and the absolute (middle panel) and relative differences (bottom panel) between JURASSIC and KOPRA. The green lines in the middle panel represent the MIPAS noise equivalent radiance.*

by JURASSIC are smaller than the radiances calculated by KOPRA. The differences in the scattering calculations for both clouds are about one percentage point larger than the differences in the extinction calculations. The difference range, however, is approximately the same for both clouds in the extinction and scattering calculations, except for the polar summer atmosphere. This is caused by micro-window 4. In the extinction calculation for cloud 2, micro-window 4 already showed a deviant behaviour compared to the other micro-windows, because of its rather small negative difference and even a positive difference for 12 km tangent height. This effect is enhanced in the scattering calculation, where only positive differences are observed for cloud 2. However, for the thin cloud the differences are larger than in the other atmospheres. The assumption that the radiance from the sun causes this behaviour, is not supported, because the differences in micro-windows 1 – 3 do not show this discrepancy and the spectra for the mid-latitude and equatorial day model atmospheres (not shown) do not show differences that differ from the mid-latitude and equatorial night model atmospheres in micro-window 4.

| Model Atmosphere | Difference Cloud 1 | | Difference Cloud 2 | |
|---|---|---|---|---|
| | total | baseline | total | baseline |
| polar winter | −7.5 – +2 % | −6 – −1 % | −4 – +1.5 % | −4 – +1 % |
| polar summer | −10 – +2 % | −7 – −2 % | −4 – +3.5 % | −4 – +2 % |
| mid-latitude night | −7 – +2 % | −6 – −2 % | −4 – +1 % | −4 – 0 % |
| equatorial night | −9.5 – +3 % | −7 – 0 % | −6 – +3 % | −5 – +2 % |

***Table 5.7:*** *Relative differences between JURASSIC and KOPRA radiances of the scattering calculation for both cloud scenarios. The total difference is given for the four micro-windows, but excluding large differences due to the 792 $cm^{-1}$ $CO_2$ line. For the baseline differences all peaks due to trace gas lines are neglected.*

The absolute differences, however, mostly exceed the MIPAS noise equivalent radiance in micro-windows 1 – 3. Only for micro-window 4 the differences are within the noise equivalent radiance, except for the polar summer model atmosphere.

### Discussion

The model comparison for the scattering module shows that the radiances calculated by JURASSIC are generally about 3.5 % smaller for the extinction calculations and 4.5 % smaller for the scattering calculations than the radiances calculated by KOPRA. Apart from that nearly constant offset, good agreement between both single scattering calculations is achieved. Because the scattering module comparison in Section 5.2.1

does not show any negative offset, the source for this effect is not considered to arise from the scattering module.

A possible explanation for the constant offset is provided by an analysis of different vertical step lengths used for the calculations in KOPRA and JURASSIC. The first indication for this is the comparison with a JURASSIC calculation performed with 1 km vertical step length. As the bottom panel of Figure 5.10 shows, besides the 10 % difference at 10 km tangent height the other tangent heights of 8, 12 and 14 km also differ between 1.5 and 2.5 % from the 100 m vertical step length in the polar winter atmosphere. In Figure 5.13 the radiances and differences for micro-windows 2 – 4, calculated with 1 km and 100 m vertical step length with JURASSIC, are juxtaposed. The differences of the radiances in the left panel calculated with 1 km vertical step length with JURASSIC and KOPRA for 8, 12 and 14 km tangent height are around the zero level. Only the radiance at 10 km tangent height is significantly smaller, as expected. In the right panel the radiances and differences calculated for a vertical step length of 100 m can be seen. Here the radiance at 10 km tangent height fits much better. However the other radiances for the other tangent heights are lower by about the amount that the comparison of the vertical profile in Figure 5.10 suggests.

A second indication that the vertical step length chosen for cloud spectra can affect the results is given in Section 5.2.1. Focusing on scenario 5, it is shown that JURASSIC can reproduce the results of KOPRA when using a vertical step length of 1 km. Yet, this result is physically not plausible. When using a vertical step length of 100 m, JURASSIC yields a physically more realistic result. Unfortunately it could not be tested if the results of KOPRA would change with a smaller vertical step length. Since a comparison of vertical profiles through a cloud with different vertical step lengths has never been performed with KOPRA (M. Höpfner personal communication), the interpretation that the difference between JURASSIC and KOPRA is caused by different vertical step lengths cannot be proven. Nevertheless, it is suggested to be the most likely explanation.

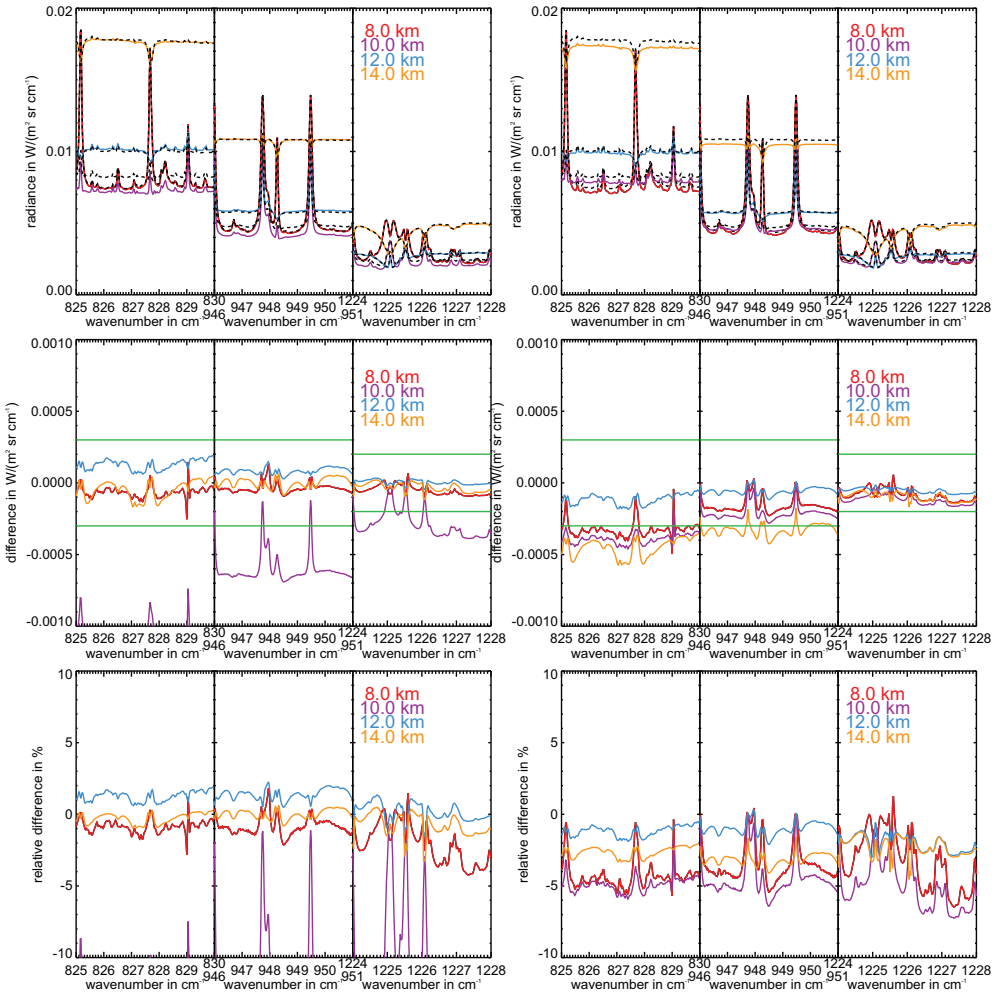


***Figure 5.13:*** *Scattering spectra for cloud 1 in polar winter model atmosphere calculated with a vertical resolution of 1 km (left panel) and a vertical resolution of 100 m (right panel) with JURASSIC (coloured solid lines) compared to KOPRA (black dashed lines) spectra with 1 km vertical step length (both panels).*

# Chapter 6

# Volcanic Ash Sensitivity Study

## 6.1 The Eyjafjallajökull Eruption

Volcanic eruptions can inject large amounts of aerosol particles into the troposphere and lower stratosphere. It is well known that atmospheric aerosol particles act as cloud condensation nuclei (CCN) on which atmospheric water vapour condenses. Similarly, a subset of the atmospheric aerosol particles act as ice nuclei (IN) that lead to ice crystal formation. The number of CCN and IN determines the number and size of the cloud particles. The size of the cloud particles has a significant impact on the radiative properties of clouds (Zhang et al., 1999) and thus has implications for climate. The cloud particle number and size also affects processes such as coagulation that lead to the growth of cloud particles to raindrops. In a case study on anvil cloud formation, Fridlind et al. (2004) show that the mid-tropospheric aerosol particles in general are a fundamental source of IN for ice crystal formation. In a recent study, Yuan et al. (2011) found that volcanic aerosol in particular modifies clouds by decreasing the droplet size and precipitation efficiency and initiating cloud formation leading to an increased cloud occurrence.

Besides the relevance of volcanic aerosol to cloud formation processes, cloud microphysical properties, and cloud radiative properties, it is also safety relevant for the air traffic and may be of economic and logistic relevance for transportation companies (airlines, rail). In April and May 2010, several European airports were closed after major eruptions of the Icelandic volcano Eyjafjallajökull. Since the decision to ground the aircrafts was solely based on model predictions of the ash dispersion conducted by the Volcanic Ash Advisory Centre (VAAC), the need for measured data became more urgent. However, due to the large variability of the volcanic ash plume, detection of volcanic ash particles in the free troposphere is challenging. The combination of

airborne in situ measurements (Schumann et al., 2011; Flentje et al., 2010a), ground-based remote sensing measurements (Ansmann et al., 2010; Flentje et al., 2010b,a; Gasteiger et al., 2011; Emeis et al., 2011), remote sensing measurements from satellites (Thomas and Prata, 2011; NASA, 2011) and model simulations (Stohl et al., 2011, Friese and Elbern, personal communication) provides a survey of the Eyjafjallajökull eruption ash particle properties and their dispersal.

The plume altitudes of Eyjafjallajökull's major eruptions reached up to about 10 km (Stohl et al., 2011). Lidar data (Flentje et al., 2010b, CALIPSO) show that the ash plume was tilted when advected over the European continent and it is detectable up to about 7 km altitude. Flentje et al. (2010a) state that their observed ozone profiles imply ash layers reaching up to 9 km. The vertical extent of the ash layer was about 100 m to 1 km. Because of the high altitudes at which the ash was detected, it is likely that the infra-red limb sounding instrument MIPAS is capable of detecting the ash cloud. The lowest tangent height of MIPAS is usually between 5.6 and 7 km over Europe in its current nominal mode. MIPAS uses a vertical sampling of 1.5 km and has a field of view of about 3 km, which it provides information from about 1.5 km below and above a tangent height.

To investigate the sensitivity of MIPAS to volcanic ash from the Eyjafjallajökull eruption, measured particle number size distributions (Schumann et al., 2011) are used to carry out radiative transfer calculations with JURASSIC. In Figure 6.1, the three number size distributions are shown. Because these distributions were measured at rather low altitudes (3.5 – 5.2 km), which are below the lowest MIPAS tangent height, an additional size distribution from the EURopean Air pollution Dispersion model (EURAD) (Hass et al., 1995), including the aerosol model Modal Aerosol Dynamic Model for Europe (MADE) (Ackermann et al., 1998), simulation at 10 km altitude is chosen for the sensitivity study and also shown in Figure 6.1. The main difference of this model size distribution from the measured size distributions is its lower concentration of particles larger than 1 $\mu$m diameter. The difference for particles smaller than 0.1 $\mu$m is not relevant, because the small particles do not play a significant role in scattering in the infra-red. Besides, these data for the small particles are also uncertain, because measurements were made only in the range between about 0.2 and 20 $\mu$m and extrapolated to smaller particle sizes. The parameters for the log-normal distributions and the nadir optical depths are given in Table 6.1. The refractive indices for volcanic aerosol are obtained from the HITRAN database.

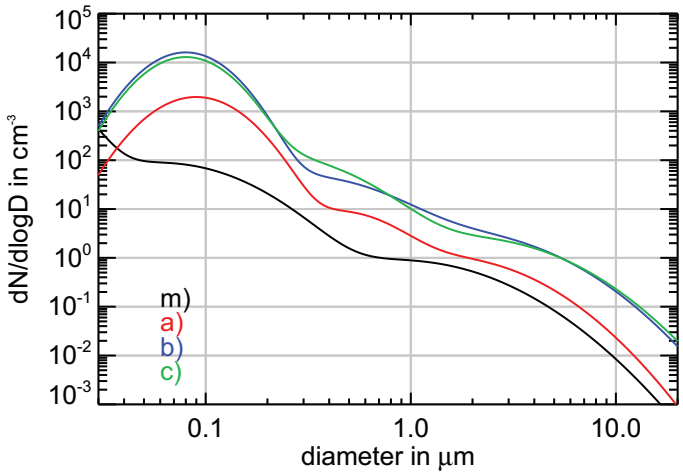


***Figure 6.1:*** *Number size distributions of volcanic ash used in the simulation of MIPAS spectra. Measurements a), b), and c) are obtained from Schumann et al. (2011) and size distribution m) is obtained from the EURAD model (Friese and Elbern, personal communication).*

| Case | Mode | $n_i$ in $cm^{-3}$ | $\mu_i$ in $\mu m$ | $\sigma_i$ | Nadir Optical Depth |
|---|---|---|---|---|---|
| a) | 1 | 2000 | 0.045 | 1.5 | $1.73 \cdot 10^{-2}$ |
| | 2 | 10 | 0.225 | 1.6 | |
| | 3 | 1.7 | 0.75 | 2.0 | |
| b) | 1 | $1.5 \cdot 10^4$ | 0.04 | 1.45 | $1.09 \cdot 10^{-1}$ |
| | 2 | 80 | 0.15 | 2.0 | |
| | 3 | 5.5 | 0.9 | 2.1 | |
| c) | 1 | $1.2 \cdot 10^4$ | 0.04 | 1.45 | $1.12 \cdot 10^{-1}$ |
| | 2 | 220 | 0.1 | 2.0 | |
| | 3 | 4.5 | 1.0 | 2.1 | |
| m) | 1 | $4.6 \cdot 10^4$ | $3.1 \cdot 10^{-3}$ | 1.7 | $6.64 \cdot 10^{-3}$ |
| | 2 | 151 | 0.031 | 2.0 | |
| | 3 | 1.7 | 0.45 | 2.2 | |

***Table 6.1:*** *The log-normal parameters for the number size distributions shown in Figure 6.1. The cases a), b), and c) are fitted to measured data shown in Schumann et al. (2011). The parameters for case m) are obtained from the EURAD model data. The nadir optical depth at 948.5 $cm^{-1}$ for a layer of 1 km thickness is given in the sixth column. The optical depth of ash clouds b) and c) are comparable to a thin cirrus cloud, the optical depth of cloud a) is comparable to an ice PSC and the optical depth of cloud m) is comparable to an STS PSC.*

## 6.2 Volcanic Ash Detectability and Discrimination with MIPAS

To investigate the effect of the scattering of volcanic ash particles on MIPAS spectra, four scenarios are chosen: 1 km and 100 m thick ash layers are located above 5 km and above 7 km. The 1 km thick ash layer ranges from 7.0 to 8.0 km for the high ash layer and from 5.0 to 6.0 km for the low ash layer. The 100 m thick ash layers range from 7.0 to 7.1 km and 5.0 to 5.1 km, respectively. The spectra calculated for a mid-latitude model atmosphere at typical MIPAS tangent heights and with a field of view convolution are shown in Figure 6.2 for the high ash layer and in Figure 6.3 for the low ash layer. To be able to distinguish the radiance enhancement due to the volcanic ash from the enhancement due to the omnipresent background aerosol, a tropospheric extinction profile for aerosol is derived from the aerosol database introduced in Chapter 2 and included into the simulation. The effect of the background aerosol compared to a clear air calculation is also visible in Figures 6.2 and 6.3.

In Figure 6.2, it can be seen that the 1 km ash layer causes significant radiance enhancements even at tangent heights 800 m above the ash cloud. The ash layer of 100 m vertical thickness causes significant radiance enhancements at the tangent height 200 m above the ash layer. Even at a tangent height 1.7 km above the ash layer, a small enhancement compared to the background aerosol spectra is visible in two micro-windows. For the low ash cloud in Figure 6.3, a significant radiance enhancement at the lowest tangent height is found in two micro-windows for both the thick and thin ash layers. For the second tangent height of 7.3 km a small radiance enhancement can be found for the 1 km thick ash layer. For the 100 m thick ash layer, no significant radiance enhancement can be observed at 7.3 km tangent height. At 8.8 km tangent height, no effect of the low cloud can be found at all. From these simulations it is concluded that MIPAS spectra are expected to be significantly affected by ash clouds of 100 m to 1 km thickness located within a 1 km range around the tangent height.

The spectra affected by the ash cloud, however, closely resemble spectra affected by typical tropospheric clouds. To examine whether ash clouds are distinguishable from cirrus clouds, the sensitivity of modelled spectra on different refractive indices and size distributions is tested. Therefore the number size distributions of the SVC with median radius of 3.6 $\mu$m and the cirrus cloud with a median radius of 81 $\mu$m from Chapter 2 are taken and the number concentrations are adjusted so that the optical depths are the same as in the ash cloud scenarios a), c) and m). The parameters for the number size distributions are given in Table 6.2. For the three scenarios, the extinction coefficient spectra and the single scattering albedo spectra for ash, SVC and cirrus are shown in Figure 6.4. When keeping the extinction coefficient constant at 948.5 $\mathrm{cm}^{-1}$ ($\sim$10.5$\mu$m), it is obvious that the extinction coefficients for ash, SVC and cirrus differ.

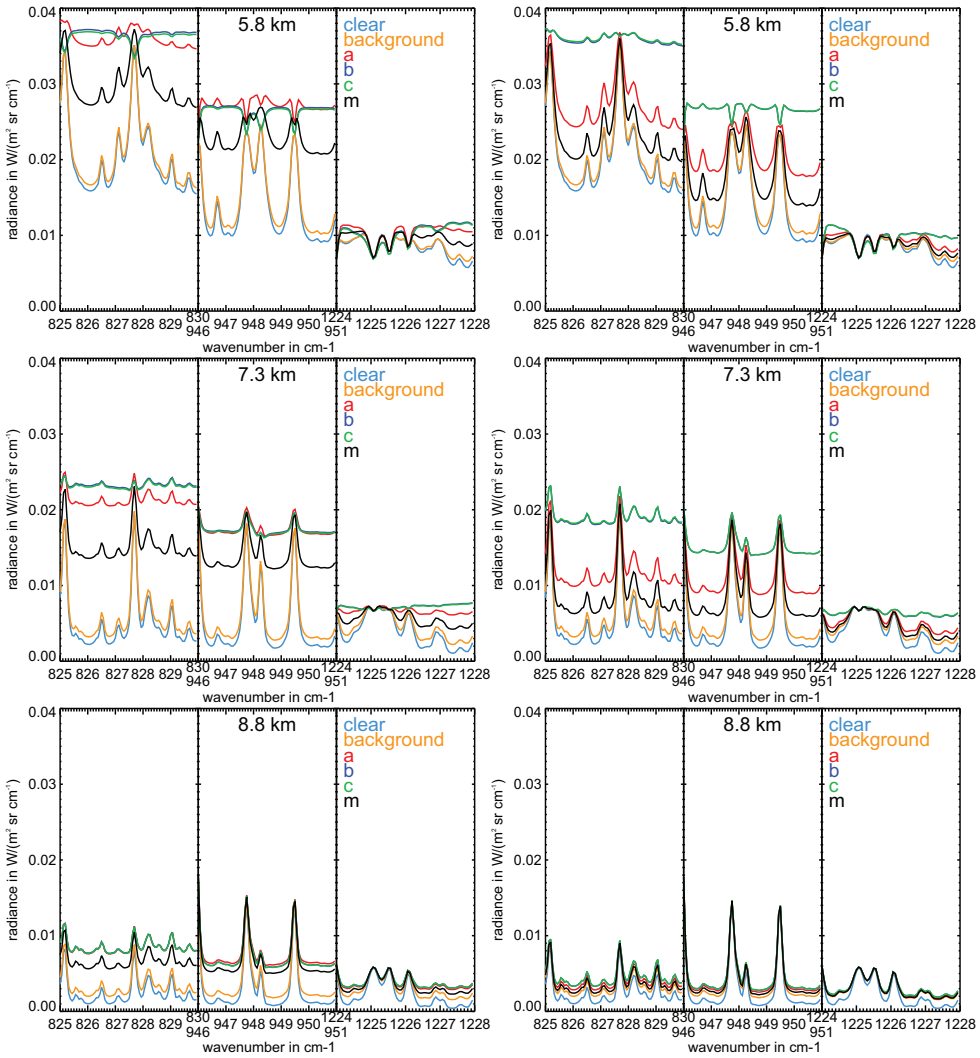


***Figure 6.2:*** *Left panel: 1 km thick cloud between 7 and 8 km. $n_i$ are constant between 7.1 and 7.9 km and decrease linearly to zero at 7.0 and 8.0 km. Right panel: 100 m thick cloud between 7.0 – 7.1 km. The cloud has sharp edges, $n_i$ are constant in the whole range.*

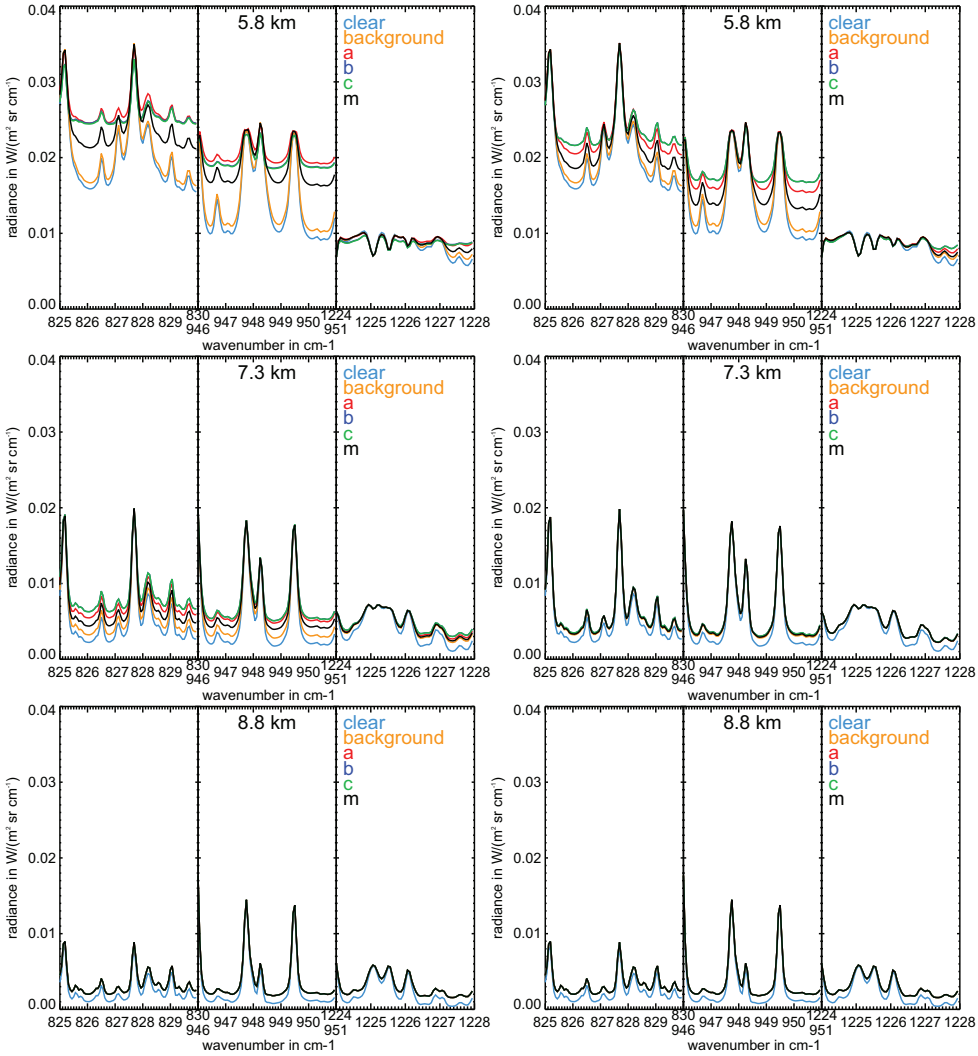


***Figure 6.3:*** *The same as in Figure 6.2, but for a cloud between 5 to 6 km in the left panel and between 5.0 to 5.1 km in the right panel.*

| Cloud Type | Case | $n_i$ in $cm^{-3}$ | $\mu_i$ in $\mu$m | $\sigma_i$ |
|---|---|---|---|---|
| SVC | a) | $2.58 \cdot 10^{-1}$ | 3.6 | 1.6 |
| | c) | 1.67 | | |
| | m) | $9.91 \cdot 10^{-2}$ | | |
| Cirrus | a) | $2.03 \cdot 10^{-4}$ | 81 | 1.8 |
| | c) | $1.32 \cdot 10^{-3}$ | | |
| | m) | $7.78 \cdot 10^{-5}$ | | |

***Table 6.2:*** *Number concentrations for an SVC and a cirrus cloud so that the optical depth at 948.5 $cm^{-1}$ is the same as for the ash cloud scenarios a, c, and m. The number concentrations for a cirrus cloud seem to be very unlikely, since ice crystal number concentrations below $1 \cdot 10^{-3}$ have not been measured (Krämer et al., 2009).*

Neither the extinction coefficient nor the single scattering albedo for the cirrus cloud show any spectral signature. For ash, the extinction coefficient has a local maximum between 8.7 and 11.5 $\mu$m and a minimum around 8.2 $\mu$m. For larger wavelengths it is also smaller. In contrast, the extinction coefficient of the SVC has a local minimum around 10.5 $\mu$m. The three micro-windows considered in this sensitivity study are the same as those used in Chapter 4 and are located at about 8.1, 10.5, and 12.1 $\mu$m. The 8.1 $\mu$m micro-window is near a local ash extinction minimum. The single scattering albedo shows that there are already differences at 10.5 $\mu$m, which indicates that the spectra will differ in that micro-window although they have the same optical depth. At 12.1 $\mu$m, the single scattering albedo becomes smaller for the SVC but larger for ash. At 8.1 $\mu$m, the single scattering albedo for the SVC is larger than for the ash.

To demonstrate the extent to which these differences affect the MIPAS spectra, for the three scenarios a), c), and m), spectra are simulated for the ash layer, SVC and cirrus cloud at 7 km altitude with 100 m and 1 km thickness. The spectra are shown in Figure 6.5 for scenario c), in Figure 6.6 for scenario a), and in Figure 6.7 for scenario m). For all three scenarios, the ash spectra differ significantly from the SVC and cirrus spectra at 5.8 and 7.3 km tangent height when all three micro-windows are considered together. The largest differences can be found in the first and second micro-window. In the top panel of Figure 6.7, it can be seen very clearly that the spectra of ash and SVC are close to each other in the second micro-window. In the first micro-window, however, there is a large difference between ash and SVC. Additionally, the ash and cirrus spectra are close to each other in the first micro-window, but differ in the second. The discrimination of ash from ice clouds is best for tangent heights within or below the cloud layer. For the optically thinner scenarios a) and m), the discrimination of ash is more likely than for the optically thicker scenario c), where the differences are rather small.

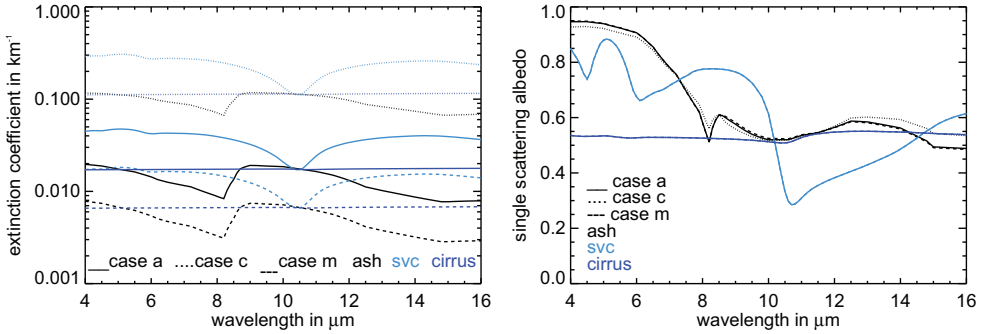


***Figure 6.4:*** *The extinction coefficients in the left panel are calculated for scenarios a) (solid lines), c) (dotted lines), and scenario m) (dashed lines) for ash (black lines), SVC (light blue lines), and cirrus cloud (dark blue lines). In the right panel, the corresponding single scattering albedos are shown. For all three scenarios the SVC and cirrus lines are indistinguishable.*

The analysis shows that MIPAS would detect an ash cloud with ash particle size distributions as observed (Schumann et al., 2011) or as modelled with EURAD. Even small layers of 100 m vertical thickness cause a significant radiance enhancement in MIPAS spectra. The sensitivity study shows that the ash layer must be located above the lowest tangent height to allow for discrimination from ice clouds.

## 6.3 Model – MIPAS Intercomparison

The EURAD model simulation suggests that the ash layer reaches up to about 7 km and higher. To test whether MIPAS detects the modelled ash layers, MIPAS observations from April 15th to April 18th 2010 are evaluated. To identify possible ash cloud contaminated profiles, EURAD model output including temperature and particle number size distributions was provided at full hours closest to the MIPAS over-path times (Friese and Elbern, personal communication). In the top panel of Figure 6.8, the particle number concentration at 7 km altitude given by the model is plotted and the MIPAS tangent coordinates are marked. In order to provide a rough indication of whether optically thick clouds are present, the tangent coordinates are also marked in METEOSAT infrared images (see Figure 6.8, bottom panel). If the METEOSAT image indicates that the MIPAS profile is measured in an ice cloud, the profile is not evaluated. For the evaluation of possible ash profiles, spectra including background aerosol from the aerosol database and spectra considering the aerosol number size distributions given in the EURAD model from the ground up to 12 km altitude are

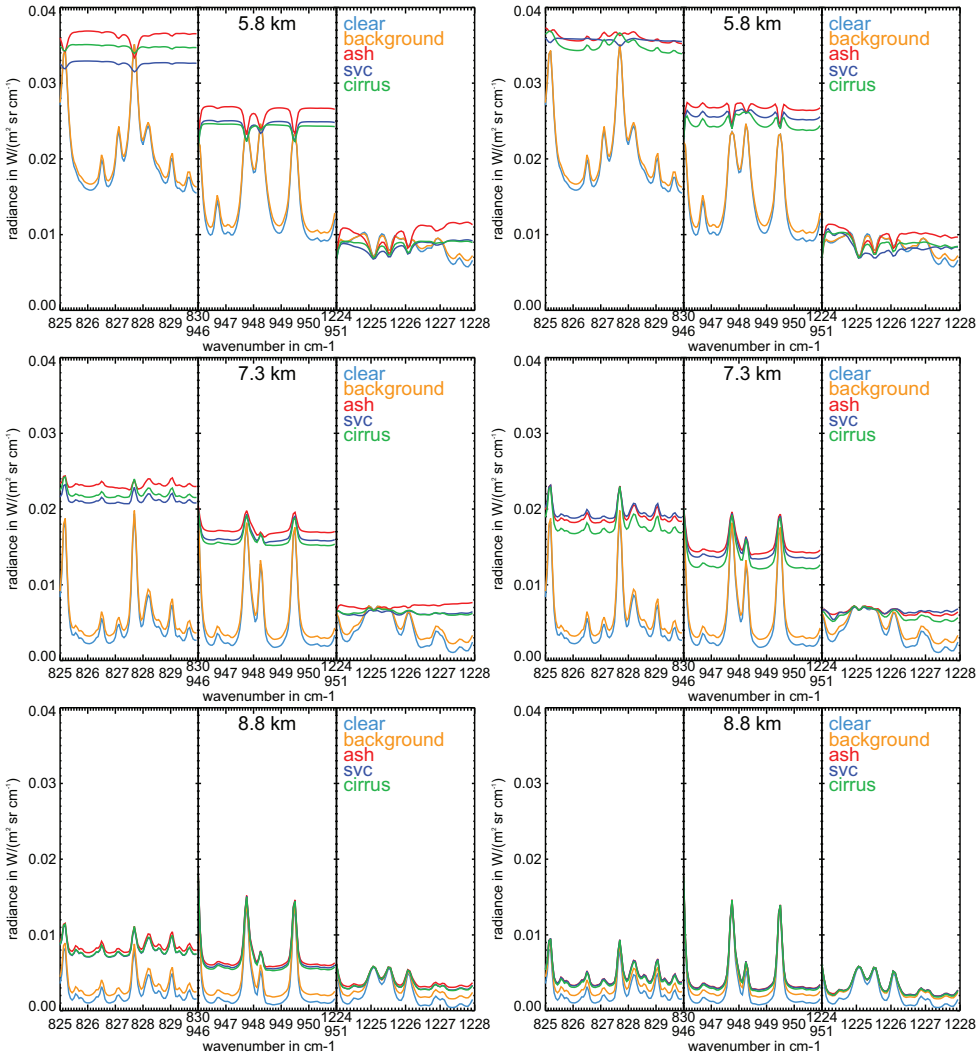


***Figure 6.5:*** *Spectra for simulations with an ash cloud, SVC and cirrus cloud of 1 km (left panel) and 100 m (right panel) thickness. The optical thickness of the clouds corresponds to ash cloud scenario c).*

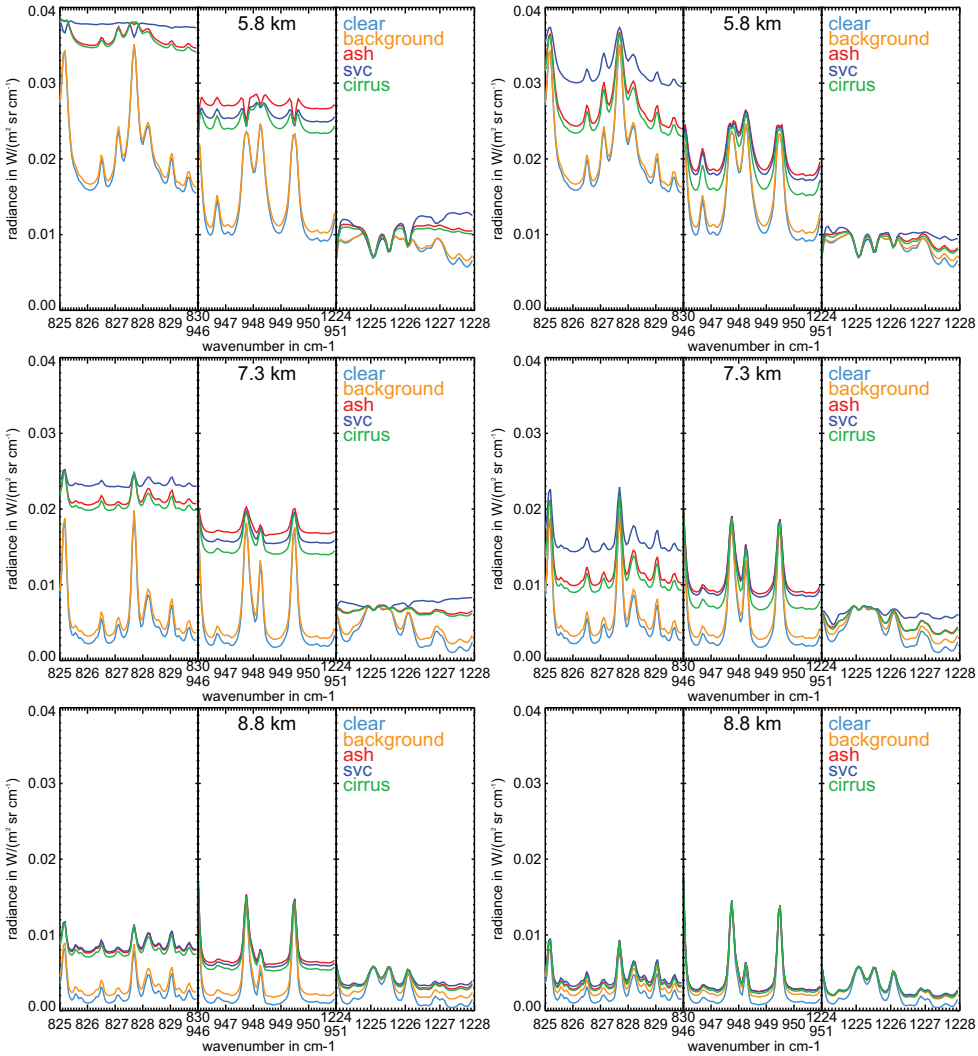


***Figure 6.6:*** *Spectra for simulations with an ash cloud, SVC and cirrus cloud of 1 km (left panel) and 100 m (right panel) thickness. The optical thickness of the clouds corresponds to ash cloud scenario a).*

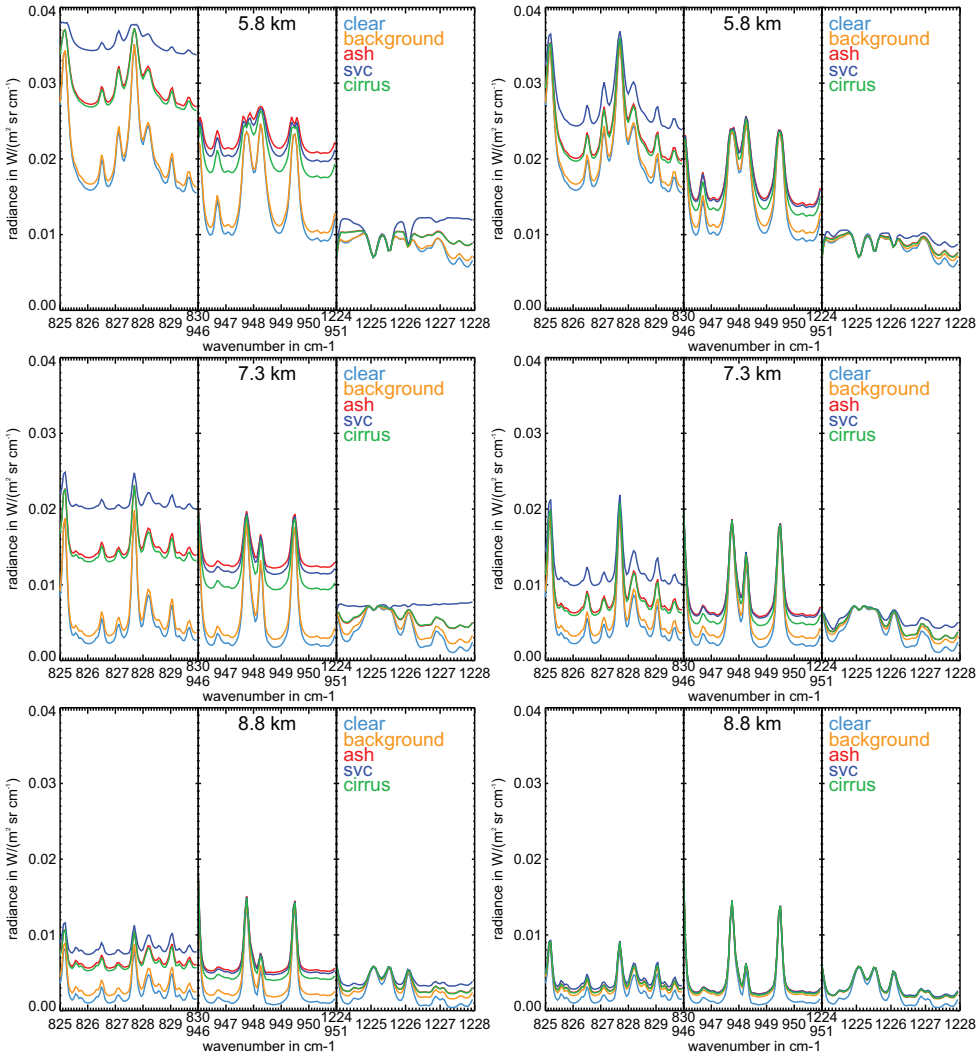


***Figure 6.7:*** *Spectra for simulations with an ash cloud, SVC and cirrus cloud of 1 km (left panel) and 100 m (right panel) thickness. The optical thickness of the clouds corresponds to ash cloud scenario m).*

calculated using JURASSIC and compared to MIPAS observations. For this purpose, the mid-latitude MIPAS reference atmosphere is modified with temperature and trace gas concentrations retrieved by Dudhia (2011) for each investigated profile. EURAD model temperatures are used for the temperature below the lowest MIPAS tangent height . The simulated spectra are then compared with those observed by MIPAS.

The simulations show that generally the background aerosol radiances range from significantly below to very close to the measured radiances. The radiances of the simulated spectra considering scattering on volcanic ash particles vary from below the measured spectra to far above. Of the 14 profiles analysed, the radiances simulated with the model ash size distribution exceed the radiances of the measured spectra for 7 profiles. As an example, the spectra for orbit 42497 profile 19, which is shown on the map and satellite image (in red) in Figure 6.8, are shown in Figure 6.9. Except for the tangent heights of 7.9 and 9.4 km, where the baselines are slightly enhanced, the simulated spectra for the background aerosol are very close to the measured spectra. The radiances of the simulated ash spectra exceed the measured radiances by far. Another 3 profiles are found where the model simulates the ash cloud at higher altitudes than the observations. The spectra do not show any significant increase in radiance. An example is shown for orbit 42482 profile 21 in Figure 6.10. Compared to the measured spectra, the background aerosol spectra in Figure 6.11 show that the two lowest tangent heights are influenced by cloud. In the volcanic ash simulation, the radiances of the lower tangent heights are closer to the measurement, but do not fit exactly, whereas the radiances of the three highest tangent heights are significantly overestimated.

The cloud type discrimination procedure is demonstrated for the example of orbit 42519 profile 39 at 7.3 km tangent height. The model particle number concentration for ash is adjusted so that the spectrum in the second micro-window fits the measured spectra, and the optical depth is calculated. The result is presented in the upper panel of Figure 6.12. It is obvious that the simulated and measured spectra in the second micro-window fit well, but the spectra in the first and third micro-window differ significantly. Thus, using ash the measured spectra in the three windows cannot be simulated. To test whether the measured spectra can be simulated with ice clouds, the number concentrations for an SVC and a cirrus cloud are estimated so that both clouds have the same optical depth as the ash cloud. In the middle panel of Figure 6.12, the simulated spectra for the SVC and the measured spectra agree in micro-windows two and three, but not in micro-window one. For the cirrus cloud the number concentration and hence the optical depth are increased so that the simulated and measured spectra in micro-window two agree reasonably well. The final number size distributions for ash, SVC and cirrus cloud are given in Table 6.3. The simulated spectra for the cirrus cloud in the bottom panel of Figure 6.12 show the best overall agreement. This suggests that MIPAS detected cirrus cloud instead of a volcanic ash layer, which the EURAD model predicted. However, the particle concentration of the fitted cirrus cloud is very low

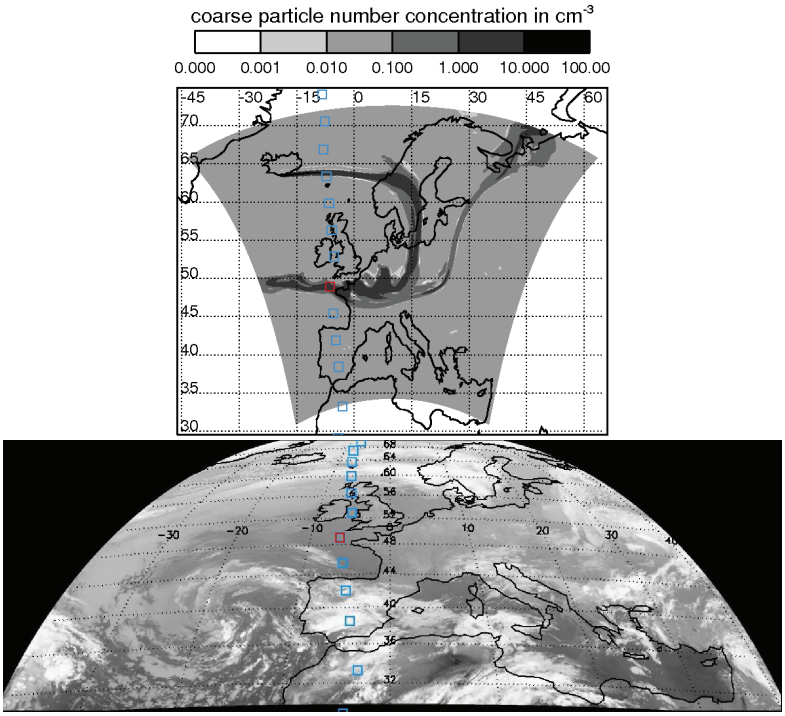


***Figure 6.8:*** *EURAD model simulation of the dispersion of volcanic ash for 16-Apr-2010 22:00 UTC at 7km altitude. The MIPAS orbit trace of the lowest tangent heights is marked with blue squares for orbit 42497. The infrared METEOSAT satellite image for channel 9 was obtained from NERC Satellite Receiving Station (2011).*

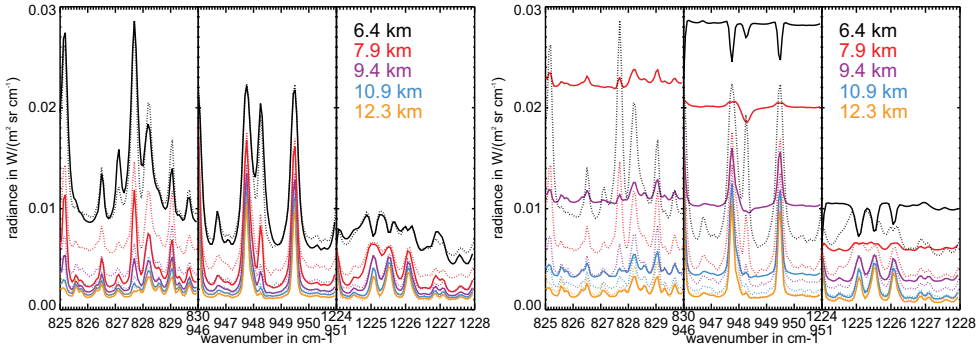


***Figure 6.9:*** *Measured (dotted lines) and simulated (solid lines) MIPAS radiances for orbit 42497 profile 19 with background aerosol (left panel) and volcanic ash (right panel). The log-normal parameters for the volcanic ash are obtained from the EURAD model.*

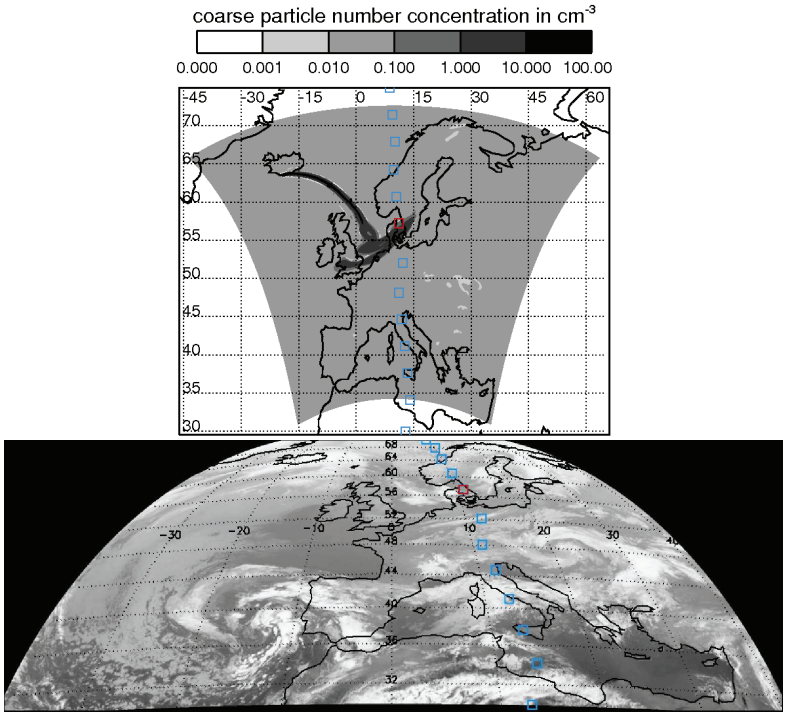


***Figure 6.10:*** *EURAD model simulation of the dispersion of volcanic ash for 15-Apr-2010 23:00 UTC at 7km altitude. The MIPAS orbit trace of the lowest tangent height is marked with blue squares for orbit 42482. The infrared METEOSAT satellite image for channel 9 was obtained from NERC Satellite Receiving Station (2011).*

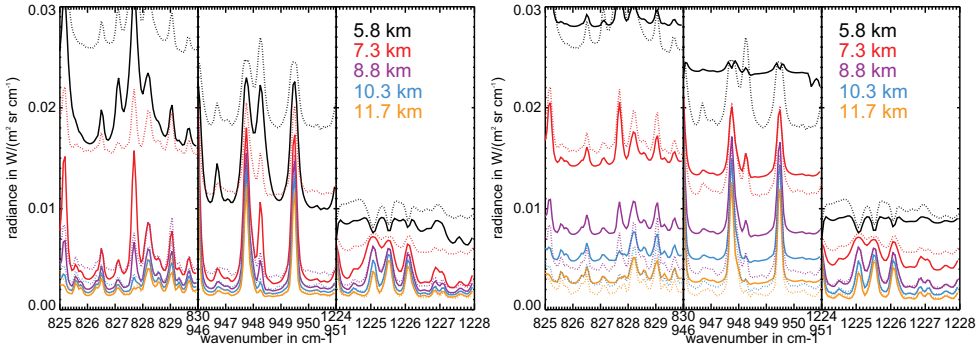


***Figure 6.11:*** *Measured (dotted lines) and simulated (solid lines) MIPAS radiances for orbit 42482 profile 21 with background aerosol (left panel) and volcanic ash (right panel). The log-normal parameters for the volcanic ash are obtained from the EURAD model.*

| Type | $n_i$ in $cm^{-3}$ | $\mu_i$ in $\mu m$ | $\sigma_i$ |
|---|---|---|---|
| ash | 5 | 0.045 | 2.2 |
| SVC | 0.289 | 3.6 | 1.6 |
| cirrus | $2.3 \cdot 10^{-4}$ | 81 | 1.8 |

***Table 6.3:*** *Particle number distributions for the clouds fitted in Figure 6.12.*

compared to the climatology presented in Krämer et al. (2009). It seems to be unlikely that a cirrus cloud with large but that few particles exists. However, it cannot be ruled out completely since the detection limit of the cloud particle data evaluated in Krämer et al. (2009) is about $4 \cdot 10^{-3} cm^{-3}$.

The sensitivity study in Section 6.2 showed that MIPAS measurements are sensitive to volcanic ash layers. For an ash layer above the lowest tangent height, it is possible to discriminate between ash and cloud particles. However, in the evaluation of selected measured MIPAS spectra over Europe in the period from April 15th to April 18th no ash spectrum could be unambiguously identified. The EURAD simulations of the dispersal of Eyjafjallajökull ash cannot be confirmed for several profiles and at high altitudes. At altitudes below 8 km, many spectra measured by MIPAS clearly show cloud signatures. Some cloud discrimination tests identified the clouds as SVC or cirrus cloud. Nonetheless, ash particles may be present in the profiles observed by MIPAS. The ash cloud could be masked by cirrus clouds, or the ash particles could be ice coated, as suggested by lidar measurements (C. Rolf, personal communication).

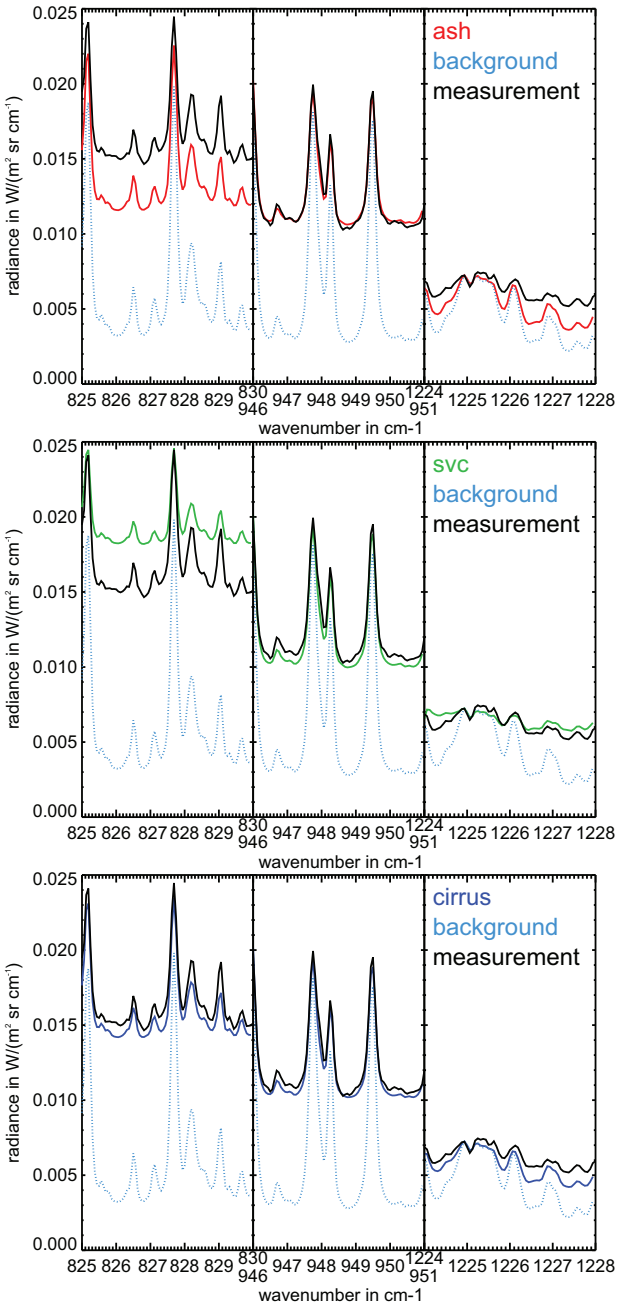


***Figure 6.12:*** *Measured MIPAS spectrum and simulated spectra for an ash cloud, SVC and cirrus cloud. The spectra are for orbit 42519 profile 39 at 7.3 km tangent height.*

# Chapter 7

# Summary and Conclusions

High-altitude clouds play an important role in the Earth's atmosphere. While polar stratospheric clouds are involved in processes leading to polar ozone destruction, cirrus clouds have an impact on the energy balance of the atmosphere. The radiative impact of high clouds is one of the least understood processes affecting the climate. Aside from this, clouds affect the measured spectra of remote sensing instruments such as Envisat MIPAS that are designed to measure temperature and to detect trace gases in the atmosphere. Cloud particles and larger aerosol particles disturb the measured radiance spectra by scattering radiance from all directions towards the instrument.

In this thesis, the scattering module for the radiative transfer model JURASSIC was developed. It either calculates the single scattering properties with Mie calculations or accesses the single scattering properties for non-spherical ice particles from an external database. The scattering module correctly accounts for surface and solar emissions. The code design makes it possible to account for single and multiple scattering on atmospheric particles. This contributes to deriving cloud properties from the measurements and to enabling trace gas retrievals in cloudy atmospheres.

The aerosol and cloud particles are introduced that can be found in the upper troposphere and stratosphere and which affect infrared limb radiance measurements. The microphysical properties required for the estimation of the single scattering properties with the Mie code are particle size, complex refractive indices and particle shape. Representative parameters are presented for PSCs, SVCs, cirrus clouds, stratospheric aerosol, and tropospheric aerosol. As no climatology of log-normal parameters for the vertical distribution of tropospheric aerosol number size distributions was available for this work, in situ measured data were collected from various publications and compiled in a new database (see Appendix A). This database is of value not only for calculating the single scattering properties at any desired wavelength, but also can be used as a

first step towards a global scale data base as requested by Clarke and Kapustin (2002): "a global-scale aerosol climatology is needed for model testing, satellite validation observations, and for any quantitative regional or global assessment of aerosol effects on the earth's system".

The Mie theory provides an exact solution of the scattering problem for spherical particles and allows the single scattering properties to be calculated that are required for radiative transfer calculations, which are the scattering coefficient, the extinction coefficient, and the phase function. For typical aerosols and cloud types, spectrally resolved extinction coefficients, single scattering albedos, and phase functions are presented and discussed. For the tropospheric aerosols the extinction coefficients for all number size distributions in the database are calculated in order to present the wide range of aerosol variability. The tropospheric aerosol extinction spectra show that exact calculations of the extinction coefficient from a number size distribution are preferable to the scaling of the extinction coefficient from a distinct wavelength to another wavelength.

The radiative transfer equation including the scattering formalism is implemented into the forward model JURASSIC. The improved step length estimation automatically determines the appropriate step length for nadir or limb geometry within given limits. An option for multiple scattering is implemented. Characteristic spectra are simulated and presented assuming single scattering on typical aerosols and clouds. The spectra for the tropospheric background aerosol show that no type discrimination is possible within the three analysed micro-windows, which are sensitive to cloud and aerosol emissions.

A detailed forward model comparison between the spectrally averaging model JURASSIC and the line-by-line models RFM and KOPRA generally showed good agreement. In the first step, clear air spectra calculated with the three models are compared. Three of the selected MIPAS micro-windows for the comparison are characterised by few gaseous contribution and hence are very sensitive to cloud and aerosol emissions. The fourth micro-window contains the $792\,\mathrm{cm}^{-1}$ $CO_2$ line centre, which is often used for temperature retrievals. The comparison shows that the spectrally averaging approach in JURASSIC achieves good agreement with the line-by-line code RFM for high spectral resolution calculations. The deviations of the baselines are small compared to the MIPAS noise equivalent radiance. Under certain conditions, such as strong temperature gradients, some line centres exceed the noise by a factor of 3 and up to a factor of 7 at the $792\,\mathrm{cm}^{-1}$ $CO_2$ peak. The comparison of RFM with KOPRA shows a very good agreement, but reveals larger differences by far between the two line-by-line models by a factor up to 55 at the $792\,\mathrm{cm}^{-1}$ $CO_2$ peak, which is caused by different methods implemented for the line mixing. However, except for the $CO_2$ line centre at $792\,\mathrm{cm}^{-1}$, the agreement between JURASSIC and KOPRA is sufficient to allow for the comparison of scattering spectra. In the second step, the spectra for five cloud sce-

narios are compared covering the range from optically thin to thick cloud conditions. Here both models agree very well within the MIPAS noise, when an appropriate step length for raytracing and cloud sampling is chosen. It is shown that JURASSIC yields physically correct results with an appropriate vertical step length of 100 m and is able to reproduce the radiances calculated with KOPRA with a vertical step length of 1 km. In the third step, clouds are added to the realistic atmospheres of the first step. The JURASSIC and KOPRA spectra show a nearly constant offset, which is accounted to cloud sampling differences due to a larger vertical step length used in the KOPRA simulations. Nevertheless, a good agreement between JURASSIC and KOPRA was found.

A sensitivity study on the detectability of volcanic ash of the Eyjafjallajökull eruption in April 2010 with MIPAS was performed. An important result is that it is possible to detect volcanic ash occurring in concentrations and size distributions indicated by in situ measurements (Schumann et al., 2011) in MIPAS measurements spectra. Even ash clouds with substantially smaller particles can be detected. However, in order to differentiate the ash cloud from a cirrus cloud, the ash cloud must be located above the lowest tangent height. The MIPAS measurements are used to assess the quality of the predictions of the location of the ash cloud by the EURAD model. It was found that the model predicts ash cloud filaments where no particles are detected in MIPAS. Further, for several profiles the model overestimates the altitude of the ash layer by up to 3 km. The spectra of profiles in which clouds are detected are more similar to ice cloud spectra. No ash cloud spectrum could be identified unambiguously.

In this thesis, the JURASSIC forward model was substantially extended in order to study scattering phenomena in the mid-infrared radiative transfer. The new code was carefully cross-checked at a high spectral resolution with well-established reference models. A first study on the detectability and discrimination of volcanic ash particles demonstrates the high potential of the scattering module for future scientific studies and potential retrieval of cloud and aerosol properties.

# Appendix A

# Aerosol Database

Many extinction measurements have been performed in the upper troposphere. However, most instruments measure at specific wavelengths in the visible or near infrared and the measured extinction coefficients cannot easily be extrapolated into the mid-infrared. Due to the large variability in the aerosol number size distribution, different size distributions can cause the same extinction coefficient at one wavelength and completely different coefficients at another wavelength (Chapter 3 Figures 3.8 to 3.10).

To be able to study aerosol effects in infrared limb measurements, it is desirable to have a climatology of vertical profiles of number size distribution and chemical composition of aerosol particles, since it is straightforward to calculate the extinction coefficient at any desired wavelength with Mie theory. The OPAC (D'Almeida et al., 1991; Hess et al., 1998) software package is a comprehensive compilation of aerosol and cloud micro-physical and optical properties. However, it mainly relies on ground-based measurements and offers just an exponential profile for the aerosol distribution in the upper troposphere.

For the purpose of this thesis, better information on seasonal and regional variability of the so-called background aerosol vertical profile in the free troposphere is required, to be able to distinguish high reaching sporadic events such as Saharan dust outbreaks or volcanic eruptions from the unperturbed state. Therefore a database of aerosol number size distributions from published data was compiled. The most common size distribution for aerosol is the lognormal distribution (Jaenicke, 1988). Hence, only lognormal parameters are considered here. In this data base, the year, month and day of the measurement are given, if available. Some entries are already averages for the free troposphere or over certain time periods. Some measurements are from high-altitude mountain stations, others from airborne instruments. The comments in the caption give more detailed information. The parameters are listed for four modes, and the last

column provides the corresponding publication. No homogenisation of the data from the different sources was performed.

| yyyy | mm | dd | hh<br>[m] | lat<br>lat | lon<br>lon | n1<br>[cm-3] | r1<br>[m-6] | s1<br>s1 | n2<br>[cm-3] | r2<br>[m-6] | s2<br>s2 | n3<br>[cm-3] | r3<br>[m-6] | s3<br>s3 | n4<br>[cm-3] | r4<br>[m-6] | s4<br>s4 | reference |
|---|---|---|---|---|---|---|---|---|---|---|---|---|---|---|---|---|---|---|
| – | – | – | 5000 | – | – | 10131.4 | 0.024 | 1.700 | 0.00 | 0.000 | 0.000 | 0.00 | 0.000 | 0.00 | 0.00 | 0.00 | 0.00 | Heintzenberg (2003)[1] |
| 2002 | 7 | 18 | 10000 | 27 | -81 | 6907.8 | 0.025 | 1.600 | 0.00 | 0.000 | 0.000 | 0.00 | 0.000 | 0.00 | 0.00 | 0.00 | 0.00 | Fridlind et al. (2004)[2] |
| 2002 | 7 | 18 | 5000 | 27 | -81 | 2763.1 | 0.025 | 1.600 | 0.00 | 0.000 | 0.000 | 0.00 | 0.000 | 0.00 | 0.00 | 0.00 | 0.00 | Fridlind et al. (2004) |
| 2002 | 7 | 18 | 2000 | 27 | -81 | 2763.1 | 0.050 | 2.500 | 0.00 | 0.000 | 0.000 | 0.00 | 0.000 | 0.00 | 0.00 | 0.00 | 0.00 | Fridlind et al. (2004) |
| 2002 | 7 | 18 | 1000 | 27 | -81 | 4144.7 | 0.110 | 1.900 | 0.00 | 0.000 | 0.000 | 0.00 | 0.000 | 0.00 | 0.00 | 0.00 | 0.00 | Fridlind et al. (2004) |
| 2002 | 7 | 18 | 1000 | 27 | -81 | 633.2 | 0.035 | 1.500 | 287.82 | 0.055 | 1.400 | 0.00 | 0.000 | 0.00 | 0.00 | 0.00 | 0.00 | Fridlind et al. (2004) |
| 1996 | 2 | 29 | 5500 | 42 | -106 | 354.6 | 0.120 | 1.610 | 0.41 | 0.960 | 2.600 | 0.00 | 0.000 | 0.00 | 0.00 | 0.00 | 0.00 | Han et al. (2003)[3] |
| 1996 | 3 | 8 | 5250 | 42 | -106 | 112.8 | 0.116 | 1.620 | 0.53 | 0.820 | 2.530 | 0.00 | 0.000 | 0.00 | 0.00 | 0.00 | 0.00 | Han et al. (2003) |
| 1996 | 3 | 15 | 5400 | 42 | -106 | 308.5 | 0.098 | 1.610 | 1.08 | 1.040 | 2.480 | 0.00 | 0.000 | 0.00 | 0.00 | 0.00 | 0.00 | Han et al. (2003) |
| 1996 | 3 | 15 | 5300 | 42 | -106 | 285.5 | 0.122 | 1.610 | 0.60 | 1.240 | 2.420 | 0.00 | 0.000 | 0.00 | 0.00 | 0.00 | 0.00 | Han et al. (2003) |
| 1996 | 3 | 8 | 2000 | 42 | -106 | 951.0 | 0.112 | 1.600 | 0.53 | 1.160 | 2.410 | 0.00 | 0.000 | 0.00 | 0.00 | 0.00 | 0.00 | Han et al. (2003) |
| 1996 | 3 | 8 | 2100 | 42 | -106 | 886.5 | 0.114 | 1.600 | 0.53 | 1.020 | 2.430 | 0.00 | 0.000 | 0.00 | 0.00 | 0.00 | 0.00 | Han et al. (2003) |
| 1996 | 3 | 8 | 2000 | 42 | -106 | 598.7 | 0.126 | 1.600 | 0.78 | 1.060 | 2.420 | 0.00 | 0.000 | 0.00 | 0.00 | 0.00 | 0.00 | Han et al. (2003) |
| 1996 | 3 | 8 | 2350 | 42 | -106 | 536.5 | 0.122 | 1.610 | 0.51 | 1.040 | 2.460 | 0.00 | 0.000 | 0.00 | 0.00 | 0.00 | 0.00 | Han et al. (2003) |
| 1996 | 3 | 10 | 2175 | 42 | -106 | 324.7 | 0.132 | 1.610 | 1.13 | 0.960 | 2.510 | 0.00 | 0.000 | 0.00 | 0.00 | 0.00 | 0.00 | Han et al. (2003) |
| 1996 | 3 | 10 | 2100 | 42 | -106 | 948.7 | 0.120 | 1.600 | 1.66 | 0.640 | 2.220 | 0.00 | 0.000 | 0.00 | 0.00 | 0.00 | 0.00 | Han et al. (2003) |
| 1996 | 6 | – | 3454 | 47 | 8 | 343.1 | 0.130 | 1.770 | 0.00 | 0.000 | 0.000 | 0.00 | 0.000 | 0.00 | 0.00 | 0.00 | 0.00 | Nyeki et al. (1998)[4] |
| 1996 | 7 | – | 3454 | 47 | 8 | 363.8 | 0.150 | 1.730 | 0.00 | 0.000 | 0.000 | 0.00 | 0.000 | 0.00 | 0.00 | 0.00 | 0.00 | Nyeki et al. (1998) |
| 1996 | 8 | – | 3454 | 47 | 8 | 446.7 | 0.110 | 1.650 | 0.00 | 0.000 | 0.000 | 0.00 | 0.000 | 0.00 | 0.00 | 0.00 | 0.00 | Nyeki et al. (1998) |
| 1996 | 9 | – | 3454 | 47 | 8 | 356.9 | 0.090 | 1.650 | 0.00 | 0.000 | 0.000 | 0.00 | 0.000 | 0.00 | 0.00 | 0.00 | 0.00 | Nyeki et al. (1998) |
| 1996 | 11 | – | 3454 | 47 | 8 | 124.3 | 0.120 | 1.590 | 0.00 | 0.000 | 0.000 | 0.00 | 0.000 | 0.00 | 0.00 | 0.00 | 0.00 | Nyeki et al. (1998) |
| 1996 | 12 | – | 3454 | 47 | 8 | 126.6 | 0.100 | 1.690 | 0.00 | 0.000 | 0.000 | 0.00 | 0.000 | 0.00 | 0.00 | 0.00 | 0.00 | Nyeki et al. (1998) |
| 1997 | 1 | – | 3454 | 47 | 8 | 156.6 | 0.090 | 1.640 | 0.00 | 0.000 | 0.000 | 0.00 | 0.000 | 0.00 | 0.00 | 0.00 | 0.00 | Nyeki et al. (1998) |
| 1997 | 2 | – | 3454 | 47 | 8 | 131.2 | 0.090 | 1.760 | 0.00 | 0.000 | 0.000 | 0.00 | 0.000 | 0.00 | 0.00 | 0.00 | 0.00 | Nyeki et al. (1998) |
| 1997 | 3 | – | 3454 | 47 | 8 | 163.5 | 0.100 | 1.770 | 0.00 | 0.000 | 0.000 | 0.00 | 0.000 | 0.00 | 0.00 | 0.00 | 0.00 | Nyeki et al. (1998) |
| 1997 | 4 | – | 3454 | 47 | 8 | 294.7 | 0.100 | 1.760 | 0.00 | 0.000 | 0.000 | 0.00 | 0.000 | 0.00 | 0.00 | 0.00 | 0.00 | Nyeki et al. (1998) |
| 1997 | 5 | – | 3454 | 47 | 8 | 285.5 | 0.100 | 1.680 | 0.00 | 0.000 | 0.000 | 0.00 | 0.000 | 0.00 | 0.00 | 0.00 | 0.00 | Nyeki et al. (1998) |
| – | – | – | 3454 | 47 | 8 | 382.2 | 0.130 | 1.730 | 0.00 | 0.000 | 0.000 | 0.00 | 0.000 | 0.00 | 0.00 | 0.00 | 0.00 | Nyeki et al. (1998)[5] |
| – | – | – | 3454 | 47 | 8 | 138.2 | 0.100 | 1.640 | 0.00 | 0.000 | 0.000 | 0.00 | 0.000 | 0.00 | 0.00 | 0.00 | 0.00 | Nyeki et al. (1998)[6] |
| – | – | – | 3454 | 47 | 8 | 228.0 | 0.100 | 1.710 | 0.00 | 0.000 | 0.000 | 0.00 | 0.000 | 0.00 | 0.00 | 0.00 | 0.00 | Nyeki et al. (1998)[7] |
| 2006 | – | – | 3816 | 36 | 101 | 4821.6 | 0.015 | 1.410 | 1148.99 | 0.045 | 1.550 | 1139.78 | 0.125 | 1.72 | 0.00 | 0.00 | 0.00 | Kivekäs et al. (2009)[8] |
| 2006 | – | – | 3816 | 36 | 101 | 2371.7 | 0.021 | 1.520 | 1188.13 | 0.047 | 1.640 | 824.33 | 0.125 | 1.71 | 0.00 | 0.00 | 0.00 | Kivekäs et al. (2009) |
| 2006 | – | – | 3816 | 36 | 101 | 329.3 | 0.026 | 1.490 | 2933.49 | 0.046 | 1.500 | 1478.26 | 0.130 | 1.71 | 0.00 | 0.00 | 0.00 | Kivekäs et al. (2009) |
| 2006 | – | – | 3816 | 36 | 101 | 306.2 | 0.022 | 1.450 | 1047.68 | 0.051 | 1.540 | 1570.36 | 0.147 | 1.71 | 0.00 | 0.00 | 0.00 | Kivekäs et al. (2009) |
| 2006 | – | – | 3816 | 36 | 101 | 944.1 | 0.020 | 1.540 | 759.85 | 0.048 | 1.530 | 1015.44 | 0.143 | 1.68 | 0.00 | 0.00 | 0.00 | Kivekäs et al. (2009) |
| 2007 | 1 | – | 1465 | 46 | 3 | 115.1 | 0.016 | 1.500 | 391.44 | 0.039 | 1.500 | 184.21 | 0.105 | 1.55 | 0.00 | 0.00 | 0.00 | Venzac et al. (2009)[9] |
| 2007 | 1 | – | 1465 | 46 | 3 | 184.2 | 0.016 | 1.400 | 529.59 | 0.037 | 1.550 | 149.67 | 0.125 | 1.50 | 0.00 | 0.00 | 0.00 | Venzac et al. (2009)[10] |
| 2007 | 1 | – | 1465 | 46 | 3 | 345.4 | 0.022 | 1.450 | 1220.37 | 0.049 | 1.500 | 345.39 | 0.140 | 1.50 | 0.00 | 0.00 | 0.00 | Venzac et al. (2009)[11] |
| 2007 | 7 | – | 1465 | 46 | 3 | 299.3 | 0.020 | 1.400 | 1496.68 | 0.042 | 1.600 | 621.70 | 0.120 | 1.60 | 0.00 | 0.00 | 0.00 | Venzac et al. (2009)[12] |
| 2007 | 7 | – | 1465 | 46 | 3 | 541.1 | 0.024 | 1.500 | 2014.76 | 0.058 | 1.500 | 2705.54 | 0.140 | 1.60 | 0.00 | 0.00 | 0.00 | Venzac et al. (2009)[13] |
| 2007 | 7 | – | 1465 | 46 | 3 | 1151.3 | 0.028 | 1.500 | 3799.27 | 0.061 | 1.500 | 2763.10 | 0.145 | 1.50 | 0.00 | 0.00 | 0.00 | Venzac et al. (2009)[14] |

***Table A.1:*** *Aerosol database.* [1]*for whole upper troposphere,* [2]*CRYSTAL-FACE,* [3]*SWYVIS Wyoming,* [4]*Jungfraujoch accumulation mode,* [5]*Jungfraujoch accumulation mode summer median,* [6]*Jungfraujoch accumulation mode winter median,* [7]*Jungfraujoch accumulation mode annual median,* [8]*Mount Waliguan China 1.5 year mean,* [9]*Puy de Dome Marine Winter,* [10]*Puy de Dome Continental Winter,* [11]*Puy de Dome Regional Winter,* [12]*Puy de Dome Marine Summer,* [13]*Puy de Dome Continental Summer,* [14]*Puy de Dome Regional Summer*

| yyyy | mm | dd | hh [m] | lat lat | lon lon | n1 [cm-3] | r1 [m-6] | s1 s1 | n2 [cm-3] | r2 [m-6] | s2 s2 | n3 [cm-3] | r3 [m-6] | s3 s3 | n4 [cm-3] | r4 [m-6] | s4 s4 | reference |
|---|---|---|---|---|---|---|---|---|---|---|---|---|---|---|---|---|---|---|
| 2008 | 1 | – | 4765 | 9 | -71 | 416.8 | 0.024 | 1.562 | 396.04 | 0.058 | 1.583 | 156.58 | 0.127 | 1.60 | 0.00 | 0.00 | 0.00 | Schmeisner et al. (2011)[1] |
| 2008 | 1 | – | 4765 | 9 | -71 | 124.3 | 0.018 | 1.562 | 589.46 | 0.039 | 1.583 | 667.75 | 0.135 | 1.60 | 0.00 | 0.00 | 0.00 | Schmeisner et al. (2011)[2] |
| 2008 | 2 | – | 4765 | 9 | -71 | 320.1 | 0.023 | 1.562 | 412.16 | 0.051 | 1.583 | 165.79 | 0.139 | 1.60 | 0.00 | 0.00 | 0.00 | Schmeisner et al. (2011)[1] |
| 2008 | 2 | – | 4765 | 9 | -71 | 57.6 | 0.016 | 1.562 | 320.06 | 0.044 | 1.583 | 379.93 | 0.139 | 1.60 | 0.00 | 0.00 | 0.00 | Schmeisner et al. (2011)[2] |
| 2008 | 3 | – | 4765 | 9 | -71 | 444.4 | 0.028 | 1.562 | 561.83 | 0.066 | 1.583 | 310.85 | 0.154 | 1.60 | 0.00 | 0.00 | 0.00 | Schmeisner et al. (2011)[1] |
| 2008 | 3 | – | 4765 | 9 | -71 | 322.4 | 0.032 | 1.562 | 425.98 | 0.092 | 1.583 | 1003.93 | 0.162 | 1.60 | 0.00 | 0.00 | 0.00 | Schmeisner et al. (2011)[2] |
| 2008 | 4 | – | 4765 | 9 | -71 | 152.0 | 0.025 | 1.562 | 541.11 | 0.072 | 1.583 | 274.01 | 0.168 | 1.60 | 0.00 | 0.00 | 0.00 | Schmeisner et al. (2011)[1] |
| 2008 | 4 | – | 4765 | 9 | -71 | 290.1 | 0.035 | 1.562 | 338.48 | 0.091 | 1.583 | 764.46 | 0.186 | 1.60 | 0.00 | 0.00 | 0.00 | Schmeisner et al. (2011)[2] |
| 2008 | 5 | – | 4765 | 9 | -71 | 122.0 | 0.024 | 1.562 | 423.68 | 0.069 | 1.583 | 149.67 | 0.196 | 1.60 | 0.00 | 0.00 | 0.00 | Schmeisner et al. (2011)[1] |
| 2008 | 5 | – | 4765 | 9 | -71 | 92.1 | 0.017 | 1.562 | 449.00 | 0.050 | 1.583 | 347.69 | 0.172 | 1.60 | 0.00 | 0.00 | 0.00 | Schmeisner et al. (2011)[2] |
| 2008 | 6 | – | 4765 | 9 | -71 | 191.1 | 0.020 | 1.562 | 554.92 | 0.054 | 1.583 | 89.80 | 0.133 | 1.60 | 0.00 | 0.00 | 0.00 | Schmeisner et al. (2011)[1] |
| 2008 | 6 | – | 4765 | 9 | -71 | 204.9 | 0.018 | 1.562 | 571.04 | 0.041 | 1.583 | 267.10 | 0.130 | 1.60 | 0.00 | 0.00 | 0.00 | Schmeisner et al. (2011)[2] |
| 2008 | 7 | – | 4765 | 9 | -71 | 193.4 | 0.022 | 1.562 | 460.52 | 0.061 | 1.583 | 20.72 | 0.208 | 1.60 | 0.00 | 0.00 | 0.00 | Schmeisner et al. (2011)[1] |
| 2008 | 7 | – | 4765 | 9 | -71 | 244.1 | 0.019 | 1.562 | 488.15 | 0.046 | 1.583 | 207.23 | 0.143 | 1.60 | 0.00 | 0.00 | 0.00 | Schmeisner et al. (2011)[2] |
| 2008 | 8 | – | 4765 | 9 | -71 | 218.7 | 0.022 | 1.562 | 326.97 | 0.049 | 1.583 | 55.26 | 0.122 | 1.60 | 0.00 | 0.00 | 0.00 | Schmeisner et al. (2011)[1] |
| 2008 | 8 | – | 4765 | 9 | -71 | 85.2 | 0.015 | 1.562 | 425.98 | 0.039 | 1.583 | 135.85 | 0.131 | 1.60 | 0.00 | 0.00 | 0.00 | Schmeisner et al. (2011)[2] |
| 2008 | 9 | – | 4765 | 9 | -71 | 76.0 | 0.017 | 1.562 | 331.57 | 0.053 | 1.583 | 23.03 | 0.137 | 1.60 | 0.00 | 0.00 | 0.00 | Schmeisner et al. (2011)[1] |
| 2008 | 9 | – | 4765 | 9 | -71 | 53.0 | 0.013 | 1.562 | 490.45 | 0.039 | 1.583 | 175.00 | 0.126 | 1.60 | 0.00 | 0.00 | 0.00 | Schmeisner et al. (2011)[2] |
| 2008 | 10 | – | 4765 | 9 | -71 | 85.2 | 0.020 | 1.562 | 497.36 | 0.058 | 1.583 | 41.45 | 0.207 | 1.60 | 0.00 | 0.00 | 0.00 | Schmeisner et al. (2011)[1] |
| 2008 | 10 | – | 4765 | 9 | -71 | 89.8 | 0.019 | 1.562 | 356.90 | 0.049 | 1.583 | 158.88 | 0.145 | 1.60 | 0.00 | 0.00 | 0.00 | Schmeisner et al. (2011)[2] |
| 2008 | 11 | – | 4765 | 9 | -71 | 363.8 | 0.024 | 1.562 | 658.54 | 0.048 | 1.583 | 59.87 | 0.135 | 1.60 | 0.00 | 0.00 | 0.00 | Schmeisner et al. (2011)[1] |
| 2008 | 11 | – | 4765 | 9 | -71 | 89.8 | 0.016 | 1.562 | 591.76 | 0.042 | 1.583 | 230.26 | 0.133 | 1.60 | 0.00 | 0.00 | 0.00 | Schmeisner et al. (2011)[2] |
| 2008 | 12 | – | 4765 | 9 | -71 | 368.4 | 0.022 | 1.562 | 449.00 | 0.053 | 1.583 | 69.08 | 0.132 | 1.60 | 0.00 | 0.00 | 0.00 | Schmeisner et al. (2011)[1] |
| 2008 | 12 | – | 4765 | 9 | -71 | 228.0 | 0.017 | 1.562 | 589.46 | 0.041 | 1.583 | 306.24 | 0.128 | 1.60 | 0.00 | 0.00 | 0.00 | Schmeisner et al. (2011)[2] |
| 1998 | 8 | – | 7000 | 52 | 14 | 322.4 | 0.018 | 1.700 | 506.57 | 0.075 | 1.800 | 0.00 | 0.000 | 0.00 | 0.00 | 0.00 | 0.00 | Schroeder et al. (2002)[3] |
| 1998 | 8 | – | 11000 | 52 | 14 | 690.8 | 0.012 | 1.700 | 253.28 | 0.100 | 1.600 | 0.00 | 0.000 | 0.00 | 0.00 | 0.00 | 0.00 | Schroeder et al. (2002)[3] |
| 1998 | 8 | – | 11000 | 52 | 14 | 115.1 | 0.015 | 2.000 | 506.57 | 0.115 | 1.450 | 0.00 | 0.000 | 0.00 | 0.00 | 0.00 | 0.00 | Schroeder et al. (2002)[4] |
| 1998 | 7 | 31 | 11300 | 52 | 14 | 241.8 | 0.070 | 2.100 | 13.82 | 0.220 | 1.600 | 0.05 | 1.000 | 1.70 | 0.00 | 0.00 | 0.00 | Petzold et al. (2002)[5] |
| 1998 | 7 | 31 | 6700 | 52 | 14 | 1151.3 | 0.047 | 2.000 | 46.05 | 0.230 | 1.400 | 0.23 | 0.900 | 1.70 | 0.00 | 0.00 | 0.00 | Petzold et al. (2002) |
| 1998 | 7 | 31 | 4000 | 52 | 14 | 759.9 | 0.045 | 2.000 | 92.10 | 0.210 | 1.400 | 0.46 | 0.700 | 1.70 | 0.00 | 0.00 | 0.00 | Petzold et al. (2002) |
| 1998 | 8 | 1 | 11300 | 52 | 14 | 368.4 | 0.080 | 1.700 | 23.03 | 0.200 | 1.600 | 0.05 | 1.000 | 1.70 | 0.00 | 0.00 | 0.00 | Petzold et al. (2002)[6] |
| 1998 | 8 | 1 | 6700 | 52 | 14 | 1105.2 | 0.070 | 1.600 | 23.03 | 0.250 | 1.400 | 0.69 | 0.900 | 1.90 | 0.00 | 0.00 | 0.00 | Petzold et al. (2002) |
| 1998 | 8 | 1 | 4000 | 52 | 14 | 1116.8 | 0.030 | 2.000 | 23.03 | 0.210 | 1.400 | 0.18 | 0.700 | 1.80 | 0.00 | 0.00 | 0.00 | Petzold et al. (2002) |
| 1998 | 8 | 9 | 11300 | 52 | 14 | 1254.9 | 0.032 | 2.000 | 3.91 | 0.280 | 1.350 | 0.18 | 0.500 | 1.70 | 0.00 | 0.00 | 0.00 | Petzold et al. (2002)[7] |
| 1998 | 8 | 9 | 6700 | 52 | 14 | 575.6 | 0.044 | 2.000 | 6.91 | 0.280 | 1.350 | 4.61 | 0.360 | 1.70 | 0.00 | 0.00 | 0.00 | Petzold et al. (2002) |
| 1998 | 8 | 9 | 4000 | 52 | 14 | 944.1 | 0.057 | 2.000 | 575.65 | 0.340 | 1.350 | 1.61 | 0.900 | 1.90 | 0.00 | 0.00 | 0.00 | Petzold et al. (2002) |
| 1998 | 8 | 10 | 6700 | 52 | 14 | 805.9 | 0.050 | 1.800 | 9.21 | 0.250 | 1.400 | 0.46 | 1.000 | 1.60 | 0.00 | 0.00 | 0.00 | Petzold et al. (2002)[8] |
| 1998 | 8 | 10 | 4000 | 52 | 14 | 621.7 | 0.050 | 2.000 | 11.51 | 0.330 | 1.350 | 0.23 | 1.400 | 2.00 | 0.00 | 0.00 | 0.00 | Petzold et al. (2002)[9] |
| 1998 | 8 | 10 | 11300 | 52 | 14 | 1158.2 | 0.040 | 2.000 | 1.84 | 0.300 | 1.400 | 0.14 | 1.000 | 1.60 | 0.00 | 0.00 | 0.00 | Petzold et al. (2002)[9] |
| 1998 | 8 | 10 | 6700 | 52 | 14 | 713.8 | 0.034 | 2.000 | 1.84 | 0.280 | 1.400 | 0.37 | 0.800 | 1.90 | 0.00 | 0.00 | 0.00 | Petzold et al. (2002) |
| 1998 | 8 | 10 | 4000 | 52 | 14 | 552.6 | 0.042 | 2.000 | 13.82 | 0.270 | 1.350 | 0.35 | 1.170 | 1.80 | 0.00 | 0.00 | 0.00 | Petzold et al. (2002) |

***Table A.2:*** *Aerosol database.* [1]*Pico Espejo dry,* [2]*Pico Espejo humid,* [3]*Lindenberg med,* [4]*Lindenberg acc,* [5]*Lindenberg flight M1,* [6]*Lindenberg flight M2,* [7]*Lindenberg flight M5,* [8]*Lindenberg flight M6,* [9]*Lindenberg flight M7*

| yyyy | mm | dd | hh<br>[m] | lat<br>lat | lon<br>lon | n1<br>[cm-3] | r1<br>[m-6] | s1<br>s1 | n2<br>[cm-3] | r2<br>[m-6] | s2<br>s2 | n3<br>[cm-3] | r3<br>[m-6] | s3<br>s3 | n4<br>[cm-3] | r4<br>[m-6] | s4<br>s4 | reference |
|---|---|---|---|---|---|---|---|---|---|---|---|---|---|---|---|---|---|---|
| 1997 | 7 | 8 | 7010 | 28 | -15 | 62.2 | 0.010 | 1.650 | 743.73 | 0.045 | 1.620 | 0.69 | 0.400 | 2.20 | 0.00 | 0.00 | 0.00 | de Reus pers. com.[1] |
| 1997 | 7 | 8 | 8534 | 28 | -15 | 17.3 | 0.011 | 1.650 | 368.41 | 0.052 | 1.650 | 0.35 | 0.450 | 1.60 | 0.00 | 0.00 | 0.00 | de Reus pers. com. |
| 1999 | 3 | – | 5750 | 4 | 74 | 69.1 | 0.008 | 1.400 | 828.93 | 0.057 | 1.500 | 11.51 | 0.180 | 1.50 | 0.00 | 0.00 | 0.00 | de Reus et al. (2001)[2] |
| 1999 | 3 | – | 10500 | 4 | 74 | 921.0 | 0.008 | 1.400 | 644.72 | 0.038 | 1.550 | 57.56 | 0.200 | 1.50 | 0.92 | 0.90 | 1.50 | de Reus et al. (2001) |
| 1998 | 1 | – | 11000 | 68 | 20 | 414.5 | 0.075 | 1.700 | 0.25 | 0.725 | 1.350 | 0.00 | 0.000 | 0.00 | 0.00 | 0.00 | 0.00 | Petzold et al. (2000)[3] |
| 1998 | 1 | – | 11000 | 68 | 20 | 257.9 | 0.094 | 1.700 | 0.16 | 0.906 | 1.350 | 3.91 | 1.150 | 1.40 | 0.00 | 0.00 | 0.00 | Petzold et al. (2000)[4] |
| 1998 | 3 | – | 5000 | 5 | -57 | 46.1 | 0.008 | 1.400 | 944.06 | 0.045 | 1.750 | 92.10 | 0.130 | 1.30 | 0.00 | 0.00 | 0.00 | Krejci et al. (2003)[5] |
| 1998 | 3 | – | 7000 | 5 | -57 | 2763.1 | 0.043 | 1.740 | 0.00 | 0.000 | 0.000 | 0.00 | 0.000 | 0.00 | 0.00 | 0.00 | 0.00 | Krejci et al. (2003) |
| 1998 | 3 | – | 9000 | 5 | -57 | 460.5 | 0.008 | 1.500 | 2809.15 | 0.037 | 1.750 | 9.21 | 0.140 | 1.35 | 1.15 | 0.22 | 2.00 | Krejci et al. (2003) |
| 1998 | 3 | – | 11300 | 5 | -57 | 2993.4 | 0.008 | 1.500 | 5641.33 | 0.031 | 1.660 | 52.96 | 0.140 | 1.30 | 6.91 | 0.22 | 2.00 | Krejci et al. (2003) |
| 1989 | 2 | 8 | 4000 | 32 | -106 | 8.6 | 0.1270 | 1.930 | 5.00e-02 | 2.331 | 1.968 | 0.000 | 0.000 | 0.00 | 0.00 | 0.00 | 0.00 | Kim et al. (1993)[6] |
| 1989 | 7 | 12 | 4000 | 32 | -106 | 233.9 | 0.1420 | 1.653 | 1.00e-01 | 2.160 | 1.846 | 0.000 | 0.000 | 0.00 | 0.00 | 0.00 | 0.00 | Kim et al. (1993)[7] |
| 1990 | 6 | 2 | 4000 | 32 | -106 | 32.7 | 0.1200 | 1.844 | 6.00e-02 | 1.331 | 2.111 | 0.000 | 0.000 | 0.00 | 0.00 | 0.00 | 0.00 | Kim et al. (1993)[8] |
| 2005 | 11 | 23 | 1000 | -13 | 132 | 349.0 | 0.0956 | 1.770 | 5.33e-01 | 0.956 | 1.790 | 0.000 | 0.000 | 0.00 | 0.00 | 0.00 | 0.00 | Deshler (2011)[9] |
| 2005 | 11 | 23 | 1500 | -13 | 132 | 379.0 | 0.0762 | 2.130 | 8.16e-01 | 0.742 | 1.980 | 0.000 | 0.000 | 0.00 | 0.00 | 0.00 | 0.00 | Deshler (2011) |
| 2005 | 11 | 23 | 2000 | -13 | 132 | 302.0 | 0.0586 | 2.030 | 2.79e-01 | 0.974 | 1.820 | 0.000 | 0.000 | 0.00 | 0.00 | 0.00 | 0.00 | Deshler (2011) |
| 2005 | 11 | 23 | 2500 | -13 | 132 | 273.0 | 0.0582 | 1.990 | 2.27e-01 | 0.921 | 1.790 | 0.000 | 0.000 | 0.00 | 0.00 | 0.00 | 0.00 | Deshler (2011) |
| 2005 | 11 | 23 | 3000 | -13 | 132 | 242.0 | 0.1232 | 1.460 | 3.72e-01 | 0.564 | 1.960 | 0.000 | 0.000 | 0.00 | 0.00 | 0.00 | 0.00 | Deshler (2011) |
| 2005 | 11 | 23 | 3500 | -13 | 132 | 504.0 | 0.0226 | 2.530 | 8.49e-03 | 2.220 | 1.170 | 0.000 | 0.000 | 0.00 | 0.00 | 0.00 | 0.00 | Deshler (2011) |
| 2005 | 11 | 23 | 4000 | -13 | 132 | 1150.0 | 0.0145 | 2.610 | 4.49e-03 | 2.060 | 1.310 | 0.000 | 0.000 | 0.00 | 0.00 | 0.00 | 0.00 | Deshler (2011) |
| 2005 | 11 | 23 | 4500 | -13 | 132 | 1480.0 | 0.0242 | 2.140 | 3.02e-03 | 1.546 | 1.320 | 0.000 | 0.000 | 0.00 | 0.00 | 0.00 | 0.00 | Deshler (2011) |
| 2005 | 11 | 23 | 5000 | -13 | 132 | 878.0 | 0.0180 | 2.410 | 7.91e-04 | 2.126 | 1.060 | 0.000 | 0.000 | 0.00 | 0.00 | 0.00 | 0.00 | Deshler (2011) |
| 2005 | 11 | 23 | 5500 | -13 | 132 | 332.0 | 0.0173 | 2.590 | 3.04e-04 | 1.608 | 1.280 | 0.000 | 0.000 | 0.00 | 0.00 | 0.00 | 0.00 | Deshler (2011) |
| 2005 | 11 | 23 | 6000 | -13 | 132 | 293.0 | 0.0204 | 2.520 | 1.59e-03 | 2.300 | 1.100 | 0.000 | 0.000 | 0.00 | 0.00 | 0.00 | 0.00 | Deshler (2011) |
| 2005 | 11 | 23 | 6500 | -13 | 132 | 301.0 | 0.0208 | 2.480 | 9.52e-04 | 2.100 | 1.870 | 0.000 | 0.000 | 0.00 | 0.00 | 0.00 | 0.00 | Deshler (2011) |
| 2005 | 11 | 23 | 8500 | -13 | 132 | 460.0 | 0.0203 | 2.240 | 5.21e-03 | 0.852 | 1.190 | 0.000 | 0.000 | 0.00 | 0.00 | 0.00 | 0.00 | Deshler (2011) |
| 2005 | 11 | 23 | 7000 | -13 | 132 | 333.0 | 0.0188 | 2.500 | 3.41e-04 | 2.160 | 1.060 | 0.000 | 0.000 | 0.00 | 0.00 | 0.00 | 0.00 | Deshler (2011) |
| 2005 | 11 | 23 | 7500 | -13 | 132 | 401.0 | 0.0266 | 2.220 | 4.90e-04 | 1.516 | 2.520 | 0.000 | 0.000 | 0.00 | 0.00 | 0.00 | 0.00 | Deshler (2011) |
| 2005 | 11 | 23 | 9000 | -13 | 132 | 480.0 | 0.0162 | 2.340 | 1.18e-02 | 0.716 | 1.230 | 0.000 | 0.000 | 0.00 | 0.00 | 0.00 | 0.00 | Deshler (2011) |
| 2005 | 11 | 23 | 10000 | -13 | 132 | 511.0 | 0.0392 | 1.770 | 2.33e-02 | 0.632 | 1.370 | 0.000 | 0.000 | 0.00 | 0.00 | 0.00 | 0.00 | Deshler (2011) |
| 2005 | 11 | 23 | 10500 | -13 | 132 | 533.0 | 0.0402 | 1.760 | 1.96e-02 | 0.612 | 1.380 | 0.000 | 0.000 | 0.00 | 0.00 | 0.00 | 0.00 | Deshler (2011) |
| 2005 | 11 | 23 | 11000 | -13 | 132 | 545.0 | 0.0332 | 1.880 | 2.46e-02 | 0.872 | 1.260 | 0.000 | 0.000 | 0.00 | 0.00 | 0.00 | 0.00 | Deshler (2011) |
| 2005 | 11 | 23 | 13500 | -13 | 132 | 563.0 | 0.0412 | 1.760 | 5.97e-02 | 0.658 | 1.460 | 0.000 | 0.000 | 0.00 | 0.00 | 0.00 | 0.00 | Deshler (2011) |
| 2005 | 11 | 23 | 14000 | -13 | 132 | 489.0 | 0.0202 | 2.190 | 1.17e-02 | 0.906 | 1.260 | 0.000 | 0.000 | 0.00 | 0.00 | 0.00 | 0.00 | Deshler (2011) |
| 2005 | 11 | 23 | 14500 | -13 | 132 | 473.0 | 0.0414 | 1.760 | 3.64e-02 | 0.574 | 1.390 | 0.000 | 0.000 | 0.00 | 0.00 | 0.00 | 0.00 | Deshler (2011) |
| 2005 | 11 | 23 | 15000 | -13 | 132 | 481.0 | 0.0204 | 2.250 | 2.51e-03 | 1.192 | 1.080 | 0.000 | 0.000 | 0.00 | 0.00 | 0.00 | 0.00 | Deshler (2011) |
| 2005 | 11 | 23 | 15500 | -13 | 132 | 426.0 | 0.0376 | 1.850 | 3.06e-02 | 0.644 | 1.350 | 0.000 | 0.000 | 0.00 | 0.00 | 0.00 | 0.00 | Deshler (2011) |
| 2005 | 11 | 23 | 16000 | -13 | 132 | 407.0 | 0.0422 | 1.760 | 3.55e-02 | 0.616 | 1.370 | 0.000 | 0.000 | 0.00 | 0.00 | 0.00 | 0.00 | Deshler (2011) |
| 2005 | 11 | 23 | 16500 | -13 | 132 | 371.0 | 0.0189 | 2.240 | 8.04e-03 | 0.904 | 1.270 | 0.000 | 0.000 | 0.00 | 0.00 | 0.00 | 0.00 | Deshler (2011) |

***Table A.3:*** *Aerosol database.*[1]*Canary Islands ACE above Dust Layer,* [2]*Indian Ocean INDOEX,* [3]*Northern Scandinavia POLSTAR2 background,* [4]*Northern Scandinavia POLSTAR2 aitken accumulation haze,* [5]*Surinam,* [6]*ALIVE1 New Mexico maximum height 4500 m,* [7]*ALIVE2 New Mexico maximum height 4500 m,* [8]*ALIVE4 New Mexico maximum height 4500 m,* [9]*051123AU asc-AU-Darwin-13S132E.SD2*

| yyyy | mm | dd | hh [m] | lat lat | lon lon | n1 [cm-3] | r1 [m-6] | s1 s1 | n2 [cm-3] | r2 [m-6] | s2 s2 | n3 [cm-3] | r3 [m-6] | s3 s3 | n4 [cm-3] | r4 [m-6] | s4 s4 | reference |
|---|---|---|---|---|---|---|---|---|---|---|---|---|---|---|---|---|---|---|
| 2005 | 11 | 23 | 3000 | -13 | 132 | 3.8 | 0.2900 | 1.240 | 4.44e-01 | 0.740 | 1.720 | 0.000 | 0.000 | 0.00 | 0.00 | 0.00 | 0.00 | Deshler (2011)[1] |
| 2005 | 11 | 23 | 3500 | -13 | 132 | 2.1 | 0.2960 | 1.240 | 2.67e-01 | 0.742 | 1.790 | 0.000 | 0.000 | 0.00 | 0.00 | 0.00 | 0.00 | Deshler (2011) |
| 2005 | 11 | 23 | 4000 | -13 | 132 | 1.6 | 0.2960 | 1.370 | 1.03e-01 | 0.888 | 1.790 | 0.000 | 0.000 | 0.00 | 0.00 | 0.00 | 0.00 | Deshler (2011) |
| 2005 | 11 | 23 | 4500 | -13 | 132 | 201.0 | 0.0562 | 1.930 | 6.00e-02 | 0.964 | 1.610 | 0.000 | 0.000 | 0.00 | 0.00 | 0.00 | 0.00 | Deshler (2011) |
| 2005 | 11 | 23 | 5000 | -13 | 132 | 272.0 | 0.0228 | 2.540 | 1.88e-03 | 2.280 | 1.190 | 0.000 | 0.000 | 0.00 | 0.00 | 0.00 | 0.00 | Deshler (2011) |
| 2005 | 11 | 23 | 5500 | -13 | 132 | 302.0 | 0.0202 | 2.570 | 7.42e-04 | 2.300 | 1.200 | 0.000 | 0.000 | 0.00 | 0.00 | 0.00 | 0.00 | Deshler (2011) |
| 2005 | 11 | 23 | 6000 | -13 | 132 | 372.0 | 0.0202 | 2.570 | 1.04e-03 | 2.320 | 1.100 | 0.000 | 0.000 | 0.00 | 0.00 | 0.00 | 0.00 | Deshler (2011) |
| 2005 | 11 | 23 | 6500 | -13 | 132 | 331.0 | 0.0193 | 2.580 | 1.10e-03 | 2.280 | 1.110 | 0.000 | 0.000 | 0.00 | 0.00 | 0.00 | 0.00 | Deshler (2011) |
| 2005 | 11 | 23 | 7000 | -13 | 132 | 323.0 | 0.0172 | 2.610 | 4.99e-04 | 2.300 | 1.120 | 0.000 | 0.000 | 0.00 | 0.00 | 0.00 | 0.00 | Deshler (2011) |
| 2005 | 11 | 23 | 7500 | -13 | 132 | 352.0 | 0.0167 | 2.620 | 9.44e-04 | 2.400 | 1.180 | 0.000 | 0.000 | 0.00 | 0.00 | 0.00 | 0.00 | Deshler (2011) |
| 2005 | 11 | 23 | 9000 | -13 | 132 | 435.0 | 0.0146 | 2.630 | 2.19e-04 | 3.120 | 1.120 | 0.000 | 0.000 | 0.00 | 0.00 | 0.00 | 0.00 | Deshler (2011) |
| 2005 | 11 | 23 | 11000 | -13 | 132 | 479.0 | 0.0330 | 1.800 | 4.05e-02 | 0.432 | 2.500 | 0.000 | 0.000 | 0.00 | 0.00 | 0.00 | 0.00 | Deshler (2011) |
| 2005 | 11 | 23 | 11500 | -13 | 132 | 490.0 | 0.0854 | 1.400 | 6.84e-02 | 0.558 | 1.830 | 0.000 | 0.000 | 0.00 | 0.00 | 0.00 | 0.00 | Deshler (2011) |
| 2005 | 11 | 23 | 12000 | -13 | 132 | 491.0 | 0.0348 | 1.870 | 6.58e-02 | 0.802 | 1.740 | 0.000 | 0.000 | 0.00 | 0.00 | 0.00 | 0.00 | Deshler (2011) |
| 2005 | 11 | 23 | 12500 | -13 | 132 | 487.0 | 0.0330 | 1.880 | 6.47e-02 | 0.754 | 1.800 | 0.000 | 0.000 | 0.00 | 0.00 | 0.00 | 0.00 | Deshler (2011) |
| 2005 | 11 | 23 | 13000 | -13 | 132 | 506.0 | 0.0286 | 1.960 | 5.19e-02 | 0.676 | 1.930 | 0.000 | 0.000 | 0.00 | 0.00 | 0.00 | 0.00 | Deshler (2011) |
| 2005 | 11 | 23 | 13500 | -13 | 132 | 526.0 | 0.0550 | 1.590 | 1.07e-01 | 0.516 | 1.910 | 0.000 | 0.000 | 0.00 | 0.00 | 0.00 | 0.00 | Deshler (2011) |
| 2005 | 11 | 23 | 14000 | -13 | 132 | 525.0 | 0.1084 | 1.360 | 1.46e-01 | 0.964 | 1.680 | 0.000 | 0.000 | 0.00 | 0.00 | 0.00 | 0.00 | Deshler (2011) |
| 2005 | 11 | 23 | 14500 | -13 | 132 | 525.0 | 0.0284 | 2.450 | 5.27e-01 | 2.000 | 1.260 | 0.000 | 0.000 | 0.00 | 0.00 | 0.00 | 0.00 | Deshler (2011) |
| 2005 | 11 | 23 | 15000 | -13 | 132 | 531.0 | 0.0386 | 2.180 | 8.14e-01 | 1.262 | 1.400 | 0.000 | 0.000 | 0.00 | 0.00 | 0.00 | 0.00 | Deshler (2011) |
| 2005 | 11 | 23 | 16000 | -13 | 132 | 558.0 | 0.0384 | 2.390 | 1.16e+00 | 1.896 | 1.290 | 0.000 | 0.000 | 0.00 | 0.00 | 0.00 | 0.00 | Deshler (2011) |
| 2005 | 11 | 23 | 16500 | -13 | 132 | 551.0 | 0.0608 | 2.030 | 3.09e+00 | 1.266 | 1.400 | 0.000 | 0.000 | 0.00 | 0.00 | 0.00 | 0.00 | Deshler (2011) |
| 2005 | 11 | 23 | 17500 | -13 | 132 | 584.0 | 0.0472 | 2.130 | 1.49e+00 | 1.208 | 1.460 | 0.000 | 0.000 | 0.00 | 0.00 | 0.00 | 0.00 | Deshler (2011)[2] |
| 2006 | 7 | 31 | 1000 | 13 | 2 | 398.0 | 0.0562 | 2.300 | 7.83e-01 | 0.898 | 1.940 | 0.000 | 0.000 | 0.00 | 0.00 | 0.00 | 0.00 | Deshler (2011) |
| 2006 | 7 | 31 | 1500 | 13 | 2 | 365.0 | 0.0550 | 2.300 | 1.92e+00 | 0.912 | 1.880 | 0.000 | 0.000 | 0.00 | 0.00 | 0.00 | 0.00 | Deshler (2011) |
| 2006 | 7 | 31 | 2000 | 13 | 2 | 331.0 | 0.0580 | 2.290 | 2.54e+00 | 0.954 | 1.850 | 0.000 | 0.000 | 0.00 | 0.00 | 0.00 | 0.00 | Deshler (2011) |
| 2006 | 7 | 31 | 2500 | 13 | 2 | 272.0 | 0.0572 | 2.300 | 1.84e+00 | 0.964 | 1.860 | 0.000 | 0.000 | 0.00 | 0.00 | 0.00 | 0.00 | Deshler (2011) |
| 2006 | 7 | 31 | 3000 | 13 | 2 | 257.0 | 0.0590 | 2.300 | 2.07e+00 | 1.032 | 1.830 | 0.000 | 0.000 | 0.00 | 0.00 | 0.00 | 0.00 | Deshler (2011) |
| 2006 | 7 | 31 | 4000 | 13 | 2 | 274.0 | 0.0594 | 2.290 | 1.83e+00 | 1.116 | 1.810 | 0.000 | 0.000 | 0.00 | 0.00 | 0.00 | 0.00 | Deshler (2011) |
| 2006 | 7 | 31 | 4500 | 13 | 2 | 261.0 | 0.0612 | 2.290 | 1.07e+00 | 1.128 | 1.830 | 0.000 | 0.000 | 0.00 | 0.00 | 0.00 | 0.00 | Deshler (2011) |
| 2006 | 7 | 31 | 5000 | 13 | 2 | 243.0 | 0.0856 | 1.970 | 1.79e+00 | 1.774 | 1.710 | 0.000 | 0.000 | 0.00 | 0.00 | 0.00 | 0.00 | Deshler (2011) |
| 2006 | 7 | 31 | 6500 | 13 | 2 | 364.0 | 0.0292 | 2.010 | 1.67e-02 | 1.054 | 1.370 | 0.000 | 0.000 | 0.00 | 0.00 | 0.00 | 0.00 | Deshler (2011) |
| 2006 | 7 | 31 | 7000 | 13 | 2 | 383.0 | 0.0286 | 2.010 | 1.66e-02 | 1.094 | 1.350 | 0.000 | 0.000 | 0.00 | 0.00 | 0.00 | 0.00 | Deshler (2011) |
| 2006 | 7 | 31 | 7500 | 13 | 2 | 345.0 | 0.0180 | 2.510 | 1.70e-03 | 2.080 | 1.170 | 0.000 | 0.000 | 0.00 | 0.00 | 0.00 | 0.00 | Deshler (2011) |
| 2006 | 7 | 31 | 8000 | 13 | 2 | 449.0 | 0.0182 | 2.240 | 6.10e-03 | 1.682 | 1.120 | 0.000 | 0.000 | 0.00 | 0.00 | 0.00 | 0.00 | Deshler (2011) |
| 2006 | 7 | 31 | 8500 | 13 | 2 | 477.0 | 0.0234 | 2.270 | 7.83e-03 | 9.480 | 1.360 | 0.000 | 0.000 | 0.00 | 0.00 | 0.00 | 0.00 | Deshler (2011) |
| 2006 | 7 | 31 | 18500 | 13 | 2 | 27.1 | 0.1466 | 1.470 | 7.11e-01 | 1.242 | 1.810 | 0.000 | 0.000 | 0.00 | 0.00 | 0.00 | 0.00 | Deshler (2011) |
| 2006 | 7 | 31 | 5000 | 13 | 2 | 242.0 | 0.0740 | 1.980 | 1.74e+00 | 1.462 | 1.710 | 0.000 | 0.000 | 0.00 | 0.00 | 0.00 | 0.00 | Deshler (2011)[3] |
| 2006 | 7 | 31 | 6500 | 13 | 2 | 360.0 | 0.0276 | 2.020 | 4.18e-02 | 0.486 | 2.500 | 0.000 | 0.000 | 0.00 | 0.00 | 0.00 | 0.00 | Deshler (2011) |
| 2006 | 7 | 31 | 8000 | 13 | 2 | 411.0 | 0.0272 | 2.020 | 1.24e-02 | 0.942 | 1.560 | 0.000 | 0.000 | 0.00 | 0.00 | 0.00 | 0.00 | Deshler (2011) |
| 2006 | 7 | 31 | 8500 | 13 | 2 | 452.0 | 0.0246 | 2.040 | 9.16e-03 | 1.016 | 1.540 | 0.000 | 0.000 | 0.00 | 0.00 | 0.00 | 0.00 | Deshler (2011) |
| 2006 | 7 | 31 | 10500 | 13 | 2 | 273.0 | 0.1108 | 1.360 | 6.77e-02 | 1.366 | 2.930 | 0.000 | 0.000 | 0.00 | 0.00 | 0.00 | 0.00 | Deshler (2011) |
| 2006 | 7 | 31 | 15000 | 13 | 2 | 625.0 | 0.0562 | 2.150 | 2.31e+00 | 1.336 | 1.220 | 0.000 | 0.000 | 0.00 | 0.00 | 0.00 | 0.00 | Deshler (2011) |
| 2006 | 7 | 31 | 18500 | 13 | 2 | 557.0 | 0.0356 | 1.920 | 2.99e-02 | 0.708 | 1.940 | 0.000 | 0.000 | 0.00 | 0.00 | 0.00 | 0.00 | Deshler (2011) |
| 2006 | 7 | 31 | 19000 | 13 | 2 | 542.0 | 0.0258 | 2.160 | 4.56e-04 | 2.380 | 1.180 | 0.000 | 0.000 | 0.00 | 0.00 | 0.00 | 0.00 | Deshler (2011) |

***Table A.4:*** *Aerosol database.* [1] *051123AU dsc-AU-Darwin-13S132E.SD2,* [2] *060731NI asc-NI-Niamey-13N-2E,SD2,* [3] *060731NI dsc-NI-Niamey-13N-2E.SD2*

| yyyy | mm | dd | hh<br>[m] | lat<br>lat | lon<br>lon | n1<br>[cm-3] | r1<br>[m-6] | s1<br>s1 | n2<br>[cm-3] | r2<br>[m-6] | s2<br>s2 | n3<br>[cm-3] | r3<br>[m-6] | s3<br>s3 | n4<br>[cm-3] | r4<br>[m-6] | s4<br>s4 | reference |
|---|---|---|---|---|---|---|---|---|---|---|---|---|---|---|---|---|---|---|
| 2006 | 8 | 17 | 1000 | 13 | 2 | 395.0 | 0.0804 | 1.890 | 3.73e+00 | 0.980 | 1.830 | 0.000 | 0.000 | 0.00 | 0.00 | 0.00 | 0.00 | Deshler (2011)[1] |
| 2006 | 8 | 17 | 2000 | 13 | 2 | 330.0 | 0.1720 | 1.300 | 4.26e+00 | 0.916 | 1.840 | 0.000 | 0.000 | 0.00 | 0.00 | 0.00 | 0.00 | Deshler (2011) |
| 2006 | 8 | 17 | 2500 | 13 | 2 | 272.0 | 0.0620 | 2.280 | 1.54e+00 | 1.578 | 1.460 | 0.000 | 0.000 | 0.00 | 0.00 | 0.00 | 0.00 | Deshler (2011) |
| 2006 | 8 | 17 | 3000 | 13 | 2 | 255.0 | 0.1716 | 1.300 | 4.11e+00 | 0.922 | 1.840 | 0.000 | 0.000 | 0.00 | 0.00 | 0.00 | 0.00 | Deshler (2011) |
| 2006 | 8 | 17 | 4000 | 13 | 2 | 272.0 | 0.1650 | 1.310 | 3.51e+00 | 0.906 | 1.860 | 0.000 | 0.000 | 0.00 | 0.00 | 0.00 | 0.00 | Deshler (2011) |
| 2006 | 8 | 17 | 4500 | 13 | 2 | 260.0 | 0.0548 | 2.310 | 1.93e+00 | 1.618 | 1.450 | 0.000 | 0.000 | 0.00 | 0.00 | 0.00 | 0.00 | Deshler (2011) |
| 2006 | 8 | 17 | 5000 | 13 | 2 | 245.0 | 0.0316 | 2.390 | 1.79e-01 | 1.516 | 1.420 | 0.000 | 0.000 | 0.00 | 0.00 | 0.00 | 0.00 | Deshler (2011) |
| 2006 | 8 | 17 | 5500 | 13 | 2 | 197.0 | 0.0372 | 2.420 | 4.08e-02 | 1.928 | 1.370 | 0.000 | 0.000 | 0.00 | 0.00 | 0.00 | 0.00 | Deshler (2011) |
| 2006 | 8 | 17 | 6000 | 13 | 2 | 285.0 | 0.0204 | 2.570 | 1.74e-02 | 1.936 | 1.280 | 0.000 | 0.000 | 0.00 | 0.00 | 0.00 | 0.00 | Deshler (2011) |
| 2006 | 8 | 17 | 6500 | 13 | 2 | 364.0 | 0.0176 | 2.550 | 2.43e-03 | 1.808 | 1.360 | 0.000 | 0.000 | 0.00 | 0.00 | 0.00 | 0.00 | Deshler (2011) |
| 2006 | 8 | 17 | 7000 | 13 | 2 | 383.0 | 0.0197 | 2.320 | 1.21e-02 | 1.484 | 1.260 | 0.000 | 0.000 | 0.00 | 0.00 | 0.00 | 0.00 | Deshler (2011) |
| 2006 | 8 | 17 | 7500 | 13 | 2 | 345.0 | 0.0184 | 2.520 | 2.54e-03 | 2.060 | 1.170 | 0.000 | 0.000 | 0.00 | 0.00 | 0.00 | 0.00 | Deshler (2011) |
| 2006 | 8 | 17 | 9000 | 13 | 2 | 483.0 | 0.0294 | 1.960 | 5.57e-02 | 1.458 | 2.410 | 0.000 | 0.000 | 0.00 | 0.00 | 0.00 | 0.00 | Deshler (2011) |
| 2006 | 8 | 17 | 9500 | 13 | 2 | 437.0 | 0.0382 | 1.770 | 2.92e-02 | 0.510 | 2.520 | 0.000 | 0.000 | 0.00 | 0.00 | 0.00 | 0.00 | Deshler (2011) |
| 2006 | 8 | 17 | 10500 | 13 | 2 | 89.8 | 0.0224 | 2.230 | 4.83e-03 | 1.622 | 1.240 | 0.000 | 0.000 | 0.00 | 0.00 | 0.00 | 0.00 | Deshler (2011) |
| 2006 | 8 | 17 | 11000 | 13 | 2 | 53.2 | 0.0242 | 2.340 | 9.52e-03 | 1.734 | 1.210 | 0.000 | 0.000 | 0.00 | 0.00 | 0.00 | 0.00 | Deshler (2011) |
| 2006 | 8 | 17 | 12500 | 13 | 2 | 52.5 | 0.0308 | 2.430 | 3.47e-04 | 2.040 | 1.080 | 0.000 | 0.000 | 0.00 | 0.00 | 0.00 | 0.00 | Deshler (2011) |
| 2006 | 8 | 17 | 13000 | 13 | 2 | 59.9 | 0.0153 | 2.970 | 0.00e+00 | 0.000 | 0.000 | 0.000 | 0.000 | 0.00 | 0.00 | 0.00 | 0.00 | Deshler (2011) |
| 2006 | 8 | 17 | 13500 | 13 | 2 | 51.7 | 0.0202 | 2.570 | 1.78e-03 | 1.360 | 1.150 | 0.000 | 0.000 | 0.00 | 0.00 | 0.00 | 0.00 | Deshler (2011) |
| 2006 | 8 | 17 | 14500 | 13 | 2 | 586.0 | 0.0183 | 2.180 | 4.46e-03 | 1.538 | 1.400 | 0.000 | 0.000 | 0.00 | 0.00 | 0.00 | 0.00 | Deshler (2011) |
| 2006 | 8 | 17 | 15000 | 13 | 2 | 438.0 | 0.0192 | 2.360 | 1.14e-03 | 2.300 | 1.140 | 0.000 | 0.000 | 0.00 | 0.00 | 0.00 | 0.00 | Deshler (2011) |
| 2006 | 8 | 17 | 15500 | 13 | 2 | 386.0 | 0.0196 | 2.280 | 7.40e-03 | 1.436 | 1.280 | 0.000 | 0.000 | 0.00 | 0.00 | 0.00 | 0.00 | Deshler (2011) |
| 2006 | 8 | 17 | 16500 | 13 | 2 | 276.0 | 0.0194 | 2.510 | 3.15e-04 | 2.160 | 1.190 | 0.000 | 0.000 | 0.00 | 0.00 | 0.00 | 0.00 | Deshler (2011) |
| 2006 | 8 | 17 | 3500 | 13 | 2 | 272.0 | 0.1656 | 1.300 | 3.30e+00 | 0.820 | 1.850 | 0.000 | 0.000 | 0.00 | 0.00 | 0.00 | 0.00 | Deshler (2011)[2] |
| 2006 | 8 | 17 | 4500 | 13 | 2 | 261.0 | 0.0320 | 2.240 | 1.23e+00 | 1.548 | 1.480 | 0.000 | 0.000 | 0.00 | 0.00 | 0.00 | 0.00 | Deshler (2011) |
| 2006 | 8 | 17 | 5000 | 13 | 2 | 244.0 | 0.1508 | 1.320 | 1.02e+00 | 0.788 | 1.970 | 0.000 | 0.000 | 0.00 | 0.00 | 0.00 | 0.00 | Deshler (2011) |
| 2006 | 8 | 17 | 5500 | 13 | 2 | 197.0 | 0.0334 | 2.450 | 5.29e-02 | 1.930 | 1.370 | 0.000 | 0.000 | 0.00 | 0.00 | 0.00 | 0.00 | Deshler (2011) |
| 2006 | 8 | 17 | 6000 | 13 | 2 | 285.0 | 0.0320 | 2.060 | 8.21e-02 | 0.594 | 2.300 | 0.000 | 0.000 | 0.00 | 0.00 | 0.00 | 0.00 | Deshler (2011) |
| 2006 | 8 | 17 | 6500 | 13 | 2 | 364.0 | 0.0248 | 2.510 | 4.15e-03 | 2.900 | 1.290 | 0.000 | 0.000 | 0.00 | 0.00 | 0.00 | 0.00 | Deshler (2011) |
| 2006 | 8 | 17 | 8000 | 13 | 2 | 449.0 | 0.0486 | 1.860 | 3.34e-02 | 0.834 | 2.210 | 0.000 | 0.000 | 0.00 | 0.00 | 0.00 | 0.00 | Deshler (2011) |
| 2006 | 8 | 17 | 8500 | 13 | 2 | 477.0 | 0.0244 | 2.320 | 4.92e-02 | 0.762 | 2.220 | 0.000 | 0.000 | 0.00 | 0.00 | 0.00 | 0.00 | Deshler (2011) |
| 2006 | 8 | 17 | 9000 | 13 | 2 | 483.0 | 0.0146 | 2.220 | 5.85e-02 | 1.370 | 1.910 | 0.000 | 0.000 | 0.00 | 0.00 | 0.00 | 0.00 | Deshler (2011) |
| 2006 | 8 | 17 | 10500 | 13 | 2 | 89.8 | 0.0662 | 1.860 | 3.95e-03 | 4.560 | 1.130 | 0.000 | 0.000 | 0.00 | 0.00 | 0.00 | 0.00 | Deshler (2011) |
| 2006 | 8 | 17 | 11000 | 13 | 2 | 53.2 | 0.0410 | 2.180 | 3.23e-02 | 1.412 | 1.940 | 0.000 | 0.000 | 0.00 | 0.00 | 0.00 | 0.00 | Deshler (2011) |
| 2006 | 8 | 17 | 11500 | 13 | 2 | 43.5 | 0.0422 | 2.290 | 5.95e-02 | 2.060 | 1.730 | 0.000 | 0.000 | 0.00 | 0.00 | 0.00 | 0.00 | Deshler (2011) |
| 2006 | 8 | 17 | 12000 | 13 | 2 | 42.8 | 0.0654 | 1.940 | 4.99e-02 | 3.300 | 1.550 | 0.000 | 0.000 | 0.00 | 0.00 | 0.00 | 0.00 | Deshler (2011) |
| 2006 | 8 | 17 | 12500 | 13 | 2 | 52.4 | 0.0418 | 2.240 | 1.14e-01 | 2.120 | 1.690 | 0.000 | 0.000 | 0.00 | 0.00 | 0.00 | 0.00 | Deshler (2011) |
| 2006 | 8 | 17 | 13000 | 13 | 2 | 59.8 | 0.0600 | 1.920 | 6.53e-02 | 4.240 | 1.450 | 0.000 | 0.000 | 0.00 | 0.00 | 0.00 | 0.00 | Deshler (2011) |
| 2006 | 8 | 17 | 14500 | 13 | 2 | 586.0 | 0.0652 | 1.580 | 1.83e-01 | 1.784 | 1.360 | 0.000 | 0.000 | 0.00 | 0.00 | 0.00 | 0.00 | Deshler (2011) |
| 2006 | 8 | 17 | 15000 | 13 | 2 | 430.0 | 0.1158 | 1.490 | 7.99e+00 | 1.888 | 1.380 | 0.000 | 0.000 | 0.00 | 0.00 | 0.00 | 0.00 | Deshler (2011) |
| 2006 | 8 | 17 | 15500 | 13 | 2 | 384.0 | 0.0890 | 1.600 | 1.75e+00 | 2.060 | 1.290 | 0.000 | 0.000 | 0.00 | 0.00 | 0.00 | 0.00 | Deshler (2011) |
| 2006 | 8 | 17 | 16000 | 13 | 2 | 354.0 | 0.0868 | 1.540 | 5.54e-01 | 1.780 | 1.340 | 0.000 | 0.000 | 0.00 | 0.00 | 0.00 | 0.00 | Deshler (2011) |

***Table A.5:*** *Aerosol database.* [1]*060817NI asc-NI-Niamey-13N-2E.SD2,* [2]*060817NI dsc-NI-Niamey-13N-2E.SD2*

| yyyy | mm | dd | hh [m] | lat lat | lon lon | n1 [cm-3] | r1 [m-6] | s1 s1 | n2 [cm-3] | r2 [m-6] | s2 s2 | n3 [cm-3] | r3 [m-6] | s3 s3 | n4 [cm-3] | r4 [m-6] | s4 s4 | reference |
|---|---|---|---|---|---|---|---|---|---|---|---|---|---|---|---|---|---|---|
| 2008 | 9 | 9 | 1000 | 13 | 2 | 355.0 | 0.0590 | 2.210 | 3.06e+00 | 1.708 | 1.640 | 0.000 | 0.000 | 0.00 | 0.00 | 0.00 | 0.00 | Deshler (2011)[1] |
| 2008 | 9 | 9 | 1500 | 13 | 2 | 343.0 | 0.1296 | 1.480 | 6.11e+00 | 1.954 | 1.580 | 0.000 | 0.000 | 0.00 | 0.00 | 0.00 | 0.00 | Deshler (2011) |
| 2008 | 9 | 9 | 2000 | 13 | 2 | 324.0 | 0.1252 | 1.470 | 7.68e+00 | 1.320 | 1.690 | 0.000 | 0.000 | 0.00 | 0.00 | 0.00 | 0.00 | Deshler (2011) |
| 2008 | 9 | 9 | 2500 | 13 | 2 | 321.0 | 0.1360 | 1.470 | 5.28e+00 | 1.890 | 1.590 | 0.000 | 0.000 | 0.00 | 0.00 | 0.00 | 0.00 | Deshler (2011) |
| 2008 | 9 | 9 | 3000 | 13 | 2 | 319.0 | 0.1360 | 1.470 | 5.72e+00 | 1.948 | 1.580 | 0.000 | 0.000 | 0.00 | 0.00 | 0.00 | 0.00 | Deshler (2011) |
| 2008 | 9 | 9 | 3500 | 13 | 2 | 329.0 | 0.0694 | 2.080 | 2.95e+00 | 1.224 | 1.760 | 0.000 | 0.000 | 0.00 | 0.00 | 0.00 | 0.00 | Deshler (2011) |
| 2008 | 9 | 9 | 6000 | 13 | 2 | 368.0 | 0.0286 | 2.230 | 7.55e-02 | 1.710 | 1.290 | 0.000 | 0.000 | 0.00 | 0.00 | 0.00 | 0.00 | Deshler (2011) |
| 2008 | 9 | 9 | 7500 | 13 | 2 | 519.0 | 0.0150 | 2.570 | 2.19e-03 | 2.280 | 1.140 | 0.000 | 0.000 | 0.00 | 0.00 | 0.00 | 0.00 | Deshler (2011) |
| 2008 | 9 | 9 | 8500 | 13 | 2 | 487.0 | 0.0158 | 2.570 | 1.93e-03 | 2.160 | 1.160 | 0.000 | 0.000 | 0.00 | 0.00 | 0.00 | 0.00 | Deshler (2011) |
| 2008 | 9 | 9 | 9500 | 13 | 2 | 517.0 | 0.0160 | 2.570 | 1.13e-03 | 2.020 | 1.070 | 0.000 | 0.000 | 0.00 | 0.00 | 0.00 | 0.00 | Deshler (2011) |
| 2008 | 9 | 9 | 10000 | 13 | 2 | 535.0 | 0.0564 | 1.590 | 6.76e-02 | 0.662 | 1.620 | 0.000 | 0.000 | 0.00 | 0.00 | 0.00 | 0.00 | Deshler (2011) |
| 2008 | 9 | 9 | 11000 | 13 | 2 | 586.0 | 0.0408 | 1.760 | 4.34e-02 | 0.898 | 1.400 | 0.000 | 0.000 | 0.00 | 0.00 | 0.00 | 0.00 | Deshler (2011) |
| 2008 | 9 | 9 | 11500 | 13 | 2 | 619.0 | 0.0400 | 1.760 | 4.08e-02 | 0.930 | 1.390 | 0.000 | 0.000 | 0.00 | 0.00 | 0.00 | 0.00 | Deshler (2011) |
| 2008 | 9 | 9 | 12500 | 13 | 2 | 653.0 | 0.0304 | 1.890 | 1.87e-02 | 0.852 | 1.440 | 0.000 | 0.000 | 0.00 | 0.00 | 0.00 | 0.00 | Deshler (2011) |
| 2008 | 9 | 9 | 13000 | 13 | 2 | 665.0 | 0.0130 | 2.620 | 6.00e-04 | 2.140 | 1.060 | 0.000 | 0.000 | 0.00 | 0.00 | 0.00 | 0.00 | Deshler (2011) |
| 2008 | 9 | 9 | 13500 | 13 | 2 | 669.0 | 0.0584 | 1.580 | 8.14e-02 | 0.658 | 1.490 | 0.000 | 0.000 | 0.00 | 0.00 | 0.00 | 0.00 | Deshler (2011) |
| 2008 | 9 | 9 | 14000 | 13 | 2 | 642.0 | 0.0350 | 1.860 | 3.70e-02 | 0.960 | 1.270 | 0.000 | 0.000 | 0.00 | 0.00 | 0.00 | 0.00 | Deshler (2011)[2] |
| 2008 | 9 | 9 | 5500 | 13 | 2 | 214.0 | 0.0780 | 2.090 | 1.39e+00 | 1.136 | 1.810 | 0.000 | 0.000 | 0.00 | 0.00 | 0.00 | 0.00 | Deshler (2011) |
| 2008 | 9 | 9 | 6000 | 13 | 2 | 335.0 | 0.0704 | 1.740 | 6.10e-01 | 0.714 | 2.050 | 0.000 | 0.000 | 0.00 | 0.00 | 0.00 | 0.00 | Deshler (2011) |
| 2008 | 9 | 9 | 8000 | 13 | 2 | 534.0 | 0.0131 | 2.680 | 2.10e-03 | 2.960 | 1.300 | 0.000 | 0.000 | 0.00 | 0.00 | 0.00 | 0.00 | Deshler (2011) |
| 2008 | 9 | 9 | 8500 | 13 | 2 | 547.0 | 0.0108 | 2.660 | 4.96e-03 | 1.832 | 1.730 | 0.000 | 0.000 | 0.00 | 0.00 | 0.00 | 0.00 | Deshler (2011) |
| 2008 | 9 | 9 | 9000 | 13 | 2 | 503.0 | 0.0177 | 2.500 | 2.50e-03 | 1.824 | 1.750 | 0.000 | 0.000 | 0.00 | 0.00 | 0.00 | 0.00 | Deshler (2011) |
| 2008 | 9 | 9 | 9500 | 13 | 2 | 532.0 | 0.0346 | 1.870 | 4.05e-02 | 0.886 | 1.820 | 0.000 | 0.000 | 0.00 | 0.00 | 0.00 | 0.00 | Deshler (2011) |
| 2008 | 9 | 9 | 10000 | 13 | 2 | 541.0 | 0.0138 | 2.670 | 9.08e-04 | 6.560 | 1.150 | 0.000 | 0.000 | 0.00 | 0.00 | 0.00 | 0.00 | Deshler (2011) |
| 2008 | 9 | 9 | 10500 | 13 | 2 | 581.0 | 0.0153 | 2.630 | 2.20e-03 | 5.440 | 1.200 | 0.000 | 0.000 | 0.00 | 0.00 | 0.00 | 0.00 | Deshler (2011) |
| 2008 | 9 | 9 | 11000 | 13 | 2 | 589.0 | 0.0386 | 1.770 | 8.46e-02 | 0.578 | 2.310 | 0.000 | 0.000 | 0.00 | 0.00 | 0.00 | 0.00 | Deshler (2011) |
| 2008 | 9 | 9 | 11500 | 13 | 2 | 606.0 | 0.0140 | 2.660 | 9.20e-04 | 6.180 | 1.170 | 0.000 | 0.000 | 0.00 | 0.00 | 0.00 | 0.00 | Deshler (2011) |
| 2008 | 9 | 9 | 12000 | 13 | 2 | 608.0 | 0.0117 | 2.720 | 9.92e-04 | 4.920 | 1.120 | 0.000 | 0.000 | 0.00 | 0.00 | 0.00 | 0.00 | Deshler (2011) |
| 2008 | 9 | 9 | 12500 | 13 | 2 | 628.0 | 0.0266 | 1.970 | 4.86e-03 | 1.706 | 2.060 | 0.000 | 0.000 | 0.00 | 0.00 | 0.00 | 0.00 | Deshler (2011) |
| 2008 | 9 | 9 | 13000 | 13 | 2 | 636.0 | 0.0198 | 2.370 | 2.51e-03 | 2.300 | 1.590 | 0.000 | 0.000 | 0.00 | 0.00 | 0.00 | 0.00 | Deshler (2011) |
| 2008 | 9 | 9 | 13500 | 13 | 2 | 637.0 | 0.0171 | 2.610 | 1.74e-03 | 5.900 | 1.180 | 0.000 | 0.000 | 0.00 | 0.00 | 0.00 | 0.00 | Deshler (2011) |
| 2008 | 9 | 9 | 14000 | 13 | 2 | 650.0 | 0.0350 | 2.030 | 2.37e-01 | 0.948 | 1.570 | 0.000 | 0.000 | 0.00 | 0.00 | 0.00 | 0.00 | Deshler (2011) |

***Table A.6:*** *Aerosol database.* [1]*080909NI asc-NI-Niamey.13N-2E.SD2,* [2]*080909NI dsc-NI-Niamey.13N-2E.SD2*

# Appendix B

# Model Comparison Spectra

In this appendix the spectra and mean difference tables for the clear air comparison in Section 5.1 and the spectra for the cloudy air comparison in Section 5.2.2 are given.

## B.1 Clear Air Comparison

### B.1.1 JURASSIC – RFM

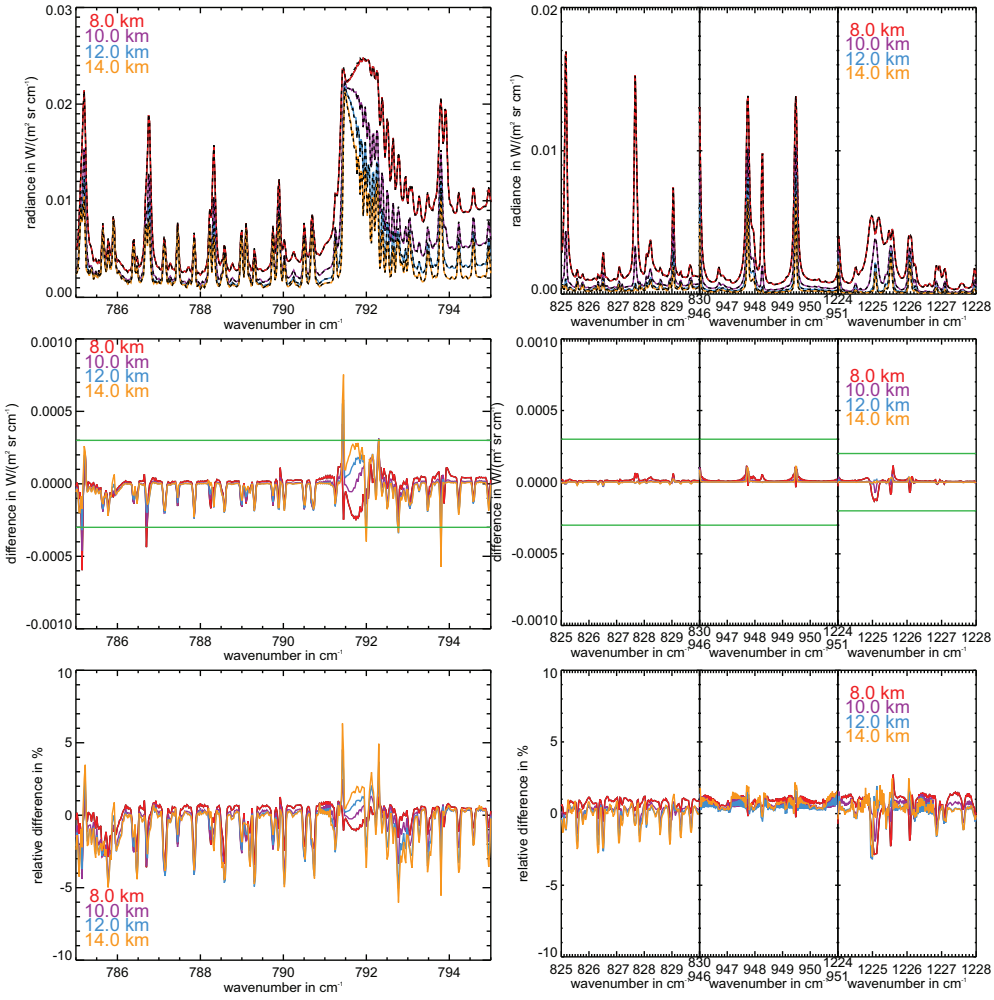


***Figure B.1:*** *Clear air limb spectra of JURASSIC (coloured solid lines) and RFM (black dashed lines) for the polar winter atmosphere for four tangent heights and the absolute and relative differences between both models (JURASSIC−RFM).*

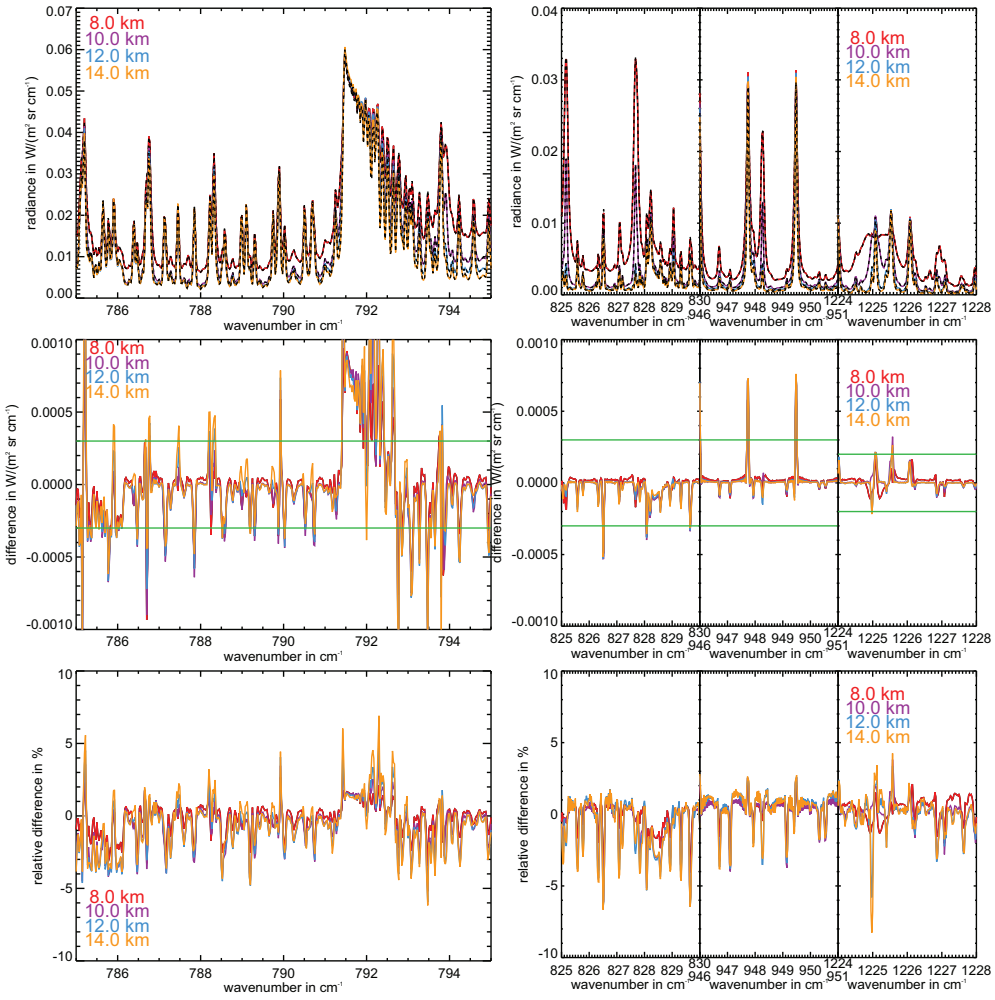


***Figure B.2:*** *Clear air limb spectra of JURASSIC (coloured solid lines) and RFM (black dashed lines) for the polar summer atmosphere for four tangent heights and the absolute and relative differences between both models (JURASSIC−RFM).*

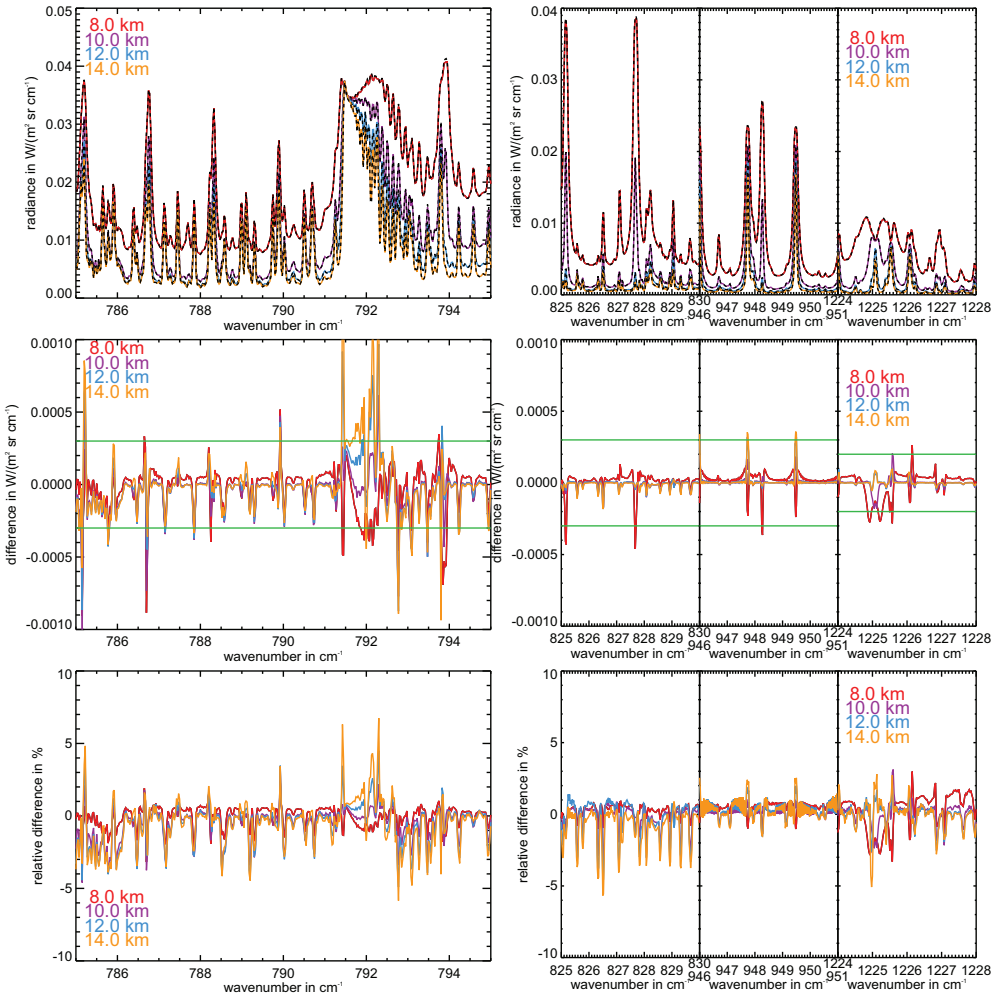


***Figure B.3:*** *Clear air limb spectra of JURASSIC (coloured solid lines) and RFM (black dashed lines) for the mid-latitude night atmosphere for four tangent heights and the absolute and relative differences between both models (JURASSIC−RFM).*

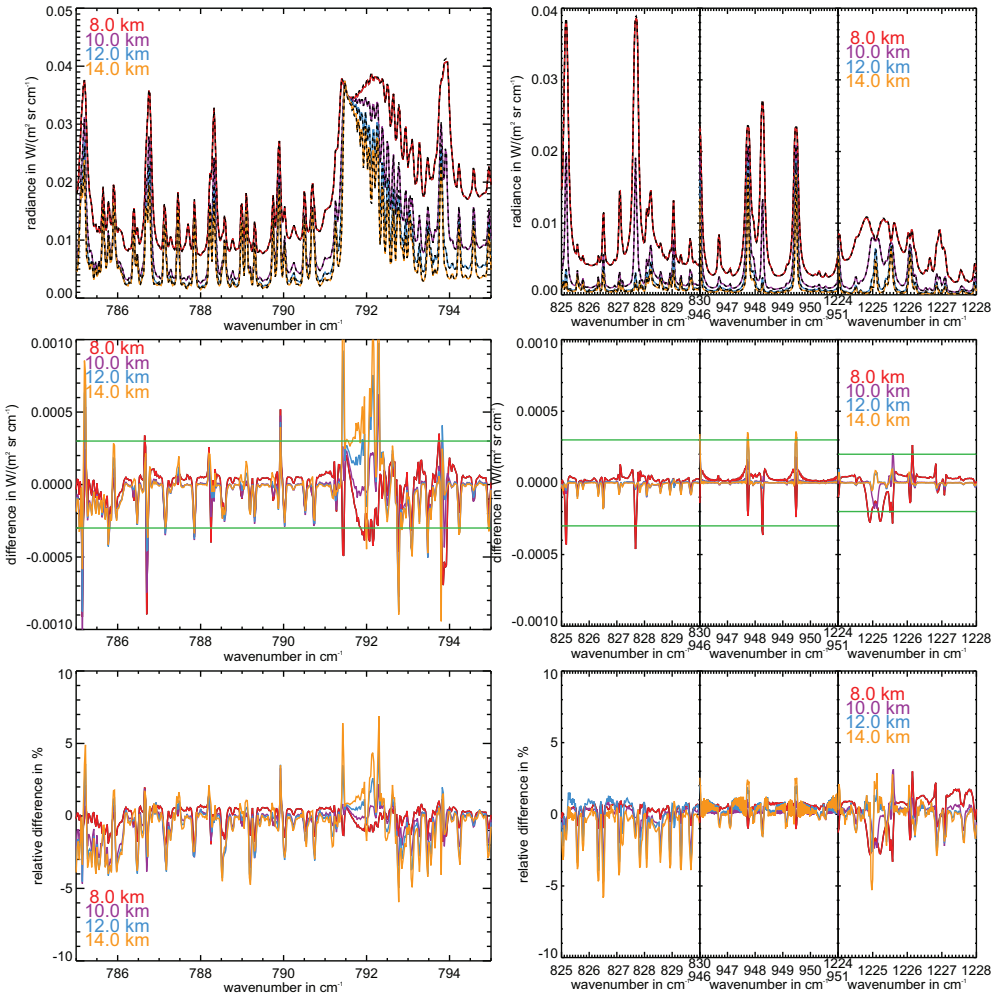


***Figure B.4:*** *Clear air limb spectra of JURASSIC (coloured solid lines) and RFM (black dashed lines) for the mid-latitude day atmosphere for four tangent heights and the absolute and relative differences between both models (JURASSIC−RFM).*

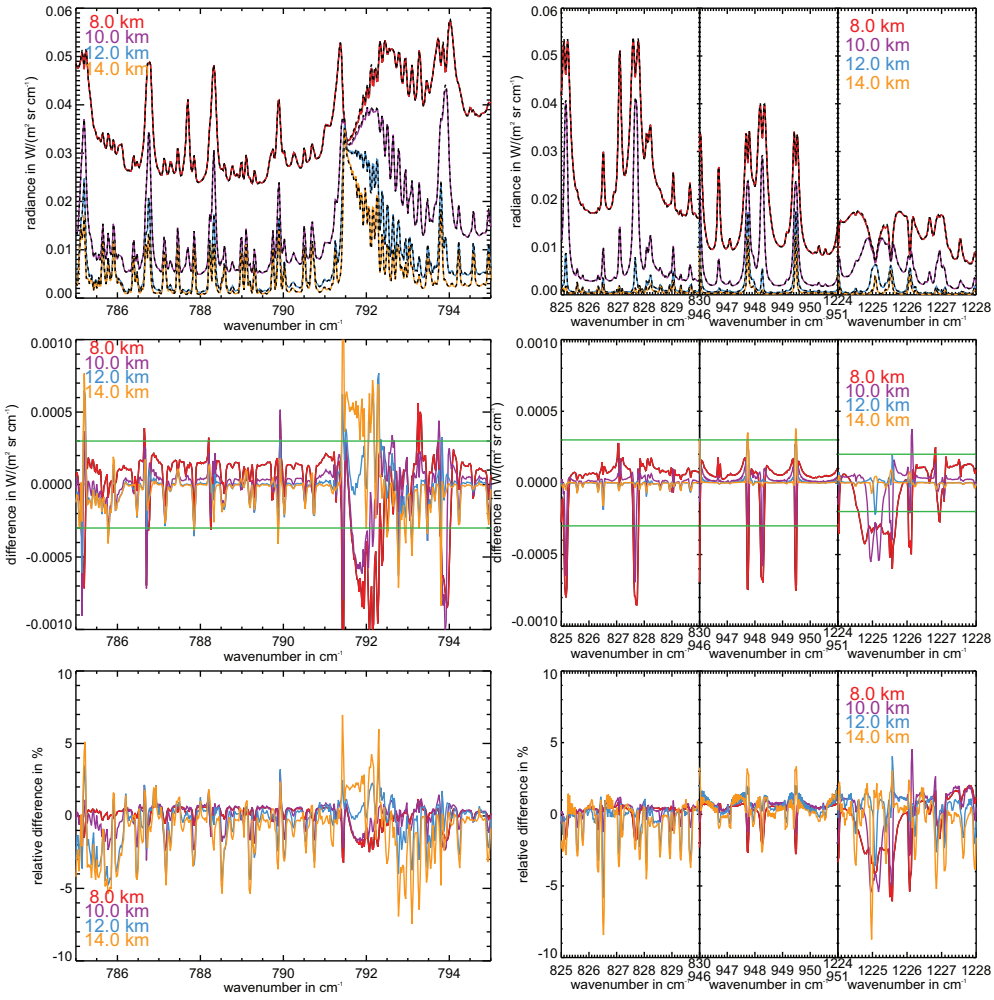


***Figure B.5:*** *Clear air limb spectra of JURASSIC (coloured solid lines) and RFM (black dashed lines) for the equatorial atmosphere for four tangent heights and the absolute and relative differences between both models (JURASSIC−RFM).*

| tangent | 785 – 795 | | | 825 – 830 | | | 946 – 951 | | | 1224 – 1228 | | |
|---|---|---|---|---|---|---|---|---|---|---|---|---|
| height | mean | $\sigma$ | % | mean | $\sigma$ | % | mean | $\sigma$ | % | mean | $\sigma$ | % |
| 8.0 | -1.8e-05 | 8.6e-05 | -0.21 | 1.2e-05 | 1.0e-05 | 0.53 | 1.6e-05 | 1.7e-05 | 0.70 | 2.1e-06 | 3.3e-05 | 0.11 |
| 10.0 | -2.6e-05 | 8.2e-05 | -0.46 | 4.4e-07 | 6.0e-06 | 0.05 | 8.4e-06 | 1.9e-05 | 0.77 | 1.5e-06 | 1.1e-05 | 0.19 |
| 12.0 | -2.6e-05 | 9.5e-05 | -0.58 | -9.5e-07 | 5.2e-06 | -0.18 | 5.3e-06 | 1.7e-05 | 0.80 | 1.5e-06 | 6.3e-06 | 0.39 |
| 14.0 | -1.9e-05 | 1.1e-04 | -0.50 | -1.2e-06 | 5.3e-06 | -0.30 | 5.3e-06 | 1.7e-05 | 1.18 | 1.4e-06 | 6.3e-06 | 0.53 |

***Table B.1:*** *Mean error, standard deviation and relative mean error between JURASSIC and RFM limb calculation for clear air polar winter atmosphere in the four micro-windows.*

| tangent | 785 – 795 | | | 825 – 830 | | | 946 – 951 | | | 1224 – 1228 | | |
|---|---|---|---|---|---|---|---|---|---|---|---|---|
| height | mean | $\sigma$ | % | mean | $\sigma$ | % | mean | $\sigma$ | % | mean | $\sigma$ | % |
| 8.0 | 9.8e-07 | 2.8e-04 | 0.01 | -2.8e-05 | 8.5e-05 | -0.38 | 3.5e-05 | 1.0e-04 | 0.61 | 1.2e-05 | 4.7e-05 | 0.24 |
| 10.0 | -2.0e-05 | 3.5e-04 | -0.13 | -4.4e-05 | 8.4e-05 | -1.35 | 2.7e-05 | 1.2e-04 | 0.78 | 1.4e-05 | 5.5e-05 | 0.50 |
| 12.0 | -5.1e-06 | 3.8e-04 | -0.04 | -4.2e-05 | 8.2e-05 | -1.95 | 2.7e-05 | 1.3e-04 | 0.98 | 6.3e-06 | 5.3e-05 | 0.35 |
| 14.0 | 2.5e-05 | 4.2e-04 | 0.19 | -4.1e-05 | 7.9e-05 | -2.11 | 2.5e-05 | 1.2e-04 | 1.10 | 6.5e-06 | 5.1e-05 | 0.45 |

***Table B.2:*** *Mean error, standard deviation and relative mean error between JURASSIC and RFM limb calculation for clear air polar summer atmosphere in the four micro-windows.*

| tangent | 785 – 795 | | | 825 – 830 | | | 946 – 951 | | | 1224 – 1228 | | |
|---|---|---|---|---|---|---|---|---|---|---|---|---|
| height | mean | $\sigma$ | % | mean | $\sigma$ | % | mean | $\sigma$ | % | mean | $\sigma$ | % |
| 8.0 | -3.1e-05 | 1.6e-04 | -0.16 | 5.7e-06 | 7.3e-05 | 0.06 | 2.3e-05 | 5.8e-05 | 0.34 | -1.1e-05 | 9.5e-05 | -0.18 |
| 10.0 | -4.7e-05 | 1.5e-04 | -0.38 | -1.2e-05 | 2.9e-05 | -0.43 | 1.1e-05 | 3.3e-05 | 0.37 | -4.2e-06 | 4.2e-05 | -0.16 |
| 12.0 | -2.5e-05 | 1.9e-04 | -0.26 | -1.2e-05 | 2.9e-05 | -0.83 | 1.4e-05 | 5.5e-05 | 0.77 | 2.0e-06 | 2.0e-05 | 0.16 |
| 14.0 | -6.9e-06 | 2.4e-04 | -0.08 | -1.6e-05 | 2.9e-05 | -1.45 | 1.4e-05 | 6.1e-05 | 1.08 | 2.7e-06 | 2.1e-05 | 0.31 |

***Table B.3:*** *Mean error, standard deviation and relative mean error between JURASSIC and RFM limb calculation for clear air mid-latitude night atmosphere in the four micro-windows.*

| tangent | 785 – 795 | | | 825 – 830 | | | 946 – 951 | | | 1224 – 1228 | | |
|---|---|---|---|---|---|---|---|---|---|---|---|---|
| height | mean | $\sigma$ | % | mean | $\sigma$ | % | mean | $\sigma$ | % | mean | $\sigma$ | % |
| 8.0 | -3.1e-05 | 1.6e-04 | -0.16 | 5.7e-06 | 7.3e-05 | 0.06 | 2.3e-05 | 5.8e-05 | 0.34 | -1.1e-05 | 9.5e-05 | -0.18 |
| 10.0 | -4.7e-05 | 1.5e-04 | -0.39 | -1.2e-05 | 2.9e-05 | -0.44 | 1.1e-05 | 3.3e-05 | 0.37 | -4.2e-06 | 4.2e-05 | -0.16 |
| 12.0 | -2.6e-05 | 1.9e-04 | -0.27 | -1.1e-05 | 2.9e-05 | -0.87 | 1.4e-05 | 5.5e-05 | 0.78 | 2.0e-06 | 2.0e-05 | 0.16 |
| 14.0 | -6.9e-06 | 2.4e-04 | -0.08 | -1.6e-05 | 2.9e-05 | -1.55 | 1.4e-05 | 6.1e-05 | 1.09 | 2.7e-06 | 2.2e-05 | 0.33 |

***Table B.4:*** *Mean error, standard deviation and relative mean error between JURASSIC and RFM limb calculation for clear air mid-latitude day atmosphere in the four micro-windows.*

| tangent | 785 – 795 | | | 825 – 830 | | | 946 – 951 | | | 1224 – 1228 | | |
|---|---|---|---|---|---|---|---|---|---|---|---|---|
| height | mean | $\sigma$ | % | mean | $\sigma$ | % | mean | $\sigma$ | % | mean | $\sigma$ | % |
| 8.0 | -6.7e-06 | 2.8e-04 | -0.02 | 1.9e-05 | 2.1e-04 | 0.07 | 1.9e-05 | 1.8e-04 | 0.12 | -8.3e-05 | 2.1e-04 | -0.65 |
| 10.0 | -2.7e-05 | 2.0e-04 | -0.17 | -4.2e-06 | 1.0e-04 | -0.06 | 1.8e-05 | 7.8e-05 | 0.33 | -2.8e-05 | 1.6e-04 | -0.48 |
| 12.0 | -1.0e-05 | 1.6e-04 | -0.13 | -9.7e-06 | 2.5e-05 | -0.69 | 2.0e-05 | 5.4e-05 | 1.09 | 1.6e-06 | 3.6e-05 | 0.11 |
| 14.0 | -9.8e-06 | 2.1e-04 | -0.17 | -1.1e-05 | 2.3e-05 | -1.51 | 1.2e-05 | 5.7e-05 | 1.44 | 6.3e-07 | 2.1e-05 | 0.11 |

***Table B.5:*** *Mean error, standard deviation and relative mean error between JURASSIC and RFM limb calculation for clear air equatorial atmosphere in the four micro-windows.*

| atm | 785 – 795 | | | 825 – 830 | | | 946 – 951 | | | 1224 – 1228 | | |
|---|---|---|---|---|---|---|---|---|---|---|---|---|
| height | mean | $\sigma$ | % | mean | $\sigma$ | % | mean | $\sigma$ | % | mean | $\sigma$ | % |
| pwin | 3.5e-06 | 6.5e-06 | 0.01 | 3.5e-06 | 3.8e-06 | 0.01 | 2.2e-06 | 3.4e-06 | 0.00 | -8.1e-06 | 2.8e-05 | -0.04 |
| psum | 7.5e-06 | 1.1e-05 | 0.01 | 6.8e-06 | 1.2e-05 | 0.01 | 4.4e-06 | 9.0e-06 | 0.01 | -8.2e-06 | 3.1e-05 | -0.04 |
| midln | 2.9e-05 | 6.4e-05 | 0.03 | 2.5e-05 | 8.3e-05 | 0.02 | 2.3e-05 | 6.4e-05 | 0.03 | -3.8e-05 | 8.8e-05 | -0.10 |
| midld | 2.9e-05 | 6.4e-05 | 0.03 | 2.5e-05 | 8.3e-05 | 0.02 | 2.3e-05 | 6.4e-05 | 0.03 | -3.8e-05 | 8.8e-05 | -0.10 |
| equ | -3.2e-05 | 7.2e-05 | -0.03 | -7.3e-06 | 1.4e-04 | -0.01 | 5.6e-05 | 9.2e-05 | 0.06 | -4.2e-05 | 1.2e-04 | -0.10 |

***Table B.6:*** *Mean error, standard deviation and relative mean error between JURASSIC and RFM nadir calculation for clear air in all atmospheres in the four micro-windows.*

### B.1.2 RFM – KOPRA

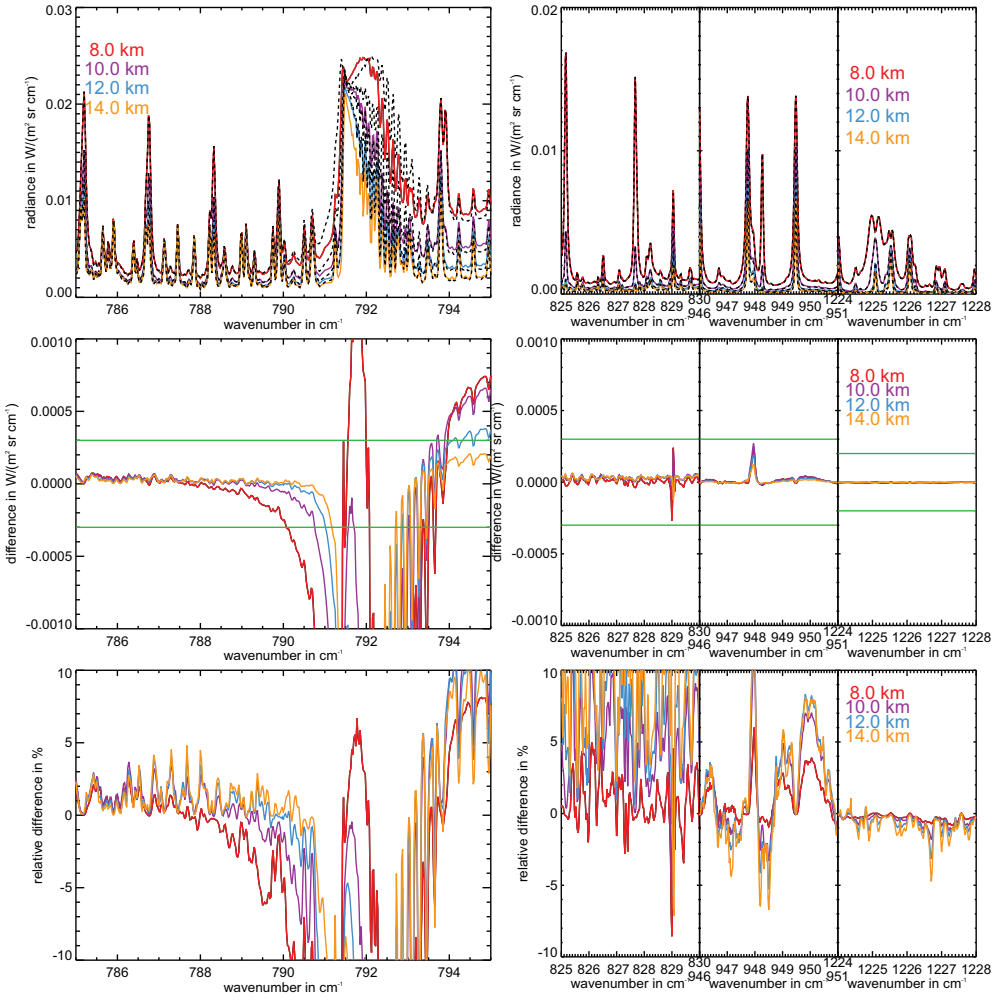


***Figure B.6:*** *Clear air limb spectra of RFM (coloured solid lines) and KOPRA (black dashed lines) for the polar winter atmosphere for four tangent heights and the absolute and relative differences between both models (RFM−KOPRA).*

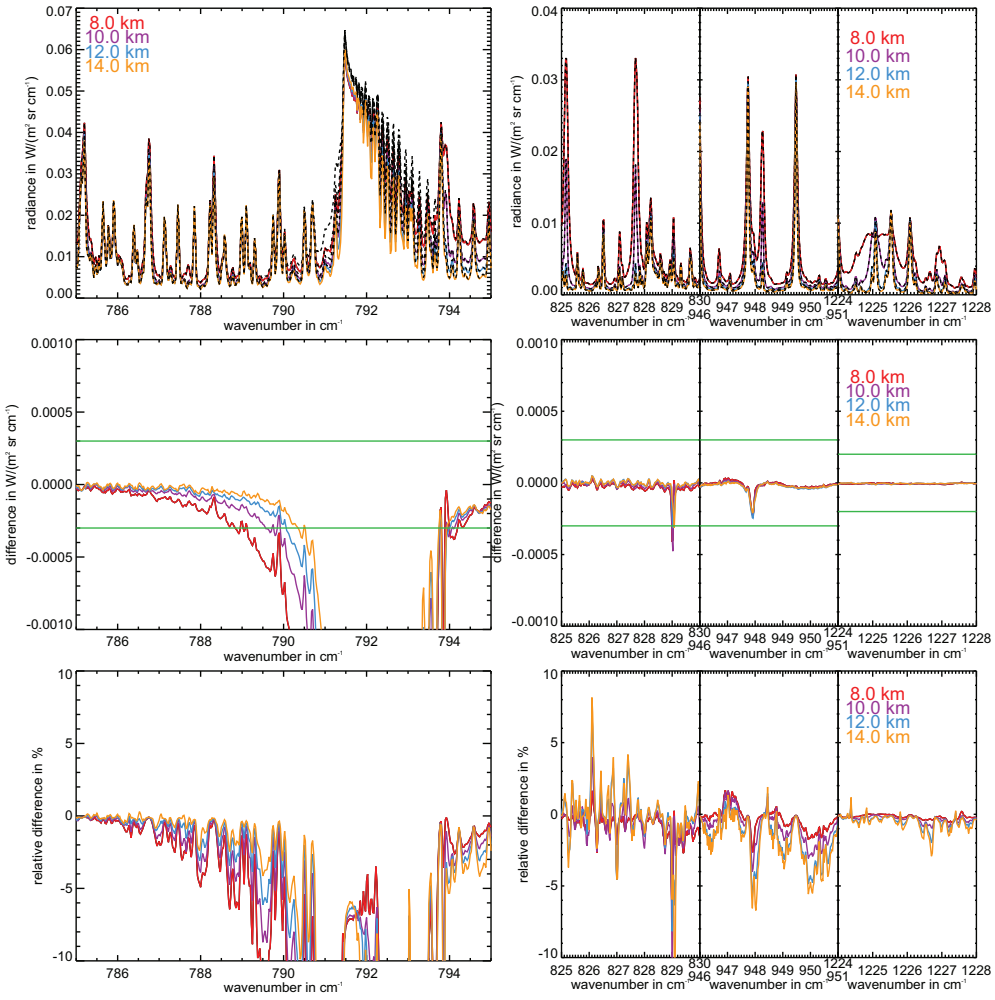


***Figure B.7:*** *Clear air limb spectra of RFM (coloured solid lines) and KOPRA (black dashed lines) for the polar summer atmosphere for four tangent heights and the absolute and relative differences between both models (RFM−KOPRA).*

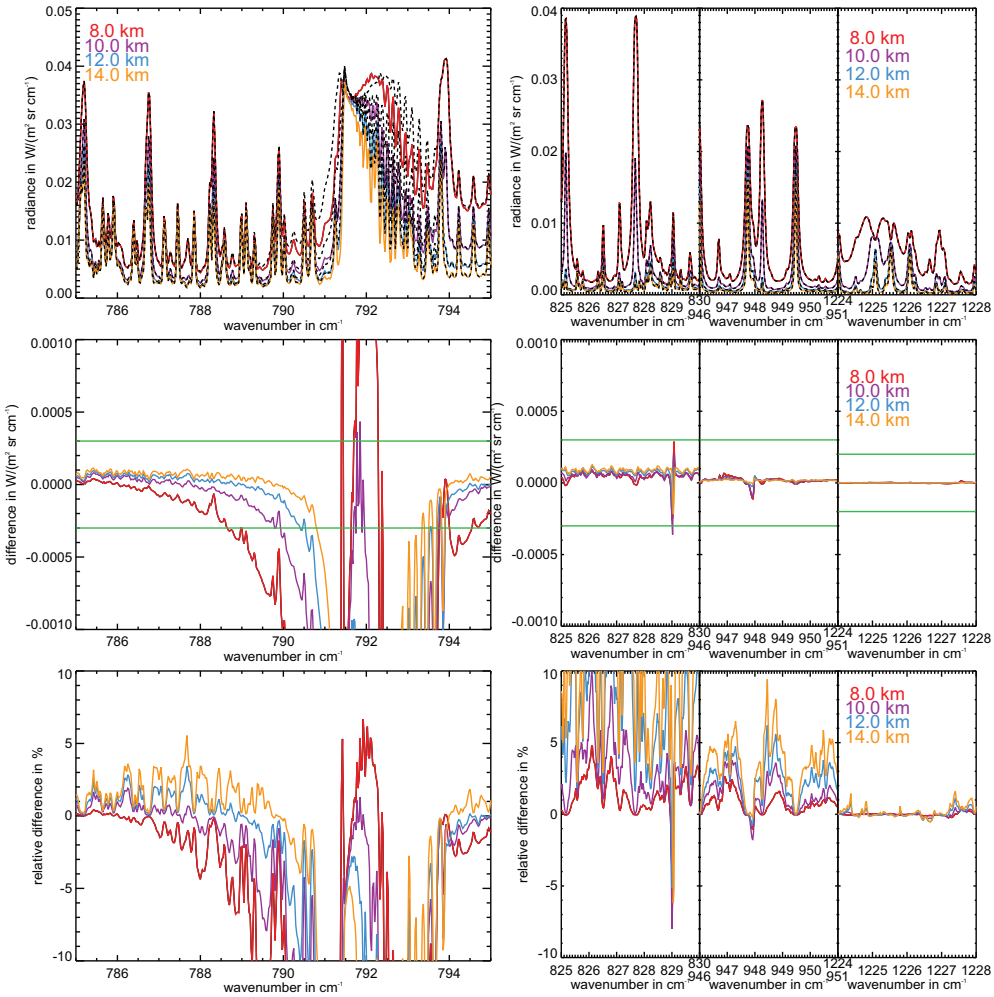


***Figure B.8:*** *Clear air limb spectra of RFM (coloured solid lines) and KOPRA (black dashed lines) for the mid-latitude night atmosphere for four tangent heights and the absolute and relative differences between both models (RFM−KOPRA).*

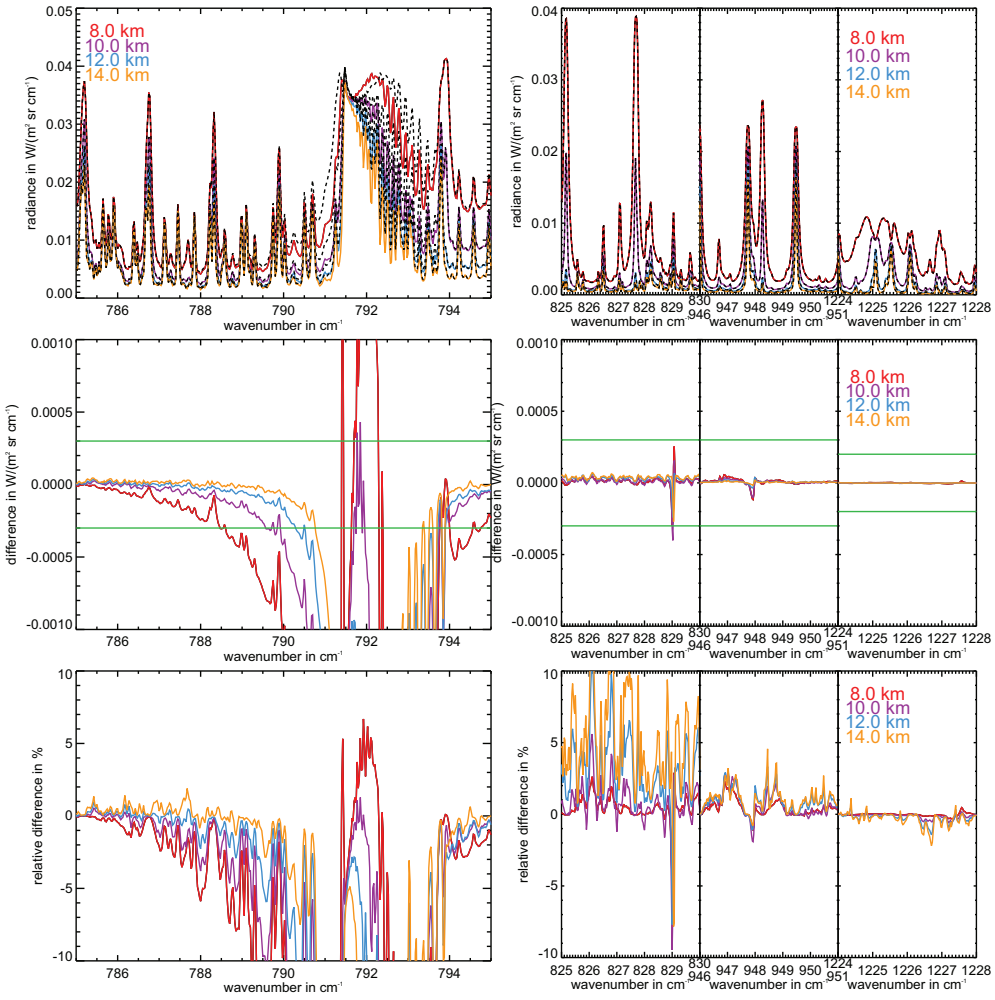


***Figure B.9:*** *Clear air limb spectra of RFM (coloured solid lines) and KOPRA (black dashed lines) for the mid-latitude day atmosphere for four tangent heights and the absolute and relative differences between both models (RFM−KOPRA).*

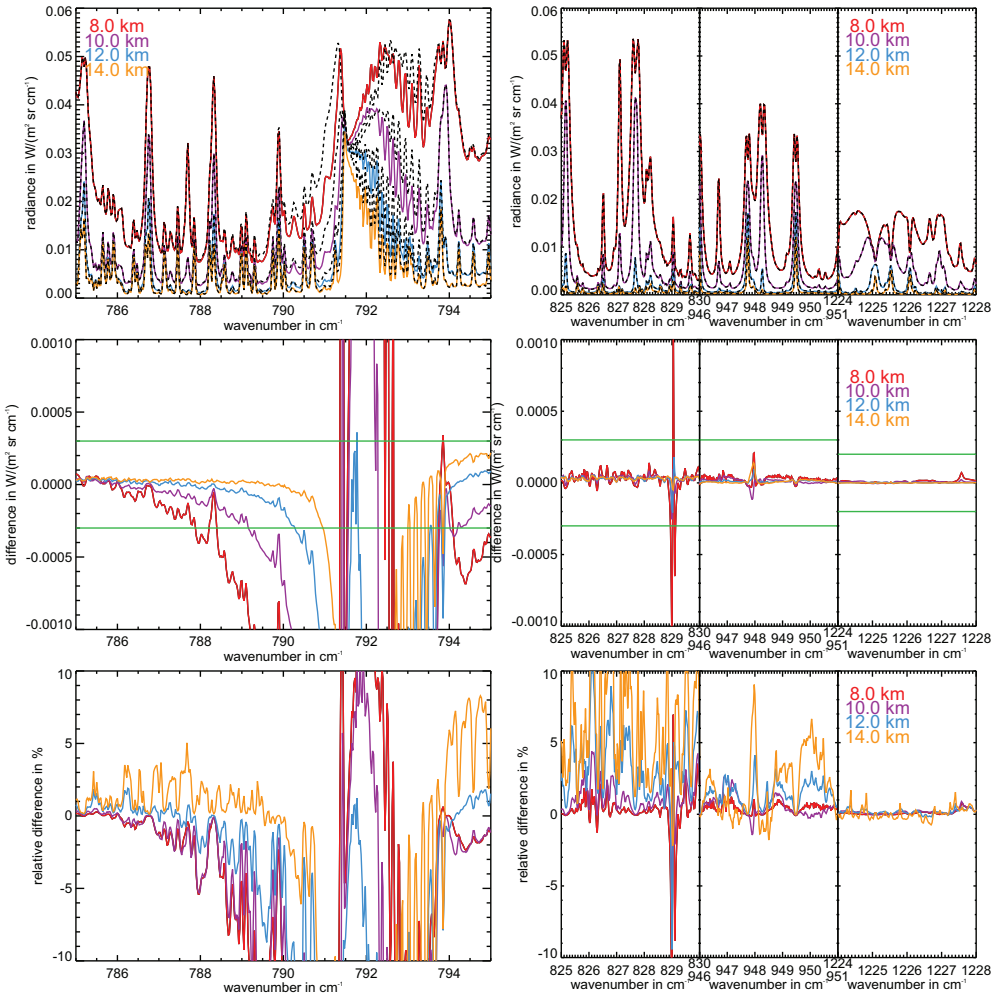


***Figure B.10:*** *Clear air limb spectra of RFM (coloured solid lines) and KOPRA (black dashed lines) for the equatorial atmosphere for four tangent heights and the absolute and relative differences between both models (RFM−KOPRA).*

### B.1.3 JURASSIC – KOPRA

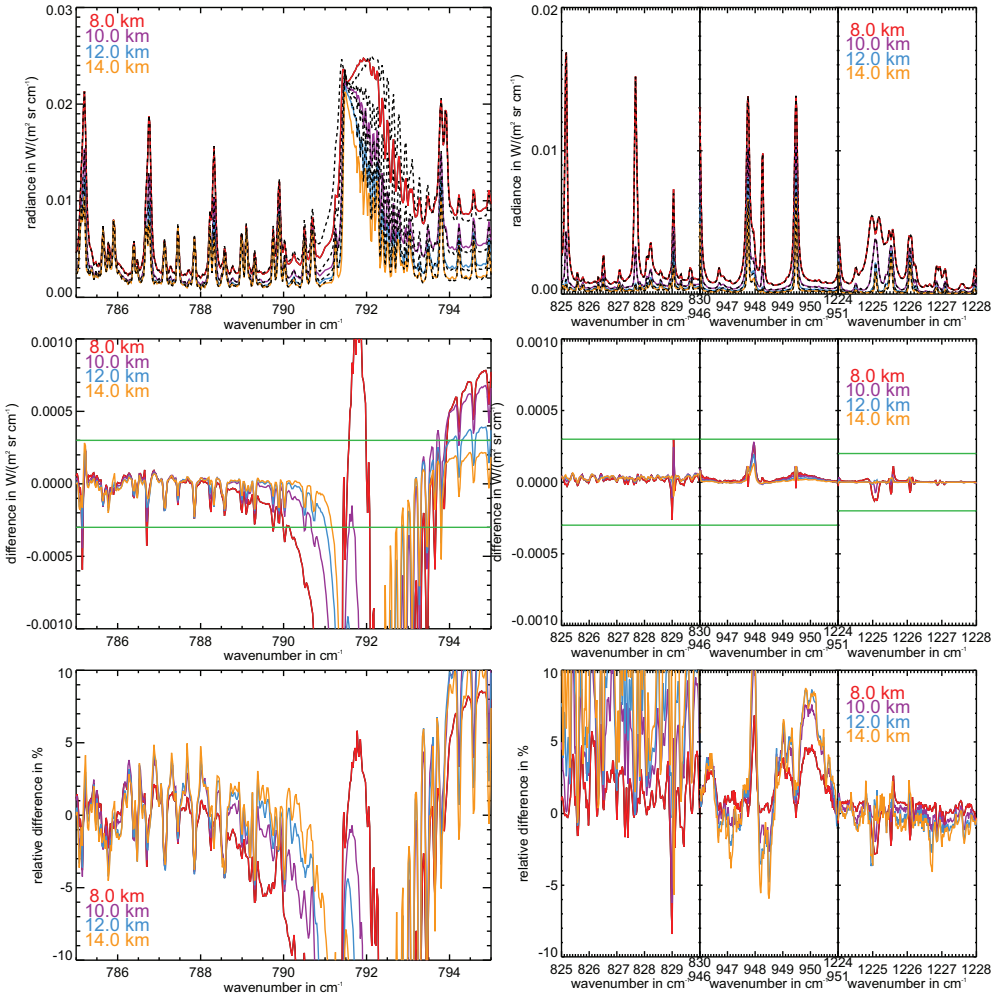


***Figure B.11:*** *Clear air limb spectra of JURASSIC (coloured solid lines) and KOPRA (black dashed lines) for the polar winter atmosphere for four tangent heights and the absolute and relative differences between both models (JURASSIC−KOPRA).*

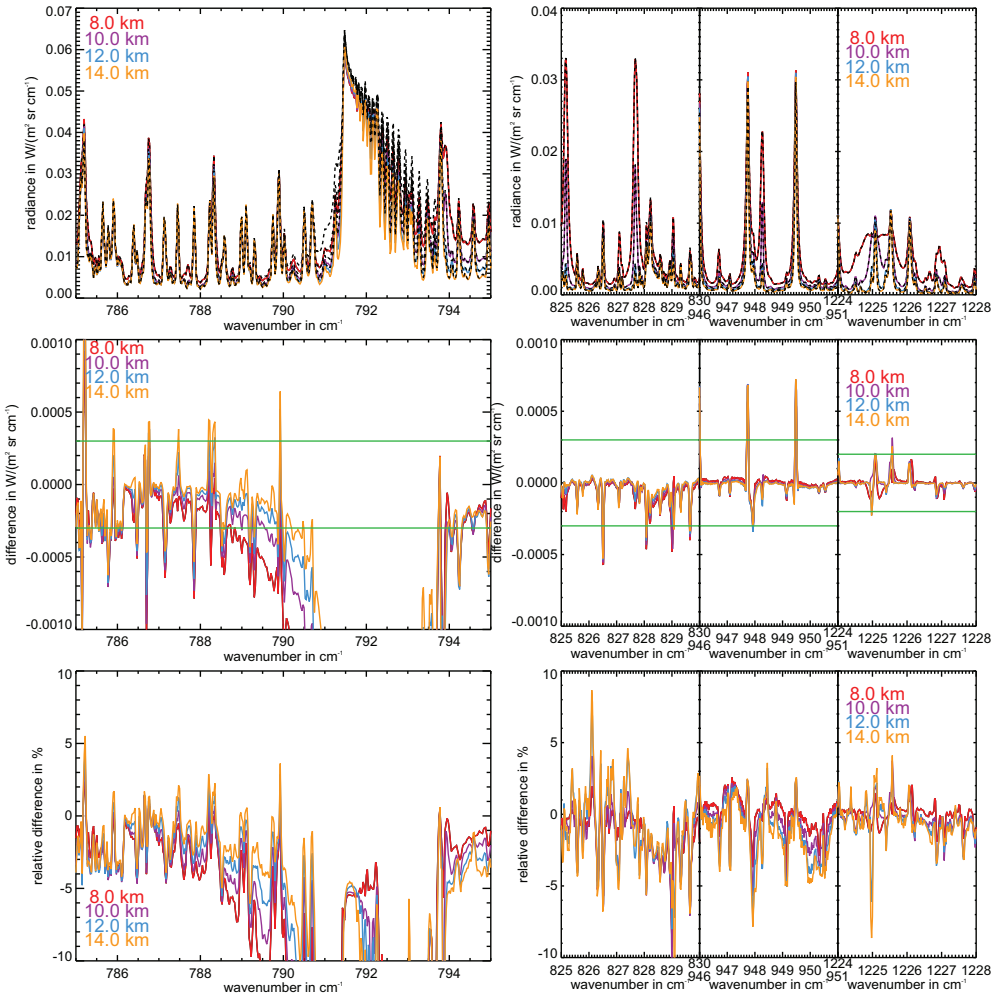


***Figure B.12:*** *Clear air limb spectra of JURASSIC (coloured solid lines) and KOPRA (black dashed lines) for the polar summer atmosphere for four tangent heights and the absolute and relative differences between both models (JURASSIC−KOPRA).*

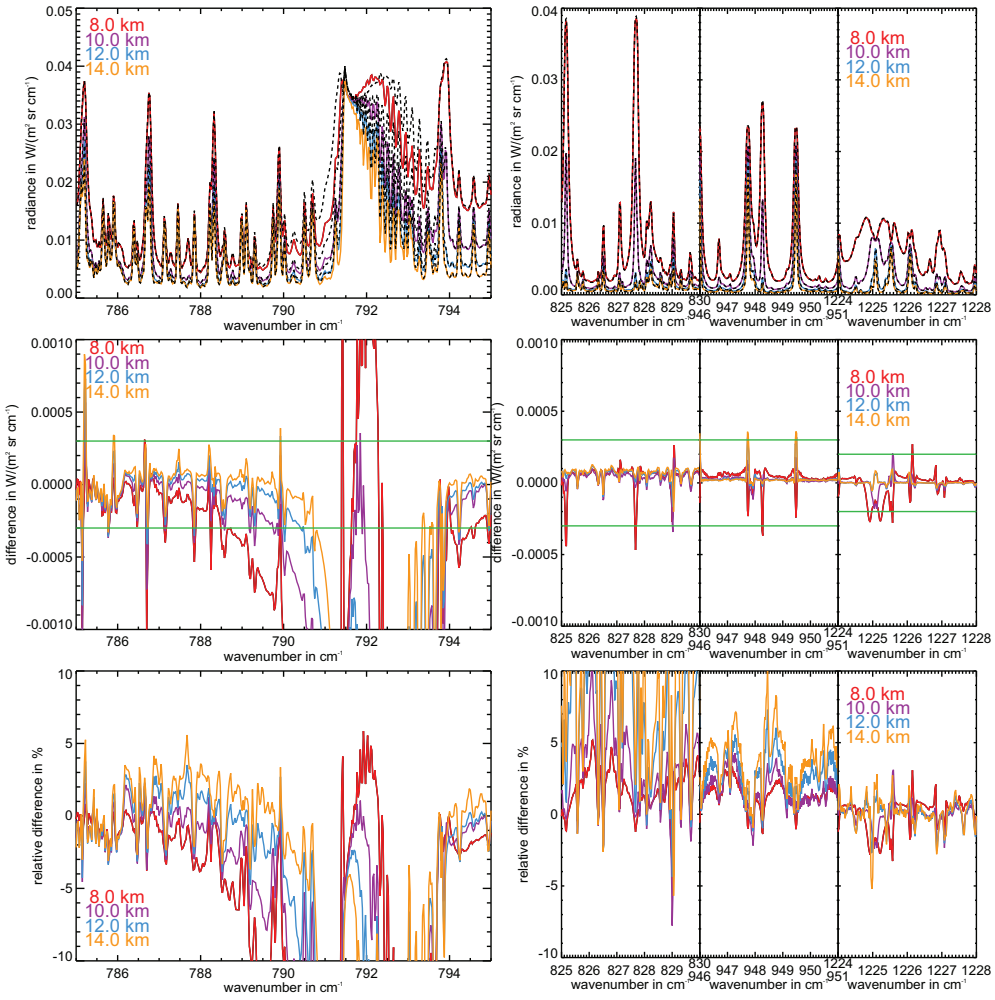


***Figure B.13:*** *Clear air limb spectra of JURASSIC (coloured solid lines) and KOPRA (black dashed lines) for the mid-latitude night atmosphere for four tangent heights and the absolute and relative differences between both models (JURASSIC−KOPRA).*

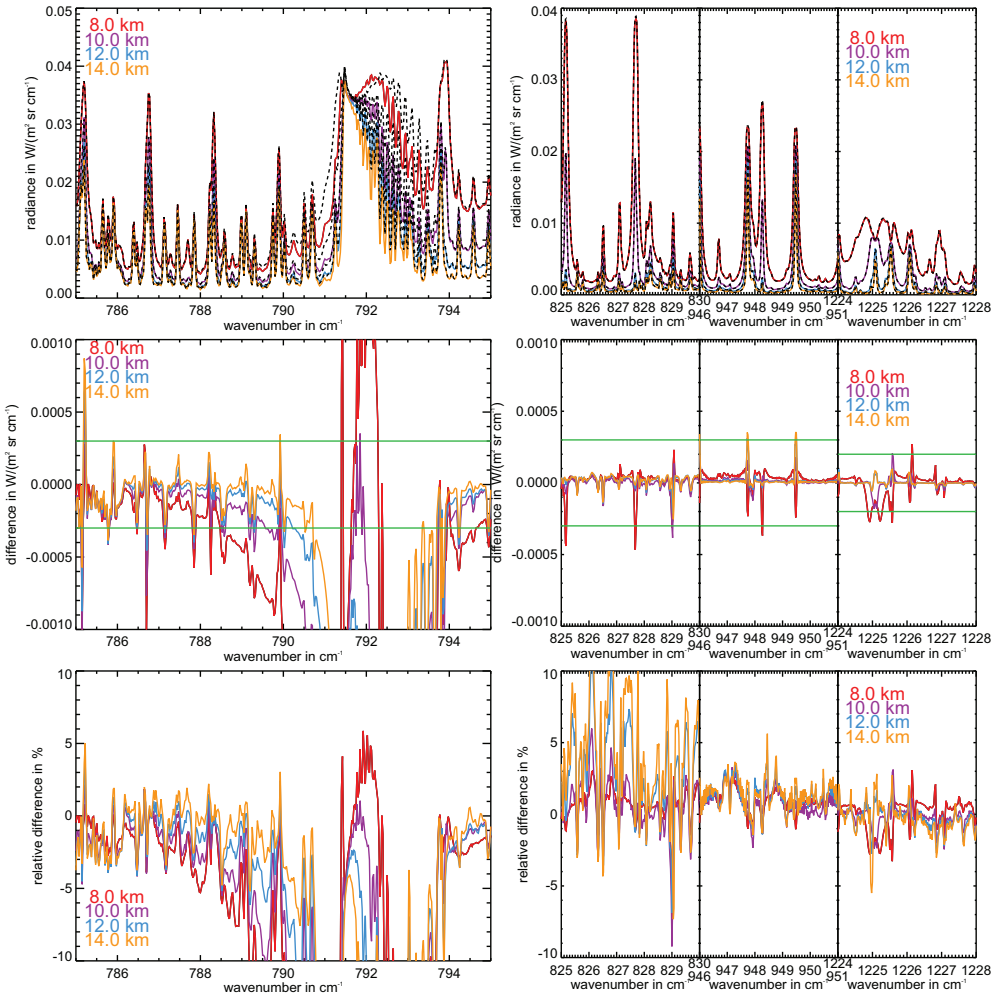


***Figure B.14:*** *Clear air limb spectra of JURASSIC (coloured solid lines) and KOPRA (black dashed lines) for the mid-latitude day atmosphere for four tangent heights and the absolute and relative differences between both models (JURASSIC−KOPRA).*

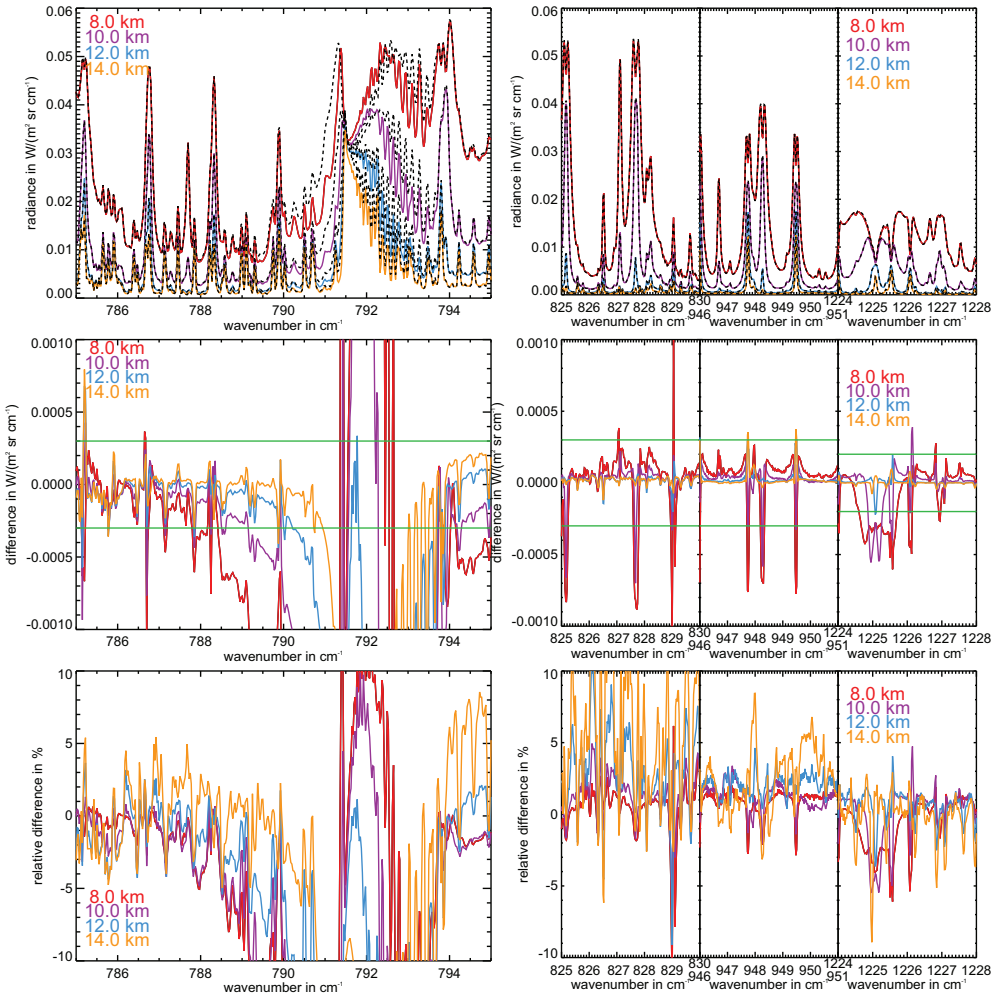


***Figure B.15:*** *Clear air limb spectra of JURASSIC (coloured solid lines) and KOPRA (black dashed lines) for the equatorial atmosphere for four tangent heights and the absolute and relative differences between both models (JURASSIC−KOPRA).*

| tangent | 785 – 795 | | | 825 – 830 | | | 946 – 951 | | | 1224 – 1228 | | |
|---|---|---|---|---|---|---|---|---|---|---|---|---|
| height | mean | $\sigma$ | % | mean | $\sigma$ | % | mean | $\sigma$ | % | mean | $\sigma$ | % |
| 8.0 | -5.6e-04 | 1.5e-03 | -6.69 | 1.7e-05 | 3.8e-05 | 0.81 | 3.1e-05 | 4.0e-05 | 1.38 | -2.1e-06 | 3.2e-05 | -0.11 |
| 10.0 | -4.2e-04 | 1.1e-03 | -7.36 | 3.2e-05 | 2.5e-05 | 3.80 | 2.6e-05 | 4.4e-05 | 2.35 | -5.1e-07 | 1.1e-05 | -0.07 |
| 12.0 | -4.0e-04 | 9.6e-04 | -8.82 | 3.0e-05 | 1.3e-05 | 5.75 | 1.8e-05 | 3.3e-05 | 2.66 | 2.6e-07 | 6.1e-06 | 0.07 |
| 14.0 | -3.7e-04 | 8.9e-04 | -9.61 | 2.9e-05 | 1.7e-05 | 7.40 | 1.3e-05 | 2.6e-05 | 2.83 | 3.4e-07 | 6.3e-06 | 0.13 |

***Table B.7:*** *Mean error, standard deviation and relative mean error between JURASSIC and KOPRA limb calculation for clear air polar winter atmosphere in the four micro-windows.*

| tangent | 785 – 795 | | | 825 – 830 | | | 946 – 951 | | | 1224 – 1228 | | |
|---|---|---|---|---|---|---|---|---|---|---|---|---|
| height | mean | $\sigma$ | % | mean | $\sigma$ | % | mean | $\sigma$ | % | mean | $\sigma$ | % |
| 8.0 | -1.6e-03 | 2.2e-03 | -8.97 | -7.6e-05 | 1.0e-04 | -1.29 | 1.5e-05 | 1.1e-04 | 0.29 | 3.9e-07 | 4.7e-05 | 0.01 |
| 10.0 | -1.5e-03 | 2.2e-03 | -9.76 | -6.6e-05 | 9.7e-05 | -2.10 | 5.5e-06 | 1.3e-04 | 0.16 | 8.1e-06 | 5.5e-05 | 0.29 |
| 12.0 | -1.4e-03 | 2.2e-03 | -9.83 | -5.0e-05 | 9.3e-05 | -2.33 | -1.2e-06 | 1.3e-04 | -0.04 | 1.7e-06 | 5.2e-05 | 0.10 |
| 14.0 | -1.3e-03 | 2.2e-03 | -9.55 | -4.7e-05 | 8.9e-05 | -2.47 | -4.2e-07 | 1.3e-04 | -0.02 | 2.4e-06 | 5.0e-05 | 0.17 |

***Table B.8:*** *Mean error, standard deviation and relative mean error between JURASSIC and KOPRA limb calculation for clear air polar summer atmosphere in the four micro-windows.*

| tangent | 785 – 795 | | | 825 – 830 | | | 946 – 951 | | | 1224 – 1228 | | |
|---|---|---|---|---|---|---|---|---|---|---|---|---|
| height | mean | $\sigma$ | % | mean | $\sigma$ | % | mean | $\sigma$ | % | mean | $\sigma$ | % |
| 8.0 | -1.3e-03 | 2.4e-03 | -7.72 | 4.0e-05 | 9.1e-05 | 0.56 | 3.7e-05 | 6.3e-05 | 0.59 | -2.0e-05 | 9.0e-05 | -0.32 |
| 10.0 | -1.1e-03 | 1.9e-03 | -8.81 | 3.6e-05 | 5.1e-05 | 1.32 | 2.6e-05 | 3.4e-05 | 0.87 | -5.7e-06 | 4.2e-05 | -0.22 |
| 12.0 | -8.6e-04 | 1.6e-03 | -8.93 | 6.3e-05 | 3.9e-05 | 4.54 | 3.1e-05 | 5.2e-05 | 1.72 | 1.9e-06 | 2.0e-05 | 0.15 |
| 14.0 | -7.2e-04 | 1.4e-03 | -8.42 | 7.1e-05 | 4.0e-05 | 6.46 | 3.1e-05 | 5.9e-05 | 2.46 | 3.2e-06 | 2.1e-05 | 0.37 |

***Table B.9:*** *Mean error, standard deviation and relative mean error between JURASSIC and KOPRA limb calculation for clear air mid-latitude night atmosphere in the four micro-windows.*

| tangent | 785 – 795 | | | 825 – 830 | | | 946 – 951 | | | 1224 – 1228 | | |
|---|---|---|---|---|---|---|---|---|---|---|---|---|
| height | mean | $\sigma$ | % | mean | $\sigma$ | % | mean | $\sigma$ | % | mean | $\sigma$ | % |
| 8.0 | -1.4e-03 | 2.4e-03 | -8.00 | 6.7e-06 | 8.5e-05 | 0.09 | 2.9e-05 | 6.1e-05 | 0.47 | -2.0e-05 | 9.0e-05 | -0.34 |
| 10.0 | -1.1e-03 | 1.9e-03 | -9.34 | -4.7e-06 | 5.0e-05 | -0.17 | 1.6e-05 | 3.5e-05 | 0.54 | -6.8e-06 | 4.2e-05 | -0.26 |
| 12.0 | -9.1e-04 | 1.6e-03 | -9.67 | 1.7e-05 | 3.9e-05 | 1.29 | 2.0e-05 | 5.3e-05 | 1.10 | 6.0e-07 | 2.0e-05 | 0.05 |
| 14.0 | -7.7e-04 | 1.4e-03 | -9.35 | 1.9e-05 | 4.0e-05 | 1.90 | 1.8e-05 | 6.0e-05 | 1.47 | 1.7e-06 | 2.2e-05 | 0.21 |

***Table B.10:*** *Mean error, standard deviation and relative mean error between JURASSIC and KOPRA limb calculation for clear air mid-latitude day atmosphere in the four micro-windows.*

| tangent | 785 – 795 | | | 825 – 830 | | | 946 – 951 | | | 1224 – 1228 | | |
|---|---|---|---|---|---|---|---|---|---|---|---|---|
| height | mean | $\sigma$ | % | mean | $\sigma$ | % | mean | $\sigma$ | % | mean | $\sigma$ | % |
| 8.0 | -1.5e-03 | 3.6e-03 | -5.63 | -4.3e-05 | 2.4e-04 | -0.26 | 9.7e-08 | 1.8e-04 | 0.00 | -1.2e-04 | 1.7e-04 | -0.97 |
| 10.0 | -1.2e-03 | 2.6e-03 | -8.60 | 1.9e-05 | 1.1e-04 | 0.30 | 2.8e-05 | 8.3e-05 | 0.55 | -2.8e-05 | 1.6e-04 | -0.50 |
| 12.0 | -8.3e-04 | 1.6e-03 | -10.33 | 1.9e-05 | 3.6e-05 | 1.41 | 3.2e-05 | 5.3e-05 | 1.79 | 2.8e-06 | 3.6e-05 | 0.20 |
| 14.0 | -6.0e-04 | 1.2e-03 | -10.47 | 1.8e-05 | 2.5e-05 | 2.58 | 2.3e-05 | 5.7e-05 | 2.60 | -1.7e-07 | 2.1e-05 | -0.03 |

***Table B.11:*** *Mean error, standard deviation and relative mean error between JURASSIC and KOPRA limb calculation for clear air equatorial atmosphere in the four micro-windows.*

| atm | 785 – 795 | | | 825 – 830 | | | 946 – 951 | | | 1224 – 1228 | | |
|---|---|---|---|---|---|---|---|---|---|---|---|---|
| height | mean | $\sigma$ | % | mean | $\sigma$ | % | mean | $\sigma$ | % | mean | $\sigma$ | % |
| pwin | 6.2e-04 | 1.5e-03 | 0.89 | 2.3e-05 | 4.6e-06 | 0.03 | 1.6e-05 | 4.1e-06 | 0.03 | 4.9e-07 | 2.8e-05 | 0.00 |
| psum | 4.5e-04 | 1.1e-03 | 0.66 | 2.2e-05 | 1.1e-05 | 0.04 | 1.6e-05 | 8.6e-06 | 0.03 | -2.5e-07 | 3.0e-05 | -0.00 |
| midln | 1.4e-03 | 3.2e-03 | 1.36 | 3.4e-05 | 7.5e-05 | 0.03 | 2.7e-05 | 6.0e-05 | 0.03 | -1.3e-05 | 9.4e-05 | -0.04 |
| midld | 1.4e-03 | 3.2e-03 | 1.36 | 3.4e-05 | 7.5e-05 | 0.03 | 2.7e-05 | 6.0e-05 | 0.03 | -1.3e-05 | 9.4e-05 | -0.04 |
| equ | 2.0e-03 | 4.0e-03 | 1.58 | 9.0e-05 | 1.8e-04 | 0.07 | 7.3e-05 | 1.1e-04 | 0.07 | 3.1e-05 | 1.6e-04 | 0.07 |

***Table B.12:*** *Mean error, standard deviation and relative mean error between JURASSIC and KOPRA nadir calculation for clear air in all atmospheres in the four micro-windows.*

## B.2 Cloudy Air Comparison

### B.2.1 JURASSIC – KOPRA - Extinction Spectra Comparison

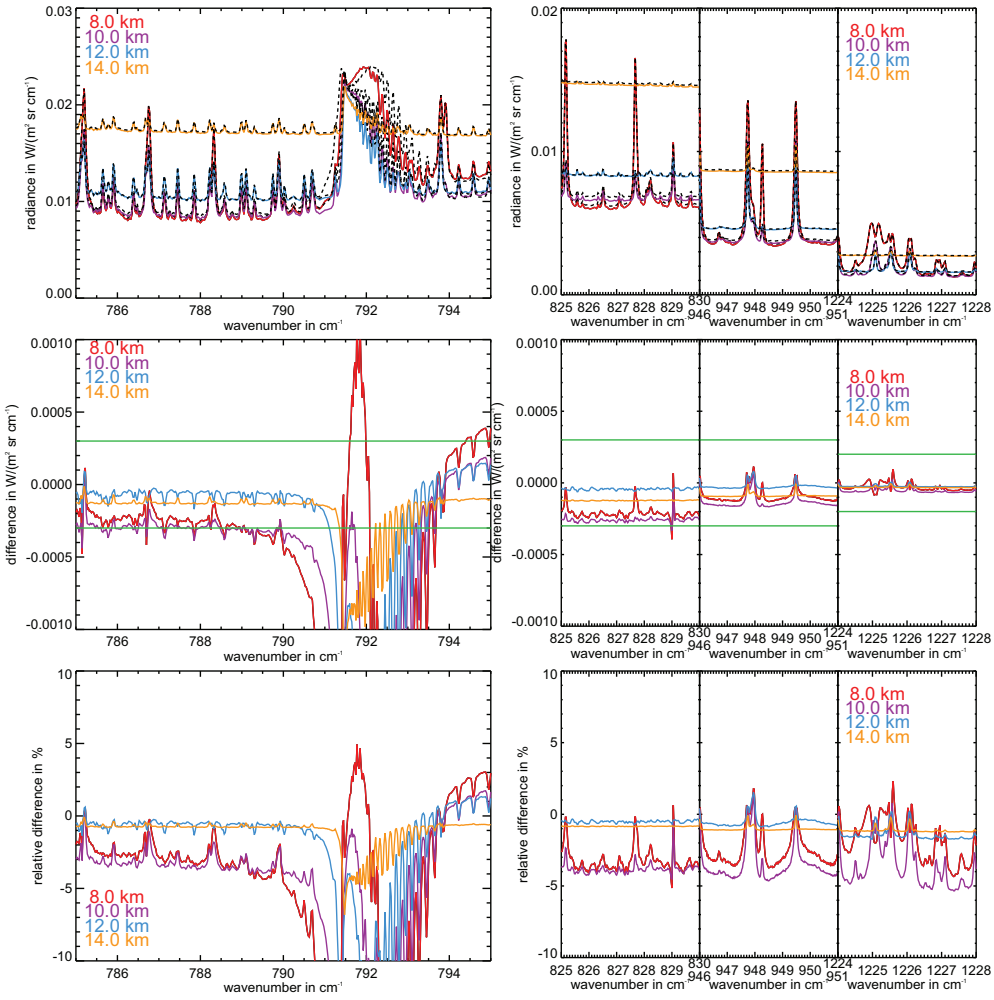


***Figure B.16:*** *Extinction spectra for cloud 1 in polar winter model atmosphere of JURASSIC (coloured solid lines) and KOPRA (black dashed lines) for four tangent heights and the absolute and relative differences between both models (JURASSIC−KOPRA).*

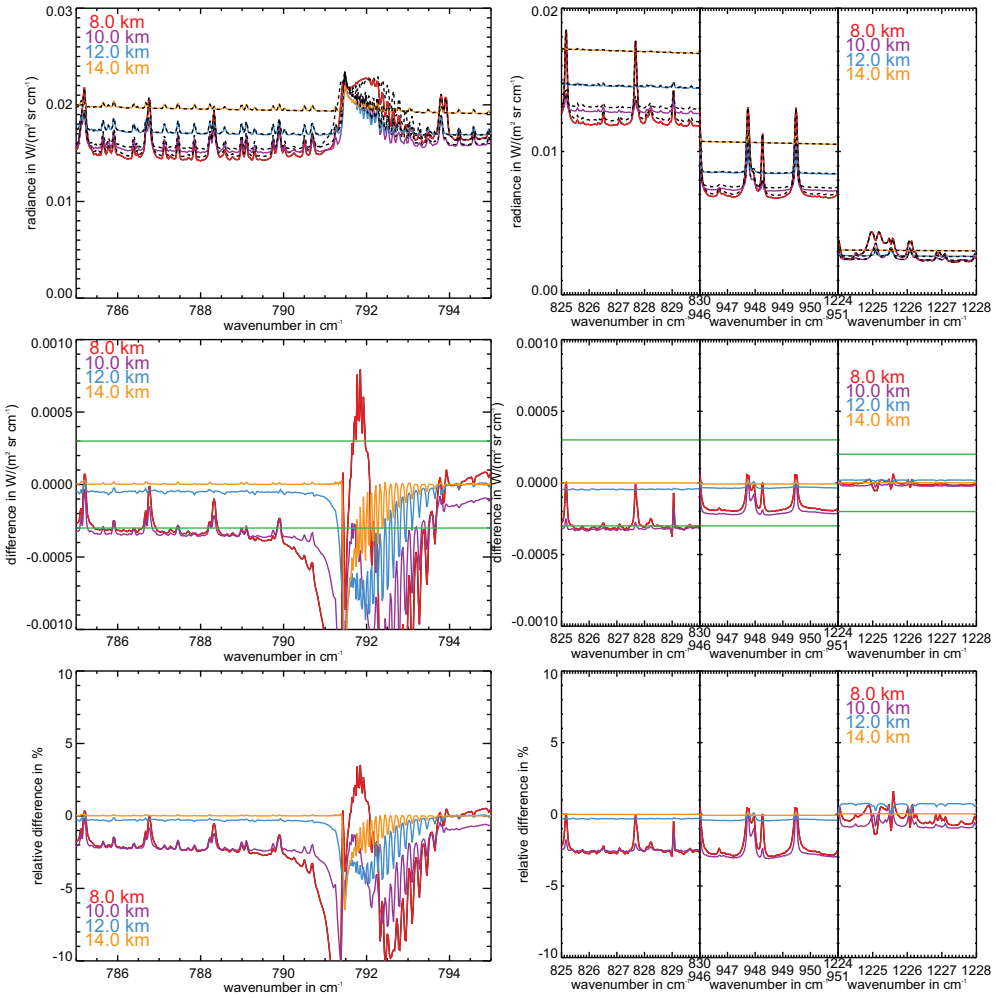


***Figure B.17:*** *Extinction spectra for cloud 2 in polar winter model atmosphere of JURASSIC (coloured solid lines) and KOPRA (black dashed lines) for four tangent heights and the absolute and relative differences between both models (JURASSIC−KOPRA).*

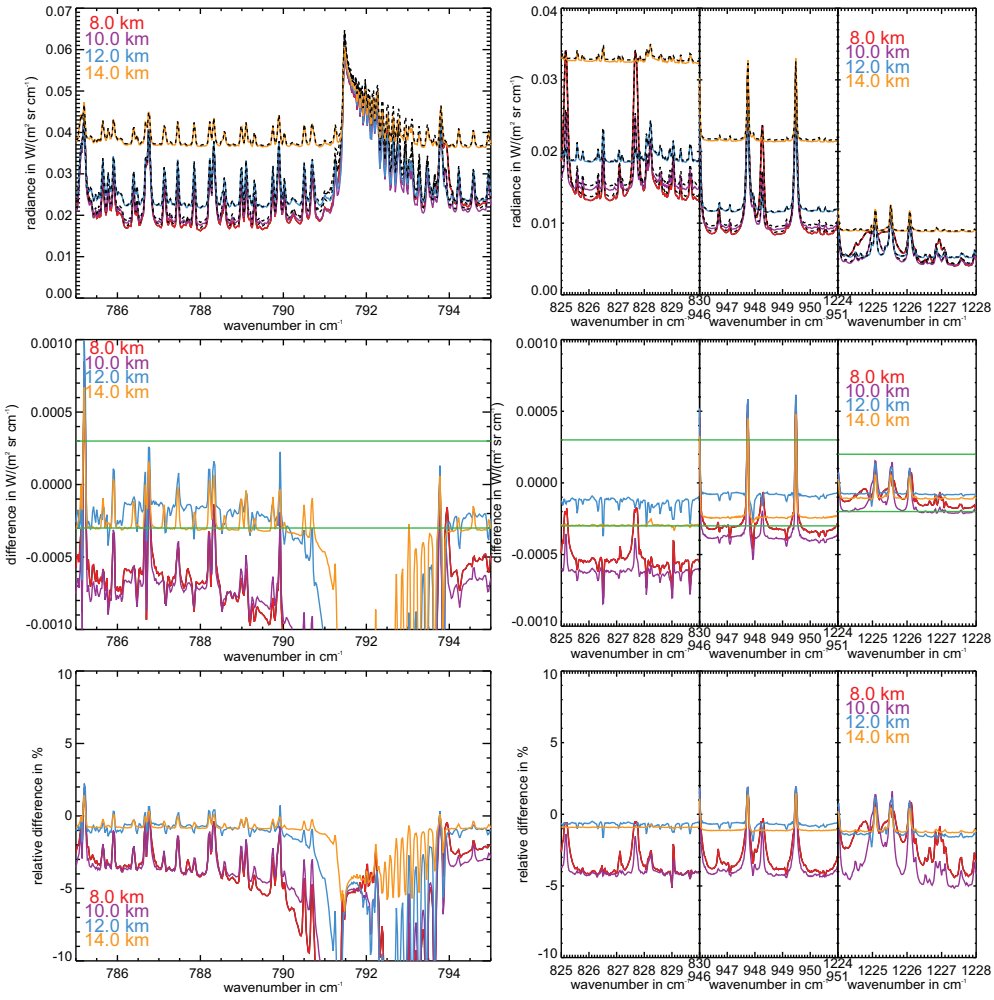


***Figure B.18:*** *Extinction spectra for cloud 1 in polar summer model atmosphere of JURASSIC (coloured solid lines) and KOPRA (black dashed lines) for four tangent heights and the absolute and relative differences between both models (JURASSIC−KOPRA).*

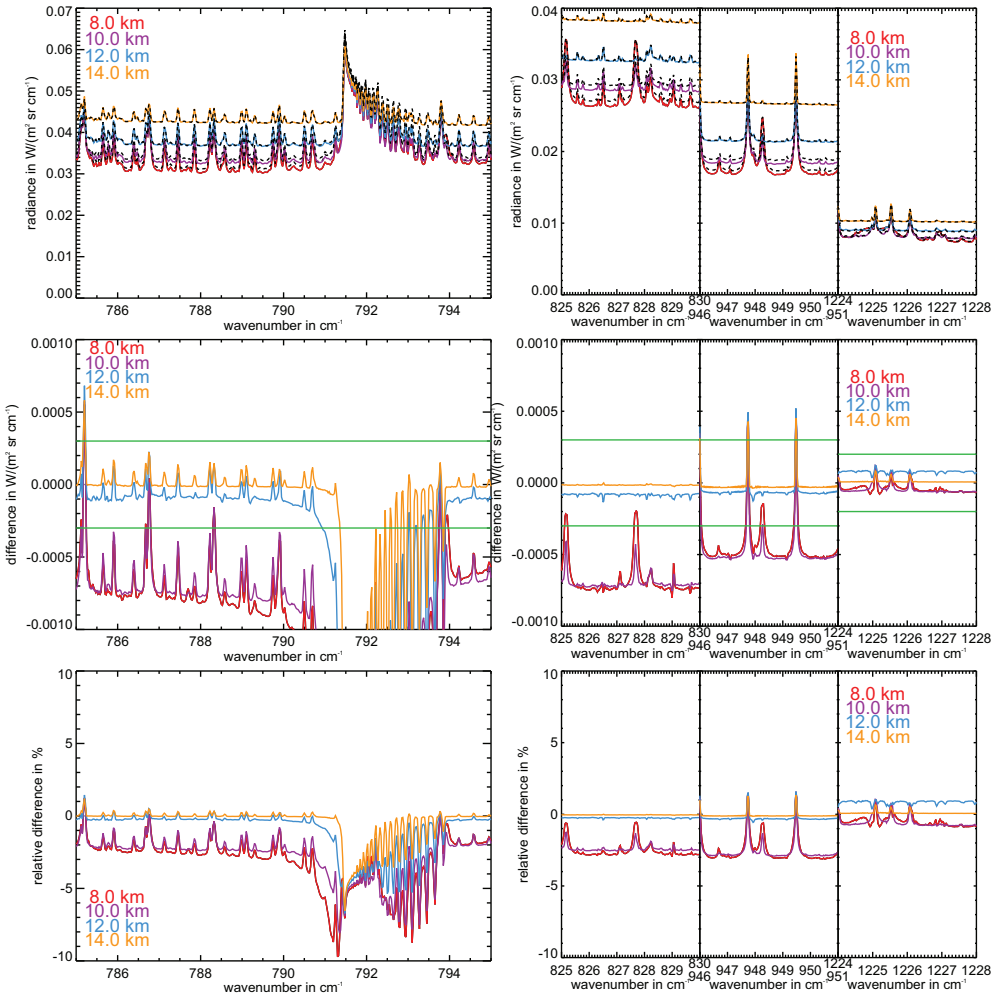


***Figure B.19:*** *Extinction spectra for cloud 2 in polar summer model atmosphere of JURASSIC (coloured solid lines) and KOPRA (black dashed lines) for four tangent heights and the absolute and relative differences between both models (JURASSIC−KOPRA).*

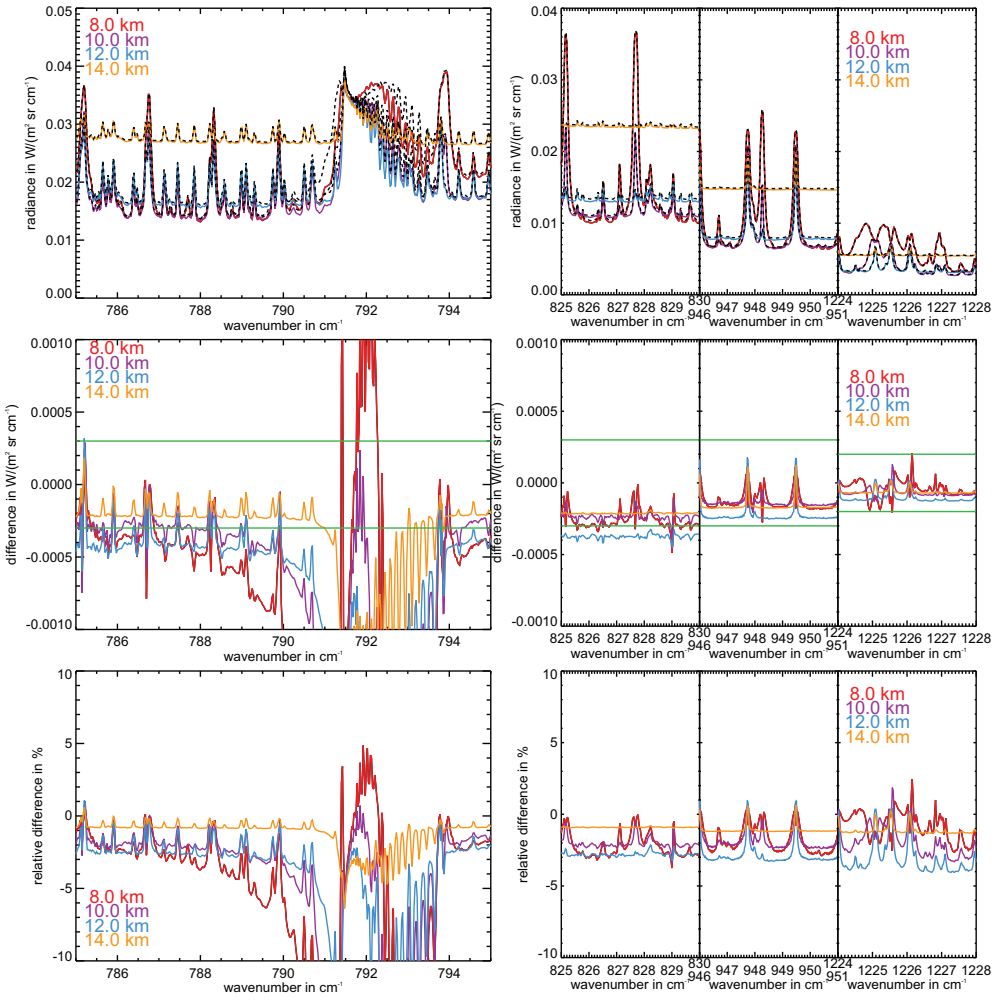


***Figure B.20:*** *Extinction spectra for cloud 1 in mid-latitude night model atmosphere of JURASSIC (coloured solid lines) and KOPRA (black dashed lines) for four tangent heights and the absolute and relative differences between both models (JURASSIC−KOPRA).*

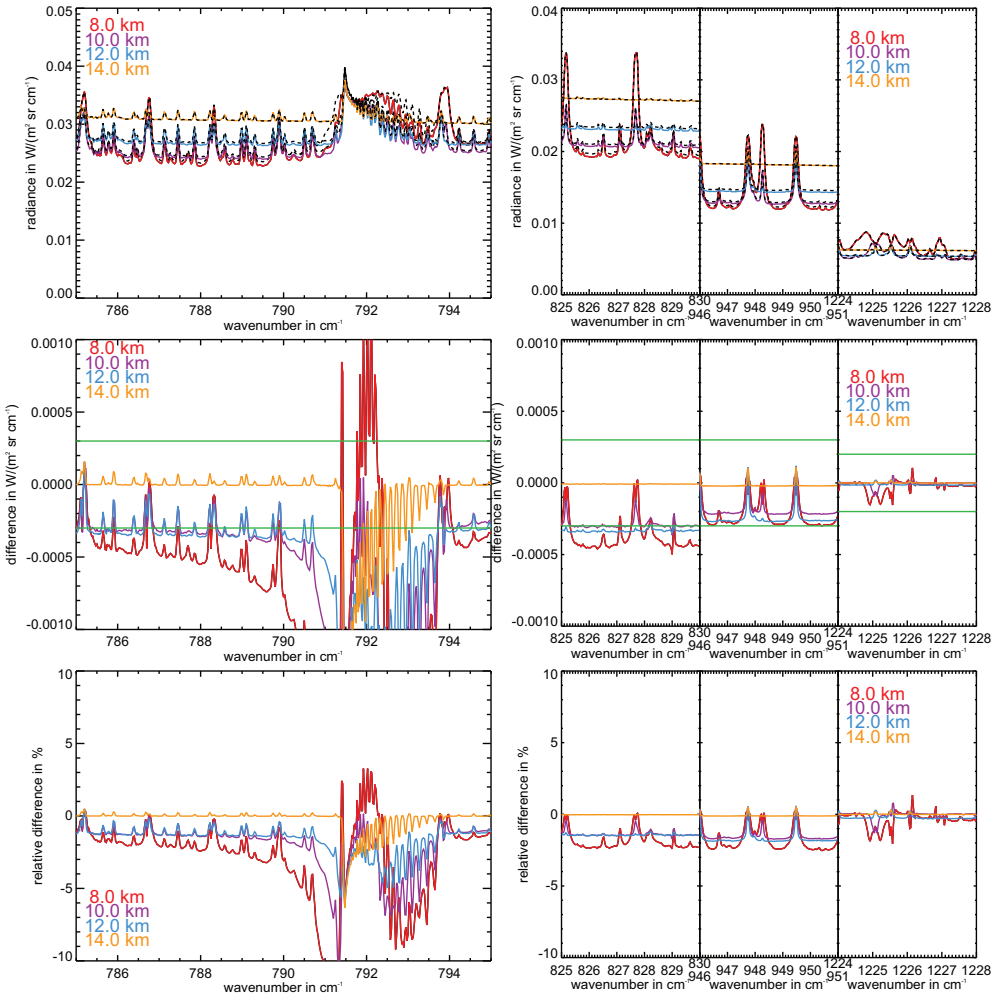


***Figure B.21:*** *Extinction spectra for cloud 2 in mid-latitude night model atmosphere of JURASSIC (coloured solid lines) and KOPRA (black dashed lines) for four tangent heights and the absolute and relative differences between both models (JURASSIC−KOPRA).*

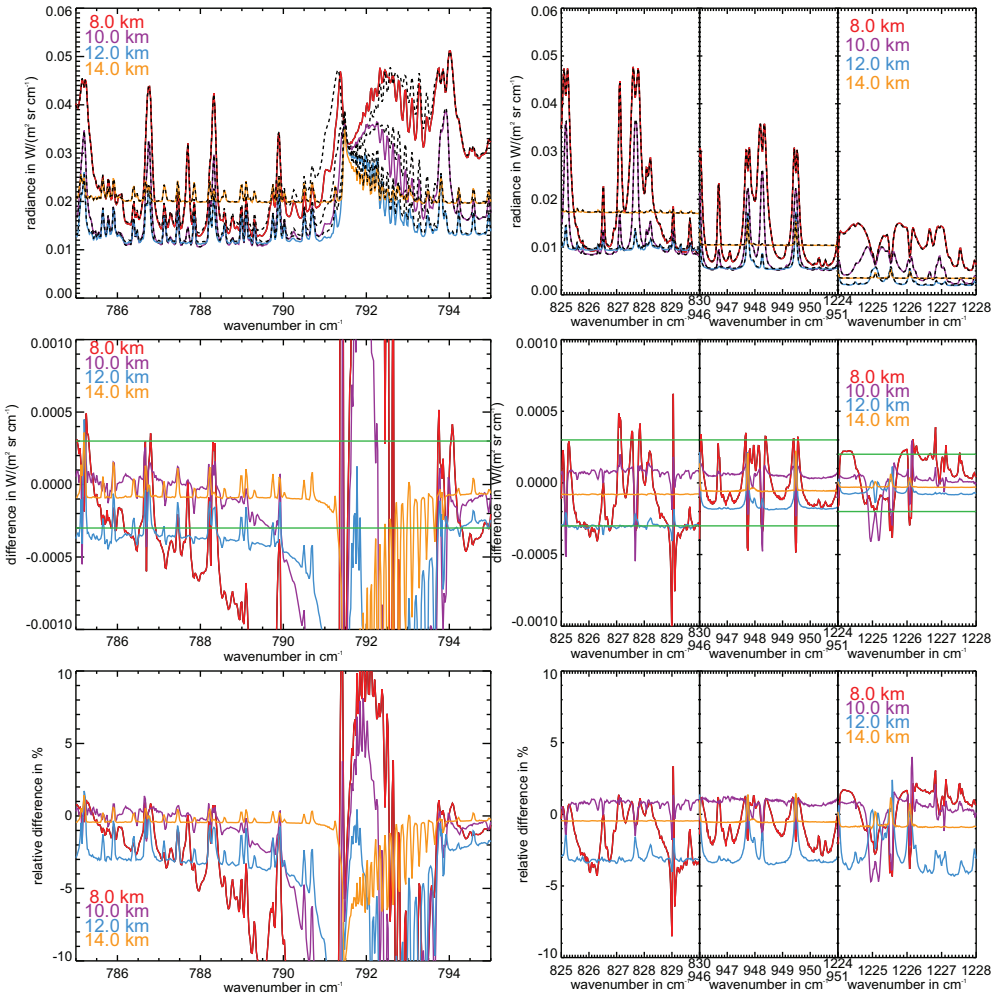


***Figure B.22:*** *Extinction spectra for cloud 1 in equatorial night model atmosphere of JURASSIC (coloured solid lines) and KOPRA (black dashed lines) for four tangent heights and the absolute and relative differences between both models (JURASSIC−KOPRA).*

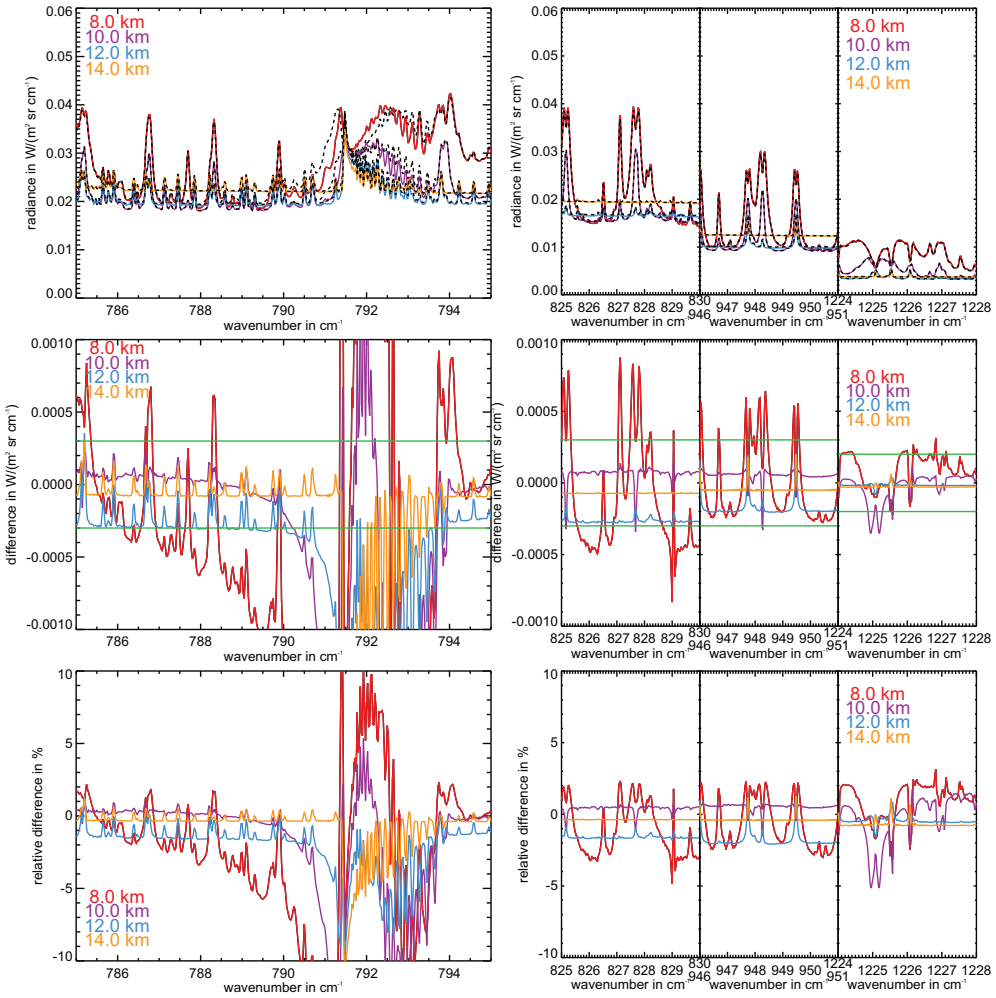


***Figure B.23:*** *Extinction spectra for cloud 2 in equatorial night model atmosphere of JURASSIC (coloured solid lines) and KOPRA (black dashed lines) for four tangent heights and the absolute and relative differences between both models (JURASSIC−KOPRA).*

### B.2.2 JURASSIC – KOPRA - Scattering Spectra Comparison

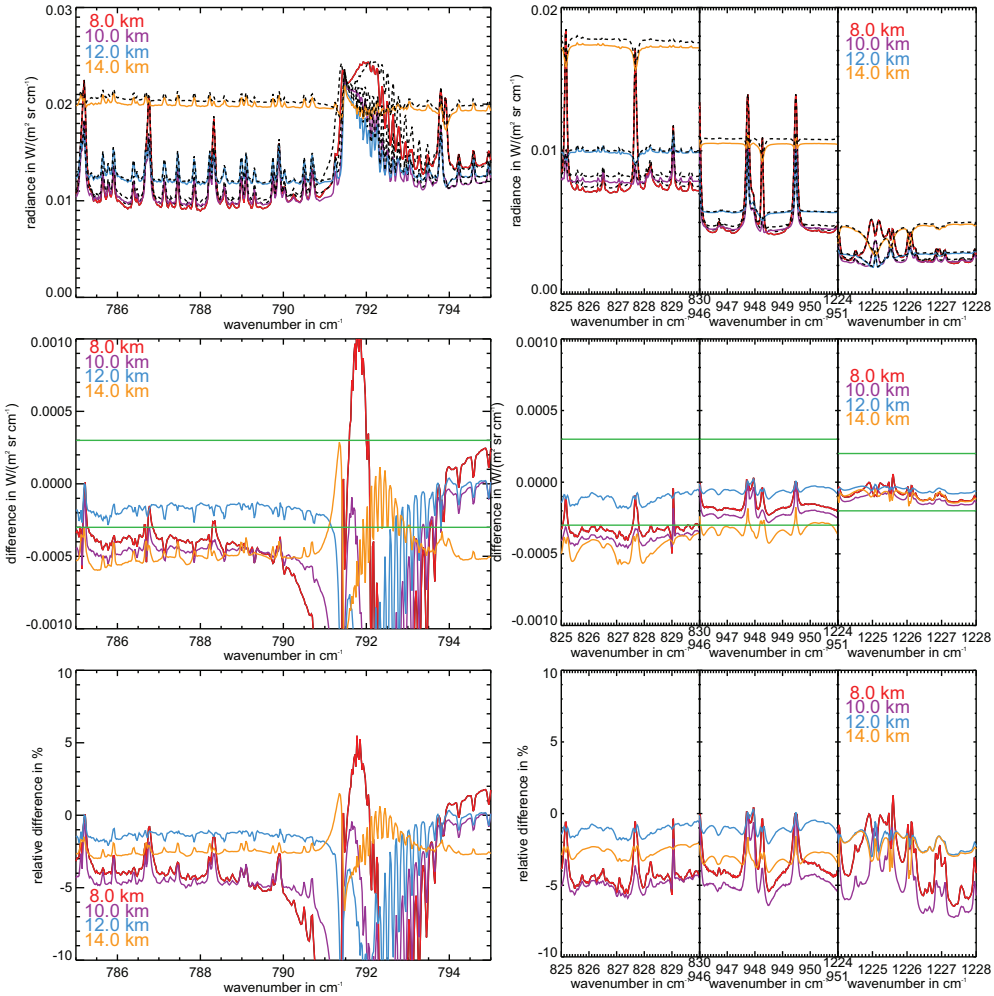


***Figure B.24:*** *Scattering spectra for cloud 1 in polar winter model atmosphere of JURASSIC (coloured solid lines) and KOPRA (black dashed lines) for four tangent heights and the absolute and relative differences between both models (JURASSIC−KOPRA).*

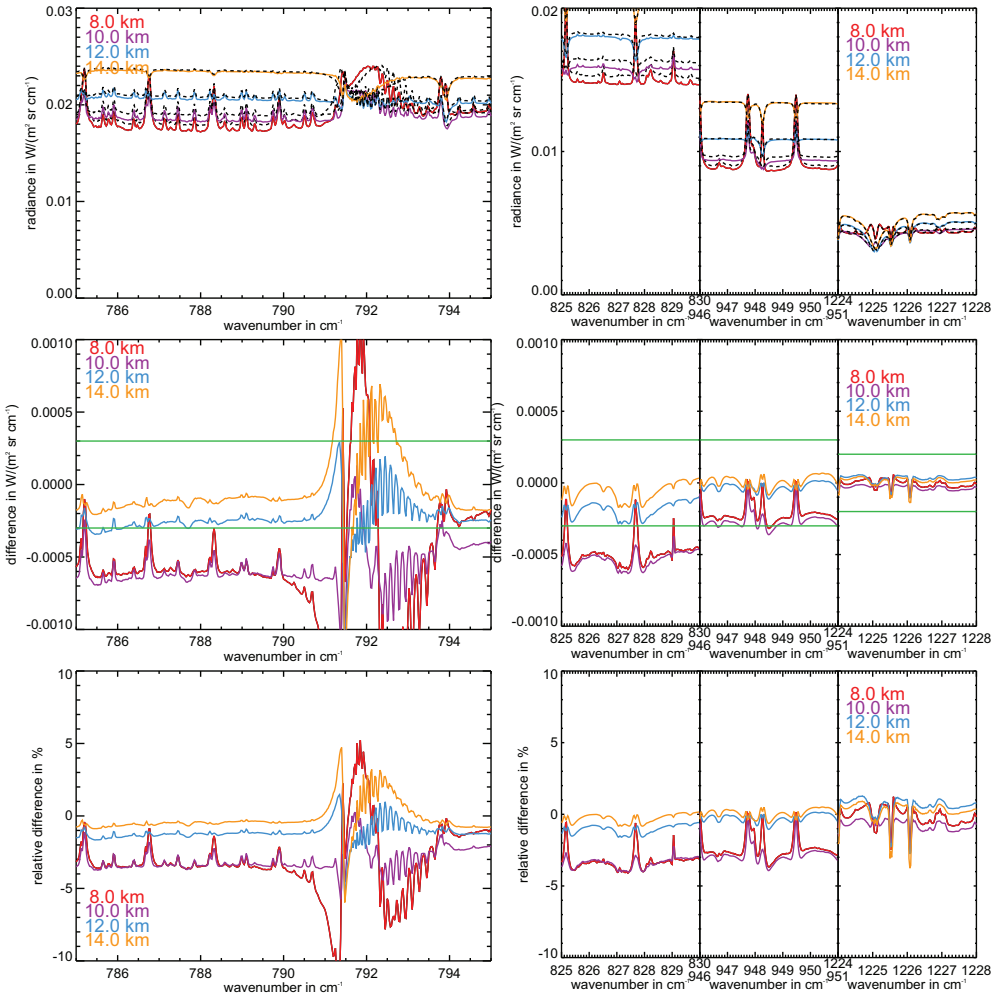


***Figure B.25:*** *Scattering spectra for cloud 2 in polar winter model atmosphere of JURASSIC (coloured solid lines) and KOPRA (black dashed lines) for four tangent heights and the absolute and relative differences between both models (JURASSIC−KOPRA).*

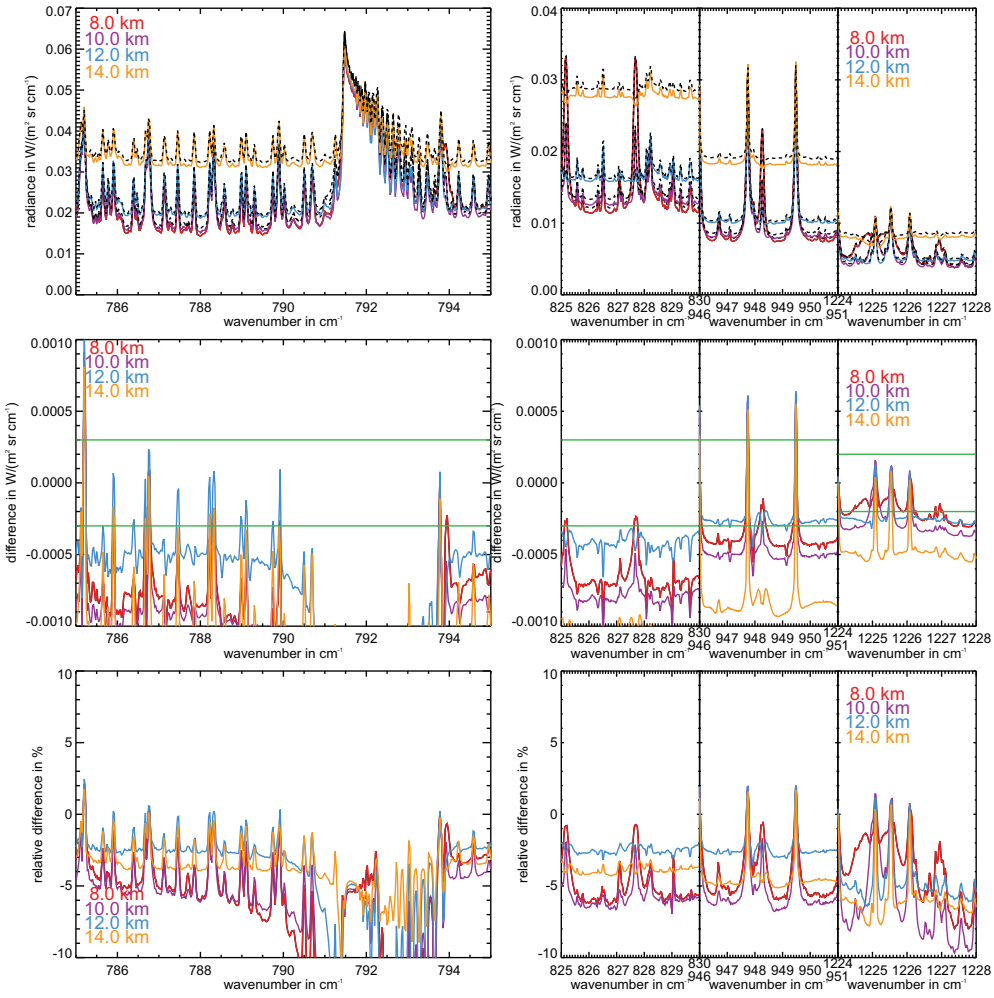


***Figure B.26:*** *Scattering spectra for cloud 1 in polar summer model atmosphere of JURASSIC (coloured solid lines) and KOPRA (black dashed lines) for four tangent heights and the absolute and relative differences between both models (JURASSIC−KOPRA).*

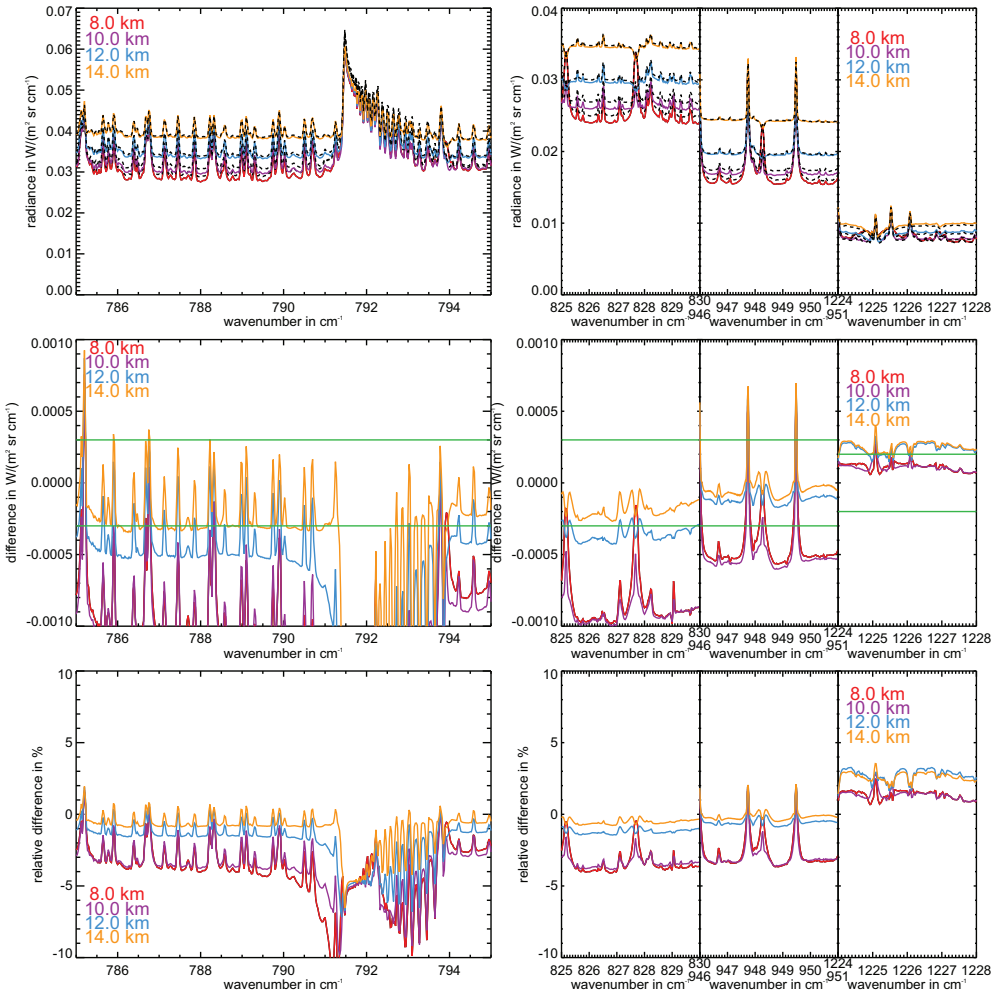


***Figure B.27:*** *Scattering spectra for cloud 2 in polar summer model atmosphere of JURASSIC (coloured solid lines) and KOPRA (black dashed lines) for four tangent heights and the absolute and relative differences between both models (JURASSIC−KOPRA).*

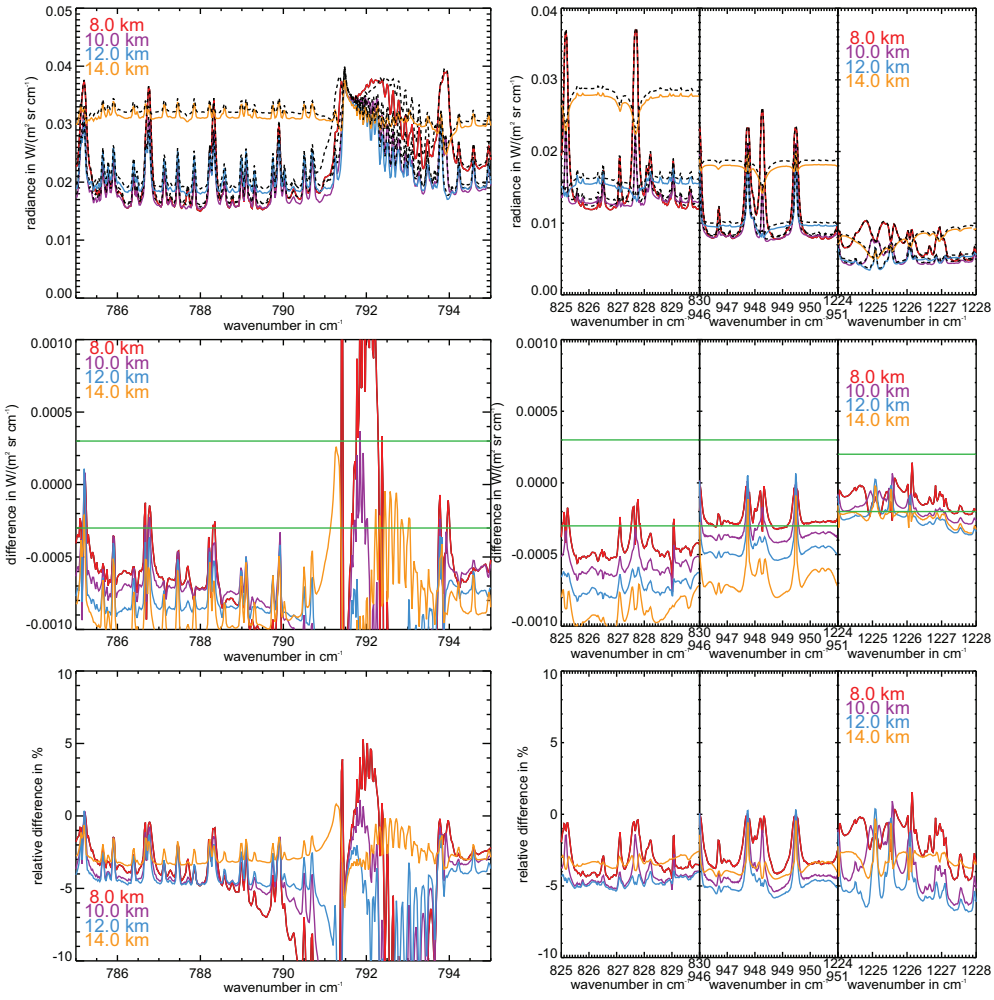


***Figure B.28:*** *Scattering spectra for cloud 1 in mid-latitude night model atmosphere of JURASSIC (coloured solid lines) and KOPRA (black dashed lines) for four tangent heights and the absolute and relative differences between both models (JURASSIC−KOPRA).*

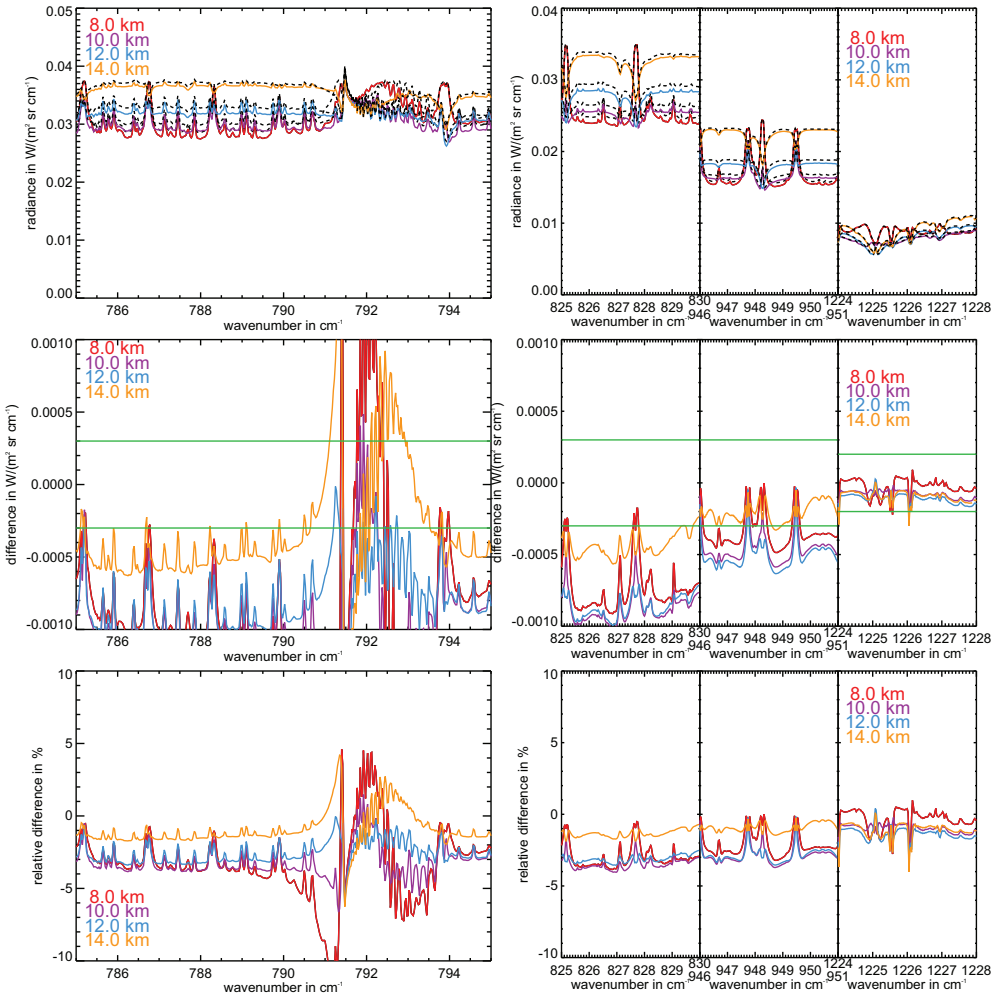


***Figure B.29:*** *Scattering spectra for cloud 2 in mid-latitude night model atmosphere of JURASSIC (coloured solid lines) and KOPRA (black dashed lines) for four tangent heights and the absolute and relative differences between both models (JURASSIC−KOPRA).*

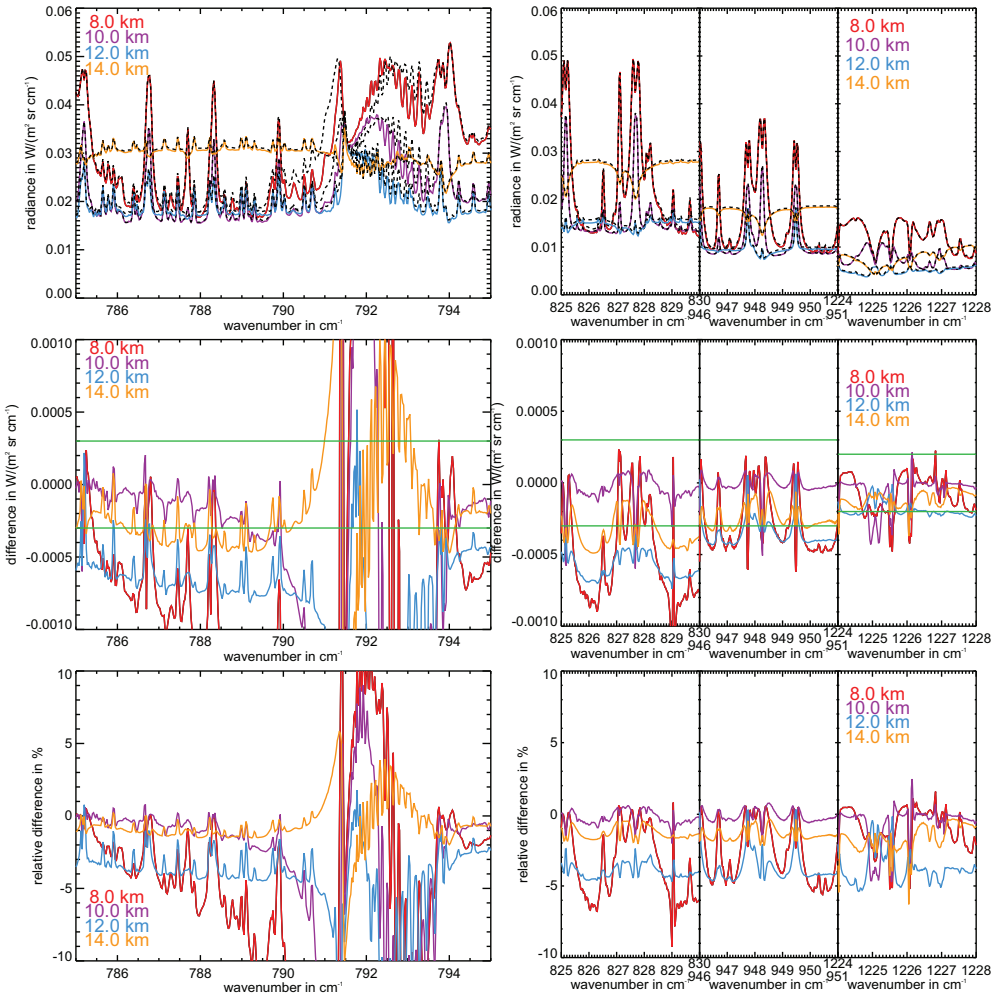


***Figure B.30:*** *Scattering spectra for cloud 1 in equatorial night model atmosphere of JURASSIC (coloured solid lines) and KOPRA (black dashed lines) for four tangent heights and the absolute and relative differences between both models (JURASSIC−KOPRA).*

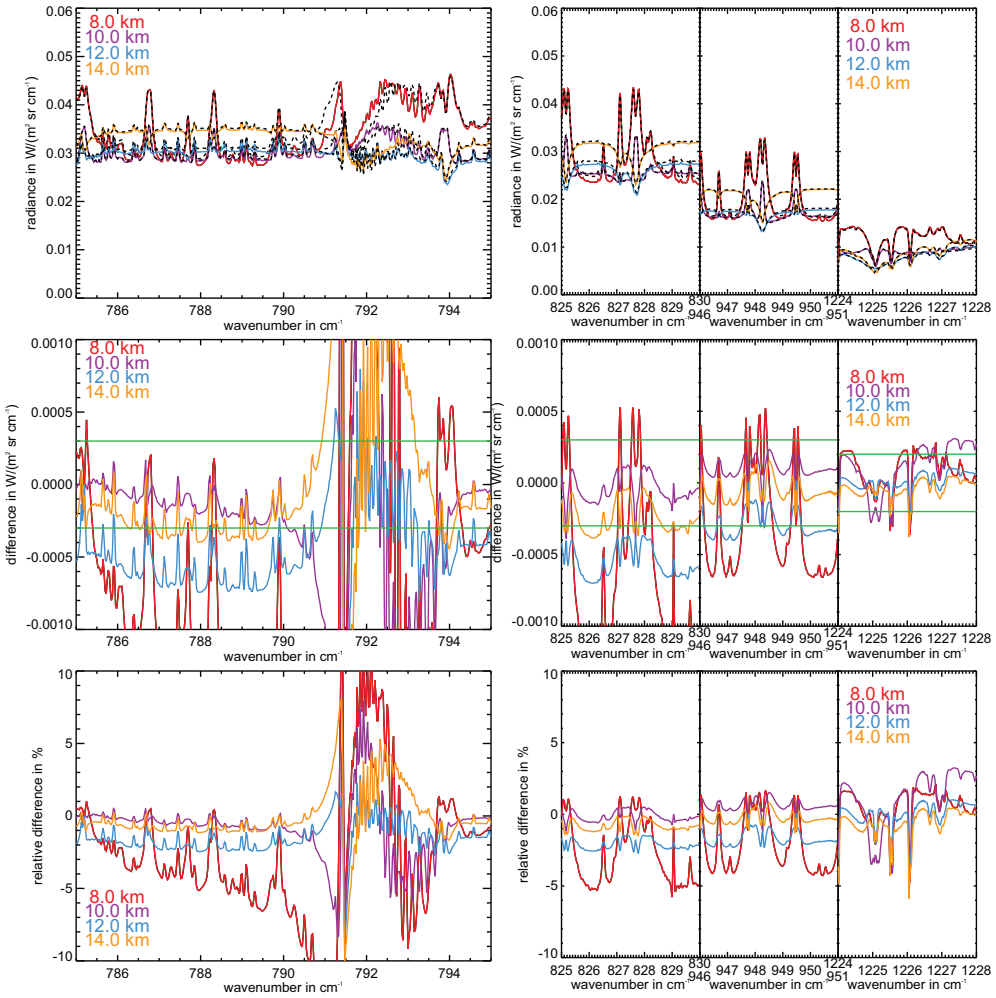


***Figure B.31:*** *Scattering spectra for cloud 2 in equatorial night model atmosphere of JURASSIC (coloured solid lines) and KOPRA (black dashed lines) for four tangent heights and the absolute and relative differences between both models (JURASSIC−KOPRA).*

# Bibliography

Ackermann, I., Hass, H., Memmesheimer, M., Ebel, A., Binkowski, F., and Shankar, U.: Modal Aerosol Dynamics Model for Europe: development and first applications, Atmos. Environment, 32, 2981–2999, 1998.

Ansmann, A., Tesche, M., Groß, S., Freudenthaler, V., Seifert, P., Hiebsch, A., Schmidt, J., Wandinger, U., Mattis, I., Müller, D., and Wiegner, M.: The 16 April 2010 major volcanic ash plume over central Europe: EARLINET lidar and AERONET photometer observations at Leipzig and Munich, Germany, Geophys. Res. Lett., 37, L13810, doi:10.1029/2010GL043809, 2010.

Baran, A. J.: On the scattering and absorption properties of cirrus cloud, J. Quant. Spectrosc. Radiat. Transfer, 89, 17–36, 2004.

Baran, A. J., Francis, P. N., and Yang, P.: A process study of the dependence of ice crystal absorption on particle geometry: Application to aircraft radiometric measurements of cirrus cloud in the terrestrial window region, J. Atmos. Sci., 60, 417–427, 2003.

Baum, B. A., Heymsfield, A. J., Yang, P., and Bedka, S. T.: Bulk scattering properties for the remote sensing of ice clouds. Part I: Microphysical data and models, J. Appl. Met., 44, 1885–1895, 2005a.

Baum, B. A., Yang, P., Heymsfield, A. J., Platnick, S., King, M. D., Hu, Y. X., and Bedka, S. T.: Bulk scattering properties for the remote sensing of ice clouds. Part II: Narrowband models, J. Appl. Met., 44, 1896–1911, 2005b.

Baum, B. A., Yang, P., Nasiri, S., Heidinger, A. K., Heymsfield, A., and Li, J.: Bulk scattering properties for the remote sensing of ice clouds. Part III: High-resolution spectral models from 100 to 3250 $cm^{-1}$, Journal of Applied Meteorology and Climatology, 46, 423–434, doi:10.1175/JAM2473.1, 2007.

Baumgardner, D., Chepfer, H., Raga, G. B., and Kok, G. L.: The shapes of very small cirrus particles derived from in situ measurements, Geophys. Res. Lett., 32, doi:10.1029/2004GL021300, 2005.

Biermann, U. M., Luo, B. P., and Peter, T.: Absorption spectra and optical constants of binary and ternary solutions of $H_2SO_4$, $HNO_3$, and $H_2O$ in the mid infrared at atmospheric temperatures, Journal of Physical Chemistry A, 104, 783–793, 2000.

Bohren, C. F. and Huffman, D. R.: Absorption and Scattering of Light by Small Particles, John Wiley & Sons, Ltd., 1983.

Carslaw, K. S., Luo, B. P., Clegg, S. L., Peter, T., Brimblecombe, P., and Crutzen, P. J.: Stratospheric aerosol growth and $HNO_3$ gas-phase depletion from coupled $HNO_3$ and water-uptake by liquid particles, Geophys. Res. Lett., 21, 2479–2482, 1994.

Clarke, A. D. and Kapustin, V. N.: A pacific aerosol survey. Part I: A decade of data on particle production, transport, evolution, and mixing in the troposphere, J. Atmos. Sci., 59, 363–382, 2002.

Cozic, J., Verheggen, B., Weingartner, E., Crosier, J., Bower, K. N., Flynn, M., Coe, H., Henning, S., Steinbacher, M., Henne, S., Coen, M. C., Petzold, A., and Baltensperger, U.: Chemical composition of free tropospheric aerosol for PM1 and coarse mode at the high alpine site Jungfraujoch, Atmos. Chem. Phys., 8, 407–423, 2008.

Curtis, A. R.: Discussion of 'A statistical model for water vapour absorption' by R. M. Goody, Quart. J. Roy. Meteorol. Soc., 78, 638–640, 1952.

D'Almeida, G. A., Shettle, E. P., and Koepke, P.: Atmospheric aerosols: global climatology and radiative characteristics, A. Deepak Pub., Hampton, Va., USA, 1991.

Davis, S., Hlavka, D., Jensen, E., Rosenlof, K., Yang, Q. O., Schmidt, S., Borrmann, S., Frey, W., Lawson, P., Voemel, H., and Bui, T. P.: In situ and lidar observations of tropopause subvisible cirrus clouds during TC4, J. Geophys. Res., 115, doi:10.1029/2009JD013093, 2010.

de Reus, M., Krejci, R., Williams, J., Fischer, H., Scheele, R., and Strom, J.: Vertical and horizontal distributions of the aerosol number concentration and size distribution over the northern Indian Ocean, J. Geophys. Res., 106, 28 629–28 641, 2001.

de Reus, M., Borrmann, S., Bansemer, A., Heymsfield, A. J., Weigel, R., Schiller, C., Mitev, V., Frey, W., Kunkel, D., Kurten, A., Curtius, J., Sitnikov, N. M., Ulanovsky, A., and Ravegnani, F.: Evidence for ice particles in the tropical stratosphere from in-situ measurements, Atmos. Chem. Phys., 9, 6775–6792, 2009.

Deshler, T.: URL `http://www-das.uwyo.edu/~deshler/Data/Aer_Meas_Wy_read_me.htm`, 2011.

Deshler, T., Nardi, B., Adriani, A., Cairo, F., Hansen, G., Fierli, F., Hauchecorne, A., and Pulvirenti, L.: Determining the index of refraction of polar stratospheric

clouds above Andoya (69 ° N) by combining size-resolved concentration and optical scattering measurements, J. Geophys. Res., 105, 3943–3953, 2000.

Deshler, T., Larsen, N., Weissner, C., Schreiner, J., Mauersberger, K., Cairo, F., Adriani, A., Di Donfrancesco, G., Ovarlez, J., Ovarlez, H., Blum, U., Fricke, K. H., and Dornbrack, A.: Large nitric acid particles at the top of an Arctic stratospheric cloud, J. Geophys. Res., 108, doi:10.1029/2003JD003479, 2003.

Deutscher Wetterdienst, ed.: Internationaler Wolkenatlas, Selbstverlag des Deutscher Wetterdienstes, Offenbach am Main, 2. edn., 1990.

Dohm, M. T., Potscavage, A. M., and Niedziela, R. F.: Infrared optical constants for carvone from the Mie inversion of aerosol extinction spectra, Journal of Physical Chemistry A, 108, 5365–5376, doi:10.1021/jp0365559, 2004.

Dudhia, A.: RFM Software User's Manual, Department of Atmospheric, Oceanic and Planetary Physics, University of Oxford, United Kingdom, http://www.atm.ox.ac.uk/rfm, 2004.

Dudhia, A.: URL `ftp.atm.ox.ac.uk/pub/user/dudhia/mipl2`, 2011.

Echle, G., von Clarmann, T., and Oelhaf, H.: Optical and microphysical parameters of the Mt. Pinatubo aerosol as determined from MIPAS-B mid-IR limb emission spectra, J. Geophys. Res., 103, 19 193–19 211, 1998.

Eckermann, S. D., Hoffmann, L., Höpfner, M., Wu, D. L., and Alexander, M. J.: Antarctic NAT PSC belt of June 2003: Observational validation of the mountain wave seeding hypothesis, Geophys. Res. Lett., 36, doi:10.1029/2008GL036629, 2009.

Emeis, S., Forkel, R., Junkermann, W., Schäfer, K., Flentje, H., Gilge, S., Fricke, W., Wiegner, M., Freudenthaler, V., Groß, S., Ries, L., Meinhardt, F., Birmili, W., Münkel, C., Obleitner, F., and Suppan, P.: Measurement and simulation of the 16/17 April 2010 Eyjafjallajökull volcanic ash layer dispersion in the northern Alpine region, Atmos. Chem. Phys., 11, 2689–2701, 2011.

Ewen, G. B. L., Grainger, R. G., Lambert, A., and Baran, A. J.: Infrared radiative transfer modelling in a 3D scattering cloudy atmosphere: Application to limb sounding measurements of cirrus, J. Quant. Spectrosc. Radiat. Transfer, 96, 45–74, 2005.

Fischer, H., Birk, M., Blom, C., Carli, B., Carlotti, M., von Clarmann, T., Delbouille, L., Dudhia, A., Ehhalt, D., Endemann, M., Flaud, J. M., Gessner, R., Kleinert, A., Koopman, R., Langen, J., López-Puertas, M., Mosner, P., Nett, H., Oelhaf, H., Perron, G., Remedios, J., Ridolfi, M., Stiller, G., and Zander, R.: MIPAS: an instrument for atmospheric and climate research, Atmos. Chem. Phys., 8, 2151–2188, 2008.

Flentje, H., Claude, H., Elste, T., Gilge, S., Köhler, U., Plass-Dülmer, C., Steinbrecht, W., Thomas, W., Werner, A., and Fricke, W.: The Eyjafjallajökull eruption in April 2010 - detection of volcanic plume using in-situ measurements, ozone sondes and lidar-ceilometer profiles, Atmos. Chem. Phys., 10, 10 085–10 092, 2010a.

Flentje, H., Heese, B., Reichardt, J., and Thomas, W.: Aerosol profiling using the ceilometer network of the German Meteorological Service, Atmos. Chem. Phys. Discuss., 3, 3643–3673, 2010b.

Francis, G. L., Edwards, D. P., Lambert, A., Halvorson, C. M., Lee-Taylor, J. M., and Gille, J. C.: Forward modeling and radiative transfer for the NASA EOS-Aura High Resolution Dynamics Limb Sounder (HIRDLS) instrument, J. Geophys. Res., 111, doi:10.1029/2005JD006270, 2006.

Francis, P. N., Foot, J. S., and Baran, A. J.: Aircraft measurements of the solar and infrared radiative properties of cirrus and their dependence on ice crystal shape, J. Geophys. Res., 104, 31 685–31 695, 1999.

Frey, W., Borrmann, S., Kunkel, D., Weigel, R., de Reus, M., Schlager, H., Roiger, A., Voigt, C., Hoor, P., Curtius, J., Krämer, M., Schiller, C., Volk, C. M., Homan, C. D., Fierli, F., Di Donfrancesco, G., Ulanovsky, A., Ravegnani, F., Sitnikov, N. M., Viciani, S., D'Amato, F., Shur, G. N., Belyaev, G. V., Law, K. S., and Cairo, F.: In-situ measurements of tropical cloud properties in the West African monsoon: upper tropospheric ice clouds, mesoscale convective system outflow, and subvisual cirrus, Atmos. Chem. Phys. Discuss., 11, 745–812, 2011.

Fridlind, A. M., Ackerman, A. S., Jensen, E. J., Heymsfield, A. J., Poellot, M. R., Stevens, D. E., Wang, D. H., Miloshevich, L. M., Baumgardner, D., Lawson, R. P., Wilson, J. C., Flagan, R. C., Seinfeld, J. H., Jonsson, H. H., VanReken, T. M., Varutbangkul, V., and Rissman, T. A.: Evidence for the predominance of mid-tropospheric aerosols as subtropical anvil cloud nuclei, Science, 304, 718–722, 2004.

Gasteiger, J., Groß, S., Freudenthaler, V., and Wiegner, M.: Volcanic ash from Iceland over Munich: mass concentration retrieved from ground-based remote sensing measurements, Atmos. Chem. Phys., 11, 2209–2223, 2011.

Geppert, G.: Numerische Methoden zur Lösung nichtlinearer, schlecht gestellter 3D-Tomographie-Probleme aus der Atmosphärenfernerkundung, Diplomarbeit, Institut für Angewandte Mathematik, Universität Jena, 2010.

Godson, W. L.: The evaluation of infra-red radiative fluxes due to atmospheric water vapour, Quart. J. Roy. Meteorol. Soc., 79, 367–379, 1953.

Goody, R.: The Transmission of Radiation Through an Inhomogeneous Atmosphere, J. Atmos. Sci., 21, 575–581, 1964.

Goody, R. M. and Yung, Y. L.: Atmospheric Radiation, Theoretical Basis, Oxford University Press, 1989.

Gordley, L. L. and Russell, J. M.: Rapid inversion of limb radiance data using an emissivity growth approximation, Appl. Optics, 20, 807–813, 1981.

Gras, J. L.: AEROSOLS — Climatology of Tropospheric Aerosols, in: Encyclopedia of Atmospheric Sciences, edited by Holton, J. R., pp. 13 – 20, Academic Press, Oxford, 2003.

Greenhough, J., Remedios, J. J., Sembhi, H., and Kramer, L. J.: Towards cloud detection and cloud frequency distributions from MIPAS infra-red observations, Adv. Space Res., 36, 800–806, 2005.

Grimsdell, A. W., Alexander, M. J., May, P. T., and Hoffmann, L.: Model study of waves generated by convection with direct validation via satellite, J. Atmos. Sci., 67, 1617–1631, 2010.

Han, Z. G., Montague, D. C., and Snider, J. R.: Airborne measurements of aerosol extinction in the lower and middle troposphere over Wyoming, USA, Atmos. Environment, 37, 789–802, 2003.

Hansen, J. E. and Travis, L. D.: Light scattering in planetary atmospheres, Space Science Review, 16, 1974.

Hanson, D. and Mauersberger, K.: Solubility and equilibrium vapor pressures of HCL dissolved in polar stratospheric cloud materials: ice and the trihydrate of nitric acid, Geophys. Res. Lett., 15, 1507–1510, 1988.

Hase, F. and Höpfner, M.: Atmospheric ray path modeling for radiative transfer algorithms, Appl. Optics, 38, 3129–3133, 1999.

Hass, H., Jakobs, H., and Memmesheimer, M.: Analysis of a Regional Model (EURAD) Near Surface Gas Concentration Predictions using Observations from Networks, Meteorol. Atmos. Phys., 57, 173–201, 1995.

Heintzenberg, J.: Aerosols — Physics and Chemistry of Aerosols, in: Encyclopedia of Atmospheric Sciences, edited by Holton, J. R., pp. 34 – 40, Academic Press, Oxford, 2003.

Hervig, M. E., Russel, J. M., Gordley, L. L., Daniels, J., Drayson, S. R., and Park, J. H.: Aerosol Effects and Corrections In the Halogen Occultation Experiment, J. Geophys. Res., 100, 1067–1079, 1995.

Hess, M., Koepke, P., and Schult, I.: Optical properties of aerosols and clouds: The software package OPAC, Bulletin of the American Meteorological Society, 79, 831–844, 1998.

Heymsfield, A. J.: Ice Particles Observed In A Cirriform Cloud At -83° C and Implications For Polar Stratospheric Clouds, J. Atmos. Sci., 43, 851–855, 1986.

Hinds, W.: Aerosol Technology. Properties, Behavior, and Measurements of Airbporne Particles, Second Edition, John Wiley & Sons, Ltd., 1999.

Hoffmann, L.: Schnelle Spurengasretrieval für das Satellitenexperiment Envisat MIPAS, Ph.D. thesis, Bergische Universität Wuppertal, Germany, ISSN 0944-2952, 2006.

Hoffmann, L. and Alexander, M. J.: Occurrence frequency of convective gravity waves during the North American thunderstorm season, J. Geophys. Res., 115, doi:10.1029/2010JD014401, 2010.

Hoffmann, L., Kaufmann, M., Spang, R., Müller, R., Remedios, J. J., Moore, D. P., Volk, C. M., von Clarmann, T., and Riese, M.: Envisat MIPAS measurements of CFC-11: retrieval, validation, and climatology, Atmos. Chem. Phys., 8, 3671–3688, 2008.

Hoffmann, L., Weigel, K., Spang, R., Schroeder, S., Arndt, K., Lehmann, C., Kaufmann, M., Ern, M., Preusse, P., Stroh, F., and Riese, M.: CRISTA-NF measurements of water vapor during the SCOUT-O3 Tropical Aircraft Campaign, Adv. Space Res., 43, 74–81, 2009.

Hofmann, D. J. and Deshler, T.: Stratospheric Cloud Observations During Formation of the Antarctic Ozone Hole In 1989, J. Geophys. Res., 96, 2897–2912, 1991.

Höpfner, M.: Study on the impact of polar stratospheric clouds on high resolution mid-IR limb emission spectra, J. Quant. Spectrosc. Radiat. Transfer, 83, 93–107, 2004.

Höpfner, M.: Charakterisierung polarer stratosphärischer Wolken mittels hochauflösender Infrarotspektroskopie, vol. 43 of *Wissenschaftliche Berichte des Instituts für Meteorologie und Klimaforschung der Universität Karlsruhe (TH)*, Universitätsverlag Karlsruhe, Karlsruhe, 2008.

Höpfner, M. and Emde, C.: Comparison of single and multiple scattering approaches for the simulation of limb-emission observations in the mid-IR, J. Quant. Spectrosc. Radiat. Transfer, 91, 275–285, 2005.

Höpfner, M., Pitts, M. C., and Poole, L. R.: Comparison between CALIPSO and MIPAS observations of polar stratospheric clouds, J. Geophys. Res., 114, doi:10.1029/2009JD012114, 2009.

Hummel, J. R., Shettle, E. P., and Longtin, D. R.: A New Background Stratospheric

Aerosol Model for Use in Atmospheric Radiation Models, AFGL-TR-88-0166, Air Force Geophysics Laboratory, Hanscom AFB, MA, 1988.

IPCC: Climate Change 2001: the scientific basis. Contribution of Working Group I to the Third Assessment Report of the Intergovernmental Panel on Climate Change, Cambridge University Press, Cambridge, UK and New York, NY, USA, edited by J. T. Houghton and others, 2001.

ISCCP: URL `http://isccp.giss.nasa.gov`, 2011.

Iwasaki, S., Maruyama, K., Hayashi, M., Ogino, S. Y., Ishimoto, H., Tachibana, Y., Shimizu, A., Matsui, I., Sugimoto, N., Yamashita, K., Saga, K., Iwamoto, K., Kamiakito, Y., Chabangborn, A., Thana, B., Hashizume, M., Koike, T., and Oki, T.: Characteristics of aerosol and cloud particle size distributions in the tropical tropopause layer measured with optical particle counter and lidar, Atmos. Chem. Phys., 7, 3507–3518, 2007.

Jaenicke, R.: 9.3.1 Physical properties, in: Landolt-Börnstein New Series – Group V Geophysics, vol. 4b, pp. 405–420, Springer, 1988.

Jaenicke, R.: Aerosol-cloud interactions, in: Aerosol–Cloud–Climate Interactions, edited by Hobbs, P. V., pp. 33–73, Academic Press, 1993.

Johns, J. W. C. and Noel, M.: Absolute Intensities In $CO_2$: The Laser Bands near 10 $\mu$m, Journal of Molecular Spectroscopy, 156, 403–414, 1992.

Junge, C. E., Manson, J. E., and Chagnon, C. W.: A World-wide Stratospheric Aerosol Layer, Science, 133, 1478–1479, 1961.

Keckhut, P., Hauchecorne, A., Bekki, S., Colette, A., David, C., and Jumelet, J.: Indications of thin cirrus clouds in the stratosphere at mid-latitudes, Atmos. Chem. Phys., 5, 3407–3414, 2005.

Kerker, M.: The Scattering of Light and Other Electromagnetic Radiation, Academic Press, New York, 1969.

Kerridge, B.: Consideration of mission studying chemistry of the UTLS – Final Report, Esa contract no 15457/01/nl/mm, ESA, 2004.

Kim, Y. J., Boatman, J. F., Gunter, R. L., Wellman, D. L., and Wilkinson, S. W.: Vertical distribution of atmospheric aerosol size distribution over south central New Mexico, Atmos. Environment, 27, 1351–1362, 1993.

Kivekäs, N., Sun, J., Zhan, M., Kerminen, V. M., Hyvarinen, A., Komppula, M., Viisanen, Y., Hong, N., Zhang, Y., Kulmala, M., Zhang, X. C., Deli-Geer, and Lihavainen, H.: Long term particle size distribution measurements at Mount Waliguan, a high-altitude site in inland China, Atmos. Chem. Phys., 9, 5461–5474, 2009.

Kleinert, A., Aubertin, G., Perron, G., Birk, M., Wagner, G., Hase, F., Nett, H., and Poulin, R.: MIPAS Level 1B algorithms overview: operational processing and characterization, Atmos. Chem. Phys., 7, 1395–1406, 2007.

Krämer, M., C. Schiller, C., Afchine, A., Bauer, R., Gensch, I., Mangold, A., Schlicht, S., Spelten, N., Sitnikov, N., Borrmann, S., de Reus, M., and Spichtinger, P.: Ice supersaturations and cirrus cloud crystal numbers, Atmos. Chem. Phys., 9, 3505–3522, 2009.

Krejci, R., Strom, J., de Reus, M., Hoor, P., Williams, J., Fischer, H., and Hansson, H. C.: Evolution of aerosol properties over the rain forest in Surinam, South America, observed from aircraft during the LBA-CLAIRE 98 experiment, J. Geophys. Res., 108, doi:10.1029/2001JD001375, 2003.

Larsen, N., Knudsen, B. M., Svendsen, S. H., Deshler, T., Rosen, J. M., Kivi, R., Weisser, C., Schreiner, J., Mauerberger, K., Cairo, F., Ovarlez, J., Oelhaf, H., and Spang, R.: Formation of solid particles in synoptic-scale Arctic PSCs in early winter 2002/2003, Atmos. Chem. Phys., 4, 2001–2013, 2004.

Lawson, R. P., Baker, B. A., Schmitt, C. G., and Jensen, T. L.: An overview of microphysical properties of Arctic clouds observed in May and July 1998 during FIRE ACE, J. Geophys. Res., 106, 14 989–15 014, 2001.

Lawson, R. P., Baker, B., Pilson, B., and Mo, Q. X.: In situ observations of the microphysical properties of wave, cirrus, and anvil clouds. Part II: Cirrus clouds, J. Atmos. Sci., 63, 3186–3203, 2006.

Lawson, R. P., Pilson, B., Baker, B., Mo, Q., Jensen, E., Pfister, L., and Bui, P.: Aircraft measurements of microphysical properties of subvisible cirrus in the tropical tropopause layer, Atmos. Chem. Phys., 8, 1609–1620, 2008.

Lee, J., Yang, P., Dessler, A. E., Gao, B.-C., and Platnick, S.: Distribution and Radiative Forcing of Tropical Thin Cirrus Clouds, J. Atmos. Sci., 66, 3721–3731, 2009.

Liou, K. N.: An Introduction to Atmospheric Radiation, Academic Press, Amsterdam, Boston, London, New York, Oxford, Paris, San Diego, San Francisco, Singapore, Sydney, Tokyo, second edn., 2002.

Lynch, D. K., Sassen, K., Starr, D., and Stephens, G., eds.: Cirrus, Oxford University Press, 2002.

Marshall, B. T., Gordley, L. L., and Chu, D. A.: BANDPAK: Algorithms for Modeling Broadband Transmission and Radiance, J. Quant. Spectrosc. Radiat. Transfer, 52, 581–599, 1994.

McFarquhar, G. M., Heymsfield, A. J., Spinhirne, J., and Hart, B.: Thin and subvisual tropopause tropical cirrus: Observations and radiative impacts, J. Atmos. Sci., 57, 1841–1853, 2000.

Mendrok, J.: The SARTre Model for Radiative Transfer in Spherical Atmosphere and its Application to the Derivation of Cirrus Cloud Properties, Ph.D. thesis, Freie Universität Berlin, Germany, 2006.

Mergenthaler, J. L., Roche, A. E., Kumer, J. B., and Ely, G. A.: Cryogenic Limb Array Etalon Spectrometer observations of tropical cirrus, J. Geophys. Res., 104, 22 183–22 194, 1999.

Mie, G.: Beiträge zur Optik trüber Medien, speziell kolloidaler Metallösungen, Annalen der Physik, 330, 376–445, 1908.

Murphy, D. M., Cziczo, D. J., Froyd, K. D., Hudson, P. K., Matthew, B. M., Middlebrook, A. M., Peltier, R. E., Sullivan, A., Thomson, D. S., and Weber, R. J.: Single-particle mass spectrometry of tropospheric aerosol particles, J. Geophys. Res., 111, doi:10.1029/2006JD007340, 2006.

NASA: URL `http://www-calipso.larc.nasa.gov/products/lidar/browse_images/show_calendar.php`, 2011.

NERC Satellite Receiving Station: URL `http://www.sat.dundee.ac.uk`, 2011.

Nyeki, S., Li, F., Weingartner, E., Streit, N., Colbeck, I., Gaggeler, H. W., and Baltensperger, U.: The background aerosol size distribution in the free troposphere: An analysis of the annual cycle at a high-alpine site, J. Geophys. Res., 103, 31 749–31 761, 1998.

Paso, R., Kauppinen, J., and Anttila, R.: Infrared Spectrum of $CO_2$ in the Region of the Bending Fundamental $\nu_2$, Journal of Molecular Spectroscopy, 79, 236–253, 1980.

Peter, T.: Microphysics and heterogeneous chemistry of polar stratospheric clouds, Annual Review of Physical Chemistry, 48, 785–822, 1997.

Peter, T., Luo, B. P., Wirth, M., Kiemle, C., Flentje, H., Yushkov, V. A., Khattatov, V., Rudakov, V., Thomas, A., Borrmann, S., Toci, G., Mazzinghi, P., Beuermann, J., Schiller, C., Cairo, F., Di Donfrancesco, G., Adriani, A., Volk, C. M., Strom, J., Noone, K., Mitev, V., MacKenzie, R. A., Carslaw, K. S., Trautmann, T., Santacesaria, V., and Stefanutti, L.: Ultrathin Tropical Tropopause Clouds (UTTCs): I. Cloud morphology and occurrence, Atmos. Chem. Phys., 3, 1083–1091, 2003.

Petty, G. W.: A first Course in Atmospheric Radiation, Sundog Publishing, 2006.

Petzold, A., Hoell, C., Karcher, B., Beuermann, J., Schiller, C., Ziereis, H., and

Schlager, H.: In situ observations of aerosol properties above ice saturation in the polar tropopause region, J. Geophys. Res., 105, 29 387–29 395, 2000.

Petzold, A., Fiebig, M., Flentje, H., Keil, A., Leiterer, U., Schroder, F., Stifter, A., Wendisch, M., and Wendling, P.: Vertical variability of aerosol properties observed at a continental site during the Lindenberg Aerosol Characterization Experiment (LACE 98), J. Geophys. Res., 107, doi:10.1029/2001JD001043, 2002.

Pitts, M. C., Poole, L. R., and Thomason, L. W.: CALIPSO polar stratospheric cloud observations: second-generation detection algorithm and composition discrimination, Atmos. Chem. Phys., 9, 7577–7589, 2009.

Press, W. H., Teukolsky, S. A., Vetterling, W. T., and Flannery, B. P.: Numerical Recipes in C, Cambridge University Press, 3rd ed. edn., 2007.

Remedios, J. J.: Extreme Atmospheric Constituent Profiles for MIPAS, in: Proceedings of ESAMS '99 - European Symposium on Atmospheric Measurements from Space, pp. 779–782, 1999.

Remedios, J. J., Leigh, R. J., Waterfall, A. M., Moore, D. P., Sembhi, H., Parkes, I., Greenhough, J., Chipperfield, M., and Hauglustaine, D.: MIPAS reference atmospheres and comparisons to V4.61/V4.62 MIPAS level 2 geophysical data sets, Atmos. Chem. Phys. Discuss., 7, 9973–10 017, 2007.

Riese, M.: Das CRISTA-Meßsystem: Struktur und Anwendungen, Ph.D. thesis, Universität Wuppertal, 1994.

Riese, M., Preusse, P., Spang, R., Ern, M., Jarisch, M., Grossmann, K.-U., and Offermann, D.: Measurements of trace gases by the Cryogenic Infrared Spectrometers and Telescopes for the Atmosphere (CRISTA) experiment, Adv. Space Res., 19, 563–566, 1997.

Riese, M., Spang, R., Preusse, P., Ern, M., Jarisch, M., Offermann, D., and Grossmann, K. U.: Cryogenic Infrared Spectrometers and Telescopes for the Atmosphere (CRISTA) data processing and atmospheric temperature and trace gas retrieval, J. Geophys. Res., 104, 16 349–16 367, 1999.

Rodgers, C. D.: Inverse Methods for Atmospheric Sounding: Theory and Practice, vol. 2 of *Series on Atmospheric, Oceanic and Planetary Physics*, World Scientific, 2000.

Rosenfield, J. E., Considine, D. B., Schoeberl, M. R., and Browell, E. V.: The impact of subvisible cirrus clouds near the tropical tropopause on stratospheric water vapor, Geophys. Res. Lett., 25, 1883–1886, 1998.

Rossow, W. B. and Schiffer, R. A.: Advances in understanding clouds from ISCCP, Bulletin of the American Meteorological Society, 80, 2261–2287, 1999.

Rother, T.: Electromagnetic Wave Scattering on Nonspherical Particles, Springer Series in Optical Sciences, Springer, Berlin, Heidelberg, 2009.

Rother, T., Schmidt, K., Wauer, J., Shcherbakov, V., and Gayet, J. F.: Light scattering on Chebyshev particles of higher order, Appl. Optics, 45, 6030–6037, 2006.

Rothman, L. S., Gordon, I. E., Barbe, A., Benner, D. C., Bernath, P. E., Birk, M., Boudon, V., Brown, L. R., Campargue, A., Champion, J. P., Chance, K., Coudert, L. H., Dana, V., Devi, V. M., Fally, S., Flaud, J. M., Gamache, R. R., Goldman, A., Jacquemart, D., Kleiner, I., Lacome, N., Lafferty, W. J., Mandin, J. Y., Massie, S. T., Mikhailenko, S. N., Miller, C. E., Moazzen-Ahmadi, N., Naumenko, O. V., Nikitin, A. V., Orphal, J., Perevalov, V. I., Perrin, A., Predoi-Cross, A., Rinsland, C. P., Rotger, M., Simeckova, M., Smith, M. A. H., Sung, K., Tashkun, S. A., Tennyson, J., Toth, R. A., Vandaele, A. C., and Vander Auwera, J.: The HITRAN 2008 molecular spectroscopic database, J. Quant. Spectrosc. Radiat. Transfer, 110, 533–572, 2009.

Sassen, K. and Campbell, J. R.: A midlatitude cirrus cloud climatology from the facility for atmospheric remote sensing. Part I: Macrophysical and synoptic properties, J. Atmos. Sci., 58, 481–496, 2001.

Sassen, K., Griffin, M. K., and Dodd, G. C.: Optical-scattering and Microphysical Properties of Subvisual Cirrus Clouds, and Climatic Implications, J. Appl. Met., 28, 91–98, 1989.

Schmeissner, T., Krejci, R., Ström, J., Birmili, W., Wiedensohler, A., Hochschild, G., Gross, J., Hoffmann, P., and Calderon, S.: Analysis of number size distributions of tropical free tropospheric aerosol particles observed at Pico Espejo (4765 m a.s.l.), Venezuela, Atmos. Chem. Phys., 11, 3319–3332, 2011.

Schneider, J., Hings, S. S., Hock, B. N., Weimer, S., Borrmann, S., Fiebig, M., Petzold, A., Busen, R., and Karcher, B.: Aircraft-based operation of an aerosol mass spectrometer: Measurements of tropospheric aerosol composition, Journal of Aerosol Science, 37, 839–857, 2006.

Schroeder, F., Karcher, B., Fiebig, M., and Petzold, A.: Aerosol states in the free troposphere at northern midlatitudes, J. Geophys. Res., 107, doi:10.1029/2000JD000194, 2002.

Schumann, U., Weinzierl, B., Reitebuch, O., Schlager, H., Minikin, A., Forster, C., Baumann, R., Sailer, T., Graf, K., Mannstein, H., Voigt, C., Rahm, S., Simmet, R., Scheibe, M., Lichtenstern, M., Stock, P., Rüba, H., Schäuble, D., Tafferner, A.,

Rautenhaus, M., Gerz, T., Ziereis, H., Krautstrunk, M., Mallaun, C., Gayet, J.-F., Lieke, K., Kandler, K., Ebert, M., Weinbruch, S., Stohl, A., Gasteiger, J., Groß, S., Freudenthaler, V., Wiegner, M., Ansmann, A., Tesche, M., Olafsson, H., and Sturm, K.: Airborne observations of the Eyjafjalla volcano ash cloud over Europe during air space closure in April and May 2010, Atmos. Chem. Phys., 11, 2245–2279, 2011.

Solomon, S., Garcia, R. R., Rowland, F. S., and Wuebbles, D. J.: On the depletion of Antarctic ozone, Nature, 321, 755–758, 1986.

Solomon, S., Borrmann, S., Garcia, R. R., Portmann, R., Thomason, L., Poole, L. R., Winker, D., and McCormick, M. P.: Heterogeneous chlorine chemistry in the tropopause region, J. Geophys. Res., 102, 21 411–21 429, 1997.

Spang, R. and Remedios, J. J.: Observations of a distinctive infra-red spectral feature in the atmospheric spectra of polar stratospheric clouds measured by the CRISTA instrument, Geophys. Res. Lett., 30, doi:10.1029/2003GL017231, 2003.

Spang, R., Eidmann, G., Riese, M., Offermann, D., Preusse, P., Pfister, L., and Wang, P. H.: CRISTA observations of cirrus clouds around the tropopause, J. Geophys. Res., 107, doi:10.1029/2001JD000698, 2002.

Spang, R., Remedios, J. J., and Barkley, M. P.: Colour indices for the detection and differentiation of cloud type in infra-red limb emission spectra, Adv. Space Res., 33, 1041–1047, 2004.

Spang, R., Griessbach, S., Höpfner, M., Dudhia, A., Hurley, J., Siddans, R., Waterfall, A., Remedios, J. J., and Sembhi., H.: Technical Note: Retrievability of MIPAS cloud parameter, Esa-esrin contract no. 20601/07/i-ol, Forschungszentrum Jülich, 2008.

Spang, R., Arndt, K., Dudhia, A., Höpfner, M., Hoffmann, L., Hurley, J., Grainger, R. G., Griessbach, S., Poulsen, C., Remedios, J., Riese, M., Sembhi, H., Siddans, R., Waterfall, A., and Zehner, C.: A Processor for Fast Cloud Parameter Retrievals of MIPAS/Envisat: Overview, Blind Tests, and Validation Results on Cloud Detection, Atmos. Chem. Phys. Discuss., submitted, 2011.

Steele, H. M., Eldering, A., Sen, B., Toon, G. C., Mills, F. P., and Kahn, B. H.: Retrieval of stratospheric aerosol size and composition information from solar infrared transmission spectra, Appl. Optics, 42, 2140–2154, 2003.

Stiller, G. P.: The Karlsruhe Optimized and Precise Radiative Transfer Algorithm (KOPRA), Tech. Rep. FZKA-6487, Forschungszentrum Karlsruhe, 2000.

Stiller, G. P., von Clarmann, T., Funke, B., Glatthor, N., Hase, F., Höpfner, M., and Linden, A.: Sensitivity of trace gas abundances retrievals from infrared limb emission spectra to simplifying approximations in radiative transfer modelling, Appl. Optics, 41, 249–280, 2002.

Stohl, A., Prata, A. J., Eckhardt, S., Clarisse, L., Durant, A., Henne, S., Kristiansen, N. I., Minikin, A., Schumann, U., Seibert, P., Stebel, K., Thomas, H. E., Thorsteinsson, T., Tørseth, K., and Weinzierl, B.: Determination of time- and height-resolved volcanic ash emissions and their use for quantitative ash dispersion modeling: the 2010 Eyjafjallajökull eruption, Atmos. Chem. Phys., 11, 4333–4351, 2011.

Thomas, H. E. and Prata, A. J.: Sulphur dioxide as a volcanic ash proxy during the AprilMay 2010 eruption of Eyjafjallajökull Volcano, Iceland, Atmos. Chem. Phys., 11, 6871–6880, 2011.

Thomason, L. and Peter, T., eds.: Stratospheric Processes And their Role in Climate SPARC – Assessment of Stratospheric Aerosol Properties (ASAP), WMO, 2006.

Tian, L., Heymsfield, G. M., Heymsfield, A. J., Bansemer, A., Li, L. H., Twohy, C. H., and Srivastava, R. C.: A Study of Cirrus Ice Particle Size Distribution Using TC4 Observations, J. Atmos. Sci., 67, 195–216, 2010.

Toon, O. B., Tolbert, M. A., Koehler, B. G., Middlebrook, A. M., and Jordan, J.: Infrared optical constants of $H_2O$, ice, amorphous nitric acid solutions, and nitric acid hydrates, J. Geophys. Res., 99, 25 631–25 654, 1994.

Ungermann, J.: Tomographic reconstruction of atmospheric volumes from infrared limb-imager measurements, Ph.D. thesis, Bergische Universität Wuppertal, Germany, ISSN 1866-1793, 2011.

Vaden, T. D., Song, C., Zaveri, R. A., Imre, D., and Zelenyuk, A.: Morphology of mixed primary and secondary organic particles and the adsorption of spectator organic gases during aerosol formation, Proceedings of the National Academy of Sciences of the United States of America, 107, 6658–6663, 2010.

Venzac, H., Sellegri, K., Villani, P., Picard, D., and Laj, P.: Seasonal variation of aerosol size distributions in the free troposphere and residual layer at the puy de Dome station, France, Atmos. Chem. Phys., 9, 1465–1478, 2009.

Virtanen, A., Joutsensaari, J., Koop, T., Kannosto, J., Yli-Pirila, P., Leskinen, J., Makela, J. M., Holopainen, J. K., Pöschl, U., Kulmala, M., Worsnop, D. R., and Laaksonen, A.: An amorphous solid state of biogenic secondary organic aerosol particles, Nature, 467, 824–827, 2010.

von Clarmann, T., Höpfner, M., Funke, B., López-Puertas, M., Dudhia, A., Jay, V., Schreier, F., Ridolfi, M., Ceccherini, S., Kerridge, B., Reburn, J., and Siddans, R.: Modelling of atmospheric mid-infrared radiative transfer: the AMIL2DA algorithm intercomparison experiment, J. Quant. Spectrosc. Radiat. Transfer, 78, 381–407, 2003.

Wagner, R., Benz, S., Mohler, O., Saathoff, H., Schnaiter, M., and Schurath, U.: Mid-infrared extinction spectra and optical constants of supercooled water droplets, Journal of Physical Chemistry A, 109, 7099–7112, 2005.

Wang, P.-H., Minnis, P., McCormick, M. P., Kent, G. S., and Skeens, K. M.: A 6-year climatology of cloud occurrence frequency from Stratospheric Aerosol and Gas Experiment II observations (1985-1990), J. Geophys. Res., 101, 29 407–29 430, 1996.

Wang, Z.-X.: Iteratively regularised methods for inverse problems in atmospheric remote sensing, Diplomarbeit, Ecole Nationale Superieure de Techniques Avancees, 2010.

Warren, S. G. and Brandt, R. E.: Optical constants of ice from the ultraviolet to the microwave: A revised compilation, J. Geophys. Res., 113, 2008.

Weigel, K.: Infrared limb emission observations of the upper troposphere, lower stratosphere with high spatial resolution, Ph.D. thesis, Bergische Universität Wuppertal, Germany, 2009.

Weigel, K., Riese, M., Hoffmann, L., Hoefer, S., Kalicinsky, C., Knieling, P., Olschewski, F., Preusse, P., Stroh, F., Spang, R., and Volk, C. M.: CRISTA-NF measurements during the AMMA-SCOUT-O3 aircraft campaign, Atmos. Meas. Tech., 3, 1437–1455, 2010.

Weinreb, M. P. and Neuendorffer, A. C.: Method to Apply Homogeneous-path Transmittance Models to Inhomogenous Atmospheres, J. Atmos. Sci., 30, 662–666, 1973.

Yang, P., Wei, H. L., Huang, H. L., Baum, B. A., Hu, Y. X., Kattawar, G. W., Mishchenko, M. I., and Fu, Q.: Scattering and absorption property database for nonspherical ice particles in the near- through far-infrared spectral region, Appl. Optics, 44, 5512–5523, 2005.

Yu, F. Q., Luo, G., Bates, T. S., Anderson, B., Clarke, A., Kapustin, V., Yantosca, R. M., Wang, Y. X., and Wu, S. L.: Spatial distributions of particle number concentrations in the global troposphere: Simulations, observations, and implications for nucleation mechanisms, J. Geophys. Res., 115, doi:10.1029/2009JD013473, 2010.

Yuan, T., Remer, L. A., and Yu, H.: Microphysical, macrophysical and radiative signatures of volcanic aerosols in trade wind cumulus observed by the A-Train, Atmos. Chem. Phys., 11, 7119–7132, 2011.

Zhang, Y., Macke, A., and Albers, F.: Effect of crystal size spectrum and crystal shape on stratiform cirrus radiative forcing, Atmospheric Research, 52, 59–75, 1999.

# Acknowledgements

First of all my sincerest thanks go to Prof. Dr. Martin Riese and Dr. Reinhold Spang, who offered me the opportunity to write this thesis at the Institute for Energy and Climate Research – Stratosphere (IEK-7) at Forschungszentrum Jülich and supported me at all times. Many thanks go also to Prof. Dr. Ralf Koppmann for the supervision of this thesis as the second examiner.

For his substantial support to my thesis I would like to thank Lars Hoffmann, who taught me how to use JURASSIC and answered my thousands of questions on atmospheric radiative transfer and on programming patiently and always encouraged me. He also contributed to the success of this thesis by proofreading the manuscript.

Special thanks go Michael Höpfner for providing KOPRA calculations and answering questions on radiative transfer and scattering problems.

I would also like to thank Anu Dudhia for providing RFM as well as Hendrik Elbern and Elmar Friese for providing the EURAD simulations.

Many thanks go to Reinhold Spang, Marc von Hobe and Rolf Müller for carefully proofreading and for always listening to me and discussing with me. I also thank J. Carter-Sigglow for revising the grammar and style of parts of the manuscript

In particular I would like to thank all IEK-7 members who create the inspiring working atmosphere and the good mood at lunch and coffee breaks.

Special thanks go to the Pommrich family for showing me that there is more life in Jülich than just the Forschungszentrum.

Finally I would like to thank my parents, my sister and my friends for supporting me at all times.

1. **Einsatz von multispektralen Satellitenbilddaten in der Wasserhaushalts- und Stoffstrommodellierung – dargestellt am Beispiel des Rureinzugsgebietes**
   von C. Montzka (2008), XX, 238 Seiten
   ISBN: 978-3-89336-508-1

2. **Ozone Production in the Atmosphere Simulation Chamber SAPHIR**
   by C. A. Richter (2008), XIV, 147 pages
   ISBN: 978-3-89336-513-5

3. **Entwicklung neuer Schutz- und Kontaktierungsschichten für Hochtemperatur-Brennstoffzellen**
   von T. Kiefer (2008), 138 Seiten
   ISBN: 978-3-89336-514-2

4. **Optimierung der Reflektivität keramischer Wärmedämmschichten aus Yttrium-teilstabilisiertem Zirkoniumdioxid für den Einsatz auf metallischen Komponenten in Gasturbinen**
   von A. Stuke (2008), X, 201 Seiten
   ISBN: 978-3-89336-515-9

5. **Lichtstreuende Oberflächen, Schichten und Schichtsysteme zur Verbesserung der Lichteinkopplung in Silizium-Dünnschichtsolarzellen**
   von M. Berginski (2008), XV, 171 Seiten
   ISBN: 978-3-89336-516-6

6. **Politikszenarien für den Klimaschutz IV – Szenarien bis 2030**
   hrsg.von P. Markewitz, F. Chr. Matthes (2008), 376 Seiten
   ISBN 978-3-89336-518-0

7. **Untersuchungen zum Verschmutzungsverhalten rheinischer Braunkohlen in Kohledampferzeugern**
   von A. Schlüter (2008), 164 Seiten
   ISBN 978-3-89336-524-1

8. **Inorganic Microporous Membranes for Gas Separation in Fossil Fuel Power Plants**
   by G. van der Donk (2008), VI, 120 pages
   ISBN: 978-3-89336-525-8

9. **Sinterung von Zirkoniumdioxid-Elektrolyten im Mehrlagenverbund der oxidkeramischen Brennstoffzelle (SOFC)**
   von R. Mücke (2008), VI, 165 Seiten
   ISBN: 978-3-89336-529-6

10. **Safety Considerations on Liquid Hydrogen**
    by K. Verfondern (2008), VIII, 167 pages
    ISBN: 978-3-89336-530-2

11. **Kerosinreformierung für Luftfahrtanwendungen**
von R. C. Samsun (2008), VII, 218 Seiten
ISBN: 978-3-89336-531-9

12. **Der 4. Deutsche Wasserstoff Congress 2008 – Tagungsband**
hrsg. von D. Stolten, B. Emonts, Th. Grube (2008), 269 Seiten
ISBN: 978-3-89336-533-3

13. **Organic matter in Late Devonian sediments as an indicator for environmental changes**
by M. Kloppisch (2008), XII, 188 pages
ISBN: 978-3-89336-534-0

14. **Entschwefelung von Mitteldestillaten für die Anwendung in mobilen Brennstoffzellen-Systemen**
von J. Latz (2008), XII, 215 Seiten
ISBN: 978-3-89336-535-7

15. **RED-IMPACT**
**Impact of Partitioning, Transmutation and Waste Reduction Technologies on the Final Nuclear Waste Disposal**
SYNTHESIS REPORT
ed. by W. von Lensa, R. Nabbi, M. Rossbach (2008), 178 pages
ISBN 978-3-89336-538-8

16. **Ferritic Steel Interconnectors and their Interactions with Ni Base Anodes in Solid Oxide Fuel Cells (SOFC)**
by J. H. Froitzheim (2008), 169 pages
ISBN: 978-3-89336-540-1

17. **Integrated Modelling of Nutrients in Selected River Basins of Turkey**
Results of a bilateral German-Turkish Research Project
project coord. M. Karpuzcu, F. Wendland (2008), XVI, 183 pages
ISBN: 978-3-89336-541-8

18. **Isotopengeochemische Studien zur klimatischen Ausprägung der Jüngeren Dryas in terrestrischen Archiven Eurasiens**
von J. Parplies (2008), XI, 155 Seiten, Anh.
ISBN: 978-3-89336-542-5

19. **Untersuchungen zur Klimavariabilität auf dem Tibetischen Plateau - Ein Beitrag auf der Basis stabiler Kohlenstoff- und Sauerstoffisotope in Jahrringen von Bäumen waldgrenznaher Standorte**
von J. Griessinger (2008), XIII, 172 Seiten
ISBN: 978-3-89336-544-9

20. **Neutron-Irradiation + Helium Hardening & Embrittlement Modeling of 9%Cr-Steels in an Engineering Perspective (HELENA)**
by R. Chaouadi (2008), VIII, 139 pages
ISBN: 978-3-89336-545-6

21. **in Bearbeitung**

22. **Verbundvorhaben APAWAGS (AOEV und Wassergenerierung) – Teilprojekt: Brennstoffreformierung – Schlussbericht**
von R. Peters, R. C. Samsun, J. Pasel, Z. Porš, D. Stolten (2008), VI, 106 Seiten
ISBN: 978-3-89336-547-0

23. **FREEVAL**
Evaluation of a Fire Radiative Power Product derived from Meteosat 8/9 and Identification of Operational User Needs
Final Report
project coord. M. Schultz, M. Wooster (2008), 139 pages
ISBN: 978-3-89336-549-4

24. **Untersuchungen zum Alkaliverhalten unter Oxycoal-Bedingungen**
von C. Weber (2008), VII, 143, XII Seiten
ISBN: 978-3-89336-551-7

25. **Grundlegende Untersuchungen zur Freisetzung von Spurstoffen, Heißgaschemie, Korrosionsbeständigkeit keramischer Werkstoffe und Alkalirückhaltung in der Druckkohlenstaubfeuerung**
von M. Müller (2008), 207 Seiten
ISBN: 978-3-89336-552-4

26. **Analytik von ozoninduzierten phenolischen Sekundärmetaboliten in *Nicotiana tabacum* L. cv Bel W3 mittels LC-MS**
von I. Koch (2008), III, V, 153 Seiten
ISBN 978-3-89336-553-1

27. **IEF-3 Report 2009. Grundlagenforschung für die Anwendung**
(2009), ca. 230 Seiten
ISBN: 978-3-89336-554-8

28. **Influence of Composition and Processing in the Oxidation Behavior of MCrAlY-Coatings for TBC Applications**
by J. Toscano (2009), 168 pages
ISBN: 978-3-89336-556-2

29. **Modellgestützte Analyse signifikanter Phosphorbelastungen in hessischen Oberflächengewässern aus diffusen und punktuellen Quellen**
von B. Tetzlaff (2009), 149 Seiten
ISBN: 978-3-89336-557-9

30. **Nickelreaktivlot / Oxidkeramik – Fügungen als elektrisch isolierende Dichtungskonzepte für Hochtemperatur-Brennstoffzellen-Stacks**
von S. Zügner (2009), 136 Seiten
ISBN: 978-3-89336-558-6

31. **Langzeitbeobachtung der Dosisbelastung der Bevölkerung in radioaktiv kontaminierten Gebieten Weißrusslands – Korma-Studie**
von H. Dederichs, J. Pillath, B. Heuel-Fabianek, P. Hill, R. Lennartz (2009), Getr. Pag.
ISBN: 978-3-89336-532-3

32. **Herstellung von Hochtemperatur-Brennstoffzellen über physikalische Gasphasenabscheidung**
von N. Jordán Escalona (2009), 148 Seiten
ISBN: 978-3-89336-532-3

33. **Real-time Digital Control of Plasma Position and Shape on the TEXTOR Tokamak**
by M. Mitri (2009), IV, 128 pages
ISBN: 978-3-89336-567-8

34. **Freisetzung und Einbindung von Alkalimetallverbindungen in kohlebefeuerten Kombikraftwerken**
von M. Müller (2009), 155 Seiten
ISBN: 978-3-89336-568-5

35. **Kosten von Brennstoffzellensystemen auf Massenbasis in Abhängigkeit von der Absatzmenge**
von J. Werhahn (2009), 242 Seiten
ISBN: 978-3-89336-569-2

36. **Einfluss von Reoxidationszyklen auf die Betriebsfestigkeit von anodengestützten Festoxid-Brennstoffzellen**
von M. Ettler (2009), 138 Seiten
ISBN: 978-3-89336-570-8

37. **Großflächige Plasmaabscheidung von mikrokristallinem Silizium für mikromorphe Dünnschichtsolarmodule**
von T. Kilper (2009), XVII, 154 Seiten
ISBN: 978-3-89336-572-2

38. **Generalized detailed balance theory of solar cells**
by T. Kirchartz (2009), IV, 198 pages
ISBN: 978-3-89336-573-9

39. **The Influence of the Dynamic Ergodic Divertor on the Radial Electric Field at the Tokamak TEXTOR**
von J. W. Coenen (2009), xii, 122, XXVI pages
ISBN: 978-3-89336-574-6

40. **Sicherheitstechnik im Wandel Nuklearer Systeme**
von K. Nünighoff (2009), viii, 215 Seiten
ISBN: 978-3-89336-578-4

41. **Pulvermetallurgie hochporöser NiTi-Legierungen für Implanat- und Dämpfungsanwendungen**
von M. Köhl (2009), XVII, 199 Seiten
ISBN: 978-3-89336-580-7

42. **Einfluss der Bondcoatzusammensetzung und Herstellungsparameter auf die Lebensdauer von Wärmedämmschichten bei zyklischer Temperaturbelastung**
von M. Subanovic (2009), 188, VI Seiten
ISBN: 978-3-89336-582-1

43. **Oxygen Permeation and Thermo-Chemical Stability of Oxygen Permeation Membrane Materials for the Oxyfuel Process**
by A. J. Ellett (2009), 176 pages
ISBN: 978-3-89336-581-4

44. **Korrosion von polykristallinem Aluminiumoxid (PCA) durch Metalljodidschmelzen sowie deren Benetzungseigenschaften**
von S. C. Fischer (2009), 148 Seiten
ISBN: 978-3-89336-584-5

45. **IEF-3 Report 2009. Basic Research for Applications**
(2009), 217 Seiten
ISBN: 978-3-89336-585-2

46. **Verbundvorhaben ELBASYS (Elektrische Basissysteme in einem CFK-Rumpf) - Teilprojekt: Brennstoffzellenabgase zur Tankinertisierung - Schlussbericht**
von R. Peters, J. Latz, J. Pasel, R. C. Samsun, D. Stolten
(2009), xi, 202 Seiten
ISBN: 978-3-89336-587-6

47. **Aging of $^{14}$C-labeled Atrazine Residues in Soil: Location, Characterization and Biological Accessibility**
by N. D. Jablonowski (2009), IX, 104 pages
ISBN: 978-3-89336-588-3

48. **Entwicklung eines energetischen Sanierungsmodells für den europäischen Wohngebäudesektor unter dem Aspekt der Erstellung von Szenarien für Energie- und $CO_2$ - Einsparpotenziale bis 2030**
von P. Hansen (2009), XXII, 281 Seiten
ISBN: 978-3-89336-590-6

49. **Reduktion der Chromfreisetzung aus metallischen Interkonnektoren für Hochtemperaturbrennstofzellen durch Schutzschichtsysteme**
von R. Trebbels (2009), iii, 135 Seiten
ISBN: 978-3-89336-591-3

50. **Bruchmechanische Untersuchung von Metall / Keramik-Verbundsystemen für die Anwendung in der Hochtemperaturbrennstoffzelle**
von B. Kuhn (2009), 118 Seiten
ISBN: 978-3-89336-592-0

51. **Wasserstoff-Emissionen und ihre Auswirkungen auf den arktischen Ozonverlust**
**Risikoanalyse einer globalen Wasserstoffwirtschaft**
von T. Feck (2009), 180 Seiten
ISBN: 978-3-89336-593-7

52. **Development of a new Online Method for Compound Specific Measurements of Organic Aerosols**
by T. Hohaus (2009), 156 pages
ISBN: 978-3-89336-596-8

53. **Entwicklung einer FPGA basierten Ansteuerungselektronik für Justageeinheiten im Michelson Interferometer**
von H. Nöldgen (2009), 121 Seiten
ISBN: 978-3-89336-599-9

54. **Observation – and model – based study of the extratropical UT/LS**
by A. Kunz (2010), xii, 120, xii pages
ISBN: 978-3-89336-603-3

55. **Herstellung polykristalliner Szintillatoren für die Positronen-Emissions-Tomographie (PET)**
von S. K. Karim (2010), VIII, 154 Seiten
ISBN: 978-3-89336-610-1

56. **Kombination eines Gebäudekondensators mit H2-Rekombinatorelementen in Leichtwasserreaktoren**
von S. Kelm (2010), vii, 119 Seiten
ISBN: 978-3-89336-611-8

57. **Plant Leaf Motion Estimation Using A 5D Affine Optical Flow Model**
by T. Schuchert (2010), X, 143 pages
ISBN: 978-3-89336-613-2

58. **Tracer-tracer relations as a tool for research on polar ozone loss**
by R. Müller (2010), 116 pages
ISBN: 978-3-89336-614-9

59. **Sorption of polycyclic aromatic hydrocarbon (PAH) to Yangtze River sediments and their components**
by J. Zhang (2010), X, 109 pages
ISBN: 978-3-89336-616-3

60. **Weltweite Innovationen bei der Entwicklung von CCS-Technologien und Möglichkeiten der Nutzung und des Recyclings von $CO_2$**
Studie im Auftrag des BMWi
von W. Kuckshinrichs et al. (2010), X, 139 Seiten
ISBN: 978-3-89336-617-0

61. **Herstellung und Charakterisierung von sauerstoffionenleitenden Dünnschichtmembranstrukturen**
von M. Betz (2010), XII, 112 Seiten
ISBN: 978-3-89336-618-7

62. **Politikszenarien für den Klimaschutz V – auf dem Weg zum Strukturwandel, Treibhausgas-Emissionsszenarien bis zum Jahr 2030**
hrsg. von P. Hansen, F. Chr. Matthes (2010), 276 Seiten
ISBN: 978-3-89336-619-4

63. **Charakterisierung Biogener Sekundärer Organischer Aerosole mit Statistischen Methoden**
von C. Spindler (2010), iv, 163 Seiten
ISBN: 978-3-89336-622-4

64. **Stabile Algorithmen für die Magnetotomographie an Brennstoffzellen**
von M. Wannert (2010), ix, 119 Seiten
ISBN: 978-3-89336-623-1

65. **Sauerstofftransport und Degradationsverhalten von Hochtemperaturmembranen für CO2-freie Kraftwerke**
von D. Schlehuber (2010), VII, 139 Seiten
ISBN: 978-3-89336-630-9

66. **Entwicklung und Herstellung von foliengegossenen, anodengestützten Festoxidbrennstoffzellen**
von W. Schafbauer (2010), VI, 164 Seiten
ISBN: 978-3-89336-631-6

67. **Disposal strategy of proton irradiated mercury from high power spallation sources**
by S. Chiriki (2010), xiv, 124 pages
ISBN: 978-3-89336-632-3

68. **Oxides with polyatomic anions considered as new electrolyte materials for solid oxide fuel cells (SOFCs)**
by O. H. Bin Hassan (2010), vii, 121 pages
ISBN: 978-3-89336-633-0

69. **Von der Komponente zum Stack: Entwicklung und Auslegung von HT-PEFC-Stacks der 5 kW-Klasse**
von A. Bendzulla (2010), IX, 203 Seiten
ISBN: 978-3-89336-634-7

70. **Satellitengestützte Schwerewellenmessungen in der Atmosphäre und Perspektiven einer zukünftigen ESA Mission (PREMIER)**
von S. Höfer (2010), 81 Seiten
ISBN: 978-3-89336-637-8

71. **Untersuchungen der Verhältnisse stabiler Kohlenstoffisotope in atmosphärisch relevanten VOC in Simulations- und Feldexperimenten**
von H. Spahn (2010), IV, 210 Seiten
ISBN: 978-3-89336-638-5

72. **Entwicklung und Charakterisierung eines metallischen Substrats für nanostrukturierte keramische Gastrennmembranen**
von K. Brands (2010), vii, 137 Seiten
ISBN: 978-3-89336-640-8

73. **Hybridisierung und Regelung eines mobilen Direktmethanol-Brennstoffzellen-Systems**
von J. Chr. Wilhelm (2010), 220 Seiten
ISBN: 978-3-89336-642-2

74. **Charakterisierung perowskitischer Hochtemperaturmembranen zur Sauerstoffbereitstellung für fossil gefeuerte Kraftwerksprozesse**
von S.A. Möbius (2010) III, 208 Seiten
ISBN: 978-3-89336-643-9

75. **Characterization of natural porous media by NMR and MRI techniques: High and low magnetic field studies for estimation of hydraulic properties**
by L.-R. Stingaciu (2010), 96 pages
ISBN: 978-3-89336-645-3

76. **Hydrological Characterization of a Forest Soil Using Electrical Resistivity Tomography**
by Chr. Oberdörster (2010), XXI, 151 pages
ISBN: 978-3-89336-647-7

77. **Ableitung von atomarem Sauerstoff und Wasserstoff aus Satellitendaten und deren Abhängigkeit vom solaren Zyklus**
von C. Lehmann (2010), 127 Seiten
ISBN: 978-3-89336-649-1

78. **18th World Hydrogen Energy Conference 2010 – WHEC2010 Proceedings**
**Speeches and Plenary Talks**
ed. by D. Stolten, B. Emonts (2012)
ISBN: 978-3-89336-658-3

78-1. **18th World Hydrogen Energy Conference 2010 – WHEC2010 Proceedings**
**Parallel Sessions Book 1:**
**Fuel Cell Basics / Fuel Infrastructures**
ed. by D. Stolten, T. Grube (2010), ca. 460 pages
ISBN: 978-3-89336-651-4

78-2. **18th World Hydrogen Energy Conference 2010 – WHEC2010 Proceedings**
**Parallel Sessions Book 2:**
**Hydrogen Production Technologies – Part 1**
ed. by D. Stolten, T. Grube (2010), ca. 400 pages
ISBN: 978-3-89336-652-1

78-3. **18th World Hydrogen Energy Conference 2010 – WHEC2010 Proceedings**
**Parallel Sessions Book 3:**
**Hydrogen Production Technologies – Part 2**
ed. by D. Stolten, T. Grube (2010), ca. 640 pages
ISBN: 978-3-89336-653-8

78-4. **18th World Hydrogen Energy Conference 2010 – WHEC2010 Proceedings**
**Parallel Sessions Book 4:**
**Storage Systems / Policy Perspectives, Initiatives and Cooperations**
ed. by D. Stolten, T. Grube (2010), ca. 500 pages
ISBN: 978-3-89336-654-5

78-5. **18th World Hydrogen Energy Conference 2010 – WHEC2010 Proceedings**
**Parallel Sessions Book 5:**
**Stategic Analysis / Safety Issues / Existing and Emerging Markets**
ed. by D. Stolten, T. Grube (2010), ca. 530 pages
ISBN: 978-3-89336-655-2

78-6. **18th World Hydrogen Energy Conference 2010 – WHEC2010 Proceedings**
**Parallel Sessions Book 6:**
**Stationary Applications / Transportation Applications**
ed. by D. Stolten, T. Grube (2010), ca. 330 pages
ISBN: 978-3-89336-656-9

78 Set (complete book series)

**18th World Hydrogen Energy Conference 2010 – WHEC2010 Proceedings**
ed. by D. Stolten, T. Grube, B. Emonts (2010)
ISBN: 978-3-89336-657-6

79. **Ultrafast voltex core dynamics investigated by finite-element micromagnetic simulations**
by S. Gliga (2010), vi, 144 pages
ISBN: 978-3-89336-660-6

80. **Herstellung und Charakterisierung von keramik- und metallgestützten Membranschichten für die $CO_2$-Abtrennung in fossilen Kraftwerken**
von F. Hauler (2010), XVIII, 178 Seiten
ISBN: 978-3-89336-662-0

81. **Experiments and numerical studies on transport of sulfadiazine in soil columns**
by M. Unold (2010), xvi, 115 pages
ISBN: 978-3-89336-663-7

82. **Prompt-Gamma-Neutronen-Aktivierungs-Analyse zur zerstörungsfreien Charakterisierung radioaktiver Abfälle**
von J.P.H. Kettler (2010), iv, 205 Seiten
ISBN: 978-3-89336-665-1

83. **Transportparameter dünner geträgerter Kathodenschichten der oxidkeramischen Brennstoffzelle**
von C. Wedershoven (2010), vi, 137 Seiten
ISBN: 978-3-89336-666-8

84. **Charakterisierung der Quellverteilung von Feinstaub und Stickoxiden in ländlichem und städtischem Gebiet**
von S. Urban (2010), vi, 211 Seiten
ISBN: 978-3-89336-669-9

85. **Optics of Nanostructured Thin-Film Silicon Solar Cells**
by C. Haase (2010), 150 pages
ISBN: 978-3-89336-671-2

86. **Entwicklung einer Isolationsschicht für einen Leichtbau-SOFC-Stack**
von R. Berhane (2010), X, 162 Seiten
ISBN: 978-3-89336-672-9

87. **Hydrogen recycling and transport in the helical divertor of TEXTOR**
by M. Clever (2010), x, 172 pages
ISBN: 978-3-89336-673-6

88. **Räumlich differenzierte Quantifizierung der N- und P-Einträge in Grundwasser und Oberflächengewässer in Nordrhein-Westfalen unter besonderer Berücksichtigung diffuser landwirtschaftlicher Quellen**
von F. Wendland et. al. (2010), xii, 216 Seiten
ISBN: 978-3-89336-674-3

89. **Oxidationskinetik innovativer Kohlenstoffmaterialien hinsichtlich schwerer Lufteinbruchstörfälle in HTR´s und Graphitentsorgung oder Aufarbeitung**
von B. Schlögl (2010), ix, 117 Seiten
ISBN: 978-3-89336-676-7

90. **Chemische Heißgasreinigung bei Biomassenvergasungsprozessen**
von M. Stemmler (2010), xv, 196 Seiten
ISBN: 978-3-89336-678-1

91. **Untersuchung und Optimierung der Serienverschaltung von Silizium-Dünnschicht-Solarmodulen**
von S. Haas (2010), ii, 202 Seiten
ISBN: 978-3-89336-680-4

92. **Non-invasive monitoring of water and solute fluxes in a cropped soil**
by S. Garré (2010), xxiv, 133 pages
ISBN: 978-3-89336-681-1

93. **Improved hydrogen sorption kinetics in wet ball milled Mg hydrides**
by L. Meng (2011), II, 119 pages
ISBN: 978-3-89336-687-3

94. **Materials for Advanced Power Engineering 2010**
ed. by J. Lecomte-Beckers, Q. Contrepois, T. Beck and B. Kuhn
(2010), 1327 pages
ISBN: 978-3-89336-685-9

95. **2D cross-hole MMR – Survey design and sensitivity analysis for cross-hole applications of the magnetometric resistivity**
by D. Fielitz (2011), xvi, 123 pages
ISBN: 978-3-89336-689-7

96. **Untersuchungen zur Oberflächenspannung von Kohleschlacken unter Vergasungsbedingungen**
von T. Melchior (2011), xvii, 270 Seiten
ISBN: 978-3-89336-690-3

97. **Secondary Organic Aerosols: Chemical Aging, Hygroscopicity, and Cloud Droplet Activation**
by A. Buchholz (2011), xiv, 134 pages
ISBN: 978-3-89336-691-0

98. **Chrom-bezogene Degradation von Festoxid-Brennstoffzellen**
von A. Neumann (2011), xvi, 218 Seiten
ISBN: 978-3-89336-692-7

99. **Amorphous and microcrystalline silicon applied in very thin tandem solar cells**
by S. Schicho (2011), XII, 190 pages
ISBN: 978-3-89336-693-4

100. **Sol-gel and nano-suspension electrolyte layers for high performance solid oxide fuel cells**
by F. Han (2011), iv, 131 pages
ISBN: 978-3-89336-694-1

101. **Impact of different vertical transport representations on simulating processes in the tropical tropopause layer (TTL)**
by F. Plöger (2011), vi, 104 pages
ISBN: 978-3-89336-695-8

102. **Untersuchung optischer Nanostrukturen für die Photovoltaik mit Nahfeldmikroskopie**
von T. Beckers (2011), xiii, 128 Seiten
ISBN: 978-3-89336-696-5

103. **Impact of contamination on hydrogenated amorphous silicon thin films & solar cells**
by J. Wördenweber (2011), XIV, 138 pages
ISBN: 978-3-89336-697-2

104. **Water and Organic Nitrate Detection in an AMS: Laboratory Characterization and Application to Ambient Measurements**
by A. Mensah (2011), XI, 111 pages
ISBN: 978-3-89336-698-9

105. **Entwicklung eines neuen Konzepts zur Steuerung der thermischen Ausdehnung von glaskeramischen Verbundwerkstoffen mit angepasster Fließfähigkeit am Beispiel der Hochtemperatur-Brennstoffzelle**
von E. Wanko (2011), xi, 134 Seiten
ISBN: 978-3-89336-705-4

106. **Tomographic reconstruction of atmospheric volumes from infrared limb-imager measurements**
by J. Ungermann (2011), xiv, 153 pages
ISBN: 978-3-89336-708-5

107. **Synthese und Identifizierung von substituierten Mg-Al-Cl Doppelhydroxidverbindungen mit Schwerpunkt IR-Spektroskopie**
von B. Hansen (2011), XII, 121 Seiten
ISBN: 978-3-89336-709-2

108. **Analysis of spatial soil moisture dynamics using wireless sensor networks**
by U. Rosenbaum (2011), xxii, 120 pages
ISBN: 978-3-89336-710-8

109. **Optimierung von APS-ZrO2-Wärmedämmschichten durch Variation der Kriechfestigkeit und der Grenzflächenrauhigkeit**
von M. E. Schweda (2011), 168 Seiten
ISBN: 978-3-89336-711-5

110. **Sorption of a branched nonylphenol isomer and perfluorooctanoic acid on geosorbents and carbon nanotubes**
by C. Li (2011), X, 102 pages
ISBN: 978-3-89336-716-0

111. **Electron Transport in the Plasma Edge with Rotating Resonant Magnetic Perturbations at the TEXTOR Tokamak**
by H. Stoschus (2011), iv, 113 pages
ISBN: 978-3-89336-718-4

112. **Diffusion and Flow Investigations in Natural Porous Media by Nuclear Magnetic Resonance**
by N. Spindler (2011), viii, 144 pages
ISBN: 978-3-89336-719-1

113. **Entwicklung und Erprobung des Hygrometer for Atmospheric Investigations**
von T. Klostermann (2011), IV, 118 Seiten
ISBN: 978-3-89336-723-8

114. **Application of functional gene arrays for monitoring influences of plant/seasons on bacterial functions and community structures in constructed wetlands (Bitterfeld, Germany)**
by J. Ning (2011), xiv, 157 pages
ISBN: 978-3-89336-724-5

115. **Wasseraustrag aus den Kathodenkanälen von Direkt-Methanol-Brennstoffzellen**
von A. Schröder (2011), VII, 228 Seiten
ISBN: 978-3-89336-727-6

116. **CITYZEN Climate Impact Studies**
ed. by M. Schultz (2011), 45 pages
ISBN: 978-3-89336-729-0

117. **Software Tools zum interoperablen Austausch und zur Visualisierung von Geodatensätzen über das Internet**
von M. Schultz, M. Decker, S. Lührs (2011), iv, 156 Seiten
ISBN: 978-3-89336-730-6

118. **Optimierung eines Leichtbaudesigns für ein SOFC-Brennstoffzellenstack**
von T. Nguyen-Xuan (2011), III, 154 Seiten
ISBN: 978-3-89336-732-0

119. **Institute of Energy and Climate Research IEK-6:**
**Nuclear Waste Management & Reactor Safety Report 2009/2010**
**Material Science for Nuclear Waste Management**
ed. by M. Klinkenberg, S. Neumeier, D. Bosbach (2011), 242 pages
ISBN: 978-3-89336-735-1

120. **Fate of the Antibiotic Sulfadiazine in Yangtze River Sediments: Transformation, Sorption and Transport**
by N. Meng (2011), XII, 111 pages
ISBN: 978-3-89336-736-8

121. **Thermodynamische Eigenschaften gasförmiger und kondensierter Verbindungen für Hochtemperaturanwendungen**
von T. Markus (2011), II, 131 Seiten
ISBN: 978-3-89336-728-3

122. **Ein neues LIF-Instrument für flugzeug- und bodengebundene Messungen von OH- und $HO_2$-Radikalen in der Troposphäre**
von S. Broch (2011), IV, 160 Seiten
ISBN: 978-3-89336-742-9

123. **Processes in the Yangtze River System - Experiences and Perspectives**
Workshop-Proceedings
ed. by S. Küpper, G. Subklew, R.-D. Wilken (2011), 83 pages
ISBN: 978-3-89336-744-3

124. **Thermo-Mechanical Properties of Mixed Ion-Electron Conducting Membrane Materials**
by B. Huang (2011), 130 pages
ISBN: 978-3-89336-746-7

125. **Growth, Etching, and Stability of Sputtered ZnO:Al for Thin-Film Silicon Solar Cells**
by J. I. Owen (2011), xv, 192 pages
ISBN: 978-3-89336-749-8

126. **Entwicklung geträgerter $Ba_{0,5}Sr_{0,5}Co_{0,8}Fe_{0,2}O_{3-\delta}$ Sauerstoff-Permeationsmembranen**
von F. Schulze-Küppers (2011), ii, 119 Seiten
ISBN: 978-3-89336-752-8

127. **Development of the 2-Component-Injection Moulding for Metal Powders**
by A. P. Cysne Barbosa (2011), XIV, 150 pages
ISBN: 978-3-89336-753-5

128. **Performance of Tungsten-Based Materials and Components under ITER and DEMO Relevant Steady-State Thermal Loads**
by G. H. Ritz (2011), X, 128 pages
ISBN: 978-3-89336-755-9

129. **Experimentelle Bestimmung und numerische Simulation von Viskositäten in Schlackesystemen unter Vergasungsbedingungen**
von T. Nentwig (2011), 156 Seiten
ISBN: 978-3-89336-756-6

130. **Development of Thin Film Oxygen Transport Membranes on Metallic Supports**
by Y. Xing (2012), iv, 117 pages
ISBN: 978-3-89336-765-8

131. **Release of Inorganic Trace Elements from High-Temperature Gasification of Coal**
by M. Bläsing (2012), XVIII, 145 pages
ISBN: 978-3-89336-772-6

132. **Rauchgasseitige Korrosion von Nickelbasislegierungen für zukünftige 700°C-Dampfkraftwerke**
von F. Lüttschwager (2012), 145 Seiten
ISBN: 978-3-89336-773-3

133. **In-Situ Raman Spectroscopy: A Method to Study and Control the Growth of Microcrystalline Silicon for Thin-Film Solar Cells**
by S. Muthmann (2012), x, 134 pages
ISBN: 978-3-89336-774-0

134. **Remote sensing of sun-induced fluorescence for improved modeling of gross primary productivity in a heterogeneous agricultural area**
by A. Schickling (2012), xvi, 135 pages
ISBN: 978-3-89336-775-7

135. **Untersuchung der Ladungsträgerkonzentration und -beweglichkeit in mikrokristallinen Siliziumlegierungen mit Hall-Effekt undThermokraft**
von C. Sellmer (2012), 159 Seiten
ISBN: 978-3-89336-778-8

136. **Development of thin film inorganic membranes for oxygen separation**
by H. J. Moon (2012), XII, 118 pages
ISBN: 978-3-89336-781-8

137. **Influence of Material and Testing Parameters on the Lifetime of TBC Systems with MCrAlY and NiPtAl Bondcoats**
by P. Song (2012), V, 126 pages
ISBN: 978-3-89336-783-2

138. **Strömungsmechanische Modellierung eines Brenngaserzeugungssystems**
von F. Scharf (2012), vi, 223 Seiten
ISBN: 978-3-89336-784-9

139. **Clouds and aerosol in infrared radiative transfer calculations for the analysis of satellite observations**
by S. Grießbach (2012), viii, 169 pages
ISBN: 978-3-89336-785-6

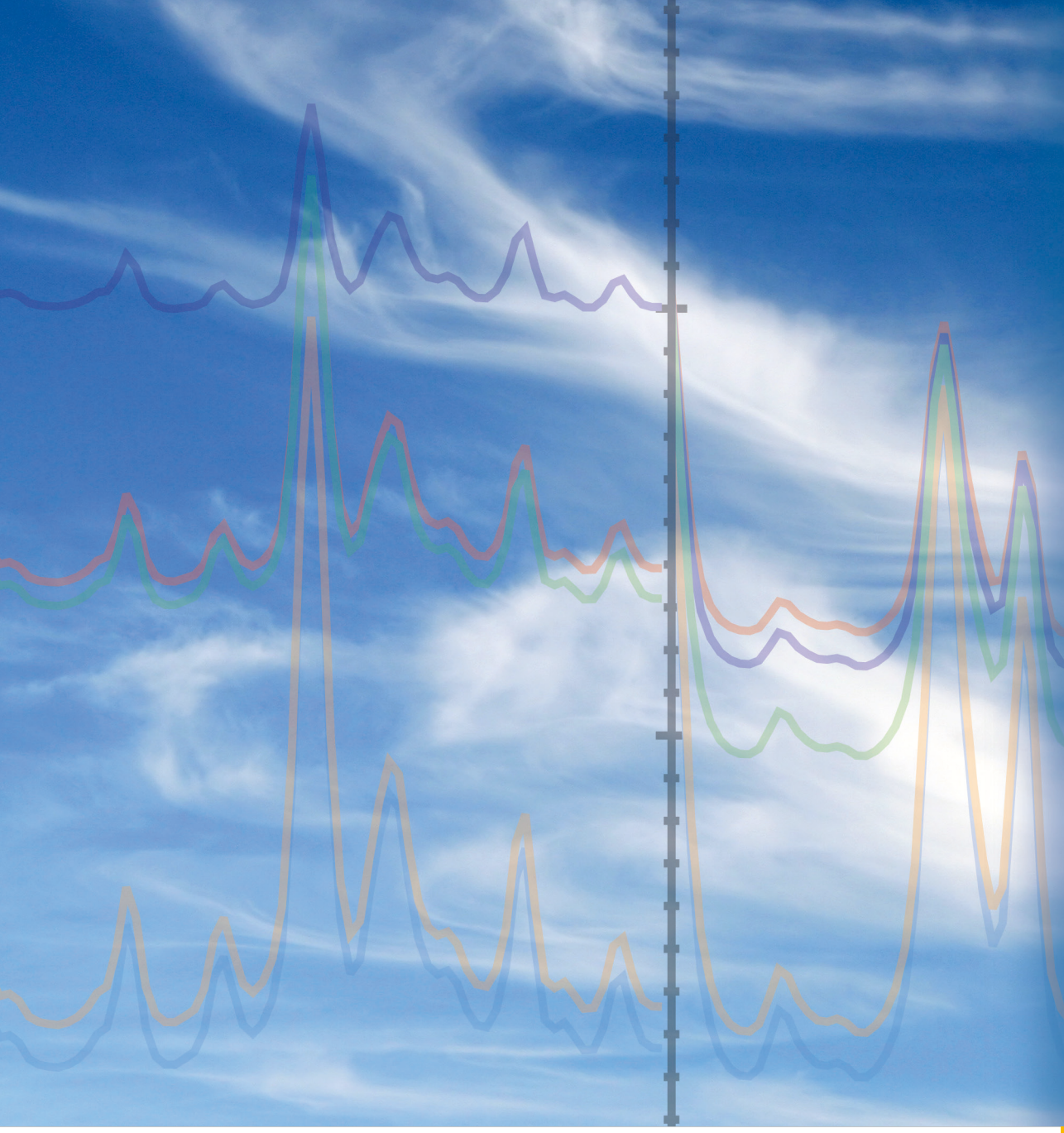

Energie & Umwelt / Energy & Environment
Band / Volume 139
ISBN 978-3-89336-785-6

JÜLICH
FORSCHUNGSZENTRUM